National Technical University of Athens

SCHOOL OF CIVIL ENGINEERING

LABORATORY OF EARTHQUAKE ENGINEERING

Doctoral Dissertation

Elastic and inelastic behaviour of rocking members of earthquake resilient structures

Evangelos Avgenakis

Civil Engineer, M.Sc. NTUA

Supervisor: Ioannis N. Psycharis, Professor NTUA

Submitted to the School of Civil Engineering, NTUA, in fulfilment of the requirements for the degree of Doctor of Philosophy

Athens, January 2020

National Technical University of Athens

SCHOOL OF CIVIL ENGINEERING

LABORATORY OF EARTHQUAKE ENGINEERING

Doctoral Dissertation

Elastic and inelastic behaviour of rocking members of earthquake resilient structures

Evangelos Avgenakis

Civil Engineer, M.Sc. NTUA

Supervisor: Ioannis N. Psycharis, Professor NTUA

Submitted to the School of Civil Engineering, NTUA, in fulfilment of the requirements for the degree of Doctor of Philosophy

Athens, January 2020

ΕΘΝΙΚΟ ΜΕΤΣΟΒΙΟ ΠΟΛΥΤΕΧΝΕΙΟ

ΣΧΟΛΗ ΠΟΛΙΤΙΚΩΝ ΜΗΧΑΝΙΚΩΝ

ΕΡΓΑΣΤΗΡΙΟ ΑΝΤΙΣΕΙΣΜΙΚΗΣ ΤΕΧΝΟΛΟΓΙΑΣ

ΔΙΔΑΚΤΟΡΙΚΗ ΔΙΑΤΡΙΒΗ

Ελαστική και ανελαστική συμπεριφορά λικνιζόμενων μελών σεισμικά ανατάξιμων κατασκευών

Ευάγγελος Αυγενάκης

Πολιτικός Μηχανικός, M.Sc. ΕΜΠ

Επιβλέπων: Ιωάννης Ν. Ψυχάρης, Καθηγητής ΕΜΠ

Υποβληθείσα στη Σχολή Πολιτικών Μηχανικών ΕΜΠ για τον επιστημονικό τίτλο του Διδάκτορα Μηχανικού

Αθήνα, Ιανουάριος 2020

National Technical University of Athens
School of Civil Engineering
Laboratory of Earthquake Engineering

Elastic and inelastic behaviour of rocking members of earthquake resilient structures

Evangelos Avgenakis
Civil Engineer, M.Sc., NTUA

Doctoral dissertation submitted to the School of Civil Engineering, NTUA in fulfilment of the requirements for the degree of Doctor of Philosophy

Advisory committee:

I. Psycharis
Professor, NTUA (Supervisor)

C. Mouzakis
Assistant Professor, NTUA

M. Fragiadakis
Assistant Professor, NTUA

Examination committee:

I. Psycharis
Professor, NTUA (Supervisor)

C. Mouzakis
Assistant Professor, NTUA

M. Fragiadakis
Assistant Professor, NTUA

G. Bouckovalas
Professor, NTUA

N. Lagaros
Associate Professor, NTUA

A. Sextos
Professor, University of Bristol, UK

I. Dimitrakopoulos
Associate Professor, Hong Kong University of Science and Technology

Στους γονείς μου,
Μανώλη και Πόπη

Ευχαριστίες

Αρχικά θα ήθελα να ευχαριστήσω θερμά τον επιβλέποντα καθηγητή μου κ. Ιωάννη Ψυχάρη για την καθοδήγηση, τη συμπαράσταση, τη βοήθεια και την εμπιστοσύνη του, τόσο για την εκπόνηση της διδακτορικής αυτής διατριβής, όσο και αρκετών άλλων ενδιαφερόντων ερευνητικών αντικειμένων με τα οποία είχα την ευκαιρία να ασχοληθώ το διάστημα αυτό. Η εκτίμησή μου προς αυτόν δεν πηγάζει μόνο από τα επιστημονικά και ακαδημαϊκά επιτεύγματά του, αλλα κυρίως από το ήθος και το χαρακτήρα του, τα οποία θεωρώ ότι συνέβαλαν καθοριστικά στην επιτυχημένη συνεργασία που είχαμε.

Στη συνέχεια θα ήθελα να ευχαριστήσω τα άλλα δύο μέλη της τριμελούς συμβουλευτικής επιτροπής, κ. Χαράλαμπο Μουζάκη και κ. Μιχαήλ Φραγκιαδάκη, με τους οποίους είχα τη χαρά να συνεργαστώ και στα πλαίσια των εκπαιδευτικών δραστηριοτήτων του εργαστηρίου όλα αυτά τα χρόνια. Θερμά ευχαριστώ επίσης τους κ. Γεώργιο Μπουκοβάλα, κ. Νικόλαο Λαγαρό, κ. Αναστάσιο Σέξτο και κ. Ηλία Δημητρακόπουλο για τη συμμετοχή τους στην επταμελή εξεταστική επιτροπή της διδακτορικής μου διατριβής.

Δεν θα μπορούσα βέβαια να μην αναφερθώ και τους ανθρώπους με τους οποίους μοιραζόμασταν καθημερινά προβληματισμούς και χαρούμενες στιγμές, κ. Ιωάννη Ταφλαμπά, Γιάννη Καλυβιώτη, Βασιλική Καρδούτσου, Χάρη Μανιατάκη, Λουτσία Καράπιττα, Λυδία Πανουτσοπούλου, Σπύρο Διαμαντόπουλο και Κωνσταντίνα Μαστροδήμου. Το χαμόγελο και η συμπαράστασή τους σε δύσκολες στιγμές συνέβαλαν στην επιτυχή ολοκλήρωση της εργασίας αυτής.

Στο σημείο αυτό θέλω να ευχαριστήσω θερμά τον καλό μου φίλο Μιχάλη, με τον οποίο μοιράστηκα κάθε καλή και κακή στιγμή της καθημερινότητάς μου όλη αυτήν την περίοδο. Η συνεχής υποστήριξη και ενθάρρυνσή του σίγουρα συνέβαλαν στο να είναι η περίοδος αυτή πιο χαρούμενη και δημιουργική.

Το μεγαλύτερο ευχαριστώ, όμως, το απευθύνω στους πιο σημαντικούς ανθρώπους της ζωής μου, τους γονείς μου Μανώλη και Πόπη, για την αγάπη και την στήριξή τους σε κάθε στιγμή και πτυχή της ζωής μου.

This research was made possible through the financial support provided by the Scholarship of the Structural Engineering Division of the School of Civil Engineering, NTUA, through the Special Account for Research Grants of NTUA.

Abstract

This dissertation presents the formulation of finite element algorithms for the prediction of the response of elastic and inelastic rocking members under static and dynamic loading. Apart from deformability along their height, the proposed formulations take the deformability of rocking members near their base into account, which is crucial for an accurate prediction of the response of rocking members under large axial forces, such as the ones used in earthquake resilient structural systems. Due to the partial loading of the rocking interface of such members, solutions regarding the semi-infinite strip from the theory of elasticity instead of the technical theory of bending are employed, since the latter cannot predict the nonlinear load distribution across the rocking interface and, as a consequence, the nonlinear stress distribution near the contact area, which is crucial for the determination of the response of deformable rocking members.

The elastic rocking member formulation is presented first, which is based on a force beam-column finite element formulation, where additional member end displacements are considered due to the partial loading of the rocking interface. This formulation is afterwards extended to include nonlinear material behaviour under monotonic loading. The nonlinear displacement distribution of the semi-infinite strip under a concentrated load at an arbitrary position across its end is examined next, for which analytical expressions are proposed. These analytical expressions are then incorporated into a macroelement formulation for cyclic response, which is based on the determination of a suitable stress distribution across the rocking interface so that the produced displacements match the target ones of the rocking surface. Finally, modifications of the previous formulation to extend its use to dynamic analyses by accounting for damping and other motion modes, namely sliding and upthrow, are presented.

The aforementioned formulations can be easily implemented in any finite element framework, such as OpenSees, and yield very fast analyses compared to conventional two-dimensional finite element codes. Comparison of the results produced by the macroelement with results from commercial finite element software and experiments show the generally very good accuracy of the produced results.

Εκτεταμένη περίληψη

Ελαστική και ανελαστική συμπεριφορά λικνιζόμενων μελών σεισμικά ανατάξιμων κατασκευών

Η παρούσα διδακτορική διατριβή παρουσιάζει τη μόρφωση αλγορίθμων πεπερασμένων στοιχείων για την περιγραφή της συμπεριφοράς ελαστικών και ανελαστικών λικνιζόμενων μελών υπό στατική και δυναμική φόρτιση. Πέρα από την παραμορφωσιμότητα κατά μήκος του μέλους, οι προτεινόμενες μορφώσεις λαμβάνουν υπόψη και την παραμορφωσιμότητα κοντά στη βάση του στοιχείου, η οποία είναι καθοριστική για την αξιόπιστη πρόβλεψη της συμπεριφοράς λικνιζόμενων μελών υπό μεγάλα αξονικά φορτία, όπως αυτά που χρησιμοποιούνται σε σεισμικά ανατάξιμα στατικά συστήματα. Λόγω της μερικής φόρτισης της διεπιφάνειας λικνισμού τέτοιων μελών, αξιοποιούνται λύσεις για την ημιάπειρη λωρίδα από τη θεωρία ελαστικότητας αντί για την τεχνική θεωρία κάμψης, καθώς η δεύτερη δεν μπορεί να προβλέψει τη μη γραμμική κατανομή τάσεων στη διεπιφάνεια και επομένως τη μη γραμμική κατανομή τάσεων κοντά στην περιοχή επαφής, η οποία είναι κρίσιμη για τον καθορισμό της συμπεριφοράς των παραμορφώσιμων λικνιζόμενων μελών.

Εισαγωγή

Η πολύπλοκη δυναμική συμπεριφορά των λικνιζόμενων σωμάτων και δομικών μελών έχει προσελκύσει το ενδιαφέρον της επιστημονικής κοινότητας τα τελευταία χρόνια, παρόλο που το φαινόμενο είναι γνωστό από την αρχαιότητα, μιας και πολλά αρχαία μνημεία έχουν χτιστεί με μέλη που επιτρέπεται να λικνίζονται.

Η λικνιστική κίνηση προκύπτει όταν ένα μέλος δεν δεσμεύεται ή δεσμεύεται μερικώς στη βάση του, έτσι ώστε να μην μπορούν να μεταβιβαστούν εφελκυστικές τάσεις διαμέσου της διεπιφάνειας, όπως θεωρείται στην κλασική τεχνική μηχανική. Όταν οι ασκούμενη οριζόντια δύναμη υπερβεί ένα όριο, το λικνιζόμενο σώμα αποσπάται από τη βάση και στρέφεται γύρω από το ένα του άκρο. Η κατακόρυφη δύναμη δρα ως δύναμη επαναφοράς που τείνει να φέρει το σώμα στην αρχική θέση ισορροπίας του.

Τα τελευταία χρόνια, αρκετές προσπάθειες έχουν γίνει για να συμπεριληφθούν λικνιζόμενα μέλη σε πραγματικές κατασκευές. Έως σήμερα, λικνιζόμενα μέλη έχουν χρησιμοποιηθεί σε βάθρα γεφυρών (σιδηροδρομική γέφυρα του South Rangitikei, Skinner κ.ά., 1980), καμινάδες (Air New Zealand Engineering Base στο Christchurch, Sharpe και Skinner, 1983) και ως υποστυλώματα ισογείου σε πληθώρα κατασκευών στη Ρωσία (Poliakov, 1974). Επιπλέον, εκτενής αναλυτική και πειραματική διερεύνηση έχει πραγματοποιηθεί σε λικνιζόμενα τοιχώματα προκατασκευασμένων κτηρίων (π.χ. Priestley, 1991, Sritharan κ.ά., 2007, Kam κ.ά., 2010, Smith κ.ά., 2010, μεταξύ άλλων). Κανονιστικές διατάξεις που αντιμετωπίζουν την εναλλακτική αυτή μέθοδο αντισεισμικού σχεδιασμού έχουν δημοσιευθεί από αρκετούς οργανισμούς (ACI 2003, fib 2003, New Zealand Standards 2006), ενώ στον Ευρωκώδικα 8 (EN 1998-1:2004), ο λικνισμός αναμένεται για μεγάλα ελαφρά οπλισμένα τοιχώματα σε ισχυρές σεισμικές διεγέρσεις. Εκτενής βιβλιογραφική επισκόπηση για τη συμπεριφορά τέτοιων ελεγχόμενων λικνιζόμενων μελών μπορεί να βρεθεί στις εργασίες των Chancellor κ.ά. (2014) και Kurama κ.ά. (2018).

Τα συμβατικά δομικά μέλη σχεδιάζονται συνήθως έτσι ώστε σταδιακά να διαρρέουν και να αναπτύσσουν βλάβες σε ένα σεισμικό γεγονός, όπως προβλέπει ο σχεδιασμός με βάση την επιτελεστικότητα. Αυτή η προσέγγιση όμως σημαίνει ότι μετά από ένα ισχυρό σεισμικό γεγονός, η κατασκευή θα πρέπει να επισκευαστεί, με σημαντικό κόστος. Επιπλέον, αν ο σεισμός είναι αρκετά ισχυρός, μπορεί να αναπτυχθούν παραμένουσες μετακινήσεις, κάνοντας τη διαδικασία επισκευής δυσκολότερη και πολυδάπανη.

Αντιθέτως, λύσεις που περιλαμβάνουν λικνιζόμενα μέλη έχουν προταθεί ώστε να επιλυθούν τα παραπάνω προβλήματα. Αρχικά, αντί για τη δημιουργία πλαστικών αρθρώσεων κοντά στα άκρα, οι οποίες θα πρέπει να επισκευαστούν μετά το σεισμικό γεγονός, τα λικνιζόμενα μέλη απλά λικνίζονται αν οι ασκούμενες δυνάμεις είναι αρκετά μεγάλες, το οποίο σημαίνει ότι η ασυνέχεια μεταξύ των δομικών μελών είναι εγγενής στο στατικό σύστημα, το οποίο έχει σχεδιαστεί για να έχει τη συμπεριφορά αυτή. Με τον τρόπο αυτό, τα λικνιζόμενα μέλη λειτουργούν ως μία μορφή μηχανικής μόνωσης, παρόμοια με τα διαρ-

ρέοντα στοιχεία, καθώς οι δυνάμεις που μεταβιβάζονται στην υπόλοιπη κατασκευή δεν μπορούν να υπερβούν το όριο που επιτρέπεται από το μηχανισμό λικνισμού. Παρομοίως με τη διαρροή, ο λικνισμός επίσης μεταβάλλει τις ιδιοσυχνότητες απόκρισης της κατασκευής, κάνοντάς την λιγότερο επιρρεπή σε συντονισμό.

Επιπροσθέτως, τα λικνιζόμενα μέλη παρουσιάζουν πολύ μικρές παραμένουσες μετακινήσεις σε σχέση με τα συμβατικά δομικά μέλη. Συνεπώς, μετά το σεισμικό γεγονός, η κατασκευή παρουσιάζει πολύ μικρής έκτασες βλάβες και σχεδόν καθόλου παραμένουσες κλίσεις, το οποίο σημαίνει ότι λίγες επισκευές θα πρέπει να γίνουν μετά το σεισμικό γεγονός για να κάνουν την κατασκευή ασφαλή ξανά, εξοικονομώντας χρόνο και χρήμα. Σε περίπτωση μετασεισμών, δε, τέτοια συστήματα που επανέρχονται από μόνα τους στην αρχική θέση ισορροπίας μπορούν να αντέξουν καλύτερα επόμενες σεισμικές διεγέρσεις από τα συμβατικά συστήματα, τα οποία θα πρέπει προηγουμένως να επιδιορθωθούν. Έτσι, τα λικνιζόμενα μέλη προτείνονται ως μια καινοτόμος μέθοδος για τη βελτίωση της σεισμικής αναταξιμότητας των κατασκευών.

Δομικά μέλη που έχουν σχεδιαστεί να λικνίζονται συνοδεύονται συνήθως από επιπρόσθετους τένοντες που διέρχονται διαμέσου των στοιχείων, οι οποίοι μπορεί να είναι μερικώς ή καθόλου συνδεδεμένοι με αυτό, συνήθως είναι προεντεταμένοι και σε κάθε περίπτωση αυξάνουν την αξονική δύναμη των μελών κατά τη διάρκεια του λικνισμού. Αυτή η επιπρόσθετη δύναμη κάνει το μέλος πιο ευσταθές και περιορίζει τον κίνδυνο ανατροπής. Η σχέση δύναμης-μετατόπισης τέτοιων συστημάτων έχει κύκλους υστέρησης μορφής «σημαίας», με το εμβαδόν της ανακυκλικής συμπεριφοράς να είναι συνήθως μικρότερο σε σχέση με αυτό των συμβατικών δομικών στοιχείων. Για το λόγο αυτό, τέτοια λικνιζόμενα μέλη συνοδεύονται συχνά από πρόσθετες διατάξεις απόσβεσης.

Παρόλο που έχουν παρουσιαστεί αρκετές αναλυτικές λύσεις σχετικά με την κίνηση του λικνιζόμενου σώματος, όπως αυτές των Housner (1963), Yim κ.ά. (1980), Psycharis και Jennings (1983), Chopra και Yim (1985), Zhang και Makris (2001), Prieto και Lourenço (2005), Dimitrakopoulos και DeJong (2012), μεταξύ άλλων, καθώς και πειραματικές διερευνήσεις και προσεγγιστικές σχέσεις για τον σχεδιασμό λικνιζόμενων συστημάτων (Priestley κ.ά., 1999, Sritharan κ.ά., 2007, Smith κ.ά., 2010, Lagomarsino, 2015, Kalliontzis και Schultz, 2017, μεταξύ άλλων), υπάρχει η ανάγκη για δημιουργία προσομοιωμάτων για την περιγραφή της συμπεριφοράς των ελεγχόμενων λικνιζόμενων μελών σε αριθμητικές αναλύσεις.

Γενικές προσεγγίσεις για την αριθμητική ανάλυση λικνιζόμενων μελών αποτελούν τα δισδιάστατα και τρισδιάστατα προσομοιώματα πεπερασμένων στοιχείων, όπου η επαφή μεταξύ των μελών λαμβάνεται υπόψη μέσω περιορισμών που υλοποιούν καταστατικές σχέσεις ή μέσω στοιχείων κόμβου, και προσομοιώματα διακριτών στοιχείων (π.χ. DEM, RBSM), στα οποία η κατασκευή προσομοιώνεται ως ένα σύνολο διακριτών σωμάτων, τα οποία αλληλεπιδρούν μεταξύ τους με κάποιον τρόπο (π.χ. Zienkiewicz και Taylor, 2005).

Τέτοιες προσεγγίσεις, όμως, θεωρούνται υπολογιστικά μη αποδοτικές για πρακτικές

αναλύσεις κατασκευών μεγάλης κλίμακας και πιο απλοποιητικές προσεγγίσεις στο πλαίσιο των μονοδιάστατων πεπερασμένων στοιχείων είναι προτιμότερες. Οι Belleri κ.ά. (2013) παρουσιάζουν και συγκρίνουν τέτοιου είδους προσεγγίσεις, συμπεριλαμβανομένων μοντέλων με στροφικό ελατήριο στη βάση του λικνιζόμενου μέλους με φαινομενολογική συμπεριφορά ροπής - στροφής, μοντέλων με στρώση κατανεμημένων ελατηρίων στη βάση χωρίς εφελκυσμό, καθώς και μοντέλα που χρησιμοποιούν διατομές με υλικό χωρίς θλίψη στη βάση. Άλλες προσεγγίσεις που έχουν προταθεί στη βιβλιογραφία συμπεριλαμβάνουν αυτές του Barthes (2012), ο οποίος προτείνει ένα στοιχείο μηδενικού μήκους που επιβάλλει τις κινηματικές σχέσεις του λικνισμού, των Penna και Galasco (2013) και Penna κ.ά. (2014), οι οποίοι αναπτύσσουν ένα μακροστοιχείο με συνολικά οκτώ βαθμούς ελευθερίας για την περιγραφή της συμπεριφοράς λικνιζόμενων πεσσών τοιχοποιίας, το οποίο συμπεριλαμβάνει στρώσεις κατανεμημένων ελατηρίων χωρίς εφελκυσμό στα άκρα του, των Vassiliou κ.ά. (2014), που υλοποιούν ένα στροφικό ελατήριο μηδενικού μήκους με υστερητική απόσβεση, των Vassiliou κ.ά. (2016), που προτείνουν ένα στοιχείο μηδενικού μήκους με διατομή που δεν αναπτύσσει εφελκυσμό για τη λικνιστική διεπιφάνεια και των Diamantopoulos και Fragiadakis (2019), οι οποίοι προσομοιώνουν διάφορες διατάξεις με λικνιζόμενα σώματα με στροφικά ελατήρια.

Οι Roh και Reinhorn (2009a), Roh και Reinhorn (2009b) και Roh και Reinhorn (2010) διερεύνησαν την εφαρμογή λικνιζομένων μελών («εξασθενημένων υποστυλωμάτων») σε κατασκευές χωρίς τένοντες, αλλά μόνο υπό το ίδιο βάρος. Αφού αναγνώρισαν τη σημασία της μη γραμμικής κατανομής τάσεων κοντά στην περιοχή επαφής, χρησιμοποιώντας μια γραμμικοποιημένη προσέγγιση της κατανομής αυτής κατέληξαν σε μία μόρφωση στοιχείου για τη μη γραμμική συμπεριφορά λικνιζόμενων μελών. Επιπλέον, συνέχισαν την έρευνά τους με την εξέταση της συμπεριφοράς σε όρους ροπής - καμπυλότητας για λικνιζόμενα μέλη, λαμβάνοντας υπόψη περισσότερα φαινόμενα, όπως τοπική σύνθλιψη κοντά στα άκρα και τη σταθεροποίηση της σχέσης ροπής - καμπυλότητας σε ανακυκλιζόμενη φόρτιση μετά τη δημιουργία βλαβών.

Ακολουθώντας τις γενικές ιδέες των παραπάνω προσομοιωμάτων, μια νέα προσέγγιση προτείνεται στην παρούσα διατριβή για τη μη γραμμική συμπεριφορά λικνιζόμενων μελών. Σε αντίθεση με τις περισσότερες προσεγγίσεις που παρουσιάζονται στη βιβλιογραφία, οι οποίες θεωρούν λικνιζόμενα μέλη με άκαμπτη βάση ή λαμβάνοντας υπόψη προσεγγιστικά την παραμορφωσιμότητα κοντά στη βάση έδρασης, στην προτεινόμενη προσέγγιση, μαζί με την παραμορφωσιμότητα κατά μήκος του μέλους, λαμβάνεται υπόψη ακριβέστερα και η παραμορφωσιμότητα κοντά στη βάση έδρασης, η οποία είναι καθοριστική για την πρόβλεψη της συμπεριφοράς λικνιζόμενων μελών σε στατικά συστήματα.

Λόγω της μερικής φόρτισης της διεπιφάνειας λικνισμού, μη γραμμικές κατανομές τάσεων αναπτύσσονται κοντά στα άκρα, οι οποίες λαμβάνονται υπόψη με το προτεινόμενο μακροστοιχείο (Σχήμα 1). Η μη γραμμικότητα αυτή σημαίνει ότι η κατανομή μετακινήσεων κατά μήκος της διατομής του μέλους είναι και αυτή μη γραμμική. Επομένως, οι

διατομές του μέλους κοντά στη διεπιφάνεια λικνισμού δεν παραμένουν επίπεδες και οι συνήθεις παραδοχές της τεχνικής θεωρίας κάμψης δεν μπορούν να εφαρμοστούν. Στην προτεινόμενη μέθοδο, η μη γραμμική κατανομή μετακινήσεων αξιοποιείται για την πρόβλεψη των μετακινήσεων στα άκρα του μέλους, οι οποίες συμπεριλαμβάνουν την επιρροή του λικνισμού, ενώ δεν υπάρχει κάποιος περιορισμός όσον αφορά τους κινηματικούς περιορισμούς (για παράδειγμα, εισαγωγή σε πλαίσιο, παρουσία τενόντων).

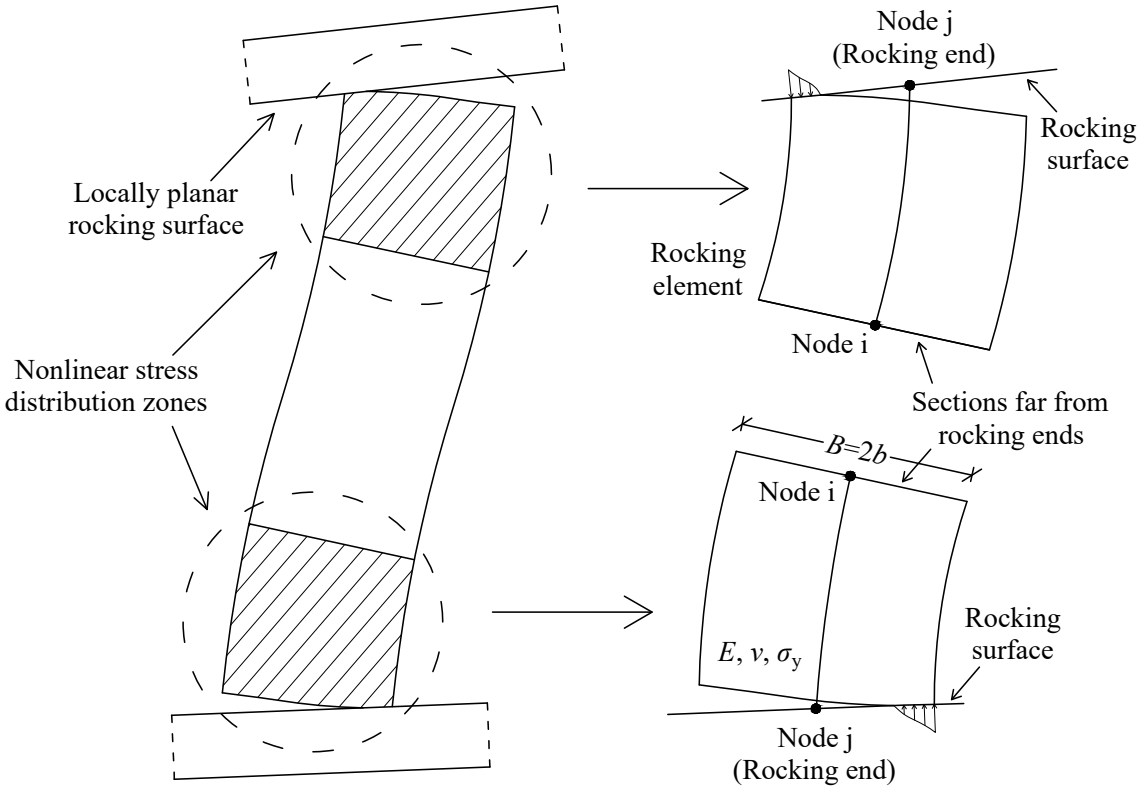

Σχήμα 1: Χρήση του μακροστοιχείου για τα τμήματα του μέλους κοντά στα λικνιζόμενα άκρα. Δύο μακροστοιχεία χρησιμοποιούνται για το λικνιζόμενο υποστύλωμα που παρουσιάζεται. Το άκρο j κάθε στοιχείου αντιστοιχεί στο λικνιζόμενο άκρο.

Η μόρφωση του ελαστικού μακροστοιχείου παρουσιάζεται πρώτα, η οποία βασίζεται στη μόρφωση στοιχείου δοκού - υποστυλώματος βασισμένο στις δυνάμεις, όπου λαμβάνονται υπόψη οι πρόσθετες μετακινήσεις στα άκρα του στοιχείου λόγω της μη γραμμικότητας τάσεων κοντά στη βάση έδρασης. Η μόρφωση αυτή επεκτείνεται στη συνέχεια για να ληφθεί υπόψη η μη γραμμικότητα υλικού σε μονοτονικές φορτίσεις. Η μη γραμμική κατανομή μετακινήσεων της ημιάπειρης λωρίδας υπό συγκεντρωμένο φορτίο σε τυχούσα θέση κατά μήκος του άκρου της εξετάζεται λεπτομερώς στη συνέχεια, για την οποία προτείνονται αναλυτικές σχέσεις. Αυτές οι σχέσεις ενσωματώνονται στη συνέχεια σε ένα μακροστοιχείο για την περιγραφή της συμπεριφοράς λικνιζόμενων σωμάτων σε ανακυκλιζόμενη φόρτιση, η οποία βασίζεται στον προσδιορισμό μίας κατάλληλης κατανομής τάσεων κατά μήκος της διεπιφάνειας λικνισμού, έτσι ώστε οι παραγόμενες μετακινήσεις να ταιριάζουν με τις στοχευόμενες. Τέλος, παρουσιάζονται τροποποιήσεις της παραπάνω

μόρφωσης για να επεκταθεί η χρήση του μακροστοιχείου και σε δυναμικές αναλύσεις, οι οποίες λαμβάνουν υπόψη κατάλληλη μορφή απόσβεσης και άλλες μορφές κίνησης, όπως η πλήρης αποκόλληση και η ολίσθηση.

Οι παραπάνω μορφώσεις μπορούν να υλοποιηθούν εύκολα σε κάποιο περιβάλλον πεπερασμένων στοιχείων, όπως το OpenSees, και δίδουν πολύ γρήγορες αναλύσεις σε σχέση με συμβατικά προσομοιώματα δισδιάστατων ή τρισδιάστατων πεπερασμένων στοιχείων. Σύγκριση των αποτελεσμάτων που παράγονται με το προτεινόμενο μακροστοιχείο με αποτελέσματα εμπορικών προγραμμάτων και πειραμάτων δείχνουν τη γενικώς πολύ καλή ακρίβεια των παραγόμενων αποτελεσμάτων.

Μόρφωση ελαστικού στοιχείου

Για να ληφθεί υπόψη η γεωμετρική μη γραμμικότητα, το στοιχείο χρησιμοποιεί την ιδέα του σωματόδετου συστήματος συντεταγμένων, το οποίο είναι ένα σύστημα χωρίς κινήσεις στερεού σώματος, οι οποίες δεν συμβάλλουν στην παραμόρφωση του μέλους. Το σύστημα αυτό έχει τρεις αντί για έξι βαθμούς ελευθερίας (Σχήμα 2). Στη βιβλιογραφία έχουν προταθεί απλές σχέσεις για τη μετάβαση από το τοπικό στο σωματόδετο σύστημα (π.χ. Neuenhofer και Filippou, 1998), οι οποίες για μετρίως μικρές μετακινήσεις δίνονται από τις σχέσεις (2.1) και (2.3). Για ένα συμβατικό ελαστικό μέλος, η σχέση δυνάμεων - μετακινήσεων στο σωματόδετο σύστημα είναι αυτή μίας αμφιέρειστης δοκού και δίνεται από την Εξ. (2.7).

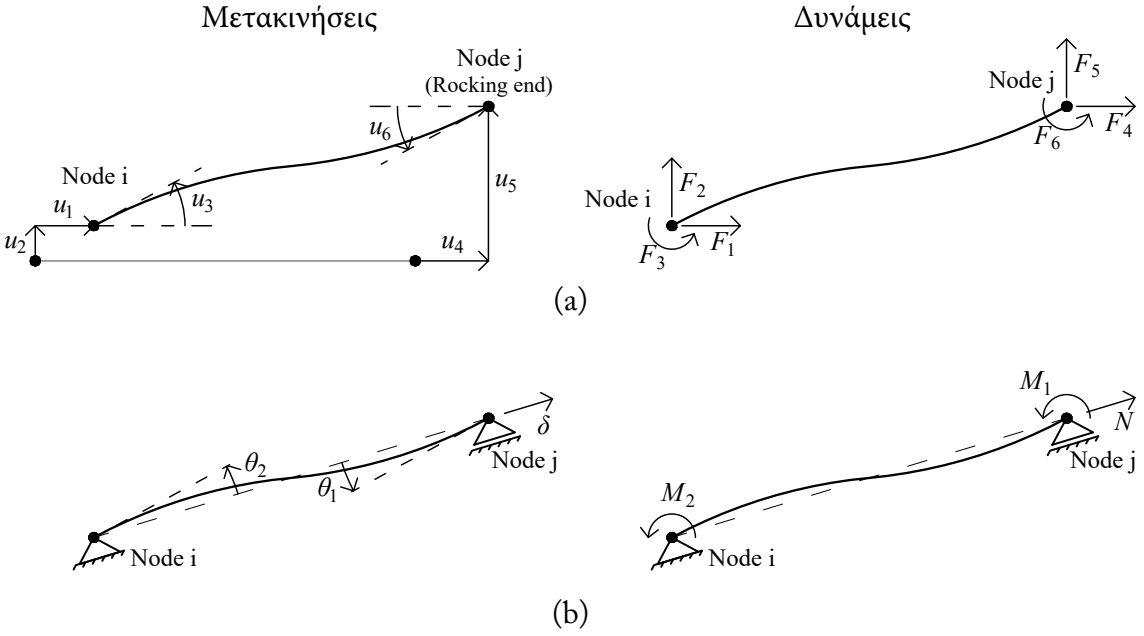

Σχήμα 2: Μετακινήσεις και δυνάμεις στο (a) τοπικό και στο (b) σωματόδετο σύστημα συνεταγμένων.

Σημειώνεται ότι το άκρο *i* του σώματος αντιστοιχεί στο άκρο με τη συμβατική συμπεριφορά, ενώ το άκρο *j* είναι το λικνιζόμενο άκρο του σώματος, που αναφέρεται όμως στην κίνηση της λικνιστικής επιφάνειας και όχι το ίδιο το άκρο του σώματος.

Εφόσον η αξονική δύναμη στο λικνιζόμενο άκρο βρίσκεται εντός του πυρήνα της διατομής (Εξ. 2.9), δεν υπάρχει λικνισμός. Αλλιώς στη διεπιφάνεια αυτή αναπτύσσεται μη γραμμική κατανομή τάσεων, η οποία είναι μηδενική σε ένα τμήμα της διατομής. Γίνεται η παραδοχή ότι η κατανομή των ορθών τάσεων στη διεπιφάνεια έχει τριγωνική μορφή, ενώ η κατανομή των διατμητικών τάσεων έχει παραβολική μορφή. Για να εξεταστεί η επιρροή της μερικής φόρτισης της βάσης έδρασης, γίνεται διαχωρισμός των παραπάνω κατανομών σε κατανομές που προβλέπει η τεχνική θεωρία κάμψης, βάσει των συνισταμένων δυνάμεων, και σε κατανομές αυτοϊσορροπούμενων τάσεων, που αν και δεν παράγουν συνισταμένες δυνάμεις, επηρεάζουν εντούτοις τις μετακινήσεις κοντά στη βάση έδρασης (Σχήμα 3).

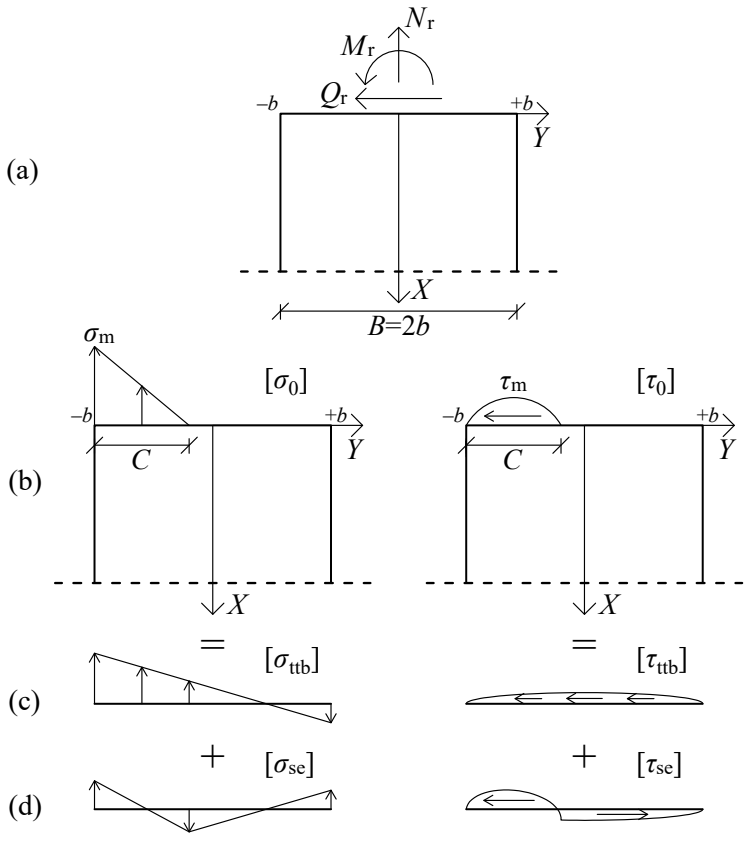

Σχήμα 3: (a) Συνισταμένες δυνάμεις στην επιφάνεια επαφής, (b) Κατανομές ορθών και διατμητικών τάσεων στη διεπιφάνεια, (c) Τάσεις βάσει της τεχνικής θεωρίας κάμψης και (d) Αυτοϊσορροπούμενες τάσεις.

Για να εξεταστεί η επιρροή των αυτοϊσορροπούμενων τάσεων, μελετάται εναλλακτικά το πρόβλημα της ημιάπειρης λωρίδας που φορτίζεται με κατανομές αυτοϊσορροπούμενων τάσεων στο άκρο της (Σχήμα 4). Ο παραλληλισμός αυτός ισχύει για την περιοχή κοντά στη βάση έδρασης, καθώς οι συνισταμένες δυνάμεις των αυτοϊσορροπούμενων κατανο-

μών τάσεων είναι μηδενικές, επομένως σύμφωνα με την αρχή Saint - Venant η επιρροή τους μακριά από την περιοχή φόρτισης είναι αμελητέα, δηλαδή θεωρούμε ότι παύει σε ένα πεπερασμένο μήκος από την περιοχή φόρτισης.

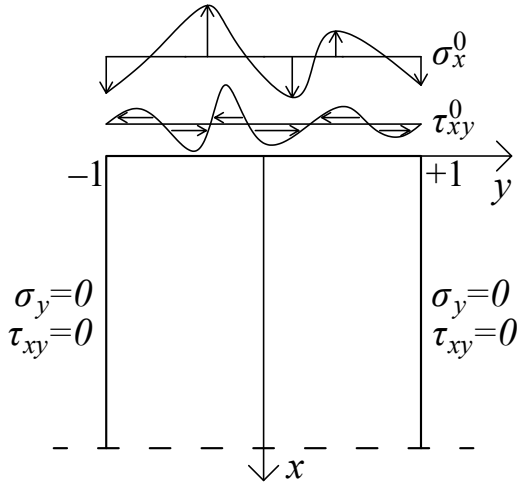

Σχήμα 4: Η ημιάπειρη λωρίδα.

Για να μελετηθεί λοιπόν η συμπεριφορά της ημιάπειρης λωρίδας στις ασκούμενες αυτοϊσορροπούμενες κατανομές τάσεων, επιστρατεύονται λύσεις από τη θεωρία ελαστικότητας και πιο συγκεκριμένα η αριθμητική μέθοδος των Gaydon και Shepherd (1964), η οποία περιγράφεται και επεκτείνεται στο αντίστοιχο κεφάλαιο της διδακτορικής διατριβής. Στη συνέχεια αξιοποιείται για να προσδιοριστούν η πρόσθετη μετακίνηση και στροφή του λικνιζόμενου άκρου που προκαλούνται από τις τυπικές κατανομές ορθών και διατμητικών τάσεων που ασκούνται στη διεπιφάνεια λικνισμού, ως η κεντρική τιμή και η κλίση, αντίστοιχα, της βέλτιστης γραμμικής κατανομής που διέρχεται από τη δημιουργούμενη μη γραμμική κατανομή μετακινήσεων κάτω από την περιοχή φόρτισης της λικνιστικής βάσης (Σχήμα 2.5). Οι μετακινήσεις αυτές στο κανονικοποιημένο σύστημα συντεταγμένων της ημιάπειρης λωρίδας προσεγγίζονται από πολυωνυμικές συναρτήσεις και δίνονται από την Εξ. (2.51).

Ο αλγόριθμος του ελαστικού μακροστοιχείου δίδεται στον Πίνακα 2.3, όπου περιγράφεται η εκτέλεση επαναλήψεων σε κάθε βήμα για δεδομένες μετακινήσεις στα άκρα του στοιχείου, το οποίο περιλαμβάνει προσδιορισμό των παραμέτρων των τυπικών κατανομών στο λικνιζόμενο άκρο του στοιχείου βάσει του δοκιμαστικού διανύσματος δυνάμεων, τον προσδιορισμό των πρόσθετων μετακινήσεων λόγω αυτοϊσορροπούμενων τάσεων στο κανονικοποιημένο και στο σωματόδετο σύστημα συντεταγμένων, τον προσδιρισμό του αντίστοιχου μητρώου ευκαμψίας και το συνδυασμό τους με τις αντίστοιχες μετακινήσεις και το μητρώο ευκαμψίας της συμβολής των συνισταμένων δυνάμεων, έτσι ώστε τελικά να υπάρχει σύγκλιση στο θεωρούμενο διάνυσμα δυνάμεων. Τελικά, το μακροστοιχείο επιστρέφει στο πρόγραμμα πεπερασμένων στοιχείων τις δυνάμεις και το αντίστοιχο μητρώο δυσκαμψίας στο τοπικό σύστημα συντεταγμένων.

Τα παραδείγματα που εξετάζονται αφορούν σε ένα λικνιζόμενο σώμα υπό σταθερό αξονικό φορτίο (Σχ. 5), λικνιζόμενο σώμα με τένοντα που εκτελεί ελεγχόμενο λικνισμό (Σχ. 2.10), καθώς και ένα πλαίσιο με ενσωματωμένο λικνιζόμενο τοίχωμα (Σχ. 2.11, 2.12). Τα αποτελέσματα που παράγονται από το προτεινόμενο μακροστοιχείο για τις παραπάνω διατάξεις συγκρίνονται με αυτά του εμπορικού προγράμματος *Abaqus*, όπου φανερώνεται η πολύ καλή ακρίβεια των αποτελεσμάτων του παραγόμενου μακροστοιχείου, ακόμα και στις παραπάνω περιπτώσεις που υπάρχει αλληλεπίδραση της λικνιστικής κίνησης με αυτήν των στοιχείων που επιβάλλουν περιορισμούς σε αυτήν. Στη συνέχεια (Σχ. 2.13 - 2.30) εξετάζεται η επιρροή διαφόρων παραμέτρων των παραπάνω διατάξεων στη συμπεριφορά του συστήματος, ενώ γίνεται και μία πρώτη διερεύνηση για την ευνοϊκή επιρροή που μπορεί να έχει η ύπαρξη λικνιζομένων τοιχωμάτων σε πλαίσια με ψευδοστατικές αναλύσεις για σεισμική διέγερση.

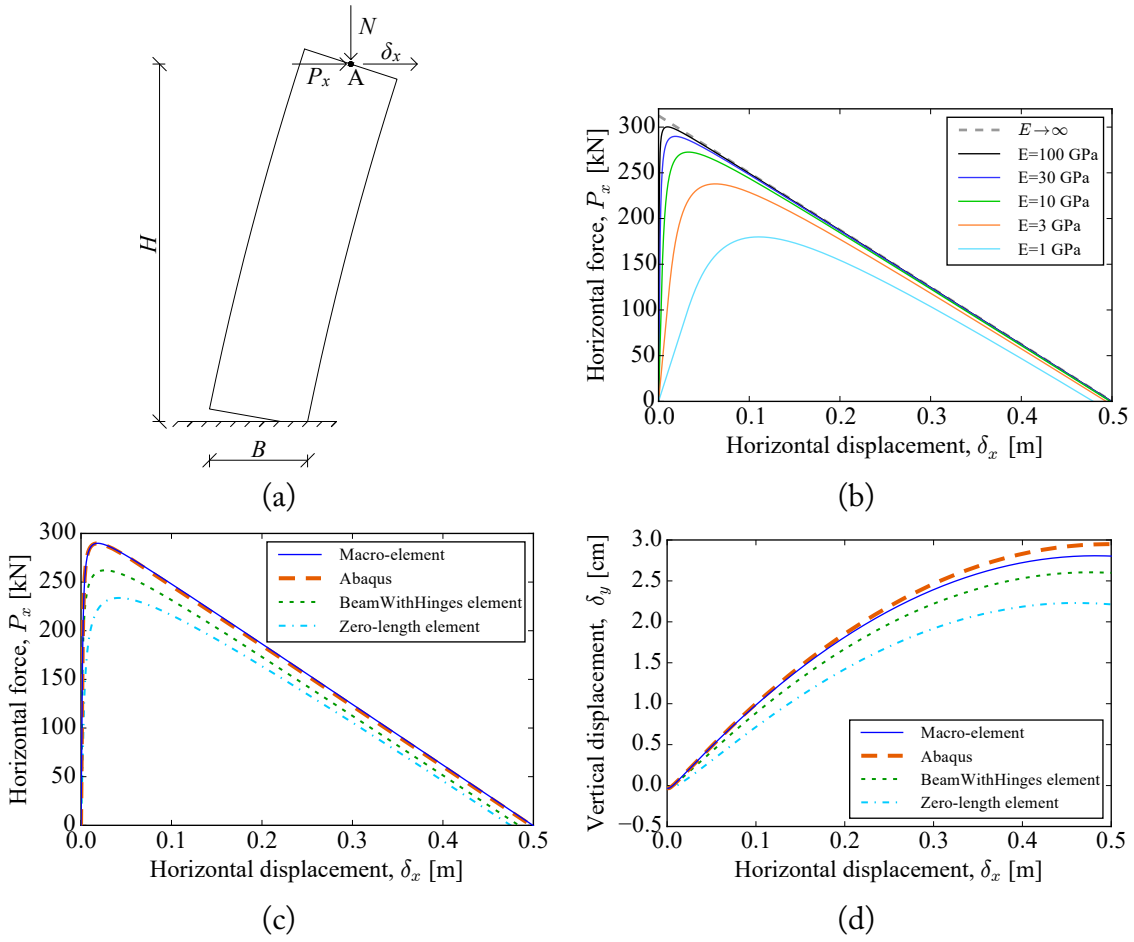

Σχήμα 5: (a) Προσομοίωμα λικνιζόμενου σώματος υπό σταθερή κατακόρυφη δύναμη, (b) Καμπύλες ικανότητας για διάφορες τιμές μέτρου ελαστικότητας, E, (c) Καμπύλες ικανότητας για $E = 30$ GPa, όπως προβλέπονται από το προτεινόμενο μακροστοιχείο, το πρόγραμμα Abaqus και απλοποιητικά προσομοιώματα και (d) Κατακόρυφη μετατόπιση όπως προβλέπεται από τα παραπάνω προσομοιώματα.

Μόρφωση ανελαστικού στοιχείου υπό μονοτονική φόρτιση

Στη συνέχεια, η μόρφωση που παρουσιάστηκε παραπάνω επεκτείνεται, έτσι ώστε να μπορεί να περιγραφεί η συμπεριφορά ανελαστικών σωμάτων με ελαστικό - τελείως πλαστικό νόμο υλικού υπό μονοτονική φόρτιση. Η βασική διαφορά σε σχέση με προηγουμένως είναι ότι πλέον η κατανομή των ορθών τάσεων παύει να είναι τριγωνική, αλλά γίνεται τραπεζοειδής.

Για το λόγο αυτό, εισάγεται μία επιπλέον παράμετρος μ (Εξ. 3.1), που περιγράφει το λόγο της θλιβόμενης ζώνης που βρίσκεται υπό διαρροή σε σχέση με το συνολικό μήκος της θλιβόμενης ζώνης. Η τραπεζοειδής φόρτιση μπορεί να θεωρηθεί ως διαφορά δύο τριγωνικών φορτίσεων (Σχ. 3.1), ενώ η παρατήρηση αυτή επεκτείνεται και στις αντίστοιχες διατμητικές φορτίσεις, όπου γίνεται και η επιπλέον υπόθεση ότι ο λόγος των μέγιστων ορθών τάσεων των παραπάνω τριγωνικών κατανομών ισούται με το λόγο των μέγιστων διατμητικών τάσεων των αντίστοιχων παραβολικών. Έτσι, μπορούν πλέον να εκφραστούν οι συνισταμένες δυνάμεις στο λικνιζόμενο άκρο του μέλους συναρτήσει του λόγου μ (Εξ. 3.2, 3.3, 3.4).

Οι πρόσθετες μετακινήσεις λόγω των παραπάνω κατανομών φόρτισης του στοιχείου υπό διαρροή υπολογίζονται με τρόπο παρόμοιο με αυτόν του ελαστικού υλικού, με τη διαφορά ότι πλέον οι παράμετροι της βέλτιστης γραμμικής κατανομής υπολογίζονται οχι βάσει της μη γραμμικής κατανομής μετακινήσεων στην περιοχή επαφής, αλλά μόνο στο τμήμα της που παραμένει ελαστικό, καθώς στο υπόλοιπο εμφανίζονται και πλαστικές μετακινήσεις. Με τον τρόπο αυτό εξάγεται η Εξ. (3.9) για την προσέγγιση των παραπάνω μετακινήσεων από αναλυτικές συναρτήσεις. Η σχέση αυτή, όπως και το αντίστοιχο μητρώο ευκαμψίας αντικαθιστά τις αντίστοιχες εξισώσεις που χρησιμοποιήθηκαν στη μόρφωση του ελαστικού στοιχείου.

Στα παραδείγματα του κεφαλαίου αυτού παρουσιάζεται η συμπεριφορά ενός λικνιζόμενου σώματος υπό σταθερή κατακόρυφη φόρτιση για διάφορες τιμές τάσης διαρροής (Σχ. 6), ενώ τα αποτελέσματα που προέκυψαν για τις μετακινήσεις στο σωματόδετο σύστημα συγκρίνονται με αυτά που προκύπτουν από το πρόγραμμα Abaqus (Σχ. 3.6, 3.7), φανερώνοντας την πολύ καλή ταύτιση των παραγόμενων αποτελεσμάτων με τις παραπάνω θεωρήσεις.

Μη γραμμική κατανομή μετακινήσεων της ημιάπειρης λωρίδας

Για τη γενίκευση της μόρφωσης του μακροστοιχείου σε ανελαστικά σώματα υπό ανακυκλιζόμενη φόρτιση, δεν μπορεί να εφαρμοστεί μεθοδολογία ανάλογη με τις προηγούμενες, λόγω της πολυπλοκότητας των κατανομών τάσεων και πλαστικών μετακινήσεων που δημιουργούνται κατά τις ανακυκλίσεις. Για τη μόρφωση του στοιχείου για ανακυκλιζόμενη φόρτιση, λοιπόν, θα πρέπει να προηγηθεί η λεπτομερής εξέταση της μη γραμμικής

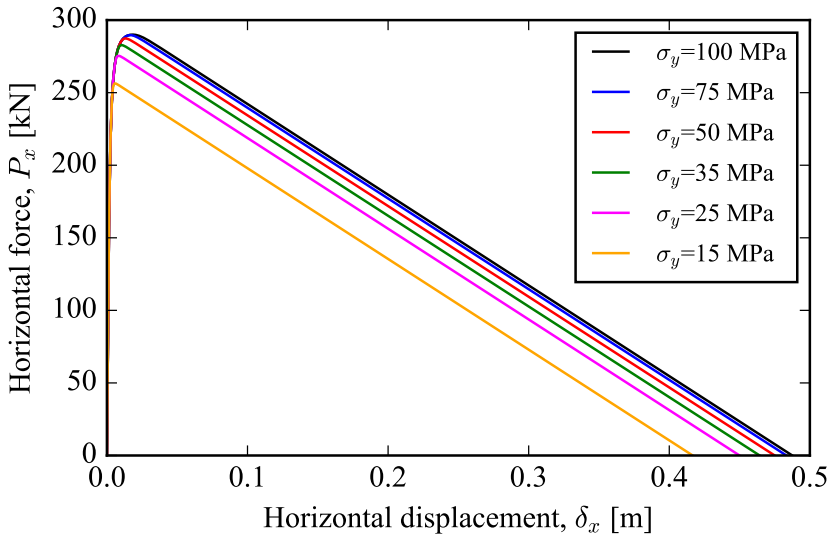

Σχήμα 6: Καμπύλες ικανότητας λικνιζόμενου σώματος υπό σταθερή κατακόρυφη δύναμη για διάφορες τιμές τάσης διαρροής, σ_y.

κατανομής μετακινήσεων της ημιάπειρης λωρίδας (Σχ. 4) υπό τυχούσα κατανομή ασκούμενων αυτοϊσορροπούμενων ορθών τάσεων στο άκρο της.

Αρχικά, εξετάζεται το απλούστερο πρόβλημα του προσδιορισμού της κατανομής μετακινήσεων λόγω αυτοϊσορροπούμενων τάσεων για συγκεντρωμένο φορτίο σε τυχούσα θέση στο άκρο της ημιάπειρης λωρίδας. Για τον αριθμητικό υπολογισμό της κατανομής αυτής, εφαρμόζεται και πάλι η μεθοδολογία των Gaydon και Shepherd (1964). Επιπλέον, εξετάζονται ξεχωριστά το συμμετικό και το αντισυμμετρικό πρόβλημα (Σχ. 4.3), για κάθε ένα από τα οποία γίνεται προσπάθεια προσδιορισμού αναλυτικών συναρτήσεων που προσεγγίζουν ορθότερα τα αριθμητικά αποτελέσματα. Οι εικόνες των τιμών των μετακινήσεων για κάθε θέση μετακίνησης και κάθε θέση ασκούμενου συγκεντρωμένου φορτίου παρουσιάζονται στα Σχήματα 7a και 7b, αντίστοιχα.

Σημειώνεται ότι η κατανομή μετακινήσεων που θα προκύψει για τα δύο παραπάνω προβλήματα θα πρέπει να ικανοποιεί διάφορους περιορισμούς. Αρχικά, θα πρέπει να ικανοποιούνται οι περιορισμοί συμμετρίας των αντίστοιχων προβλημάτων, αλλά και η ιδιότητα του θεωρήματος Maxwell-Betti που ισχύει και στην περίπτωση αυτή (Εξ. 4.5, 4.15, αντίστοιχα για το συμμετρικό και το αντισυμμετρικό πρόβλημα). Οι παραπάνω συμμετρίες φαίνονται καθαρά στο Σχ. 7. Ακόμα, επειδή οι ασκούμενες κατανομές τάσεων που εξετάζονται είναι αυτοϊσορροπούμενες, δηλαδή οι συνισταμένες δυνάμεις είναι μηδενικές, αυτό σημαίνει ότι και τα ολοκληρώματα μηδενικής και πρώτης τάξης των μετακινήσεων θα πρέπει να είναι και αυτά μηδενικά (Εξ. 4.3, 4.4).

Ο προσδιορισμός των ζητούμενων αναλυτικών συναρτήσεων γίνεται σταδιακά, αναγνωρίζοντας σε κάθε στάδιο τη βασική μορφή της κατανομής των μετακινήσεων, οι οποίες όμως παρουσιάζουν και χαρακτηριστικές μορφές ασυνέχειας. Σε πρώτο στάδιο, αναγνω-

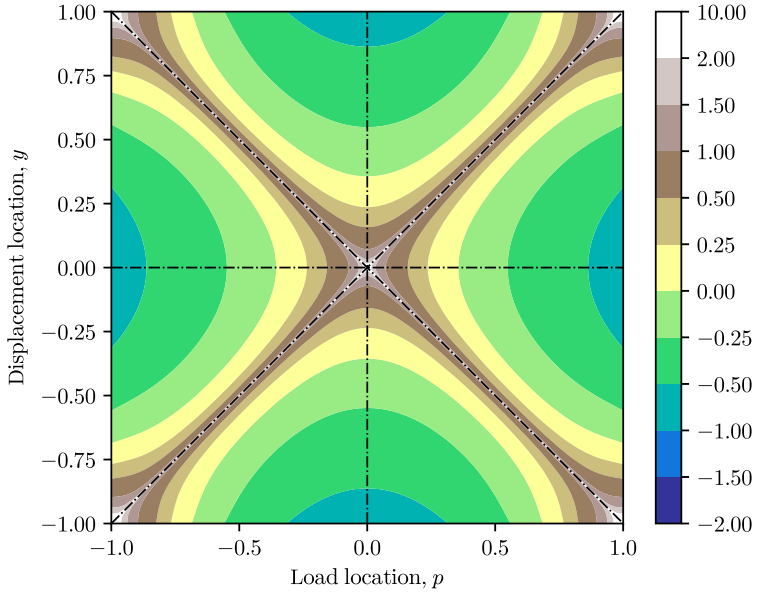

(a)

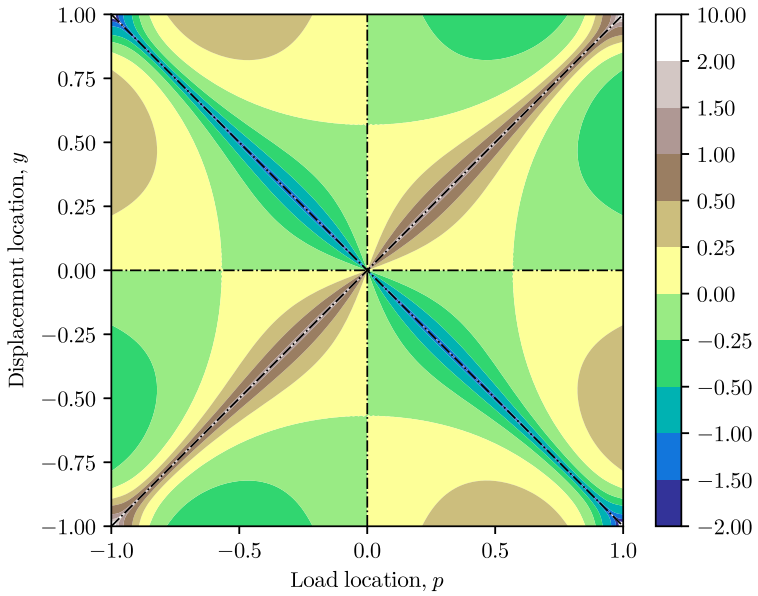

(b)

Σχήμα 7: Συναρτήσεις μετακίνησης της ημιάπειρης λωρίδας για (a) το συμμετρικό και (b) το αντισυμμετρικό πρόβλημα.

ρίζεται η σχέση που υπάρχει μεταξύ του προβλήματος της ημιάπειρης λωρίδας με αυτό του ημιάπειρου χώρου που χρησιμοποιείται συχνά σε γεωτεχνικά προβλήματα, καθώς η βασική μορφή της συνάρτησης που κυριαρχεί είναι η λογαριθμική κατανομή μετακινήσεων του ημιχώρου υπό συγκεντρωμένο φορτίο (Εξ. 4.7), η οποία για το συμμετικό και το αντισυμμετρικό πρόβλημα αντιστοιχεί στις Εξ. (4.8) και (4.17), αντίστοιχα. Αν αφαιρεθούν οι λογαριθμικές αυτές συναρτήσεις από τις αρχικές κατανομές (Σχ. 4.6, 4.9), φαίνεται ότι

εξαφανίζονται οι ασυνέχειες που παρατηρούνται στις διαγωνίους.

Επειδή όμως τα ολοκληρώματα που παράγουν οι παραπάνω συναρτήσεις κατά μήκος της ημιάπειρης λωρίδας δεν είναι μηδενικά, όπως απαιτείται, εισάγονται επιπλέον οι συναρτήσεις των Εξ. (4.10) και (4.19), αντίστοιχα, οι οποίες εξισορροπούν τα ολοκληρώματα των παραπάνω συναρτήσεων. Αφαιρώντας τις συναρτήσεις αυτές από τις αρχικές κατανομές μετακινήσεων, προκύπτουν οι εικόνες των Σχ. 4.7 και 4.10, αντίστοιχα.

Για τις εναπομένουσες κατανομές μετακινήσεων, αναγνωρίζεται ότι εξακολουθεί να υπάρχει μία λογαριθμική μορφή ασυνέχειας για μετακίνηση και φόρτιση κοντά στα άκρα της ημιάπειρης λωρίδας. Για το λόγο αυτό, δοκιμάζεται η χρήση των συναρτήσεων των Εξ. (4.11) και (4.20), με τις αντίστοιχες συναρτήσεις εξισορρόπησης ολοκληρωμάτων των Εξ. (4.12) και (4.21), μαζί με τις συμμετικές και αντισυμμετρικές πολυωνυμικές συναρτήσεις των Εξ. (4.13) και (4.22), αντίστοιχα για το συμμετρικό και το αντισυμμετρικό πρόβλημα. Για τον προσδιορισμό των βέλτιστων συντελεστών των παραπάνω συναρτήσεων χρησιμοποιούνται οι αλγόριθμοι βελτιστοποίησης της βιβλιοθήκης επιστημονικών υπολογισμών *SciPy* σε γλώσσα *Python*.

Η τελική συνάρτηση που περιγράφει τη μετακίνηση σε μία θέση y της ημιάπειρης λωρίδας για μοναδιαίο συγκεντρωμένο φορτίο στη θέση p παρουσιάζεται στην Εξ. 4.24, ενώ ενδεικτικές μορφές κατανομών μετακινήσεων παρουσιάζονται στο Σχ. 8, όπου φαίνεται και η πολύ καλή ταύτιση μεταξύ των αριθμητικών αποτελεσμάτων και της προτεινόμενης αναλυτικής σχέσης.

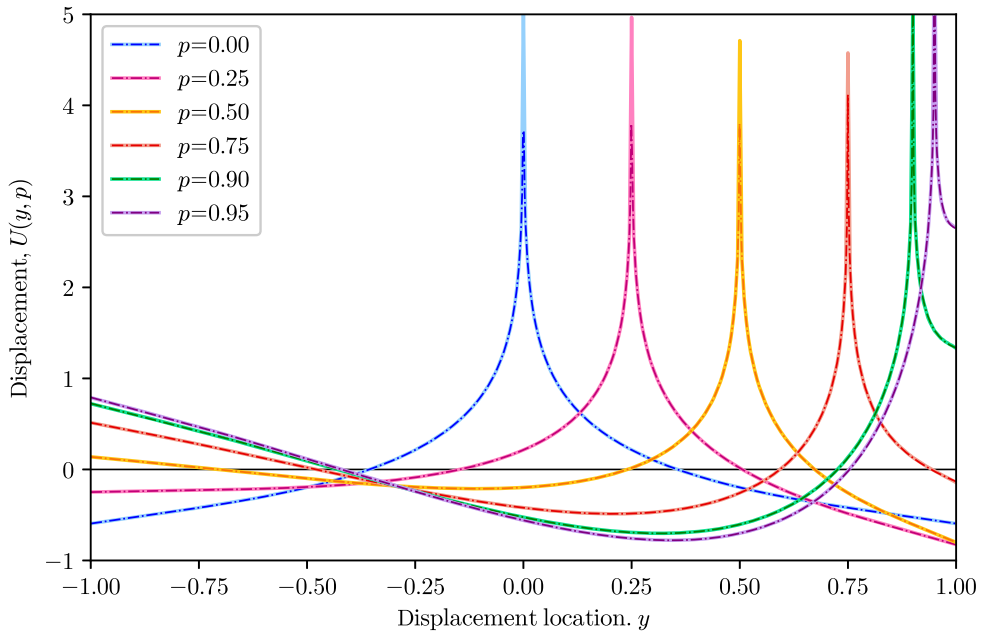

Σχήμα 8: Κατανομή μετακινήσεων για διάφορες θέσεις μοναδιαίας συγκεντρωμένης φόρτισης: Σύγκριση αριθμητικών αποτελεσμάτων (συμπαγείς γραμμές) με την προτεινόμενη αναλυτική έκφραση (διακεκομμένες γραμμές).

Στη συνέχεια, εξετάζονται οι περιπτώσεις ορθογωνικής και τριγωνικής φόρτισης (Σχ. 4.13), οι οποίες μπορούν να θεωρηθούν ως ολοκληρώματα συνεχών συγκεντρωμένων φορτίων (Εξ. 4.29 και 4.31, αντίστοιχα), με τα ολοκληρώματα των συναρτήσεων να δίδονται στο Παράρτημα 4.Α. Ενδεικτικές μορφές μετακινήσεων για τις παραπάνω φορτίσεις παρουσιάζονται στα Σχ. 4.14 και 4.16, αντίστοιχα.

Βάσει των παραπάνω συναρτήσεων μπορεί πλέον να εξεταστεί ακριβέστερα η συμπεριφορά του λικνιζόμενου σώματος. Πιο συγκεκριμένα, ως εφαρμογή του κεφαλαίου αυτού εξετάζεται η κατανομή τάσεων που ασκείται στη διεπιφάνεια, καθώς και η κατανομή μετακινήσεων του σώματος που δεν βρίσκεται σε επαφή με την επιφάνεια λικνισμού. Για τον παραπάνω σκοπό, πραγματοποιείται διακριτοποίηση της περιοχής επαφής σώματος - βάσης, ενώ υπολογίζονται οι τιμές των τάσεων στα ενδιάμεσα σημεία, έτσι ώστε η κατανομή μετακινήσεων στην περιοχή αυτή να είναι γραμμική, η οποία αντιστοιχεί σε επίπεδη επιφάνεια λικνισμού. Για τον υπολογισμό των μετακινήσεων για την τμηματικά αυτή γραμμική κατανομή τάσεων, γίνεται διαχωρισμός της σε τριγωνικές κατανομές, για τις οποίες οι μετακινήσεις μπορούν να υπολογιστούν αναλυτικά βάσει των συναρτήσεων που προέκυψαν παραπάνω.

Εφαρμόζοντας την παραπάνω διαδικασία για διάφορες τιμές μήκους επαφής σώματος - βάσης, προκύπτουν οι κατανομές τάσεων του Σχ. 9 και οι κατανομές μετακινήσεων της βάσης του σώματος που δεν βρίσκεται σε επαφή με τη βάση έδρασης του Σχ. 4.21, όπου φαίνεται ότι και στις δύο περιπτώσεις οι κατανομές είναι αρκετά μη γραμμικές. Παρόλα αυτά, επιβεβαιώνεται ότι οι πρόσθετες μετακινήσεις που χρησιμοποιούνται για τη μόρφωση του ελαστικού στοιχείου με τη διαδικασία προσέγγισης της μη γραμμικής κατανομής μετακινήσεων για γραμμική θεωρούμενη φόρτιση, βρίσκονται πολύ κοντά στις πραγματικές τιμές (Σχ. 4.23).

Μόρφωση ανελαστικού στοιχείου υπό ανακυκλιζόμενη φόρτιση

Έχοντας διατυπώσει αναλυτικές εκφράσεις για τη μη γραμμική κατανομή μετακινήσεων που παράγει μία τυχούσα φόρτιση ορθών τάσεων στο άκρο της ημιάπειρης λωρίδας, οι εκφράσεις αυτές μπορούν να αξιοποιηθούν και να ενσωματωθούν στον αλγόριθμο ενός μακροστοιχείου για την περιγραφή της στατικής ανακυκλιζόμενης συμπεριφοράς λικνιζόμενων σωμάτων.

Όπως αναφέρθηκε προηγουμένως, ενώ για μονοτονικές φορτίσεις η υπόθεση τυπικών κατανομών ασκούμενων τάσεων και η γραμμικοποίηση των παραγόμενων μη γραμμικών κατανομών μετακινήσεων παράγει ικανοποιητικά αποτελέσματα, στην περίπτωση της ανακυκλιζόμενης φόρτισης, λόγω της πολυπλοκότητας των κατανομών τάσεων και δημιουργούμενων πλαστικών μετακινήσεων, μία τέτοια προσέγγιση με υπόθεση γραμμι-

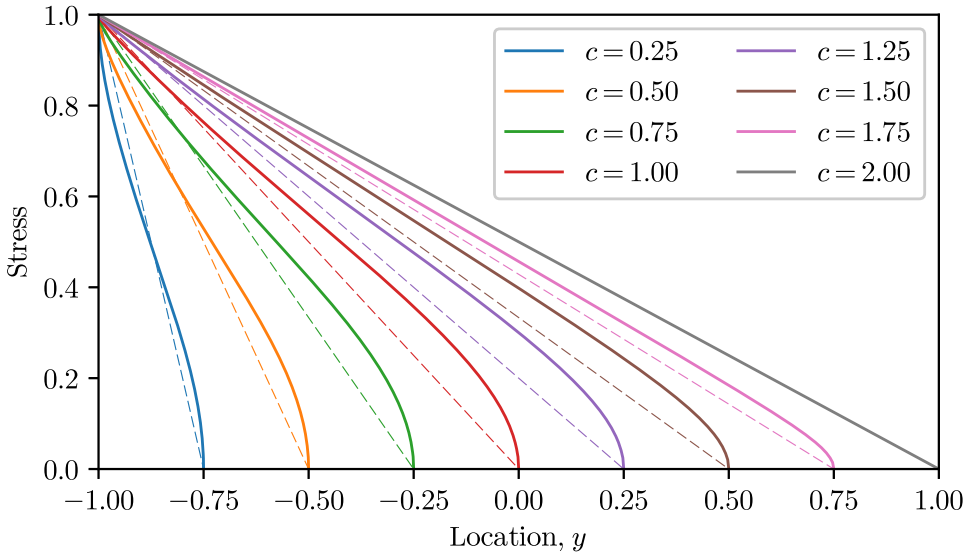

Σχήμα 9: Κατανομή τάσεων για διάφορα μήκη επαφής, c, οι οποίες προκαλούν γραμμική κατανομή μετακινήσων κάτω από τη φόρτιση. Οι αντίστοιχες γραμμικές κατανομές τάσεων για κάθε μήκος επαφής σημειώνονται με διακεκομμένες γραμμές.

κής κατανομής ανηγμένων παραμορφώσεων στη διεπιφάνεια δημιουργεί προβλήματα.

Για το λόγο αυτό, η αντιμετώπιση της περίπτωσης της ανακυκλιζόμενης φόρτισης ακολουθεί μία διαφορετική τακτική: Σε κάθε βήμα γίνεται προσδιορισμός μίας κατάλληλης κατανομής ασκούμενων ορθών τάσεων, έτσι ώστε οι παραγόμενες μετακινήσεις της διεπιφάνειας λικνισμού να ταυτίζονται με τις στοχευόμενες μετακινήσεις για τη θέση αυτή που απαιτεί το πρόγραμμα πεπερασμένων στοιχείων. Στο Σχ. 10 φαίνονται η αρχική και παραμορφωμένη θέση του λικνιζόμενου σώματος και της λικνιστικής επιφάνειας. Η γραμμοσκιασμένη περιοχή αντιστοιχεί στην παραμορφωμένη θέση του σώματος, όπου παρουσιάζονται μόνο οι παραμορφώσεις παράλληλα στη φόρτιση για ευκρίνεια. Οι ορθές τάσεις, $[\sigma]$, καθώς και οι διατμητικές τάσεις, οι οποίες ασκούνται στη λικνιστική διεπιφάνεια, προκαλούν ελαστικές μετακινήσεις, $[u_{\text{el}}]$, οι οποίες αναπτύσσονται καθ' όλο το πλάτος (με μπλε χρώμα), ενώ αρνητικές πρόσθετες (πλαστικές) μετακινήσεις $[u_{\text{a}}]$ αναπτύσσονται στην περιοχή υπό διαρροή (με κόκκινο χρώμα) και θετικές πρόσθετες («κενά») μετακινήσεις $[u_{\text{a}}]$ δημιουργούνται μεταξύ του λικνιζόμενου σώματος και της επιφάνειας λικνισμού (με πράσινο χρώμα), έτσι ώστε οι συνολικές μετακινήσεις να ταιριάζουν με αυτές της λικνιστικής επιφάνειας (κόμβος j του στοιχείου), $[u_{\text{rs}}]$ (με καφέ χρώμα). Προϋπάρχουσες πλαστικές μετακινήσεις δεν θεωρούνται στο σχήμα για απλοποίηση.

Πιο συγκεκριμένα, γίνεται διακριτοποίηση της διεπιφάνειας λικνισμού σε κόμβους ελέγχου, σε κάθε έναν από τους οποίους είναι άγνωστη μία ποσότητα, ανάλογα με το αν ο κόμβος αυτός θεωρείται ότι έχει ελαστική συμπεριφορά, βρίσκεται υπό διαρροή ή αν έχει αποκολληθεί από τη βάση έδρασης. Στην περίπτωση της ελαστικής συμπεριφοράς άγνω-

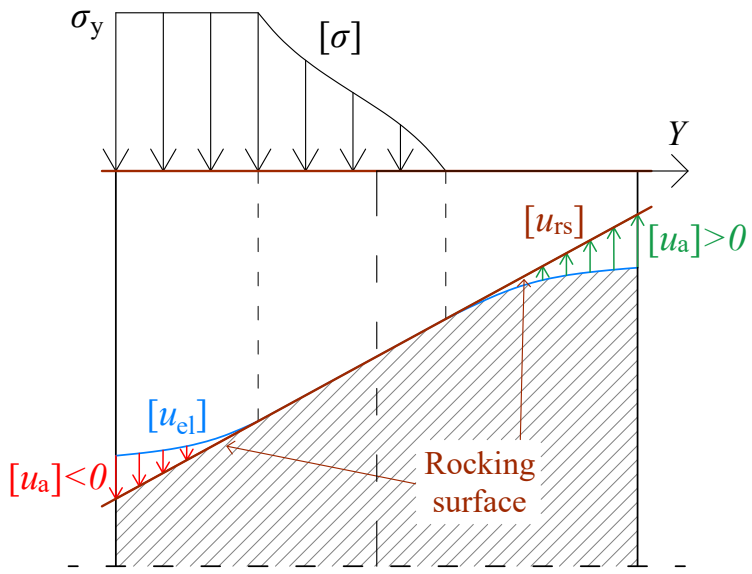

Σχήμα 10: Κατανομή τάσεων που ασκούνται στην λικνιστική επιφάνεια και μετακινήσεις που παράγονται στην ανελαστική, την ελαστική και την περιοχή χωρίς επαφή, οι οποίες ταιριάζουν με αυτές της λικνιστικής επιφάνειας.

στη ποσότητα είναι η ασκούμενη τάση, ή ισοδύναμα, η ελαστική ανηγμένη παραμόρφωση, στην περίπτωση της διαρροής άγνωστη είναι η πρόσθετη πλαστική μετακίνηση κατά το συγκεκριμένο βήμα με την τάση να είναι γνωστή και ίση με την τάση διαρροής, ενώ στην περίπτωση της απώλειας επαφής, άγνωστη ποσότητα είναι η πρόσθετη μετακίνηση που απαιτείται να προστεθεί στη μετακίνηση του σώματος ώστε να προκύψει η μετακίνηση της επιφάνειας λικνισμού, δηλαδή το κενό που δημιουργείται μεταξύ σώματος - βάσης, με την τάση να είναι γνωστή και ίση με τη μηδενική. Οι παραπάνω ποσότητες σε αδιαστατοποιημένη μορφή μπορούν να εκφραστούν ταυτόχρονα μέσω μίας μεταβλητής w (Εξ. 5.3, Σχ. 5.3).

Για τη διατήρηση όμως της συνέχειας και ομαλότητας των παραγόμενων από το μακροστοιχείο αποτελεσμάτων, δεν αρκεί ο προσδιορισμός των παραπάνω ποσοτήτων μόνο στους κόμβους ελέγχου, αλλά θα πρέπει να προσδιορίζονται και οι αντίστοιχες κατανομές στα διαστήματα μεταξύ των κόμβων ελέγχου. Ο ακριβής προσδιορισμός των σημείων μετάβασης από μία μορφή συμπεριφοράς σε μία άλλη είναι δύσκολος και υπολογιστικά μη αποδοτικός. Για το λόγο αυτό, στη μόρφωση του μακροστοιχείου χρησιμοποιείται μία απλοποίηση, η οποία όμως δίδει πολύ καλά αποτελέσματα. Πιο συγκεκριμένα, παρατηρείται ότι μία απόκλιση ελαστικών ανηγμένων παραμορφώσεων από τη γραμμική κατανομή στο εσωτερικό του διαστήματος παράγει μία απόκλιση από τη γραμμική κατανομή για τις μετακινήσεις, οι οποίες συνδέονται προσεγγιστικά με τη σχέση της Εξ. (5.19). Βάσει της σχέσης αυτής λοιπόν, μπορούν να τροποποιηθούν οι ελαστικές ανηγμένες παραμορφώσεις, ώστε να δημιουργηθεί συμβατότητα με τις πρόσθετες μετακινήσεις. Αποδεικνύεται ότι αν στη γραμμική κατανομή που παράγεται ενώνοντας τις τροποποιημένες τιμές στα άκρα του διαστήματος προστεθεί το αντίθετο της απόκλισης της κατανομής πλαστικών

μετακινήσεων από την αντίστοιχη γραμμική κατανομή, οι διάφορες περιοχές συμπεριφοράς (ελαστική, ανελαστική, αποκόλληση) οριοθετούνται από τα σημεία τομής της παραπάνω κατανομής με τις οριζόντιες ευθείες που αντιστοιχούν στις τιμές $w = 0$ και $w = \varepsilon_y$.

Οι δημιουργούμενες από την παραπάνω διαδικασία κατανομές τάσεων ή ισοδύναμα ανηγμένων ελαστικών παραμορφώσεων παράγουν μετακινήσεις στα σημεία ελέγχου. Αρχικά, παράγονται μετακινήσεις στα άκρα του στοιχείου λόγω των συνισταμένων δυνάμεων στις θέσεις αυτές, βάσει της τεχνικής θεωρίας κάμψης. Ακόμα, παράγονται επιπλέον μετακινήσεις στη διεπιφάνεια λινισμού λόγω των αυτοϊσορροπούμενων ορθών τάσεων, οι οποίες υπολογίζονται αφού η δημιουργούμενη κατανομή τάσεων χωριστεί σε απλά σχήματα (τρίγωνα, τραπέζια), για τα οποία είναι γνωστές οι σχέσεις υπολογισμού των παραγόμενων μετακινήσεων, βάσει της συνάρτησης μη γραμμικής κατανομής μετακινήσεων της ημιάπειρης λωρίδας που παρουσιάστηκε παραπάνω. Επιπλέον, η συμβολή των αυτοϊσορροπούμενων τάσεων στις μετακινήσεις λαμβάνεται υπόψη απλοποιητικά, θεωρώντας παραβολική κατανομή τάσεων με άκρα αυτά της περιοχής επαφής, για την οποία με τρόπο παρόμοιο με αυτόν που έγινε για το ελαστικό στοιχείο προκύπτουν οι προσεγγιστικές σχέσεις των Εξ. (5.13) και (5.14).

Πέραν των παραπάνω μετακινήσεων θα πρέπει να ληφθούν επιπλέον υπόψη οι πρόσθετες μετακινήσεις που αντιστοιχούν στο κενό σώματος - βάσης στην περίπτωση περιοχής αποκόλλησης, οι πρόσθετες πλαστικές μετακινήσεις σε περιοχές υπό διαρροή και οι πλαστικές μετακινήσεις που έχουν δημιουργηθεί σε προηγούμενα βήματα. Το άθροισμα όλων των παραπάνω μετακινήσεων στη διεπιφάνεια λικνισμού, θα πρέπει να ισούται με τη στοχευόμενη γραμμική κατανομή μετακινήσεων που ορίζεται για το λικνιζόμενο άκρο του μέλους από το πρόγραμμα πεπερασμένων στοιχείων. Για την επίτευξη του στόχου αυτού, εκτελούνται επαναλήψεις με διορθωμένες σε κάθε επανάληψη τιμές w στις θέσεις των κόμβων ελέγχου.

Στα παραδείγματα του κεφαλαίου εξετάζεται αρχικά ένα λικνιζόμενο σώμα υπό σταθερή κατακόρυφη δύναμη (Σχ. 5.10), για το οποίο παρουσιάζονται οι καμπύλες δύναμης - μετατόπισης για διάφορες τιμές πλήθους κόμβων ελέγχου (Σχ. 11), από όπου φαίνεται η πολύ καλή προσέγγιση που γίνεται για το εσωτερικό των διαστημάτων. Ακόμα, παρουσιάζονται οι κατανομές ελαστικών ανηγμένων παραμορφώσεων και πλαστικών μετακινήσεων για διάφορες χρονικές στιγμές στον πρώτο ημικύκλο φόρτισης (Σχ. 12) και οι κατανομές πλαστικών μετακινήσεων μέχρι το τέλος της ανακυκλιζόμενης φόρτισης (Σχ. 5.13). Επιπλέον, συγκρίνονται τα αποτελέσματα που παράγει το προτεινόμενο μακροστοιχείο με τα αντίστοιχα πειραματικά για ένα λικνιζόμενο τοίχωμα οπλισμένου σκυροδέματος με τένοντες (Σχ. 13) και έναν πεσσό τοιχοποιίας (Σχ. 5.15), από όπου φαίνεται ότι παρόλο που το προτεινόμενο στοιχείο δεν μπορεί να λάβει υπόψη του πολύπλοκους νόμους ανακύκλισης υλικών, είναι σε θέση να προσεγγίσει ικανοποιητικά τη συνολική συμπεριφορά των μελών αυτών, δεδομένων των πειραματικών αβεβαιοτήτων.

Ιδιαίτερη έμφαση δίνεται, τέλος, στη σημασία της σωστής θεώρησης της παραμορ-

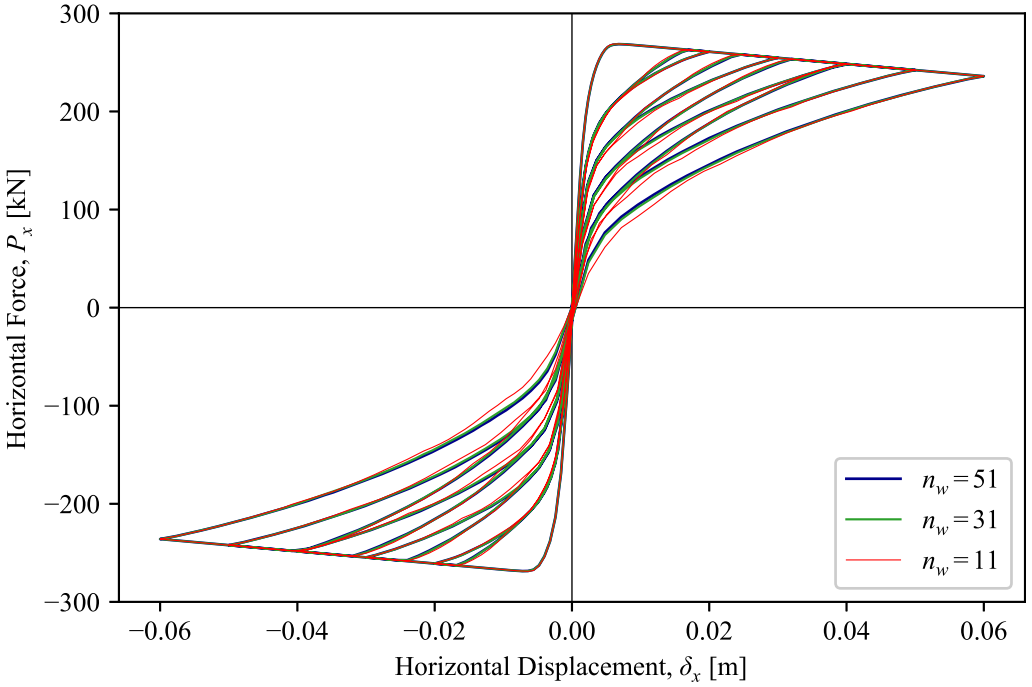

Σχήμα 11: Λικνιζόμενο σώμα υπό σταθερή κατακόρυφη δύναμη: Καμπύλες οριζόντιας μετατόπισης - οριζόντιας επιβαλλόμενης δύναμης σε ανακυκλιζόμενη φόρτιση για διάφορες τιμές πλήθους κόμβων ελέγχου, n_w.

φωσιμότητας και της ανελαστικότητας των λικνιζόμενων σωμάτων μέσω σύγκρισης των παραπάνω αποτελεσμάτων με αυτά αντίστοιχων προσομοιωμάτων όπου τα λικνιζόμενα σώματα θεωρούνται άκαμπτα ή ελαστικά (Σχ. 14), από όπου φαίνεται ότι μεταξύ των παραπάνω μοντέλων παρατηρούνται σημαντικές αποκλίσεις και επομένως αν δεν ληφθεί υπόψη η παραμορφωσιμότητα ή η ανελαστικότητα των σωμάτων εισάγονται σημαντικά σφάλματα στην προβλεπόμενη συμπεριφορά.

Στο παράρτημα του κεφαλαίου παρουσιάζεται μία εναλλακτική μέθοδος επίλυσης του προβλήματος προσδιορισμού της κατάλληλης κατανομής τάσεων στη διεπιφάνεια λικνισμού ως πρόβλημα βελτιστοποίησης, το οποίο όμως δεν προτιμάται γενικώς λόγω υπολογιστικού φόρτου και προβλημάτων σύγκλισης.

Μόρφωση ανελαστικού στοιχείου για δυναμικές αναλύσεις

Η μόρφωση του μακροστοιχείου του προηγούμενου κεφαλαίου αφορούσε στατικές ανακυκλιζόμενες φορτίσεις. Για τη χρήση του όμως σε δυναμικές αναλύσεις είναι απαραίτητες κάποιες τροποποιήσεις, για να ληφθεί υπόψη η απόσβεση του στοιχείου και άλλου είδους κινήσεις πέραν της καθαρά λικνιστικής, όπως η πλήρης αποκόλληση από τη βάση έδρασης και η ολίσθηση.

Όσον αφορά στην απόσβεση, γίνεται θεώρηση απόσβεσης παρόμοια με την απόσβεση ανάλογη της τρέχουσας δυσκαμψίας, η οποία σε επίπεδο τάσεων δίδεται από την Εξ. (6.5).

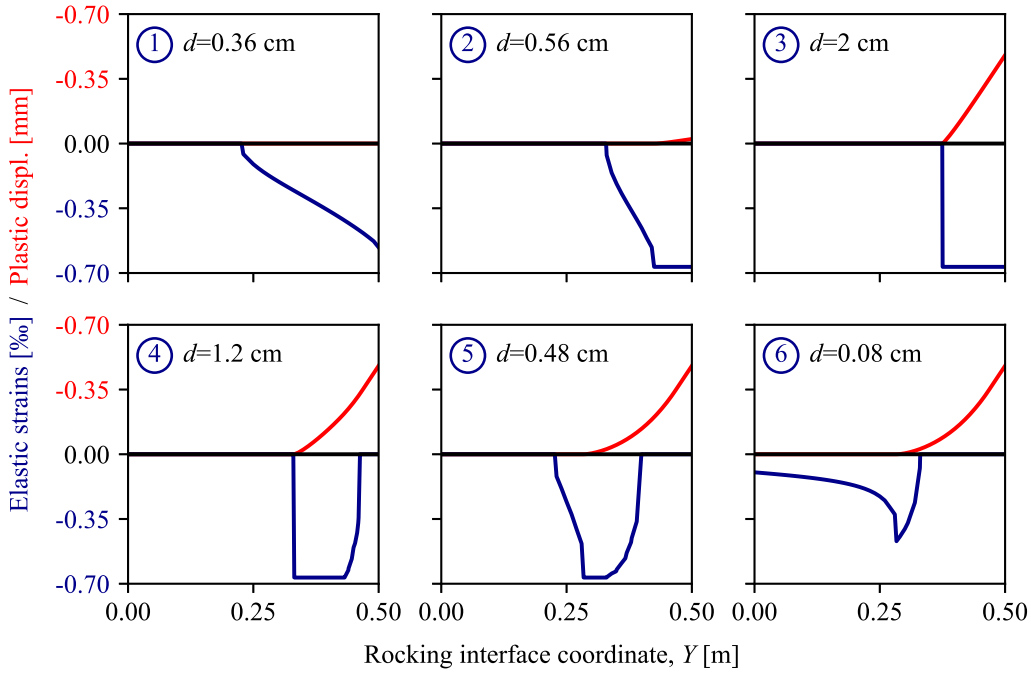

(a)

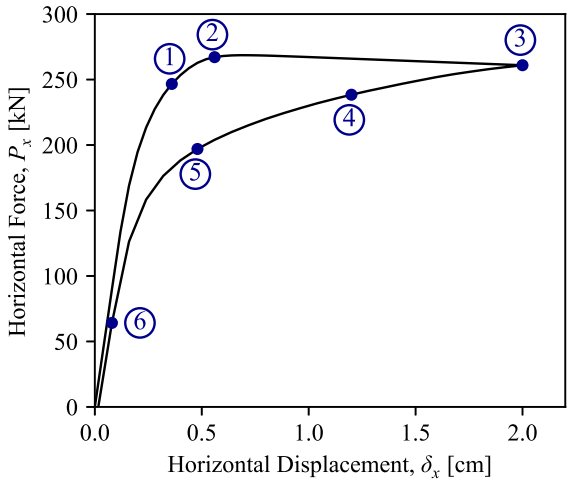

(b)

Σχήμα 12: (a) Ελαστικές παραμορφώσεις (μπλε καμπύλες) και πλαστικές μετακινήσεις (κόκκινες καμπύλες) που αναπτύσσονται στη λικνιστική διεπιφάνεια κατά τον πρώτο ημικύκλο φόρτισης. Παρουσιάζεται το δεξί ημιπλάτος της διεπιφάνειας. (b) Αντίστοιχα σημεία στην καμπύλη φόρτισης - αποφόρτισης.

Ιδιαίτερη μέριμνα πρέπει να ληφθεί έτσι ώστε να ικανοποιείται η συνθήκη περί μη ανάπτυξης εφελκυστικών τάσεων στη διεπιφάνεια λικνισμού, η οποία σημαίνει ότι το άθροισμα των τάσεων που παράγουν παραμορφώσεις και των τάσεων απόσβεσης θα πρέπει να είναι πάντα μη εφελκυστικό (Εξ. 6.8). Ο ρυθμός μεταβολής των τάσεων στη διεπιφάνεια, όμως, δεν υπολογίζεται από τις ταχύτητες στα άκρα του στοιχείου, λόγω της αυξημένης δυσκολίας, αλλά αριθμητικά σύμφωνα με την Εξ. (6.9). Με τον τρόπο αυτό προκύπτει η

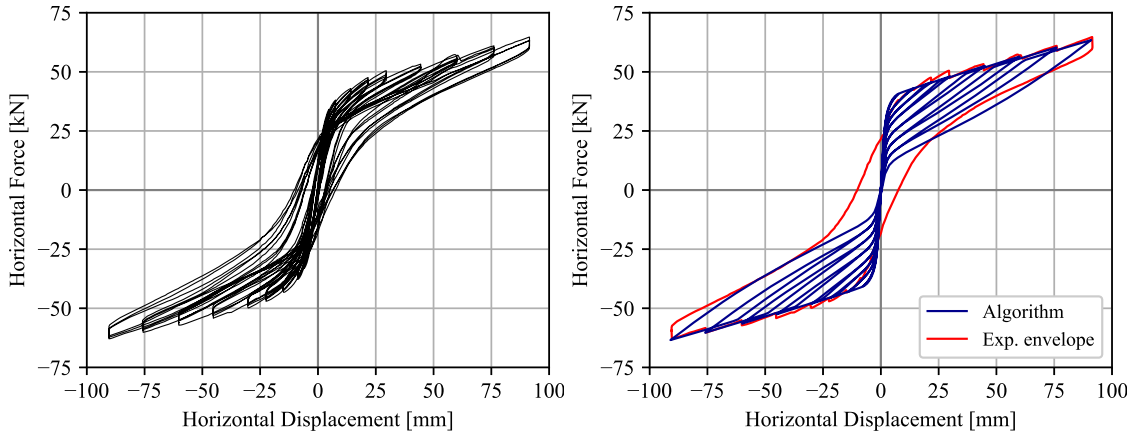

Σχήμα 13: (a) Πειραματική καμπύλη φόρτισης - αποφόρτισης για την ανακυκλική συμπεριφορά του δοκιμίου οπλισμένου σκυροδέματος με τένοντες SRW-B (Twigden κ.ά., 2017); (b) Απόκριση σύμφωνα με το προτεινόμενο μακροστοιχείο (μπλε καμπύλες) και σύγκριση με την περιβάλλουσα των πειραματικών αποτελεσμάτων (κόκκινη καμπύλη).

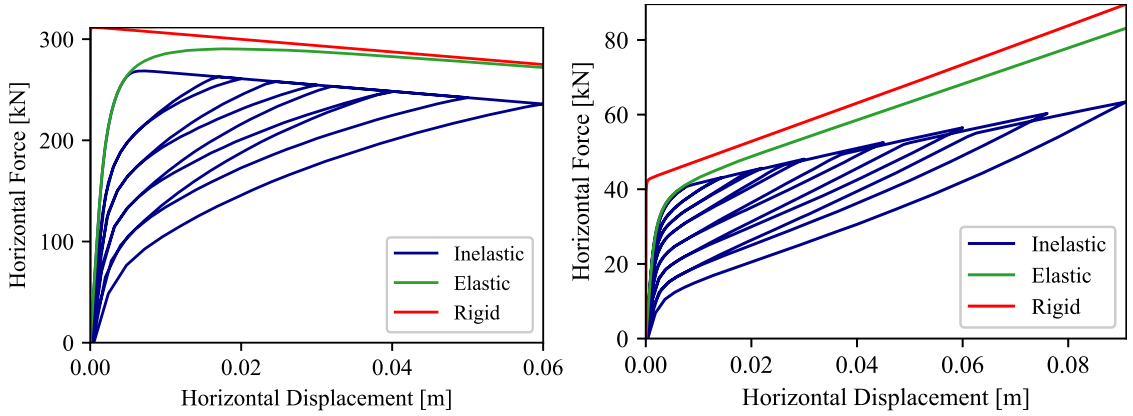

Σχήμα 14: Σύγκριση των καμπύλων δύναμης - μετατόπισης της ανακυκλικής συμπεριφοράς όπως προβλέπεται από το μακροστοιχείο για τα παραδείγματα (a) Σταθερής αξονικής δύναμης και (b) Τοιχώματος Ω.Σ. με τένοντες, με αποτελέσματα προσομοιωμάτων τα οποία θεωρούν το λικνιζόμενο σώμα άκαμπτο ή ελαστικό. Παρουσιάζονται μόνο οι θετικοί ημιάξονες.

ανισότητα (6.10).

Για να ισχύει η παραπάνω ανισότητα, γίνεται τροποποίηση του τρόπου καθορισμού των ελαστικών ανηγμένων παραμορφώσεων και πρόσθετων μετακινήσεων βάσει των w σύμφωνα με τις σχέσεις των Εξ. (6.12) και (6.13), ενώ παρόμοια τροποποίηση γίνεται και στη διαδικασία καθορισμού των διάφορων περιοχών στο εσωτερικό των διαστημάτων (Σχ. 6.2). Ακόμα, οι συνολικές κανονικοποιημένες δυνάμεις παραμορφωσιμότητας και απόσβεσης στο σωματόδετο σύστημα δίνονται από την Εξ. (6.22).

Όσον αφορά στην πλήρη αποκόλληση και την ολίσθηση, θα πρέπει να αναφερθεί ότι

και τα δύο φαινόμενα αντιμετωπίζονται με τον ίδιο τρόπο, καθώς η πλήρης αποκόλληση θεωρείται ουσιαστικά ως μία περίπτωση ολίσθησης με μηδενική αξονική δύναμη. Για να ληφθεί υπόψη η ολίσθηση, εισάγεται μία νέα μεταβλητή s που εκφράζει την κάθετη στην απαραμόρφωτη θέση του σώματος μετατόπιση του λικνιζόμενου άκρου. Επιπλέον, εισάγεται ένα νέο ενδιάμεσο σύστημα συντεταγμένων, όπου η ολίσθηση αυτή έχει αφαιρεθεί (Σχ. 6.1).

Για τον καθορισμό της ολίσθησης, εφαρμόζεται το κριτήριο ολίσθησης Coulomb (Ανισ. 6.23). Σε συνήθεις κατασκευές, προκύπτει ότι για να ισχύει το παραπάνω κριτήριο, θα πρέπει ισοδύναμα να ισχύει η ανισότητα (6.38). Σε κάθε βήμα ελέγχεται αν ισχύει η ανισότητα αυτή με την υπάρχουσα κανονικοποιημένη ως προς το μήκος ολίσθηση $\tilde{s}$, αλλιώς μεταβάλλεται ώστε η μία από τις δύο ανισότητες που δεν ικανοποιείται, να ικανοποιείται ως ισότητα.

Επιπλέον, εισάγεται ένας απλούστερος τρόπος υπολογισμού των μετακινήσεων λόγω των αυτοϊσορροπούμενων ορθών τάσεων που βασίζεται στη συνισταμένη αξονική και ροπή κάθε διαστήματος (Εξ. 6.52). Καθώς οι παραγόμενες μετακινήσεις εξαρτώνται μόνο από τις συνισταμένες δυνάμεις των διαστημάτων, μπορεί μετά την εκτέλεση κάθε επιτυχημένου βήματος να γίνεται απλοποίηση (διγραμμικοποίηση) των κατανομών ελαστικών ανηγμένων παραμορφώσεων και πλαστικών μετακινήσεων, καθώς αυτό μειώνει σημαντικά το υπολογιστικό κόστος στην περίπτωση της δυναμικής ανάλυσης.

Στη συνέχεια γίνεται επιβεβαίωση της δυνατότητας του μακροστοιχείου να προβλέψει την απώλεια ενέργειας που θεωρείται συνήθως για άκαμπτα σώματα, βάσει της αρχής διατήρησης στροφορμής. Φαίνεται λοιπόν ότι για πολύ μεγάλο μέτρο ελαστικότητας και συντελεστή απόσβεσης, οι αποκρίσεις σε ελεύθερες ταλαντώσεις, παλμική κίνηση ημιτονοειδούς μορφής και σε καταγεγραμμένη σεισμική κίνηση πλησιάζουν πολύ ικανοποιητικά τις θεωρητικά προβλεπόμενες αποκρίσεις άκαμπτων σωμάτων (Σχ. 15, 6.5 - 6.9). Το παραπάνω συμπέρασμα επιβεβαιώνεται και από τα Σχ. 16, 6.10, 6.12, όπου παρουσιάζονται οι ισοδύναμοι λόγοι απώλειας ενέργειας κατά την κρούση, οι οποίοι αν χρησιμοποιηθούν στην αναλυτική λύση, δίδουν ίδια μετακίνηση κατά τον πρώτο ημικύκλο ταλάντωσης με αυτήν του μακροστοιχείου, από όπου φαίνεται ότι καθώς αυξάνεται το μέτρο ελαστικότητας ή ο συντελεστής απόσβεσης, ο ισοδύναμος λόγος απώλειας ενέργειας σχεδόν ταυτίζεται με τον θεωρητικώς προβλεπόμενο για άκαμπτα σώματα με ανελαστική κρούση.

Η ικανότητα του τροποποιημένου συντελεστή απώλειας ενέργειας να περιγράψει την πραγματική συμπεριφορά του σώματος, όπως προκύπτει από το προτεινόμενο μακροστοιχείο, εξετάζεται στα Σχ. 17, 6.14, 6.15, από όπου φαίνεται ότι η χρήση ενός τροποποιημένου συντελεστή έναντι του θεωρητικού δίνει αποτελέσματα πολύ πιο κοντά σε αυτά που προβλέπονται από το μακροστοιχείο.

Ακόμα, παρουσιάζεται η συμπεριφορά ενός παραμορφώσιμου λικνιζόμενου σώματος σε ελεύθερες ταλαντώσεις, παλμική κίνηση ημιτονοειδούς μορφής και σε καταγεγραμμένη σεισμική κίνηση, ανάλογα με τις τιμές διαφόρων παραμέτρων, όπως είναι το μέτρο

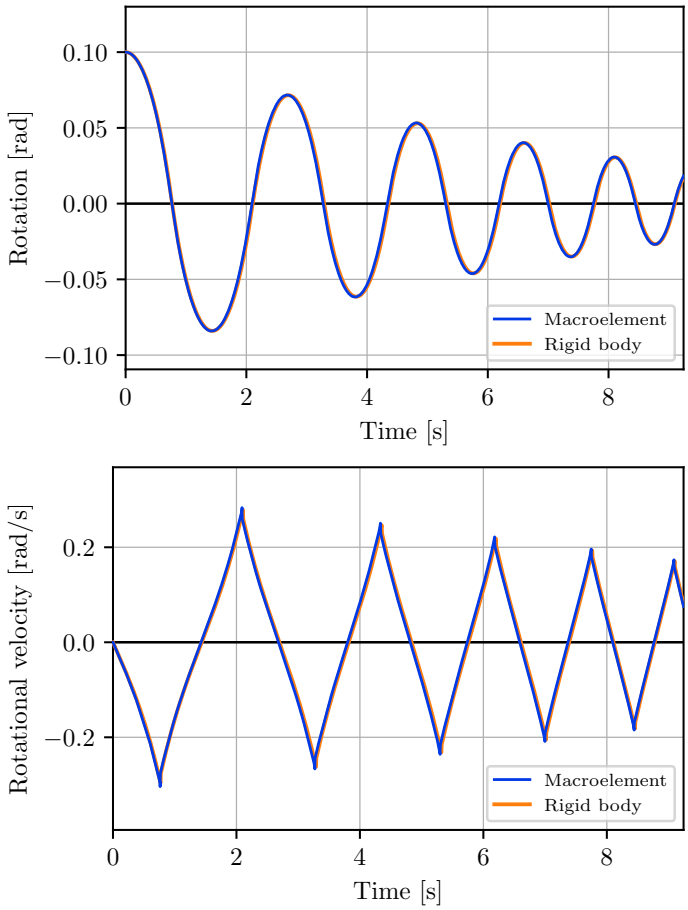

Σχήμα 15: Στροφή και γωνιακή ταχύτητα για ελεύθερη ταλάντωση άκαμπτου σώματος με $\theta_0/\alpha = 0.5$ για $\alpha = 0.2$, όπως προκύπτουν από το μακροστοιχείο (μπλε καμπύλες) και τη θεωρητική λύση (πορτοκαλί καμπύλες).

ελαστικότητας ή ο συντελεστής απόσβεσης (Σχ. 6.16 - 6.18), η τάση διαρροής του σώματος (Σχ. 6.19 - 6.21) και ο συντελεστής τριβής (Σχ. 6.22 - 6.24).

Συμπεράσματα

Στην παρούσα διδακτορική διατριβή παρουσιάστηκε η μόρφωση μακροστοιχείων για παραμορφώσιμα λικνιζόμενα σώματα. Αρχικά παρουσιάστηκε η μόρφωση του ελαστικού μακροστοιχείου, με την οποία φάνηκε ότι ο λικνισμός και η παραμόρφωση δεν είναι στην πραγματικότητα ξεχωριστά φαινόμενα. Καθώς οι διατομές του μέλους κοντά στη διεπιφάνεια λικνισμού δεν παραπέμνουν επίπεδες, η τεχνική θεωρία κάμψης που εφαρμόζεται συνήθως για στοιχεία δοκού - υποστυλώματος κρίνεται ανεπαρκής για την πρόβλεψη της συμπεριφοράς λικνιζόμενων μελών και για το λόγο αυτό χρησιμοποιήθηκε το πρόβλημα της ημιάπειρης λωρίδας από τη θεωρία ελαστικότητας για την εξέταση την επιρροής της μη γραμμικότητας τάσεων κοντά στην περιοχή επαφής σώματος - βάσης. Τα αποτελέσματα για την ημιάπειρη λωρίδα ενσωματώθηκαν σε ένα στοιχείο δοκού - υπο-

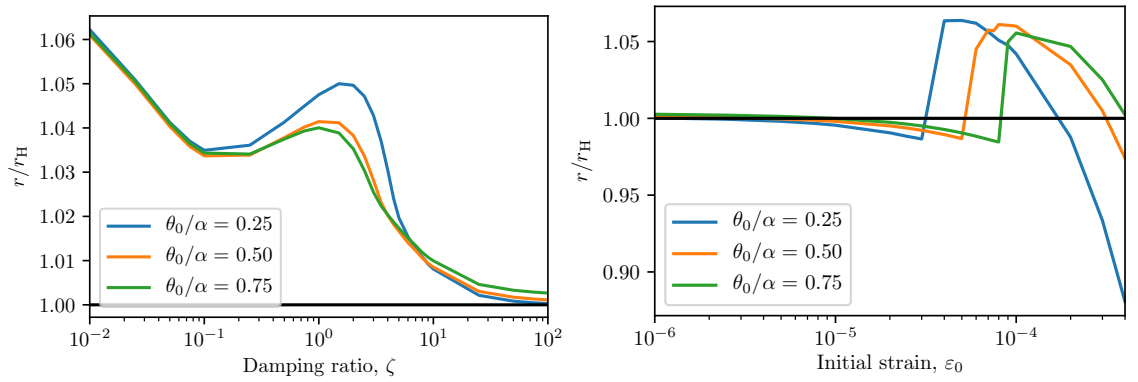

(a) (b)

Σχήμα 16: Λόγος του τροποποιημένου συντελεστή απώλειας κινητικής ενέργειας προς τον αντίστοιχο θεωρητικό συντελεστή του Housner για (a) ένα άκαμπτο σώμα με μεταβλητό λόγο απόσβεσης, ζ, και (b) για ένα σώμα με σχεδόν άπειρο λόγο απόσβεσης με μεταβλητή αρχική παραμόρφωση, ϵ_0. Ο λόγος λυγηρότητας που έχει θεωρηθεί είναι $\alpha = 0.2$.

στυλώματος βασισμένο στις δυνάμεις για να ληφθούν υπόψη οι πρόσθετες μετακινήσεις που οφείλονται στη μη γραμμικότητα τάσεων κατά μήκος της διεπιφάνειας λικνισμού. Η πολύ καλή ακρίβεια του ελαστικού μακροστοιχείου αποδείχτηκε μέσω σύγκρισης των παραγόμενων αποτελεσμάτων για χαρακτηριστικές περιπτώσεις λικνιζόμενων μελών με αντίστοιχα αποτελέσματα προσομοιωμάτων στο πρόγραμμα *Abaqus*. Ακόμα, φάνηκε ότι για μέλη υπό υψηλή αξονική δύναμη, η παραμορφωσιμότητά τους επηρεάζει σημαντικά την απόκρισή τους, ενώ κάποια πρώτα αποτελέσματα έδειξαν τη θετική επιρροή που μπορεί να έχει η ενσωμάτωση λικνιζόμενων μελών σε πλαίσια όσον αφορά στη σεισμική τους συμπεριφορά.

Για να ληφθεί υπόψη η ανελαστικότητα, η περίπτωση της μονοτονικής φόρτισης μπορεί να αντιμετωπιστεί μέσω επέκτασης των εκφράσεων για τις πρόσθετες μετακινήσεις λόγω των αυτοϊσορροπούμενων τάσεων, ώστε να ανταποκρίνονται σε κατανομές τάσεων έπειτα από διαρροή. Η ίδια διαδικασία, όμως, δεν μπορεί να εφαρμοστεί στην περίπτωση ανακυκλιζόμενης φόρτισης, λόγω των πολύπλοκων κατανομών τάσεων και πλαστικών μετακινήσεων που δημιουργούνται κατά την αντιστροφή της φόρτισης. Για να επιλυθεί το συγκεκριμένο πρόβλημα, θα πρέπει αρχικά να προσδιοριστεί η μη γραμμική κατανομή μετακινήσεων στο λικνιζόμενο άκρο για τυχούσα κατανομή τάσεων στο άκρο αυτό, το οποίο επιτυγχάνεται μέσω ολοκλήρωσης των προτεινόμενων αναλυτικών εκφράσεων που αναφέρονται στη δράση ενός συγκεντρωμένου φορτίου σε τυχούσα θέση στο άκρο της ημιάπειρης λωρίδας. Μέσω των εκφράσεων αυτών δείχτηκε ότι ακόμα και για ένα ελαστικό σώμα, τόσο η κατανομή τάσεων στην περιοχή επαφής, όσο η κατανομή μετακινήσεων στην περιοχή που δεν βρίσκεται σε επαφή με τη βάση έδρασης, είναι μη γραμμικές.

Οι προηγούμενες αναλυτικές εκφράσεις ενσωματώθηκαν σε έναν αλγόριθμο για την περιγραφή της συμπεριφοράς ανελαστικών λικνιζόμενων σωμάτων σε ανακυκλιζόμενη φόρτιση, ο οποίος βασίζεται στον προσδιορισμό κατάλληλης κατανομής τάσεων στη διε-

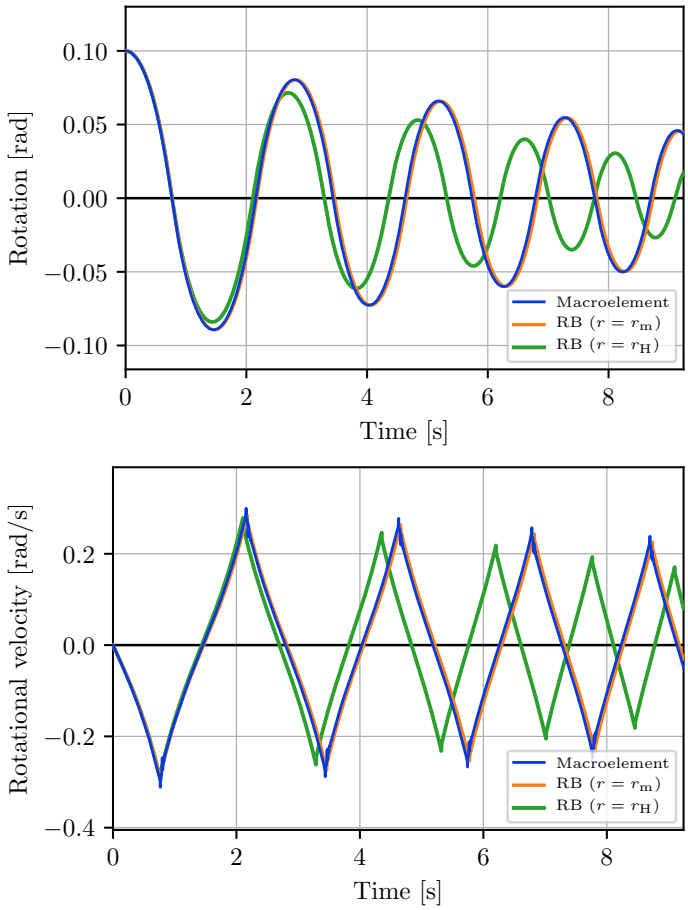

Σχήμα 17: Στροφή και γωνιακή ταχύτητα παραμορφώσιμου λικνιζόμενου σώματος με $\alpha = 0.2$, $\epsilon_0 = 5 \cdot 10^{-6}$ και $\zeta = 5\%$ σε ελεύθερες ταλαντώσεις με $\theta_0/\alpha = 0.5$, όπως προβλέπονται από το μακροστοιχείο (μπλε καμπύλες), την αναλυτική λύση του άκαμπτου σώματος με τροποποιημένο συντελεστή απώλειας ενέργειας (πορτοκαλί καμπύλες) και την αναλυτική λύση του άκαμπτου σώματος με τον θεωρητικό συντελεστή απώλειας ενέργειας (πράσινες καμπύλες).

πιφάνεια λικνισμού, έτσι ώστε οι παραγόμενες μετακινήσεις, μαζί με τυχόν προϋπάρχουσες πλαστικές μετακινήσεις, να ταιριάζουν με τις στοχευόμενες μετακινήσεις στο λικνιζόμενο άκρο. Σχολιάστηκε ακόμα η μορφή των παραγόμενων κατανομών τάσεων και πλαστικών μετακινήσεων, ενώ τα αποτελέσματα που παράγονται για διατάξεις λικνιζόμενων τοιχωμάτων που παρουσιάζονται στη βιβλιογραφία συγκρίθηκαν με τα αντίστοιχα πειραματικά, δείχοντας ότι παρά την απλότητα του νόμου υλικού που θεωρήθηκε, τα βασικά χαρακτηριστικά της ανακυκλικής συμπεριφοράς μπορούν να προβλεφθούν. Επιπλέον, συγκρίνοντας τα παραπάνω αποτελέσματα με αυτά αντίστοιχων προσομοιωμάτων, όπου τα λικνιζόμενα μέλη θεωρήθηκαν άκαμπτα ή ελαστικά, αποδείχτηκε ότι τόσο η παραμορφωσιμότητα όσο και η ανελαστικότητα θα πρέπει να λαμβάνονται υπόψη καταλλήλως για μία ακριβέστερη πρόβλεψη της λικνιστικής συμπεριφοράς τέτοιων σωμάτων.

Η προηγούμενη μόρφωση επεκτάθηκε, τέλος, έτσι ώστε να εξεταστεί η δυναμική συμπεριφορά, μέσω της ενσωμάτωσης κατάλληλης διατύπωσης για την απόσβεση και για

άλλες μορφές κίνησης, δηλαδή την πλήρη αποκόλληση και την ολίσθηση, οι οποίες συνυπάρχουν συνήθως μαζί με το λικνισμό. Όσον αφορά στην απόσβεση, χρησιμοποιήθηκε μία διατύπωση παρόμοια με αυτήν της απόσβεσης ανάλογης με την τρέχουσα δυσκαμψία, ενώ λήφθηκε μέριμνα έτσι ώστε το άθροισμα των τάσεων που προκαλούν παραμόρφωση και των τάσεων απόσβεσης κατά μήκος της διεπιφάνειας λικνισμού να είναι πάντα μηεφελκυστικό. Αυτός ο περιορισμός ορίζει τη μέγιστη τάση παραμόρφωσης που μπορεί να αναπτυχθεί σε κάθε βήμα. Για να ληφθεί υπόψη η ολίσθηση και η πλήρης αποκόλληση, η οποία θεωρείται ως ειδική περίπτωση της ολίσθησης για μηδενική αξονική δύναμη, εισάγεται μία νέα μεταβλητή που εκφράζει τη μετατόπιση λόγω ολίσθησης και ένα νέο σύστημα συντεταγμένων, ενώ η ολίσθηση προσδιορίζεται έτσι ώστε να ικανοποιείται σε κάθε βήμα ένα κριτήριο τριβής Coulomb.

Το προτεινόμενο μακροστοιχείο μπορεί να ενσωματωθεί σε κάθε περιβάλλον πεπερασμένων στοιχείων, εκτελώντας πολύ γρηγορότερες αναλύσεις σε σχέση με συμβατικά προγράμματα πεπερασμένων στοιχείων, ενώ παρέχει πολύ καλή ακρίβεια. Αρχικά διατυπώθηκε για τη διερεύνηση της συμπεριφοράς λικνιζόμενων μελών που χρησιμοποιούνται σε διατάξεις σεισμικά ανατάξιμων κατασκευών που παρουσιάζονται στη βιβλιογραφία, τα οποία μπορεί να αναπτύξουν μεγάλες αξονικές δυνάμεις κατά την κίνησή τους και επομένως η παραμορφωσιμότητα και ανελαστικότητά τους θα πρέπει να ληφθούν υπόψη για μία ακριβέστερη πρόβλεψη της συμπεριφοράς τους. Πιστεύεται ότι το προτεινόμενο μακροστοιχείο θα προσφέρει περισσότερη αυτοπεποίθηση στους μηχανικούς όσον αφορά στην υπολογιστική ανάλυση κατασκευών με λικνιζόμενα μέλη, τα οποία θεωρούνται ως μία πολλά υποσχόμενη λύση για τη βελτίωση της σεισμικής συμπεριφοράς νέων ή ενισχυμένων κατασκευών, συμβάλλοντας στην τεκμηρίωση των κανονισμών για τον σχεδιασμό τους και προωθώντας την επιστημονική εξέλιξη στον σημαντικό αυτό τομέα.

Το προτεινόμενο μακροστοιχείο, όμως, παρέχει σημαντικά αποτελέσματα και όσον αφορά στη δυναμική απόκριση ελεύθερα ιστάμενων σωμάτων, ιδιαίτερα όσον αφορά στην αλληλεπίδραση μεταξύ λικνισμού, ολίσθησης, πλήρους αποκόλλησης, παραμορφωσιμότητας, ανελαστικότητας και απόσβεσης κατά τις κρούσεις. Για το λόγο αυτό, θεωρείται ότι θα συμβάλλει στην εξέλιξη της διερεύνησης της συμπεριφοράς μεμονωμένων λικνιζόμενων σωμάτων, καθώς οι υπάρχουσες θεωρητικές λύσεις άκαμπτων σωμάτων δεν μπορούν να λάβουν υπόψη τους τις παραπάνω αλληλεπιδράσεις και των αποτελεσμάτων τους κατά τις κρούσεις.

Κάποια σημεία που χρήζουν περαιτέρω διερεύνησης είναι:

- Αναλυτικότερη διερεύνηση της αλληλεπίδρασης μεταξύ του λικνισμού, της ολίσθησης, της πλήρους αποκόλλησης, της παραμορφωσιμότητας, της ανελαστικότητας και της απόσβεσης κατά τις κρούσεις.

- Καθορισμός του συντελεστή απώλειας ενέργειας για παραμορφώσιμα λικνιζόμενα μέλη με ένα εύρος τιμών ιδιοτήτων και διερεύνηση της ικανότητάς του να περιγρά-

φει την απώλεια ενέργειας κατά την κίνησή τους για τυχούσες δυναμικές φορτίσεις.

- Διερεύνηση της βελτίωσης της σεισμικής συμπεριφοράς των κατασκευών μέσω χρήσης λικνιζόμενων μελών αντί για συμβατικά μέλη και εξέταση βέλτιστων διατάξεων για τα μέλη αυτά.
- Επέκταση του μακροστοιχείου σε τρισδιάστατα σώματα.
- Επέκταση του μακροστοιχείου για να λαμβάνει υπόψη μεγάλες στροφές, έτσι ώστε η συμπεριφορά χθαμαλών λικνιζόμενων σωμάτων να μπορεί να προσδιοριστεί ακριβέστερα.
- Επέκταση του μακροστοιχείου, ώστε να λαμβάνει υπόψη τυχόν χαλαρό οπλισμό ή άλλες μερικές συνδέσεις στη διεπιφάνεια σώματος - βάσης, οι οποίες προτείνονται σε κάποιες διατάξεις λικνιζόμενων μελών που παρουσιάζονται στη βιβλιογραφία και επηρεάζουν τη λικνιστική κίνηση, ιδιαίτερα κατά τις ανακυκλίσεις.

Contents

1 Introduction

The complex mechanics of the motion of rocking bodies and structural members have attracted attention from the scientific community in recent years, although the phenomenon is known from ancient times, as many ancient monuments were built with members allowed to rock.

The rocking motion occurs when a member is unrestrained or partially restrained at its base, so that tensile stresses cannot be transmitted, as considered in classical structural mechanics. Given that the imposed forces are large enough, the rocking body detaches from the ground and rotates about one of its corners. The vertical force acts as the restoring force that tends to bring the body back to its original equilibrium position.

1.1 Analytic formulations

The simplest structure exhibiting rocking motion is the solitary rigid rocking block depicted in Fig. 1.1. Observations regarding the state of such bodies after a seismic event were used by seismologists over a century ago to deduce earthquake characteristics (Milne and Omori, 1893; Kirkpatrick, 1927, among others). However, a more in-depth examination of the dynamic response of rocking bodies began with the seminal work by Housner (1963), who concluded that rocking bodies are more stable that they seem, especially as size increases.

The equation of motion of the rectangular rigid rocking block is:

$$\frac{\ddot{\theta}}{p^2} = -\sin\left[\alpha\,\mathrm{sgn}(\theta) - \theta\right] - \frac{\ddot{u}_g}{g}\cos\left[\alpha\,\mathrm{sgn}(\theta) - \theta\right] \tag{1.1}$$

where θ is the rotation of the block, α is the angle expressing the slenderness of the block ($\tan\alpha = b/h$, Fig. 1.1), $\ddot{u}_g$ is the ground acceleration and p is a frequency parameter defined for the rectangular rocking block as:

$$p = \sqrt{3g/4R} \tag{1.2}$$

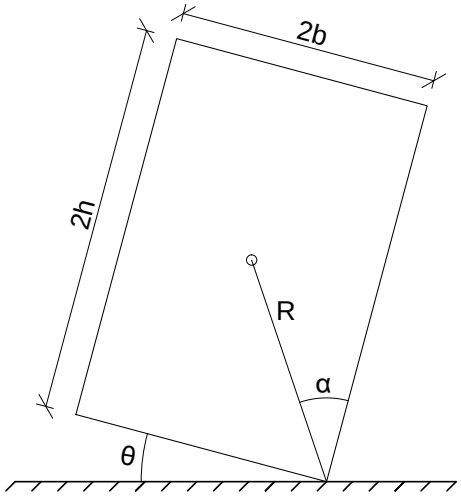

Figure 1.1: Solitary rigid rocking block.

where R is the semi-length of the diagonal of the block (Fig. 1.1).

Assuming that bouncing and sliding do not occur, the transition between the rotational motions around the two corners involves only an impact which is assumed to be perfectly inelastic and produces energy loss. Housner assumed that during the impact, the angular momentum about the next rotating point is conserved, so he concluded that the ratio of the kinetic energies, or equivalently, the square of the ratio of the rotational velocities after and before the impact for a rectangular rigid rocking block is

$$r = \left(\frac{\dot{\theta}_2}{\dot{\theta}_1}\right)^2 = \left(1 - \frac{3}{2}\sin^2\alpha\right)^2 \tag{1.3}$$

where r is called the apparent coefficient of restitution. The notion of the coefficient of restitution introduced by Housner is still used today. However, experimental results show that this coefficient of restitution is usually larger than the theoretical value predicted by Eq. (1.3).

The dynamic response of the rigid rocking block has been of interest for many researchers after the seminal work by Housner. The dynamic response to typical harmonic or pulse excitations, resembling near-field earthquake excitations, has been extensively studied by Spanos and Koh (1984), Tso and Wong (1989), Anooshehpoor et al. (1999), Zhang and Makris (2001), Dimitrakopoulos and DeJong (2012) and Voyagaki et al. (2013), among others, while other researchers, such as Yim et al. (1980), Makris and Konstantinidis (2003), Dimitrakopoulos and Paraskeva (2015), Bachmann et al. (2018), Giouvanidis and Dimitrakopoulos (2018) have examined the rocking response to earthquake records. In contrast to conventional structures, the response of the rocking block is highly nonlinear and, as a result, small changes in the rocking body or the excitation characteristics may produce large changes in the rocking response. It is interesting to note that if a rocking

body overturns by a ground motion of particular intensity, that does not necessarily mean that the same body will overturn by a scaled ground motion of higher intensity.

As mentioned above, the solution of the equation of motion of the rocking block requires that each time an impact is detected, the numerical integration scheme is stopped and a reduction in the rotational velocity is performed, based on the coefficient of restitution. Of particular interest is the work by Prieto et al. (2004), Prieto and Lourenço (2005) and Peña et al. (2007), where this velocity reduction is performed by introducing a mathematically equivalent, highly nonlinear impact force in the equation of motion, which can be solved in a uniform manner throughout the whole time history.

Despite the importance of the simple rocking model introduced by Housner, its shortcomings regarding its ability to predict the response of structures deviating from the assumptions of the planar rigid block with fixed rotation points on a rigid base, became soon evident, so more refined models which took into account aspects not included in the original rocking model emerged. Of high interest are the works by Ishiyama (1982) and Shenton and Jones (1991), where other rigid body motions are taken into account, such as sliding, which may or may not be combined with rocking, and translational/rotational free-flight.

Another aspect of Housner's model that has gained much attention is the coefficient of restitution. Several experiments of almost rigid rocking blocks have been performed (e.g. Lipscombe and Pellegrino, 1993; Peña et al., 2007; ElGawady et al., 2011; Čeh et al., 2018; Klaboe et al., 2018, among others), showing that the real apparent coefficient of restitution is not in agreement with Housner's prediction, which usually overestimates the energy loss. Housner's coefficient of restitution is only dependent on the geometric characteristics of the rocking block, but in reality it is also dependent on material properties, since bodies are not absolutely rigid. Furthermore, motions other than pure rocking are exhibited, such as bouncing, indicating that Housner's assumption of perfectly plastic impact is not in agreement with the experiments. A modified coefficient of restitution has been proposed by Kalliontzis et al. (2016) and Kalliontzis and Sritharan (2018) and probabilistic analyses have been performed by Chatzis et al. (2017), considering that the reaction during impact does not act on the corner of the body but on the interior of the rocking base, implicitly taking into account the deformability of the rocking body during impact.

Moreover, other impact formulations have been used instead of some form of Housner's coefficient of restitution. One such formulation by Giouvanidis and Dimitrakopoulos (2017a) uses Newton's contact law, which is widely used in nonsmooth dynamics, referring to the ratio of the contact point velocity before and after impact. Other formulations found in literature include those by Yilmaz et al. (2009) and Zhao et al. (2019), where alternative forms of the coefficient of restitution are employed.

Most of the aforementioned works refer to rigid bodies rocking on rigid surfaces. The

rigidity of both the body and the surface means that impacts are instantaneous and generally take place on the corner of the rigid body. In reality though, since rocking bodies are not infinitely rigid, impacts in nature are not absolutely instantaneous and contact between the body are the rocking surface takes place in a wider region than just a corner of the body and, as a consequence, energy losses do not happen instantly but more gradually. That is the reason why many researchers have tried to examine more refined models, which take into account some form of deformability.

One such attempt was to replace the rigid base with an elastic foundation. Psycharis and Jennings (1983) studied the dynamics of slender rigid blocks sitting on elastic foudations in two forms, namely a continuous layer of compression-only springs and dashpots (Winkler foundation) and a simpler, but equivalent model with compression-only springs and dashpots at two locations under the rigid rocking block (Fig. 1.2). In a following paper (Psycharis and Jennings, 1985), the upthrow of the rocking body is also examined. The problem of the viscoelastic foundation has been studied by many researchers from then on, including Palmeri and Makris (2008b), Palmeri and Makris (2008a) and Chatzis and Smyth (2011), among others.

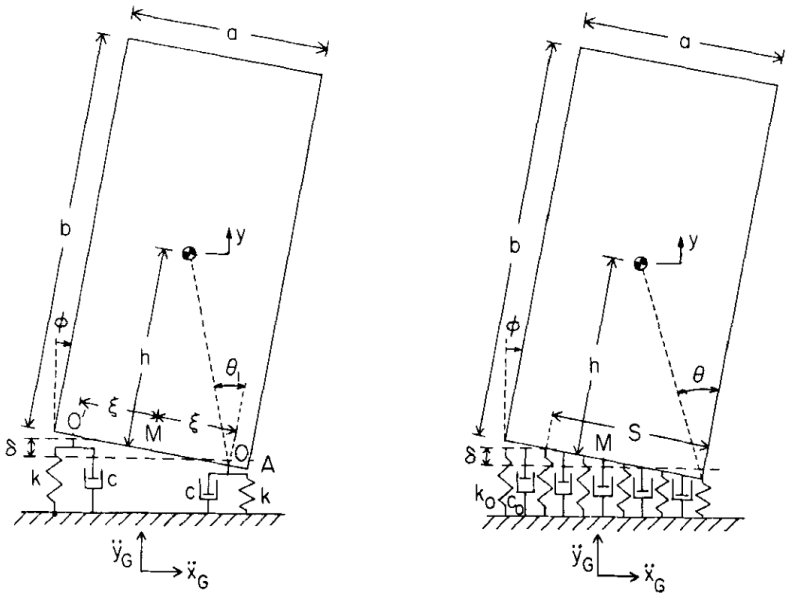

Figure 1.2: Deformable foundation models (Psycharis and Jennings, 1983).

From early on, it was understood that not only deformability at the foundation, but also deformability along the height of the rocking body should be taken into account for a more accurate prediction of flexible rocking bodies, leading to refined models, which take into account the interaction between the deformations of the structure and its rocking motion. Several researchers have studied the dynamic response of single- or multi- degree of freedom systems rocking on rigid or elastic foundations, including Psycharis (1983), Chopra and Yim (1985), Ichinose (1986), Psycharis (1991), Oliveto et al. (2003), Acikgoz

and DeJong (2012), Vassiliou et al. (2015) and Acikgoz and DeJong (2016), among others.

Several other models involving rigid rocking bodies have been presented in literature. Psycharis (1990) examined the rocking response of two-block assemblies, whose response involves several rocking modes. Ther and Kollár (2018) introduced a computational model for the prediction of the dynamic response of multi-block assemblies. Another structural system involving rocking members is the rocking frame, which involves several parallel rigid rocking columns capped with a rigid beam. This model has been examined by Makris and Vassiliou (2013) and Dimitrakopoulos and Giouvanidis (2015). Its two-storey counterpart has been studied by Allen et al. (1986), while a structural system with a deformable cantilever representing conventional storeys on top of a rocking first floor has been examined by Bachmann et al. (2017).

Tendons can also be used in rocking members to increase their stability. Although tendons impose large axial forces on rocking members, meaning that the deformability plays a major role in their response, rigid body simplifications have been presented in literature, referring to solitary rocking bodies (Vassiliou and Makris, 2015) or the rocking frame (Makris and Vassiliou, 2014; Dimitrakopoulos and Giouvanidis, 2015; Giouvanidis and Dimitrakopoulos, 2017b), which can model bridges with rocking piers.

Some other models which have been examined include a masonry arch comprised of four rocking parts (Oppenheim, 1992), rocking bodies on a seismically isolated base (Vassiliou and Makris, 2012) and a rocking body with extended base, on which it is able to roll on (Bachmann et al., 2019). The equivalence of the equations of motion of several of the models mentioned in the previous paragraphs with the solitary rocking block is presented in DeJong and Dimitrakopoulos (2014).

All of the aforementioned models involve bodies whose rocking motion is planar. Unless the seismic excitation is uniaxial and the body is absolutely symmetric with respect to this axis, or the width of the body in the perpendicular direction is substantially larger than the examined one, the three-dimensional motion needs to be taken into account for a more accurate prediction of the spatial rocking motion, which involves another motion mode called wobbling, referring to the rotation of the body about the vertical axis. Generally, neglecting this motion mode by examining only the planar rocking motion gives unconservative results. The interaction between rocking and wobbling of cylindrical bodies is examined in Stefanou et al. (2011) and Vassiliou et al. (2017), while Vassiliou (2018) study the response of a group of cylindrical bodies capped with a rigid slab. Regarding prismatic bodies, Chatzis and Smyth (2012) examine the rocking response of such bodies on elastic foundation, while in Chatzis and Smyth (2013), the motion of prismatic bodies on wheels is studied.

1.2 Structural members exhibiting rocking motion

Although structural members exhibiting rocking motion were extensively used in ancient temples, many of which have withstood many earthquakes, showing the seismic resilience of those structures, not many contemporary structures have been designed to rock. Up to date, rocking members have been applied in case of bridge piers (e.g. the South Rangitikei Railway Bridge, Skinner et al., 1980) and chimneys (e.g. at Air New Zealand Engineering Base at Christchurch, Sharpe and Skinner, 1983), while many Russian structures have been constructed in the last decades with a ground floor consisting of rocking columns (Poliakov, 1974).

Figure 1.3: The South Rangitikei Railway Bridge.

Although the number of real structures designed to rock during a seismic event is not large, a significant amount of analytical and experimental work has been performed in the last three decades regarding structural members exhibiting rocking motion. In fact, the application of the concept of rocking is particularly suited to precast structures, which have been gaining attention over the last years. A state-of-the-art analysis of rocking applications to precast structures can be found in Kurama et al. (2018).

Instead of conventional connections used in precast strucures (called "emulative" connections), which are designed to mimic the response and performance of equivalent cast-in-place monolithic concrete joints, another type of connections called "jointed" connections have emerged, which utilize the separation of the structural members at beam-column or panel-foundation interfaces. In this case, instead of the formation of plastic hinges at member ends, the connections are designed to allow controlled rocking through the inherent discontinuity between members, thus reducing member damage. In practice, apart from this inherent discontinuity between structural members, these connec-

tions also include unbonded post-tensioned tendons to provide a restoring force. However, since this configuration alone leads to a nearly nonlinear-elastic behaviour under reversed-cyclic loading, meaning limited hysteretic energy dissipation and possibly large displacements, additional supplemental energy dissipation components, such as mild steel or friction/sliding devices are used.

Jointed connections utilizing controlled rocking have been tested in moment-resisting frames, usually consisting of multi-storey columns and single-bay beams. Post-tensioned tendons are used to establish the connection between the columns and the beams, although as previously mentioned, mild steel rebars may accompany the tendons ("hybrid" frames), in order to provide energy dissipation during the opening and closing of the connections, apart from their contribution to the moment resistance. Several experimental projects have been performed on such frames (Cheok and Lew, 1993, Stone et al., 1995), but the most known one is the USA-Japan cooperative research program on PREcase Seismic Structural Systems (PRESSS), whose goal was to develop design recommendations which would allow confident use of such systems in practice and develop new materials, concepts and technologies for precast construction, suitable for seismic application (Priestley, 1991). The program included the test of a five-storey building, shown in Fig. 1.4, which included four different ductile structural frame configurations.

Jointed connections have also been tested in structural walls. Many researchers have examined the response and design of solitary (uncoupled) precast walls featuring gap opening across horizontal connections using only unbonded post-tensioned steel, such as Kurama et al. (2002), Perez et al. (2007) and Erkmen and Schultz (2009), among others. As mentioned earlier, the unbonded post-tensioned tendons offer low energy dissipation, so configurations with supplemental energy dissipation components in uncoupled rocking walls have also been examined by Kurama (2000), Ajrab et al. (2004) and Restrepo and Rahman (2007), among others. Hybrid wall systems that contain mild steel across the horizontal joints apart from post-tensioned tendons have also been presented in the works by Holden et al. (2003), Smith et al. (2011) and Smith et al. (2013), among others.

On the other hand, coupled rocking walls are equipped with ductile vertical joint connections which yield or slip during wall rocking, leading to energy dissipation, while allowing for easy replacement after the seismic event. Such systems have been investigated by Aaleti and Sritharan (2009), Sritharan et al. (2015) and Twigden et al. (2017), among others. For the PRESSS research program mentioned above, the jointed wall system shown in Fig. 1.4 was also part of the study (Sritharan et al., 2007).

The jointed connection configuration has been also investigated in the case of bridge piers, where special details have been examined to minimize the damage at the column-to-foundation and column-to-cap-beam joints (e.g. Mander and Cheng, 1997; Restrepo et al., 2011; Guerrini et al., 2014, among others). Furthermore, segmental column configurations have been investigated, where all joints can develop rocking (e.g. Hewes and

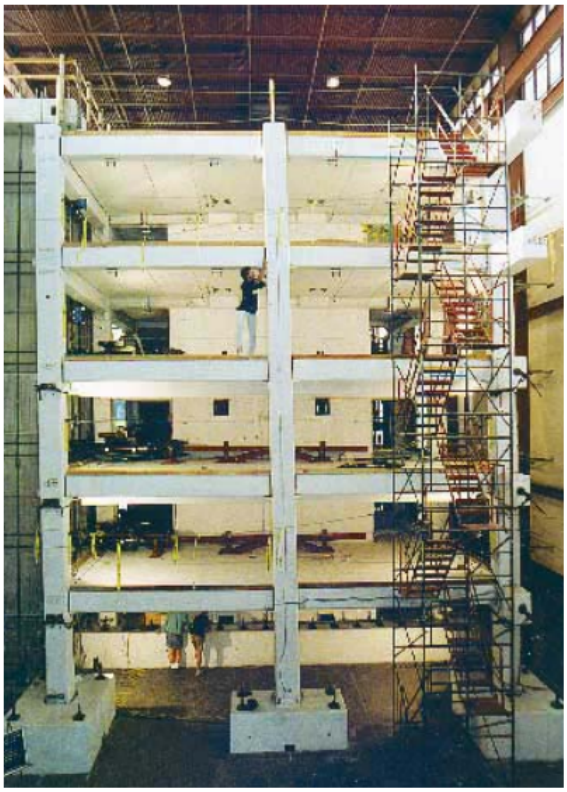

Figure 1.4: The PRESSS test building (Priestley et al., 1999)

Priestley, 2002; Kim et al., 2010; Motaref et al., 2013, among others).

Apart from the previous structural configurations, rocking is also expected for masonry shear walls, which are expected to detach from their base and rock during a strong seismic event. Several studies have been published presenting experimental results and design methodologies for such configurations, which consider the rocking motion and the deformability of these members (Magenes and Calvi, 1997; Madan et al., 2008; Lagomarsino, 2015; Kalliontzis and Schultz, 2017, among others). Furthermore, steel moment-resisting frames with rocking beam-to-column connections or rocking horizontal joints have also been examined, which are similar to the concrete systems described above (e.g. Christopoulos et al., 2002; Kim and Christopoulos, 2008; Lin et al., 2013; Wiebe et al., 2013, among others). A state-of-the-art review which also includes steel rocking systems can be found in Chancellor et al. (2014).

Guidelines addressing this alternative seismic design have been published by several organizations (ACI 2003, ACI 2014, fib 2003, New Zealand Standards 2006), while in Eurocode 8 (EN 1998-1:2004), rocking is anticipated for large lightly reinforced walls during strong earthquakes.

Conventional structural elements are usually designed to gradually yield and develop damage during an earthquake, as performance-based design suggests. However, this approach means that after a strong earthquake, the building has to be repaired, with signifi-

cant cost. What is more, if the earthquake is strong enough, large residual displacements may develop, making the repairing process harder and more costly.

In contrast, the solutions involving rocking members presented above overcome some of these problems. First of all, instead of the formation of plastic regions near element ends, which have to be repaired after an earthquake, rocking members simply rock if the imposed forces are large enough, meaning that this discontinuity between the structural members is inherent in the structural system, which is designed to have such a response. This way, rocking elements act as mechanical isolators, similarly to yielding elements, as the forces acting on the structure cannot exceed the maximum values allowed by the rocking mechanism. Similarly to yielding, rocking also modifies the natural periods of the system, making the structure less prone to resonance.

Furthermore, rocking elements present very small residual displacements in contrast to conventional structural members, exhibiting a "flag-shaped" hysteretic behaviour. That is why they are also known in literature as self-centering systems. As a result, after an earthquake the structure exhibits little damage and almost no residual drifts, meaning that few repairs have to be made after the seismic event to make the structure safe to be used again, saving money and time. Also, in the case of aftershocks, these self-centering systems are able to withstand sequential ground motions better than conventional systems, which may need to be repaired to function properly. So, rocking elements are proposed as an innovative way to improve the seismic resilience of structures. This approach may be further developed to be used as a quick and relatively inexpensive way of strengthening of existing buildings, as these rocking members can be prefabricated and installed in buildings when needed.

1.3 Existing finite element modelling techniques for modelling the rocking response

As described in the previous sections, various analytic solutions exist regarding the motion of the rocking block, as well as approximate methodologies for the design of rocking systems. Most of the former assume that the body or at least its base is rigid. This assumption is, however, far from reality for rocking bodies included in usual structural configurations. Regarding the latter, several assumptions regarding the stress distributions and member deformations near their end and the interaction between rocking and deformability are usually made, which may not be sufficiently documented. Apart from that, in many cases, the experimental or numerical results of specific examined configurations are used to calibrate the aforementioned elements of the proposed methodologies, making difficult the generalization of their application.

In addition, most of these methodologies have not been implemented in finite element

formulations, thus few computational models have been proposed, which can be incorporated in a general finite element framework, in order predict the response of structural configurations which include rocking members. From the above, it is evident that there is a necessity to develop a model able to describe the response of deformable rocking bodies and restrained rocking systems, which can be implemented in a general finite element framework. This will enable a more accurate prediction of the response of structures with rocking members in seismic scenarios, allowing for their more confident design, which will also lead to their more widespread use.

General approaches for the numerical evaluation of the response of rocking structures include two-dimensional (2D) or three-dimensional (3D) finite element models, where contact between elements is taken into account using constraints implementing special constitutive relations or by using explicit joint elements, and discrete element models (e.g. the discrete element method - DEM or the rigid bodies spring model - RBSM), where the structure is idealized as an assemblage of discrete blocks, interacting with each other in some way (e.g. Zienkiewicz and Taylor, 2005).

However, these approaches are considered computationally inefficient for large-scale practical structural analyses and simplified approaches in the context of one-dimensional (1D) finite elements are preferable. Belleri et al. (2013) present and compare such approaches, which have been used by several researchers.

One approach is to use a compression-only fiber section at the end of the rocking member. However, this approach fails to capture accurately the gradual transition from a nonlinear compression-only stress distribution at the rocking interface to a linear one further from the rocking surface and, as a result, the produced results are highly dependent on the distance between these sections.

Another approach uses a layer of compression only springs between the rigid rocking body and the rocking surface to account for the deformability near the rocking interface. The main drawback of this approach is that the value used for the spring striffness is not clear and is usually determined from the equivalence of the axial stiffness between the original deformable rocking member and the spring layer model, which however fails to predict correctly the whole rocking motion. In practical applications, the stiffness of the springs may also be determined so that the results of experimental tests performed are matched.

Such an approach is used extensively in works involving the response of rocking masonry walls. In Penna et al. (2014), a simplified macro-element with a total of eight degrees of freedom is used. Six of them belong to zero-length interfaces above and below the main element, while the remaining two belong to the central, assumed rigid, panel. The axial and rotational deformations, influenced by the rocking motion, that is the separation of the panel from the other members, are concentrated on the two zero-length interfaces, while the panel maintains only the ability of shear deformations. The formulation of these

extra zero-length elements is based on the activation of only the compressive portion of the end sections of the member, optionally also taking into account the yielding of the material. A similar approach is used by Vassiliou et al. (2016), proposing a zero-length compression-only fiber section element for the rocking interface.

Another simple model commonly used contains a rotational spring between the base of the rocking member and the rocking surface, which describes the static moment-rotation law of the rocking member. The calculation of this relationship is straightfoward for solitary rigid rocking members and presents negative stiffness after rocking inititates. However, the use of such a relationship for restrained rocking members is deemed problematic, since such an approach does not allow for the correct prediction of the axial motion of the member and, as a result, the effect of the restrained imposed on the rocking motion (e.g. through tendons) is ignored. Vassiliou et al. (2014) use such an approach together with a viscous damper calibrated so that the energy loss produced for a harmonic excitation is equal to the one expected for Housner's impact model. Diamantopoulos and Fragiadakis (2019) also use various implementations of rotational springs to solve structural configurations including rocking members, where impacts are detected and treated explicitly.

Some other approaches have also appeared in literature. Roh and Reinhorn (2009a), Roh and Reinhorn (2009b), and Roh and Reinhorn (2010), after recognizing the importance of the nonlinear stress zone near the contact surfaces, use a linearization of this zone in order to represent the modified force and stiffness distributions along the element in a simplified manner, arriving at a stiffness matrix formulation for the nonlinear behavior of rocking columns. Furthermore, they continue their research by examining the moment-curvature diagrams of rocking elements taking more effects into account, such as local crushing near the ends of the rocking surface and the stabilization of the moment-curvature curve for cyclic dynamic analyses after damage occurs. Barthes (2012) presents a zero-length two-node rocking element used to represent the behaviour of the rigid rocking interface between structural elements, which is governed by kinematic constraints imposed using the Augmented Lagrangian Method.

What is important to note here is that most of the aforementioned approaches use classical damping (mass-proportional and/or tangent-stiffness-proportional) to model the damping of the elements. However, as presented previously, rocking elements also exhibit loss of energy during the impacts, which is concentrated in a limited amount of time. Such form of energy loss may be of less importance when constrained rocking elements are considered, in contrast to solitary rocking elements, however its contribution to energy damping has not been investigated thoroughly.

1.4 General concepts and work significance

The main drawbacks of the aforementioned approaches are that the interface between the rocking body and its base is assumed to be rigid, the deformability of the rocking body near the contact area is only approximately taken into account or that the axial motion of the member is not considered. Such limitations are deemed problematic for the accurate prediction of the response of restrained rocking members or members under large axial forces, in general.

In this dissertation, a macroelement formulation for the prediction of the response of rocking members is proposed, which is able to take into account the deformability both along the height of the members, as well as near the contact with the base. The main characteristic of rocking bodies is that, in contrast to conventional structural members, tensile stresses cannot develop across the rocking interface, meaning that the stress distribution across this interface is nonlinear. This stress nonlinearity means that the displacement distribution of the fibers across the width of the element is also nonlinear. Thus, member sections in these zones do not remain flat, so the usual approximations used in the technical theory of bending (e.g. Housner and Vreeland, 1965) cannot by used. As a result, the more general theory of elasticity is used instead, which is considered an invaluable tool for the accurate prediction of deformable rocking bodies.

It is noted that the consideration of the deformability near the contact area is crucial for the accurate prediction of the rocking motion of rocking members under large axial forces, such as tendon- or beam-restrained members, where there is an interaction between rocking and the restraining member, or even solitary rocking bodies during impacts, where explicit energy loss assumptions must otherwise be adopted.

The macroelement can be incorporated in a general finite element framework, such as *OpenSees* (Mazzoni et al., 2006) and is used for the rocking ends of a rocking member, where, as described earlier, nonlinear stress distributions are expected to develop (Fig. 1.5). The macroelement can be used to predict the response of solitary rocking bodies, as well as rocking members included in structures (e.g. tendon-restrained shear walls) in a consistent manner, without any restriction concerning the kinematic constraints.

With the help of the proposed macroelement, the examination of the response of rocking members in structural configurations using computational models will be a much easier task, and as a result it will promote scientific progress in this area. This is considered important, since, although the use of rocking members is a much promising solution for the improvement of the seismic performance of newly designed or retrofitted structures, as explained above, further research is needed in order to gain confidence on their use.

Furthermore, it is considered to provide significant contribution towards the examination of the response of solitary rocking bodies, especially with that regards the energy loss during impacts, since a closer examination of the member response during an impact

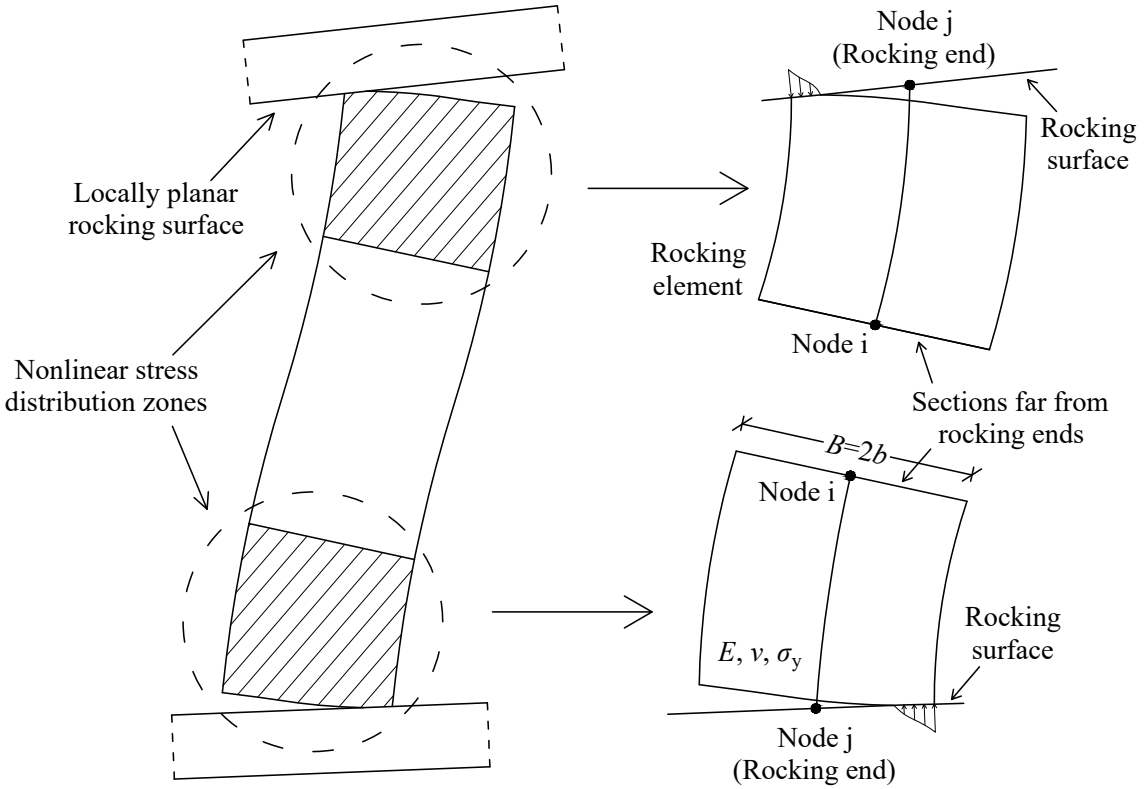

Figure 1.5: Use of the macroelement for the member segments near the rocking ends, where nonlinear stress distributions develop. Two rocking macroelements are used for the rocking column shown, one for each rocking end. Node j of each element refers to the corresponding rocking end.

is only possible when the member is considered deformable, both along its height and across its base, and, as a result, the impact is not instantaneous.

1.5 Thesis outline

The macroelement presented in this thesis is gradually built from simpler to more complex formulations. Each chapter builds upon the formulations and concepts of the previous chapters, so ultimately the formulation of a macroelement for the prediction of the cyclic or dynamic response of inelastic rocking bodies is presented.

In *Chapter 2*, the formulation of the macroelement for the elastic rocking body is presented, where the main concepts used throughout the thesis are introduced. In this chapter, it is shown that for an accurate prediction of the response of deformable rocking bodies, the nonlinear stress distribution near the rocking surface must be taken into account, which cannot be considered by the technical theory of bending used in usual beam-column element formulations. The nonlinear stress distributions across the rocking interface are separated into technical theory of bending distributions according to the resultant forces and self-equilibrating stress distributions, which do not contribute to the resultant forces

but influence the local displacements near the rocking interface, which however are crucial for the determination of the rocking motion.

For the examination of the influence of the self-equilibrating stresses, the model of the semi-infinite strip is used to examine the area of the rocking body near the rocking surface. The nonlinear stress distribution for the semi-infinite strip is calculated according to the theory of elasticity and, more specifically, in this dissertation the numerical methodology proposed by Gaydon and Shepherd (1964) is implemented. Analytical expressions are thus derived for the additional displacements produced by the self-equilibrating normal and shear stresses due to triangular normal and parabolic shear stress distributions across the rocking interface. The aforementioned results are incorporated in a force-based beam-column algorithm (Neuenhofer and Filippou, 1998), which uses a corotational coordinate system, and the produced macroelement can be used in any finite element framework, such as OpenSees.

Three characteristic rocking body configurations are examined: a rocking body under constant vertical force, a tendon-restrained rocking body and a rocking wall inside a single-bay frame. These examples are analyzed using both the proposed macroelement and the commercial finite element program *Abaqus*, while comparison of the results shows the excellent accuracy of the proposed algorithm, which furthermore yields much faster analyses. In addition, parametric investigations of the aforementioned configurations using the proposed macroelement show the effect of member deformability on their response, while the positive effect of the inclusion of rocking members in frames on their seismic response is also shown.

Chapter 3 describes the extension of the previous formulation to account for material inelasticity for monotonic loading. For this reason, a trapezoidal instead of a triangular normal stress distribution is taken into account due to material yielding. Analytical expressions for the additional displacements due to this load are presented, according to the semi-infinite strip results, which are incorporated into the macroelement.

Chapter 4 examines thoroughly the problem of the determination of the displacements across the semi-infinite strip under arbitrary self-equilibrating normal loads on its end. More specifically, analytic expressions are proposed for the displacement function for a concentrated normal load at an arbitrary position across the end of the semi-infinite strip, which must exhibit specific properties. The singularities of this function are examined and its relationship with the displacement function of the similar semi-infinite space problem is recognized.

For an arbitrary normal load distribution, this load can be considered as the integral of continuous concentrated loads and thus the aforementioned analytical expressions must be integrated. The necessary expressions for the calculation of the displacements due to rectangular and triangular loads are provided. The results regarding the triangular loads are used next to calculate the nonlinear stress distribution across the rocking surface, so

that this surface remains planar, as well as the nonlinear displacement distribution of the non-contact region of the rocking body.

In *Chapter 5*, a macroelement formulation for the prediction of the response of inelastic rocking bodies under cyclic loading is proposed. In this case, due to the development of plastic displacements and unloading, typical stress distributions cannot be used as in the monotonic case, but are determined from the target member end displacements using the displacement distribution of the semi-infinite strip.

For this reason, the rocking interface is discretized into control points and a target displacement is assigned to each one according to the member end target displacements. For each iteration, a stress or additional plastic or "gap" displacement is assigned to each node, according to whether an elastic, an inelastic or a non-contact response is assumed, respectively. In order to achieve smoothness of the solution, an approximate methodology is proposed so that the stress and displacement distributions across the intervals between control points are determined from the control point values. The sum of the displacements produced by the resultant forces, the self-equilibrating normal and shear stresses, the additional plastic or "gap" displacements and the preexisting plastic displacements must match the target displacement at each control point.

The response of an inelastic rocking body under constant vertical force is examined next, paying special attention to the stress distribution across the rocking interface and the gradual formation of plastic displacements. Furthermore, the results produced by the macroelement for a tendon-restrained rocking concrete wall and a calcium-silicate brick rocking masonry wall are compared with experimental results, showing a very good agreement given the experimental uncertainties. Comparison of the previous results with ones of corresponding rigid or elastic rocking body models shows that member deformability and material inelasticity must be appropriately taken into account for an accurate estimation of the rocking member motion.

Chapter 6 extends the cyclic macroelement formulation to include the treatment of damping and other motion modes important for the dynamic response of rocking bodies, namely upthrow (complete detachment from the rocking surface) and sliding. Regarding damping, a formulation similar to tangent-stiffness-proportional damping is used, taking into account that the total stress across the rocking interface is always non-tensile and the physical constraints of the problem are not violated. Regarding upthrow and sliding, these motion modes are taken into account in a uniform manner by introducing an intermediate coordinate system that uses a new internal variable representing the displacement due to sliding, which is determined so that a Coulomb friction criterion is adhered to.

Using the proposed formulation, the effect of the damping coefficient and the modulus of elasticity of solitary rocking bodies on the energy loss is examined, where is its shown that the energy loss of almost rigid almost infinitely damped bodies is very close to the one predicted by Housner (1963). In addition, the effect of various parameters, such as

the modulus of elasticity, the damping coefficient, the yield stress and the friction angle on the response of a deformable solitary rocking body under free oscillations, a sine-pulse excitation and a recorded ground motion is examined.

Finally, *Chapter 7* summarizes the key and novel points of this dissertation and proposes suggestions for future research.

2 Modeling of elastic rocking bodies

In this chapter, the formulation for the elastic rocking bodies is presented, which introduces the basic concepts, all more complex models presented in the following chapters build upon. It is noted that, some of the notation was changed with respect to the original corresponding paper (Avgenakis and Psycharis, 2017) in order to be consistent with the notation used in other chapters of this thesis.

2.1 Element coordinate systems

In order to account for the geometric nonlinearity, the macro-element formulation uses the notion of a coordinate system without rigid body modes, which do not contribute to the element forces, an idea which has been extensively used in corotational finite element formulations (e.g. De Borst et al., 2012). This natural (or corotational) coordinate system corresponds to a reference system of a simply supported beam, which has three, instead of six, degrees of freedom (Fig. 2.1b): The axial elongation, δ, the chord rotation at the rocking end, θ_1, and the chord rotation at the other end, θ_2. The forces acting on the respective degrees of freedom, $\mathbf{F}_{\mathrm{n}}$, are the axial force, N, the moment at the rocking end, M_1, and the moment at the other end, M_2.

Transformations between the local and the corotational coordinate system exist, which consider large member displacements (e.g. De Borst et al., 2012). However, for moderately small displacements, the following simple transformations between the local and the corotational coordinate system can be used (e.g. Neuenhofer and Filippou, 1998):

If $\mathbf{u}_{\mathrm{e}} = [u_1, u_2, u_3, u_4, u_5, u_6]^T$ is the vector of the six local system displacements (Fig. 2.1a) and $\mathbf{u}_{\mathrm{n}} = [\delta, \theta_1, \theta_2]^T$ is the vector of the three corotational system displacements (Fig. 2.1b), the conversion between the two vectors is given by

$$\mathbf{u}_{\mathrm{n}} = \mathbf{T}\,\mathbf{u}_{\mathrm{e}} \tag{2.1}$$

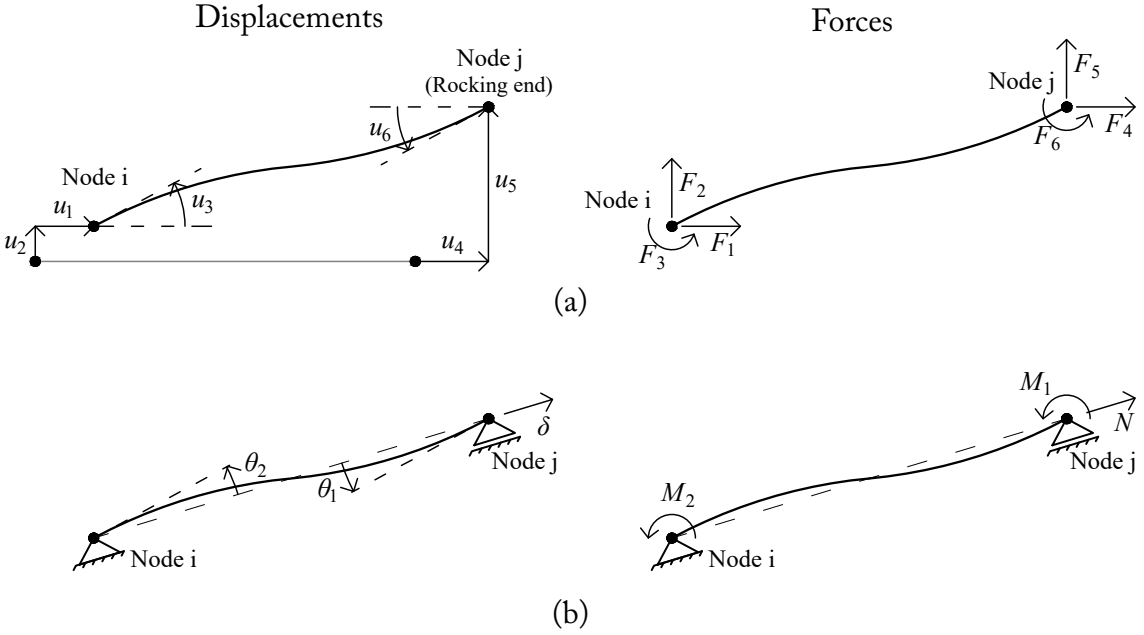

Figure 2.1: (a) Local member displacements and forces, required by the general finite element framework and (b) Corotational member displacements and forces used by the element formulation.

with

$$\mathbf{T} = \begin{bmatrix} -1 & -\frac{1}{2}\frac{u_5 - u_2}{L} & 0 & 1 & \frac{1}{2}\frac{u_5 - u_2}{L} & 0 \\ 0 & \frac{1}{L} & 0 & 0 & -\frac{1}{L} & 1 \\ 0 & \frac{1}{L} & 1 & 0 & -\frac{1}{L} & 0 \end{bmatrix} \tag{2.2}$$

where L is the original length of the member and u_2, u_5 are the transverse displacements in the local coordinate system (Fig. 2.1a).

Similarly, given the vector of nodal forces in the corotational coordinate system, $\mathbf{F}_{\mathrm{n}} = [N, M_1, M_2]^T$ (Fig. 2.1b), the forces in the local coordinate system, $\mathbf{F}_{\mathrm{e}} = [F_1, F_2, F_3, F_4, F_5, F_6]^T$ (Fig. 2.1a), are given by:

$$\mathbf{F}_{\mathrm{e}} = \mathbf{T}^{*}\,\mathbf{F}_{\mathrm{n}} \tag{2.3}$$

where

$$\mathbf{T}^{*} = \begin{bmatrix} -1 & -\frac{u_5 - u_2}{L} & 0 & 1 & \frac{u_5 - u_2}{L} & 0 \\ 0 & \frac{1}{L} & 0 & 0 & -\frac{1}{L} & 1 \\ 0 & \frac{1}{L} & 1 & 0 & -\frac{1}{L} & 0 \end{bmatrix}^{T} \tag{2.4}$$

The corresponding stiffness matrix in the local system, $\mathbf{K}_{\mathrm{e}}$, is given by:

$$\mathbf{K}_{\mathrm{e}} = \mathbf{T}_{\mathrm{g}} + \mathbf{T}^{*}\,\mathbf{K}_{\mathrm{n}}\,\mathbf{T}^{*\mathrm{T}} \tag{2.5}$$

where $\mathbf{K}_{\text{n}}$ is the corotational system stiffness matrix and

$$\mathbf{T}_{\text{g}} = \frac{N}{L}\begin{bmatrix} 0 & 0 & 0 & 0 & 0 & 0 \\ 0 & 1 & 0 & 0 & -1 & 0 \\ 0 & 0 & 0 & 0 & 0 & 0 \\ 0 & 0 & 0 & 0 & 0 & 0 \\ 0 & -1 & 0 & 0 & 1 & 0 \\ 0 & 0 & 0 & 0 & 0 & 0 \end{bmatrix} \tag{2.6}$$

is an additional matrix term due to the geometric nonlinearity with N being the member axial force.

As can be seen in Figs. 1.5 and 2.1, node i of the element has a conventional response (fixed with the connecting element), while node j is the rocking end of the element. The displacements of node j refer to the displacements of the corresponding node at the rocking surface and not to the node at the end of the rocking member. The rocking surface is assumed to remain planar throughout the whole response, meaning that these displacements (translational and rotational) fully describe the linear displacement distribution across the rocking surface.

No limitation is imposed on the displacements of node *j* of the element, meaning that the rocking surface can translate and rotate during the response. For example, in case of the rocking wall shown in Fig. 1.5, which is placed between two beams in one floor of a building, the rocking surfaces on the beam sides are considered to remain planar within the length of the wall, but the beams can move and rotate following the deformation of the whole building. This allows for a greater flexibility regarding the models that can be examined using the proposed macroelement.

It should be emphasized that, since node *j* of the element is attached to the rocking surface and not the body itself, the rigid body modes assumed for the transformation between the local and the corotational coordinate systems correspond to the element as a whole and not just the rocking body. Furthermore, the rigid body rotation assumed for the element, $(u_5 - u_2)/L$, should not be confused with the rotation due to rocking used in rocking literature. For example, a deformed fixed cantilever does have a rigid body rotation in the previous context but has no rotation due to rocking. Besides, the proposed formulation does not treat rocking and deformability as separate phenomena and does not introduce independent variables for each one.

For a conventional elastic member, which does not exhibit rocking motion, the response in the simply supported beam natural coordinate system is linear. Thus, given the natural system nodal forces of the element, $\boldsymbol{F}_{\text{n}}$, the natural system displacements according to the technical theory of bending, $\mathbf{u}_{\text{ttb}}$, are simply given by:

$$\mathbf{u}_{\text{ttb}} = \boldsymbol{f}_{\text{ttb}}\, \boldsymbol{F}_{\text{n}} \tag{2.7}$$

with $\boldsymbol{f}_{\text{ttb}}$ being the flexibility matrix of a simply supported beam, including shear deformation effects (e.g. Przemieniecki, 2012):

$$\boldsymbol{f}_{\text{ttb}} = \begin{bmatrix} \frac{L}{EA} & 0 & 0 \\ 0 & \frac{L}{3EI} + \frac{\alpha}{GAL} & -\frac{L}{6EI} + \frac{\alpha}{GAL} \\ 0 & -\frac{L}{6EI} + \frac{\alpha}{GAL} & \frac{L}{3EI} + \frac{\alpha}{GAL} \end{bmatrix} \tag{2.8}$$

where E is Young's modulus, G is the shear modulus, A is the area of the member section, I is the moment of inertia of the member section and α is the shear shape factor with $\alpha \approx 1.2$ for rectangular cross sections (the shear deformations contribution can be neglected by setting $\alpha = 0.0$).

It should be noted, that in the aforementioned relationships, $P - \delta$ (element internal) effects are not taken into account, since they are not considered important for the formulation of the macro-element.

2.2 Influence of rocking on the element response under given nodal forces

If one of the supports of the member cannot allow the development of tensile stresses, the stress distributions across the interface section differ from those of the technical theory of bending and the response in the natural coordinate system is no longer linear after the initiation of the rocking motion. More specifically, since node j of the element of Fig. 2.1b is assumed to be the rocking end (Fig. 1.5), this happens if the resultant axial force at the rocking interface is located outside the kern of the section, that is if

$$\left| \frac{M_1}{N} \right| > \frac{B}{6} \tag{2.9}$$

where B is the width of the member and M_1 and N are the moment and the axial force at the rocking end, respectively.

Let us assume a member with semi-width $b = B/2$ with the coordinate system and the forces at the rocking end as depicted in Fig. 2.2a, which has a contact length C with the base. For a given natural system force vector, $\boldsymbol{F}_{\text{n}}$, the forces at the rocking end, $\boldsymbol{F}_{\text{r}} = [N_{\text{r}}, M_{\text{r}}, Q_{\text{r}}]^{\text{T}}$, normalized with respect to the member thickness, d, are given by

$$\boldsymbol{F}_{\text{r}} = \boldsymbol{S}_1 \, \boldsymbol{F}_{\text{n}} \tag{2.10}$$

where

$$\boldsymbol{S}_1 = \frac{1}{d} \begin{bmatrix} 1 & 0 & 0 \\ 0 & 1 & 0 \\ 0 & -\frac{1}{L} & -\frac{1}{L} \end{bmatrix} \tag{2.11}$$

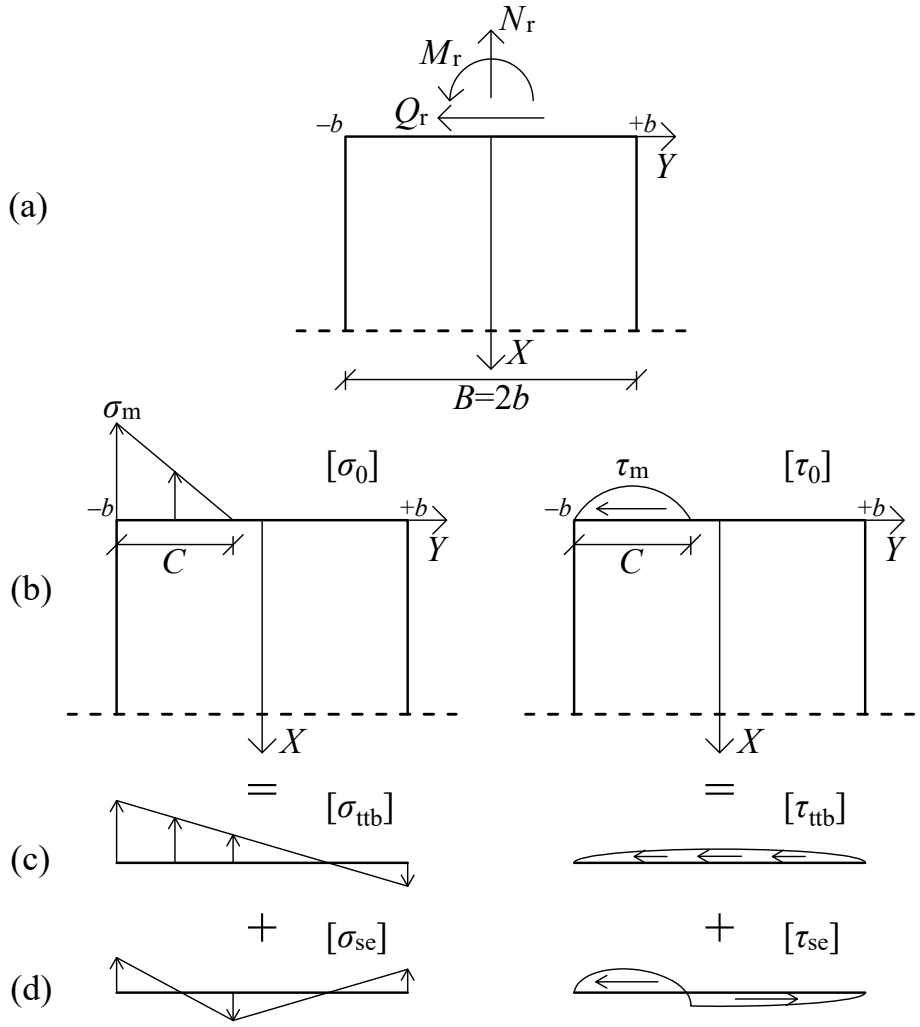

Figure 2.2: (a) Resultant forces at the contact side; (b) Normal and shear stress distributions considered at the rocking interface; (c) Stresses according to the technical theory of bending; and (d) Self-equilibrating stresses.

Without loss of generality, we can assume $M_r > 0$, thus stresses develop at the interval $[-b, -b + C]$. The following stress distributions are considered at the interface between the rocking body and the base (Fig. 2.2b):

(a) *Normal stresses* $[\sigma_0]$ which have a triangular distribution. The maximum value is σ_m at the edge $Y = -b$, while the stresses become zero after length C, that is at $Y = -b + C$.

(b) *Shear stresses* $[\tau_0]$ which are assumed to have a parabolic distribution. Their value is zero at $Y = -b$ and $Y = -b + C$, while the maximum value τ_m occurs at $Y = -b + C/2$.

Therefore, the stress distribution parameter vector for these stress distributions, $\boldsymbol{R} =$

$[C, \sigma_{\mathrm{m}}, \tau_{\mathrm{m}}]^{\mathrm{T}}$, is:

$$\boldsymbol{R} = \begin{Bmatrix} 3\left(b + \dfrac{|M_{\mathrm{r}}|}{N_{\mathrm{r}}}\right) \\ \dfrac{2}{3}\dfrac{N_{\mathrm{r}}}{b + \frac{|M_{\mathrm{r}}|}{N_{\mathrm{r}}}} \\ \dfrac{1}{2}\dfrac{Q_{\mathrm{r}}}{b + \frac{|M_{\mathrm{r}}|}{N_{\mathrm{r}}}} \end{Bmatrix} \tag{2.12}$$

where $N_{\mathrm{r}} < 0$ denotes compression.

As mentioned above, the stress distributions across the rocking interface differ from those of the technical theory of bending. However, since the element material is considered elastic, the principle of superposition holds, so the effect of these stress distributions can be calculated by separating them into two parts:

(i) *Stresses according to the technical theory of bending*, which act on the whole section and can be calculated as usual from the resultant section forces; and

(ii) *Self-equilibrating stresses*, which do not produce resultant forces, but influence the local deformations of the member near the contact zone.

The contribution of the technical theory of bending stresses to the member flexibility matrix and displacements can be calculated according to Eqs. (2.8) and (2.7).

The influence of the self-equilibrating stresses can be more easily evaluated by examining the normalized problem referring to a member with semi-width $b = 1$, which is loaded in the interval $[-1, -1 + c]$, where $c = C/b$ is the normalized contact length. It is noted that the stresses at a point (X, Y) of the general problem are equal to those calculated for the normalized problem at normalized coordinates $x = X/b$, $y = Y/b$ (Gaydon, 1965).

For the normalized problem, the load parameter vector $\boldsymbol{r} = [c, \widetilde{\sigma}_{\mathrm{m}}, \widetilde{\tau}_{\mathrm{m}}]^T$ is given by:

$$\boldsymbol{r} = \boldsymbol{S}_2 \, \boldsymbol{R} \tag{2.13}$$

where

$$\boldsymbol{S}_2 = \begin{bmatrix} \dfrac{1}{b} & 0 & 0 \\ 0 & 1 & 0 \\ 0 & 0 & \rho \end{bmatrix} \tag{2.14}$$

with $\rho = \mathrm{sgn}\,(M_{\mathrm{r}})$ denoting the signum function of M_{r}.

For the forces at the rocking end, $\boldsymbol{F}_{\mathrm{r}}$, the normal and shear stress distributions according to the technical theory of bending, $[\sigma_{\mathrm{ttb}}]$ and $[\tau_{\mathrm{ttb}}]$, are calculated first (Fig. 2.2c). By subtracting these stress distributions from the ones assumed for the rocking interface, $[\sigma_0]$ and $[\tau_0]$, shown in Fig. 2.2b, one can derive the self-equilibrating stress distributions

that need to be considered (Fig. 2.2d). These self-equilibrating normal and shear stress distributions, given in terms of the normalized problem, are:

$$\widetilde{\sigma}_{\text{se}}(y) = \begin{cases} \widetilde{\sigma}_{\text{m}} \left[\left(1 - \frac{1}{c} - \frac{c}{4} \right) + \left(\frac{3c}{4} - \frac{c^2}{4} - \frac{1}{c} \right) y \right] & \text{for } -1 \leq y \leq -1 + c \\ \widetilde{\sigma}_{\text{m}} \left[\left(-\frac{c}{4} \right) + \left(\frac{3c}{4} - \frac{c^2}{4} \right) y \right] & \text{for } -1 + c \leq y \leq 1 \end{cases} \tag{2.15}$$

$$\widetilde{\tau}_{\text{se}}(y) = \begin{cases} \widetilde{\tau}_{\text{m}} \left[\left(\frac{4(c-1)}{c^2} - \frac{c}{2} \right) + \left(\frac{4(c-2)}{c^2} \right) y + \left(-\frac{4}{c^2} + \frac{c}{2} \right) y^2 \right] & \text{for } -1 \leq y \leq -1 + c \\ \widetilde{\tau}_{\text{m}} \left[-\frac{c}{2} + \frac{c}{2} y^2 \right] & \text{for } -1 + c \leq y \leq 1 \end{cases} \tag{2.16}$$

2.3 Self-equilibrating stresses contribution

Semi-infinite strip problem

In order to examine the effect of the self-equilibrating stresses of Eqs. (2.15) and (2.16) on the normalized simply-supported beam member of semi-width $b = 1$, it is useful to notice that, since the self-equilibrating stresses do not produce resultant forces, their effect far from the loaded area is insignificant, as the Saint-Venant assumption suggests.

For this reason, instead of solving the problem of a simply-supported beam loaded on its one end with self-equilibrating stress distributions, the equivalent semi-infinite strip problem, loaded on its end ($x = 0, -1 \leq y \leq 1$) with these self-equilibrating stress distributions, is solved instead (Fig. 2.3). This is possible, because, as will be shown later, there is a compatibility between the active degrees of freedom of the two models. It should be noted, that, in contrast to the well-known semi-infinite space, the semi-infinite strip is stress-free at its sides ($y = \pm 1$).

The stress distribution problem of a semi-infinite strip with semi-width $b = 1$ is solved with the method developed by Gaydon and Shepherd (1964), using stress functions of certain form. This method is then extended in order to solve the rocking body problem.

The problem considered is that of a semi-infinite strip $x \geq 0$, $-1 \leq y \leq 1$ with self-equilibrating stresses at the end, $x = 0$, σ_x^0 and τ_{xy}^0. These self-equilibrating stress distributions are decomposed into symmetric (σ_x^0 even and τ_{xy}^0 odd in y) and antisymmetric (σ_x^0 odd and τ_{xy}^0 even in y) parts, since for each one, stress functions of different form need to be assumed.

The stress distribution produced by the self-equilibrating loads of the symmetric or antisymmetric problem can be derived using a stress function ϕ that satisfies the biharmonic equation:

$$\nabla^4 \phi = 0 \tag{2.17}$$

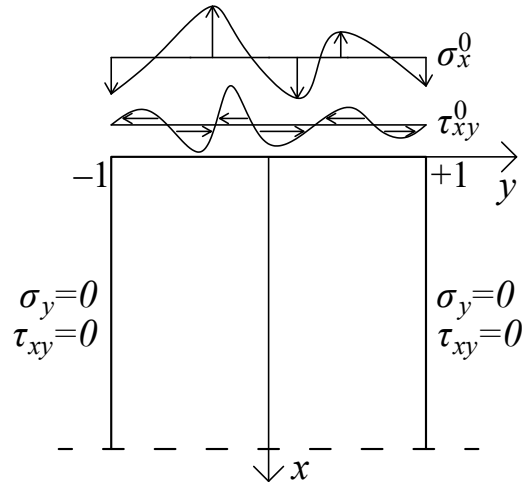

Figure 2.3: Normalized semi-infinite strip problem.

and the following boundary conditions:

$$\begin{aligned} \phi_{xx} = \phi_{yy} = 0, \text{ on } y = \pm 1 \\ \phi_{yy} = \sigma_x^0, \quad \phi_{xy} = -\tau_{xy}^0, \text{ on } x = 0 \end{aligned} \tag{2.18}$$

in which ϕ_{xx}, ϕ_{yy} and ϕ_{xy} denote the second derivative of ϕ with respect to the corresponding variables. Furthermore, as the stresses are self-equilibrating and expected to vanish as $x \to \infty$, the following condition must also hold:

$$\phi \to 0, \text{ as } x \to \infty \tag{2.19}$$

The stress functions used by Gaydon and Shepherd (1964) to solve this problem have the form

$$\phi(x, y) = 2 \sum_j \mathrm{Re} \left[(A_j + iB_j) \frac{e^{k_j x}}{k_j^2} \Phi_j(y) \right] \tag{2.20}$$

where the functions $\Phi_j(y)$ are expanded with respect to some other functions $Y_i(y)$:

$$\Phi_j(y) = \begin{cases} \sum_i a_{ij} Y_i(y) & \text{(S)} \\ \sum_i b_{ij} Y_i(y) & \text{(A)} \end{cases} \tag{2.21}$$

for the symmetric (S) and the antisymmetric (A) problem, respectively.

A step-by-step presentation of the procedure proposed by Gaydon and Shepherd (1964) for the calculation of the terms needed for the determination of the stress function, as well as for the calculation of the stress components at any point with coordinates (x, y), is described in the following:

1. Calculate the constants $k_j = -a_j + ib_j$, with $a_j > 0, b_j > 0$, from the first n_j complex roots of equations

$$\begin{aligned} \sin 2k_j + 2k_j = 0 \quad \text{(S)} \\ \sin 2k_j - 2k_j = 0 \quad \text{(A)} \end{aligned} \tag{2.22}$$

sorted in ascending magnitude order.

2. Calculate the constants λ_i and μ_i, from the first n_i positive real roots of equations

$$\begin{aligned} &\tan\lambda_i + \tanh\lambda_i = 0 \quad \text{(S)} \\ &\tan\mu_i - \tanh\mu_i = 0 \quad \text{(A)} \end{aligned} \tag{2.23}$$

sorted in ascending magnitude order. For the method to give good results, Gaydon and Shepherd (1964) suggest that more λ_is and μ_is than k_js should be used (e.g. n_j=10, n_i=20). In the present work, as computers have evolved tremendously compared to the time the original paper was written, a far greater number of these constants are numerically evaluated and used (n_j=500, n_i=1000), in order to capture more accurately stress distributions even for small contact lengths.

3. For each k_j and λ_i or μ_i calculated in steps 1 and 2, calculate the constants a'_{ij}, b'_{ij} and a''_{ij}, b''_{ij} from:

$$\begin{aligned} \frac{a_{ij}}{k_j^2} = a'_{ij} + ib'_{ij} &= 4\sqrt{2}\,(k_j \sin k_j + \lambda_i \cos k_j \tanh\lambda_i)\left[\frac{1}{(\lambda_i^2+k_j^2)^2} - \frac{1}{(\lambda_i^2-k_j^2)^2}\right] \quad \text{(S)} \\ \frac{b_{ij}}{k_j^2} = a''_{ij} + ib''_{ij} &= 4\sqrt{2}\,(k_j \cos k_j + \mu_i \sin k_j \coth\mu_i)\left[\frac{1}{(\mu_i^2+k_j^2)^2} - \frac{1}{(\mu_i^2-k_j^2)^2}\right] \quad \text{(A)} \end{aligned} \tag{2.24}$$

4. For the terms a_j, b_j calculated in step 1 and $a'_{ij}, b'_{ij}, a''_{ij}, b''_{ij}$ calculated in step 3, formulate the $2n_i \times 2n_j$ matrix $\boldsymbol{A}$, in the form:

$$\boldsymbol{A} = \begin{bmatrix} \ddots & \vdots & \vdots & \iddots \\ \cdots & C_{ij} & D_{ij} & \cdots \\ \cdots & E_{ij} & F_{ij} & \cdots \\ \iddots & \vdots & \vdots & \ddots \end{bmatrix} \tag{2.25}$$

where

$$\begin{aligned} C_{ij} &= 2a'_{ij} \\ D_{ij} &= -2b'_{ij} \\ E_{ij} &= 2a_j a'_{ij} + 2b_j b'_{ij} \\ F_{ij} &= 2b_j a'_{ij} - 2a_j b'_{ij} \end{aligned} \quad \text{(S)} \quad \text{or} \quad \begin{aligned} C_{ij} &= 2a''_{ij} \\ D_{ij} &= -2b''_{ij} \\ E_{ij} &= 2a_j a''_{ij} + 2b_j b''_{ij} \\ F_{ij} &= 2b_j a''_{ij} - 2a_j b''_{ij} \end{aligned} \quad \text{(A)} \tag{2.26}$$

5. Formulate the matrix $\boldsymbol{M}$, which is given by

$$\boldsymbol{M} = (\boldsymbol{A}^{\mathrm{T}}\,\boldsymbol{A})^{-1}\,\boldsymbol{A}^{\mathrm{T}} \tag{2.27}$$

The values used until now are independent of the loading, so they can be calculated once and for all.

6. For each λ_i or μ_i calculated in step 2, calculate the coefficients α_i, β_i regarding the loading:

$$\begin{aligned} \alpha_i &= \frac{1}{\lambda_i^4}\int_{-1}^{1}\sigma_x^0 Y_i''\mathrm{d}y \\ \beta_i &= -\frac{1}{\lambda_i^4}\int_{-1}^{1}\tau_{xy}^0 Y_i^{(3)}\mathrm{d}y \end{aligned} \quad \text{(S)} \quad \text{or} \quad \begin{aligned} \alpha_i &= \frac{1}{\mu_i^4}\int_{-1}^{1}\sigma_x^0 Y_i''\mathrm{d}y \\ \beta_i &= -\frac{1}{\mu_i^4}\int_{-1}^{1}\tau_{xy}^0 Y_i^{(3)}\mathrm{d}y \end{aligned} \quad \text{(A)} \tag{2.28}$$

where

$$\begin{aligned} Y_i(y) &= \frac{1}{\sqrt{2}}\left(\frac{\cos\lambda_i y}{\cos\lambda_i} - \frac{\cosh\lambda_i y}{\cosh\lambda_i}\right) \quad \text{(S)} \\ Y_i(y) &= \frac{1}{\sqrt{2}}\left(\frac{\sin\mu_i y}{\sin\mu_i} - \frac{\sinh\mu_i y}{\sinh\mu_i}\right) \quad \text{(A)} \end{aligned} \tag{2.29}$$

The terms α_i, β_i are arranged into a vector $\boldsymbol{\ell}$:

$$\boldsymbol{\ell} = \begin{bmatrix} \alpha_1 & \beta_1 & \cdots & \alpha_i & \beta_i & \cdots & \alpha_{n_i} & \beta_{n_i} \end{bmatrix}^T \tag{2.30}$$

7. Calculate the load-dependent vector $\boldsymbol{L}$ from the equation:

$$\boldsymbol{L} = \boldsymbol{M}\,\boldsymbol{\ell} \tag{2.31}$$

8. For each k_j calculated in step 1, calculate the parameters P_j, Q_j, R_j, S_j, U_j, V_j, dependent on coordinate y, using the following equations:

$$\begin{aligned} P_j + iQ_j &= \begin{cases} -(\cos 2k_j + 3)\cos k_j y + 2k_j y \sin ky & \text{(S)} \\ -(\cos 2k_j - 3)\sin k_j y + 2k_j y \cos ky & \text{(A)} \end{cases} \\ R_j + iS_j &= \begin{cases} (\cos 2k_j + 1)\sin ky + 2k_j y \cos k_j y & \text{(S)} \\ -(\cos 2k_j - 1)\cos ky - 2k_j y \sin k_j y & \text{(A)} \end{cases} \\ U_j + iV_j &= \begin{cases} (\cos 2k_j - 1)\cos k_j y - 2k_j y \sin k_j y & \text{(S)} \\ (\cos 2k_j + 1)\sin k_j y - 2k_j y \cos k_j y & \text{(A)} \end{cases} \end{aligned} \tag{2.32}$$

the real and imaginary parts of which are arranged into the following vectors:

$$\boldsymbol{Y}_{\mathrm{PQ}} = \begin{bmatrix} \vdots \\ P_j \\ Q_j \\ \vdots \end{bmatrix} \quad \boldsymbol{Y}_{\mathrm{RS}} = \begin{bmatrix} \vdots \\ R_j \\ S_j \\ \vdots \end{bmatrix} \quad \boldsymbol{Y}_{\mathrm{UV}} = \begin{bmatrix} \vdots \\ U_j \\ V_j \\ \vdots \end{bmatrix} \tag{2.33}$$

9. For each a_j and b_j calculated in step 1, form the the $2n_j \times 2n_j$ banded matrix $\boldsymbol{X}$, dependent on coordinate x, as:

$$\boldsymbol{X} = \begin{bmatrix} \ddots & \ddots & 0 & 0 \\ \ddots & 2e^{-a_j x}\cos b_j x & -2e^{-a_j x}\sin b_j x & 0 \\ 0 & -2e^{-a_j x}\sin b_j x & -2e^{-a_j x}\cos b_j x & \ddots \\ 0 & 0 & \ddots & \ddots \end{bmatrix} \tag{2.34}$$

10. Calculate the stresses at point (x, y) from by the following equations:

$$\begin{aligned} \sigma_x &= \boldsymbol{L}^{\mathrm{T}}\, \boldsymbol{X}\, \boldsymbol{Y}_{\mathrm{PQ}} \\ \tau_{xy} &= \boldsymbol{L}^{\mathrm{T}}\, \boldsymbol{X}\, \boldsymbol{Y}_{\mathrm{RS}} \\ \sigma_y &= \boldsymbol{L}^{\mathrm{T}}\, \boldsymbol{X}\, \boldsymbol{Y}_{\mathrm{UV}} \end{aligned} \tag{2.35}$$

where $\boldsymbol{L}$ is dependent on the loading, $\boldsymbol{X}$ is dependent on coordinate x and $\boldsymbol{Y}_{\mathrm{PQ}}$, $\boldsymbol{Y}_{\mathrm{RS}}$, $\boldsymbol{Y}_{\mathrm{UV}}$ are dependent on coordinate y.

Application to the rocking body

Stress loading at the rocking interface In order to apply the aforementioned procedure to the self-equilibrating stresses of Eqs. (2.15) and (2.16), the stresses have to be decomposed into symmetric and antisymmetric parts, as mentioned above.

Then, the necessary coefficients α_i and β_i for the assumed stress distributions are calculated from equations (2.28), which can be carried out with the help of a symbolic algebra system, such as the Matlab symbolic math toolbox. The results for the stress distributions of Eqs. (2.15) and (2.16) are given in Table 2.1*.

Table 2.1: Load coefficients α_i, β_i

Problem	Auxiliary terms	Load coefficients
Symmetric problem	$l_1 = \dfrac{\cosh\left[\lambda_i(c-1)\right]}{\cosh\lambda_i}$ $l_2 = -\dfrac{\sinh\left[\lambda_i(c-1)\right]}{\cosh\lambda_i}$ $l_3 = \dfrac{\cos\left[\lambda_i(c-1)\right]}{\cos\lambda_i}$ $l_4 = \dfrac{\sin\left[\lambda_i(c-1)\right]}{\cos\lambda_i}$	$\alpha_i = \dfrac{\widetilde{\sigma}_{\mathrm{m}}}{\sqrt{2}\lambda_i^4 c}(l_3 - l_1)$ $\beta_i = \dfrac{2\sqrt{2}\widetilde{\tau}_{\mathrm{m}}}{\lambda_i^4 c^2}(2l_3 - 2l_1 + \lambda_i c l_4 - \lambda_i c l_2)$
Antisymmetric problem	$l_1 = \dfrac{\sinh\left[\mu_i(c-1)\right]}{\sinh\mu_i}$ $l_2 = -\dfrac{\cosh\left[\mu_i(c-1)\right]}{\sinh\mu_i}$ $l_3 = \dfrac{\sin\left[\mu_i(c-1)\right]}{\sin\mu_i}$ $l_4 = -\dfrac{\cos\left[\mu_i(c-1)\right]}{\sin\mu_i}$	$\alpha_i = \dfrac{\widetilde{\sigma}_{\mathrm{m}}}{\sqrt{2}\mu_i^4 c}(l_3 - l_1)$ $\beta_i = \dfrac{2\sqrt{2}\widetilde{\tau}_{\mathrm{m}}}{\mu_i^4 c^2}(2l_3 - 2l_1 + \mu_i c l_4 - \mu_i c l_2)$

Stress distributions along the member length In Fig. 2.4a, the stress distributions σ_x across the member sections at various X/B values along the member length are shown, for

*In the original paper, there is a typographical error regarding the l_2 term of the symmetric problem.

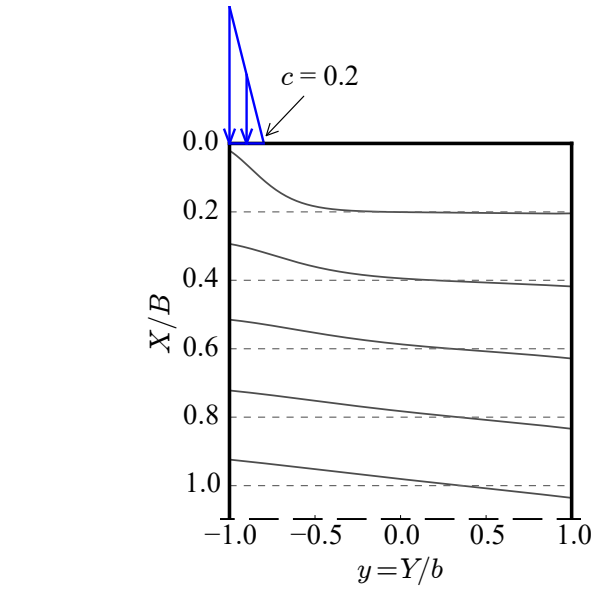

(a)

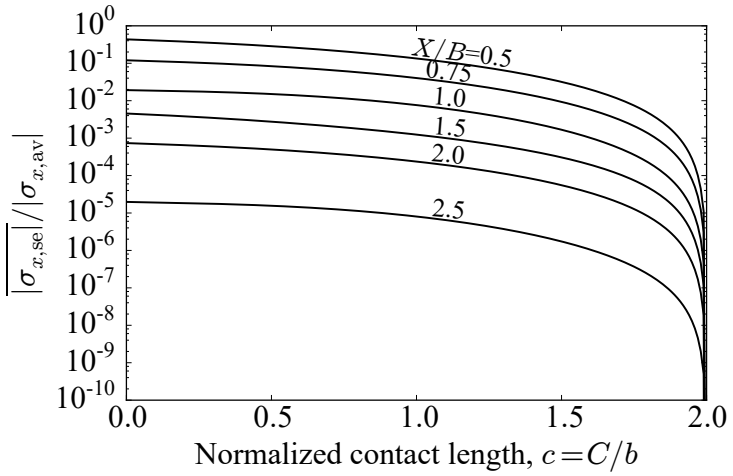

(b)

Figure 2.4: (a) Nonlinear stress distributions at various sections along the member length for partial normal stress loading at the top side and (b) variation of the ratio of the average absolute self-equilibrating stresses over the average total normal stress across the section with the normalized contact length.

a normal stress distribution load with contact length $c = 0.2$. In order to derive the total stress distributions, the stresses according to the technical theory of bending and those produced by the self-equilibrating stresses (Eq. 2.35) have to be added.

It can be seen that the compression-only triangular distribution at $X/B = 0$ gradually approaches the linear stress distribution of the technical theory of bending for sections far from the loaded area. Theoretically, the stresses produced by the self-equilibrating stress loading exist up to an infinite length. However, as can be seen from Fig. 2.4a, the stress distribution is practically linear even for $X/B = 1.0$. This suggests that, for the self-equilibrating stresses contribution, the substitution of a member with length $L \geq B$ with a semi-infinite strip would not introduce significant error to the expected member response. In contrast, if the member examined has length significantly smaller than B, the section at node i of the element (Fig. 2.1) does not remain flat and, thus, a beam-column element with conventional degrees of freedom may be unsuitable.

This is better presented in Fig. 2.4b, where the average of the absolute values of the self-equilibrating stresses $\sigma_{x,\mathrm{se}}$ across the member section, normalized with respect to the absolute mean stress value, are shown for various X/B values along the member length, for different normalized contact lengths, c. As can be seen, for $X = B$, there is about a 2% average error if a linear stress distribution is assumed instead of the real one containing the self-equilibrating stresses contribution. This suggests again that a choice of a member with length $L \geq B$ would be adequate for the problem examined herewith.

Fiber elongations due to the self-equilibrating stresses The problem considered is a plane stress problem, therefore the strain ϵ_x is given by:

$$\epsilon_x = \frac{1}{E}(\sigma_x - \nu\,\sigma_y) \tag{2.36}$$

and the elongation of the semi-infinite strip fiber located at coordinate y is:

$$u(y) = \int_0^\infty \epsilon_x \mathrm{d}x = \frac{1}{E}\left(\int_0^\infty \sigma_x \mathrm{d}x - \nu \int_0^\infty \sigma_y \mathrm{d}x\right) \tag{2.37}$$

As mentioned before, the self-equilibrating stresses are expected to virtually vanish in a small distance from the loaded edge of the strip (Fig. 2.4), so there is no practical difference between the elongation at coordinate y of the semi-infinite strip and that of a finite length member, provided the length is large enough.

Forming a new $2n_j \times 2n_j$ banded matrix $\boldsymbol{J}$ in the form:

$$\boldsymbol{J} = \begin{bmatrix} \ddots & \ddots & 0 & 0 \\ \ddots & \dfrac{a_j}{a_j^2+b_j^2} & -\dfrac{b_j}{a_j^2+b_j^2} & 0 \\ 0 & -\dfrac{b_j}{a_j^2+b_j^2} & -\dfrac{a_j}{a_j^2+b_j^2} & \ddots \\ 0 & 0 & \ddots & \ddots \end{bmatrix} \tag{2.38}$$

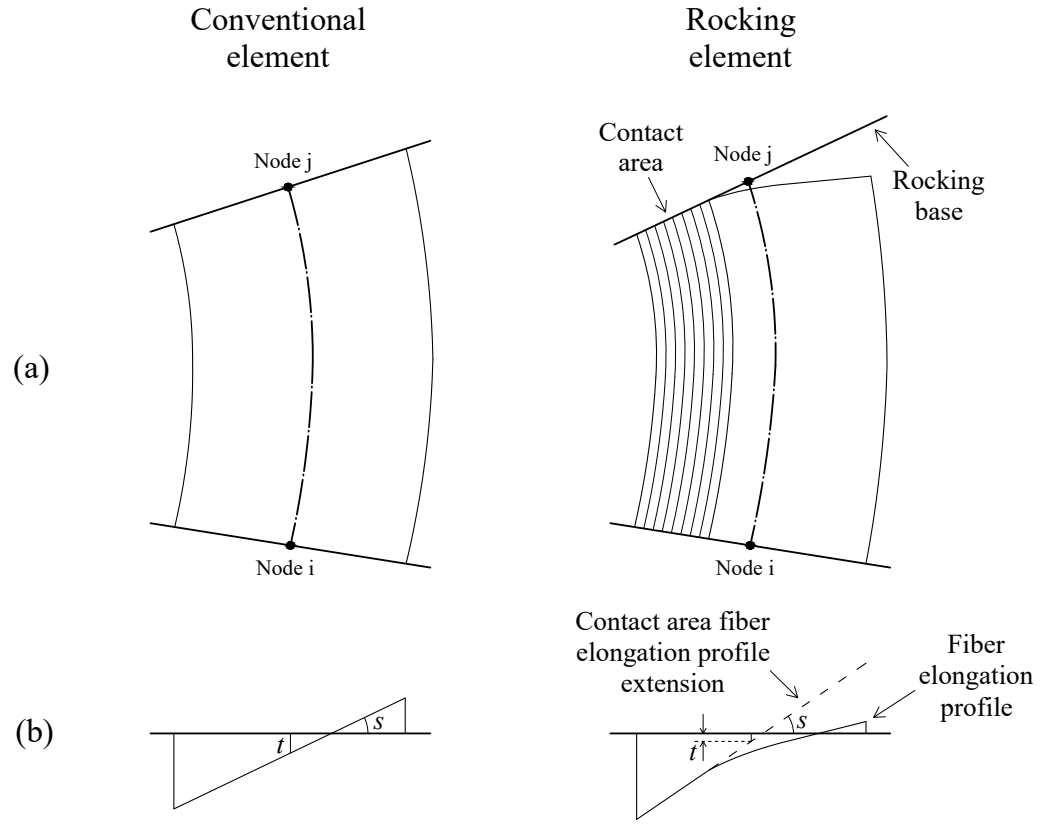

Figure 2.5: (a) Deformed shapes and (b) fiber elongation profiles for a conventional and a rocking element.

it can be proven that the elongation of the fiber at y is given by:

$$u(y) = \frac{2}{E} \boldsymbol{L}^{\mathrm{T}} \boldsymbol{J} \left(\boldsymbol{Y}_{\mathrm{PQ}} - \nu \, \boldsymbol{Y}_{\mathrm{UV}} \right) \tag{2.39}$$

Nodal displacements due to the self-equilibrating stresses In Fig. 2.5a, the deformed shape of a conventional and a rocking element are shown, while in Fig. 2.5b the corresponding fiber elongation profiles are presented, which are the integrals of the deformations along the member length for each fiber across the member section.

For a conventional element, it can be seen that the fiber elongation profile is linear across the member section. Its value in the middle of the section, t, corresponds to the relative axial displacement between nodes i and j, while its slope, s, corresponds to the relative rotation between nodes i and j.

For a rocking element, the influence of the self-equilibrating stresses on the fiber elongation profile has to be considered. By applying Eq. (2.39) for various fibers across the semi-infinite strip for the self-equilibrating loads given in Eqs. (2.15) and (2.16), it can be seen that the fiber elongation profile across the element due to the self-equilibrating stresses is nonlinear. This means that the total fiber elongation profile is also nonlinear, as shown in Fig. 2.5b for the rocking element.

In this case however, only the fibers of the contact area of the element extend to the rocking base, since a gap forms between the rest of the interface section and the rocking base. Thus, the relative axial elongation and the relative rotation between nodes i and j (node j remains fixed to the rocking base) are determined from the fiber elongation profile of the contact area only. More specifically, the relative axial elongation corresponds to t, which is the value of the contact area fiber elongation profile, or its extension, in the middle of the section, while the relative rotation corresponds to s, which is the slope of the contact area fiber elongation profile (Fig. 2.5b). It is noted that the length of the gap at a fiber of the element that is not in contact with the rocking base is evaluated from the difference between the corresponding values of the contact area fiber elongation profile extension (dashed line in Fig. 2.5b) and the true fiber elongation profile (solid line in Fig. 2.5b).

As mentioned above, specific stress distributions, $[\sigma_0]$ and $[\tau_0]$, were assumed at the contact area (Fig. 2.2), without imposing any direct constraint regarding the fiber elongation profile. As a result, the integration of the strains along the fibers results in a contact area that is approximately flat, but not exactly flat. However, for the real problem involving a rigid base mat, the sections at nodes i and j of the element remain flat. To overcome this problem, the elongation profile $u(y)$ of the semi-infinite strip fibers across the contact region $[-1, -1 + c]$ is interpolated by a linear function $g(y) = \delta_0 + \theta\, y$.

Since the self-equilibrating stresses are considered to influence the displacements of the rocking end only (node j), it is evident that the parameters δ_0 and θ of the linear approximation correspond to the normalized problem additional axial elongation and rotation of node j of the element due to the self equilibrating stresses.

In order to calculate the terms δ_0 and θ, the square error between the elongation, $u(y)$, and the linear approximation, $g(y)$:

$$\mathrm{SE} = \int_{-1}^{-1+c} (u(y) - g(y))^2 \mathrm{d}y \tag{2.40}$$

has to be minimized. Setting the derivatives of SE with respect to the two unknown parameters δ_0 and θ to zero leads to:

$$\begin{aligned} \int_{-1}^{-1+c} (\delta_0 + \theta y)\mathrm{d}y &= \int_{-1}^{-1+c} u(y)\mathrm{d}y \\ \int_{-1}^{-1+c} y(\delta_0 + \theta y)\mathrm{d}y &= \int_{-1}^{-1+c} yu(y)\mathrm{d}y \end{aligned} \tag{2.41}$$

By defining the following quantities for the symmetric problem:

$$\begin{aligned}
T_{1j} &= \frac{1}{k_j^2}((\cos 2k_j + 1)\sin\left[k_j(c-1)\right] + 2k_j(c-1)\cos\left[k_j(c-1)\right]) \\
T_{2j} &= \frac{1}{k_j^3}((\cos 2k_j - 1)\cos\left[k_j(c-1)\right] - 2k_j(c-1)\sin\left[k_j(c-1)\right]) \\
T_{3j} &= \frac{4}{k_j^2}\left(-\sin k_j - \sin\left[k_j(c-1)\right]\right) \\
T_{4j} &= \frac{4}{k_j^3}(-\cos\left[k_j(c-1)\right] + \cos k_j) - \frac{4}{k_j^2}\left((c-1)\sin\left[k_j(c-1)\right] - \sin k_j\right)
\end{aligned} \tag{2.42}$$

and for the antisymmetric one:

$$\begin{aligned}
T_{1j} &= \frac{1}{k_j^2}(-(\cos 2k_j - 1)\cos\left[k_j(c-1)\right] - 2k_j(c-1)\sin\left[k_j(c-1)\right]) \\
T_{2j} &= \frac{1}{k_j^3}((\cos 2k_j + 1)\sin\left[k_j(c-1)\right] - 2k_j(c-1)\cos\left[k_j(c-1)\right]) \\
T_{3j} &= \frac{4}{k_j^2}(\cos k_j - \cos\left[k_j(c-1)\right]) \\
T_{4j} &= \frac{4}{k_j^3}(\sin\left[k_j(c-1)\right] + \sin k_j) - \frac{4}{k_j^2}((c-1)\cos\left[k_j(c-1)\right] + \cos k_j)
\end{aligned} \tag{2.43}$$

which are arranged into vectors:

$$\boldsymbol{T}_1 = \begin{bmatrix} \vdots \\ \mathrm{Re}(T_{1j}) \\ \mathrm{Im}(T_{1j}) \\ \vdots \end{bmatrix} \quad \boldsymbol{T}_2 = \begin{bmatrix} \vdots \\ \mathrm{Re}(T_{2j}) \\ \mathrm{Im}(T_{2j}) \\ \vdots \end{bmatrix} \quad \boldsymbol{T}_3 = \begin{bmatrix} \vdots \\ \mathrm{Re}(T_{3j}) \\ \mathrm{Im}(T_{3j}) \\ \vdots \end{bmatrix} \quad \boldsymbol{T}_4 = \begin{bmatrix} \vdots \\ \mathrm{Re}(T_{4j}) \\ \mathrm{Im}(T_{4j}) \\ \vdots \end{bmatrix} \tag{2.44}$$

and setting:

$$\begin{aligned}
\boldsymbol{T}_{\mathrm{A}} &= (1+\nu)\boldsymbol{T}_1 + \nu\boldsymbol{T}_3 \\
\boldsymbol{T}_{\mathrm{B}} &= (1+\nu)(\boldsymbol{T}_2 + (c-1)\boldsymbol{T}_1) + \nu\boldsymbol{T}_4
\end{aligned} \tag{2.45}$$

the fiber elongation integrals involved in the error minimization process (Eq. 2.41), arranged into vector form, are equal to

$$\boldsymbol{H} = \begin{Bmatrix} \int_{-1}^{c-1} u(y)\mathrm{d}y \\ \int_{-1}^{c-1} yu(y)\mathrm{d}y \end{Bmatrix} = \begin{Bmatrix} \frac{2}{E}\boldsymbol{L}^{\mathrm{T}}\boldsymbol{I}_s\boldsymbol{T}_{\mathrm{A}} \\ \frac{2}{E}\boldsymbol{L}^{\mathrm{T}}\boldsymbol{I}_s\boldsymbol{T}_{\mathrm{B}} \end{Bmatrix} \tag{2.46}$$

where

$$\boldsymbol{I}_s = \begin{bmatrix} 1 & 0 & 0 & \cdots \\ 0 & -1 & 0 & \cdots \\ 0 & 0 & 1 & \cdots \\ \vdots & \vdots & \vdots & \ddots \end{bmatrix} \tag{2.47}$$

is a $2n_j \times 2n_j$ identity matrix, with alternating sign diagonal entries.

Then, the solution of Eq. (2.41) with respect to the displacement vector of the normalized self-equilibrating stresses problem, $\boldsymbol{u}_{\text{sen}} = [\delta_0, \theta]^{\text{T}}$, can be calculated as:

$$\boldsymbol{u}_{\text{sen}} = \boldsymbol{G}\,\boldsymbol{H} \tag{2.48}$$

where

$$\boldsymbol{G} = \begin{bmatrix} 4\dfrac{c^2 - 3c + 3}{c^3} & -6\dfrac{c-2}{c^3} \\ -6\dfrac{c-2}{c^3} & \dfrac{12}{c^3} \end{bmatrix} \tag{2.49}$$

Polynomial approximation Although the displacement vector of the normalized problem, $\boldsymbol{u}_{\text{sen}}$, can be evaluated analytically from Eq. (2.48), the programming of the aforementioned procedure is difficult and error-prone. Furthermore, large matrix computations are needed for an accurate prediction of the rocking response and numerical problems may arise for extreme loading conditions (very small c values).

For this reason, a polynomial approximation of the results produced by Eq. (2.48) is proposed for practical purposes, leading to faster and more robust analyses. Since the response is elastic, it can be concluded that the results are linear with respect to parameters E, $\widetilde{\sigma}_{\text{m}}$ and $\widetilde{\tau}_{\text{m}}$, but nonlinear with respect to c.

In Figs. 2.6 and 2.7, the variation of the terms $\delta_0 \cdot E$ and $\theta \cdot E$ versus c, summed for the symmetrical and the antisymmetrical self-equilibrating stresses problems, is presented for the cases $\widetilde{\sigma}_{\text{m}} = 1$, $\widetilde{\tau}_{\text{m}} = 0$ and $\widetilde{\sigma}_{\text{m}} = 0$, $\widetilde{\tau}_{\text{m}} = 1$, respectively, as given by the aforementioned algorithm.

It is seen that, a sixth-order polynomial approximation with respect to c could approximate these results very well. Combining the contributions of the normal and shear stress loadings and using the polynomial term vector $\boldsymbol{P}_c$:

$$\boldsymbol{P}_c = \begin{bmatrix} c^6 & c^5 & c^4 & c^3 & c^2 & c & 1 \end{bmatrix}^T \tag{2.50}$$

the displacement vector of the normalized problem, $\boldsymbol{u}_{\text{sen}}$ is given by the simple equation:

$$\boldsymbol{u}_{\text{sen}} = \frac{1}{E} \begin{Bmatrix} \left(\widetilde{\sigma}_{\text{m}}\,\boldsymbol{V}_\sigma^{\text{T}} + \widetilde{\tau}_{\text{m}}\,\boldsymbol{V}_\tau^{\text{T}}\right)\boldsymbol{P}_c \\ \left(\widetilde{\sigma}_{\text{m}}\,\boldsymbol{R}_\sigma^{\text{T}} + \widetilde{\tau}_{\text{m}}\,\boldsymbol{R}_\tau^{\text{T}}\right)\boldsymbol{P}_c \end{Bmatrix} \tag{2.51}$$

in which

$$\begin{aligned} \boldsymbol{V}_\tau &= \boldsymbol{V}_{\tau 0} + \nu \boldsymbol{V}_{\tau\nu} \\ \boldsymbol{R}_\tau &= \boldsymbol{R}_{\tau 0} + \nu \boldsymbol{R}_{\tau\nu} \end{aligned} \tag{2.52}$$

and the polynomial constant term $\boldsymbol{V}_\sigma$ and $\boldsymbol{R}_\sigma$ (for the normal stress contribution) and $\boldsymbol{V}_{\tau 0}, \boldsymbol{V}_{\tau\nu}, \boldsymbol{R}_{\tau 0}, \boldsymbol{R}_{\tau\nu}$ (for the shear stress contribution) vectors given in Table 2.2.

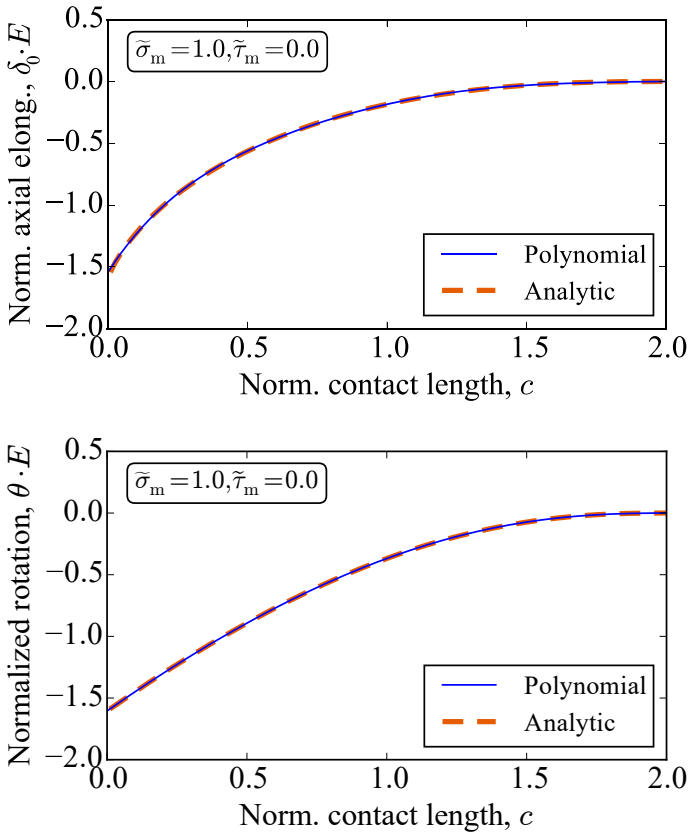

Figure 2.6: Comparison of the polynomial approximation of the displacements due to the self-equilibrating stresses with the analytical ones for $\tilde{\sigma}_m = 1$ and $\tilde{\tau}_m = 0$.

Table 2.2: Polynomial approximation constant term vectors

Variable	Normal stress contribution	Shear stress contribution	
		Initial ($\nu = 0$)	Poisson contribution
Axial elongation	$\boldsymbol{V}_\sigma = \begin{Bmatrix} -0.14037854 \\ 1.07433666 \\ -3.27895019 \\ 5.21236946 \\ -5.03768666 \\ 3.53446688 \\ -1.54848601 \end{Bmatrix}$	$\boldsymbol{V}_{\tau 0} = \begin{Bmatrix} 0.14011255 \\ -1.03832545 \\ 3.14663483 \\ -5.10229407 \\ 5.24787354 \\ -4.29185461 \\ 2.32362116 \end{Bmatrix}$	$\boldsymbol{V}_{\tau\nu} = \begin{Bmatrix} -0.25429070 \\ 1.50539731 \\ -3.32745999 \\ 3.28199994 \\ -1.23274655 \\ 0.41773556 \\ -0.81923393 \end{Bmatrix}$
Rotation	$\boldsymbol{R}_\sigma = \begin{Bmatrix} 0.00789778 \\ -0.02324461 \\ 0.01957321 \\ -0.05687364 \\ -0.29653127 \\ 1.58546022 \\ -1.60460828 \end{Bmatrix}$	$\boldsymbol{R}_{\tau 0} = \begin{Bmatrix} 0.09467078 \\ -0.56967025 \\ 1.40705038 \\ -1.77499182 \\ 1.46712861 \\ -2.19739528 \\ 2.38392243 \end{Bmatrix}$	$\boldsymbol{R}_{\tau\nu} = \begin{Bmatrix} -0.15256642 \\ 0.90318091 \\ -2.01631572 \\ 1.95898230 \\ -0.53950050 \\ 0.21059622 \\ -0.81153594 \end{Bmatrix}$

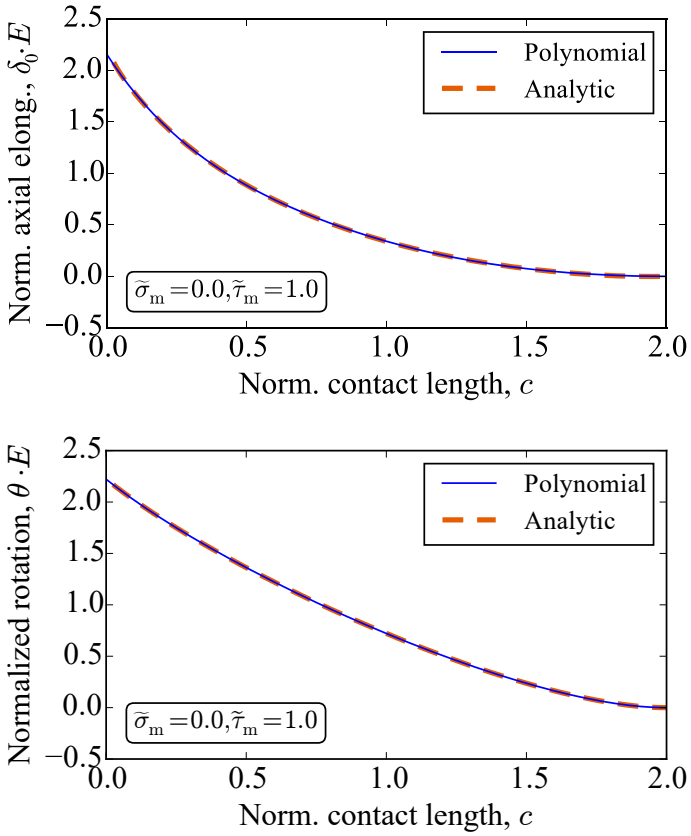

Figure 2.7: Comparison of the polynomial approximation of the displacements due to the self-equilibrating stresses with the analytical ones for $\tilde{\sigma}_m = 0$ and $\tilde{\tau}_m = 1$ (ν=0.2).

Generalized width and load direction problem Up to now, the normalized semi-infinite strip problem was examined considering a semi-infinite strip of semi-width $b = 1$ loaded in the region $[-1, -1 + c]$ at $x = 0$. In order to use the results for the general case, the relationship of the displacements between the normalized and the general problem has to be identified.

Since the stresses at point (X, Y) of the general problem equal those at point (x, y) of the normalized one (Gaydon, 1965), taking into account Eq. (2.37) and suitable variable substitutions, it can be concluded that the fiber elongation profile of the general problem, $U(Y)$, is given by: $U(Y) = b \cdot u(y)$. Likewise, by following a linearization procedure for the contact area fiber elongation profile of the general problem similar to the one presented above for the normalized case and by considering the symmetry between the opposite load direction cases, it can be proven that the following relationships hold:

$$\begin{aligned} \Delta_0 &= b \cdot \delta_0 \\ \Theta &= \rho \cdot \theta \end{aligned} \tag{2.53}$$

where Δ_0 and Θ are the axial elongation and the rocking end rotation of the general problem due to the self-equilibrating stresses, respectively, and $\rho = \text{sgn}\,(M_r)$.

Furthermore, since the effect of the self-equilibrating stresses is local and only the degrees of freedom of the axial elongation and the rotation of the rocking end are considered to be influenced, it is evident that there is a direct compatibility with the simply-supported beam natural coordinate system considered for the element. Thus, the contribution of the self-equilibrating stresses to the natural system displacements is given by:

$$\boldsymbol{u}_{\text{se}} = \boldsymbol{S}_3\, \boldsymbol{u}_{\text{sen}} \tag{2.54}$$

where

$$\boldsymbol{S}_3 = \begin{bmatrix} b & 0 \\ 0 & \rho \\ 0 & 0 \end{bmatrix} \tag{2.55}$$

Self-equilibrating stresses contribution flexibility matrix For the formulation of the rocking macro-element, the flexibility matrix of the self-equilibrating stresses contribution is necessary. This matrix is evaluated from the following expression:

$$\boldsymbol{f}_{\text{se}} = \frac{\partial \boldsymbol{u}_{\text{se}}}{\partial \boldsymbol{F}_{\text{n}}} = \frac{\partial \boldsymbol{u}_{\text{se}}}{\partial \boldsymbol{u}_{\text{sen}}} \frac{\partial \boldsymbol{u}_{\text{sen}}}{\partial \boldsymbol{r}} \frac{\partial \boldsymbol{r}}{\partial \boldsymbol{R}} \frac{\partial \boldsymbol{R}}{\partial \boldsymbol{F}_{\text{r}}} \frac{\partial \boldsymbol{F}_{\text{r}}}{\partial \boldsymbol{F}_{\text{n}}} = \boldsymbol{S}_3\, \boldsymbol{f}_{\text{sen}}\, \boldsymbol{S}_2\, \boldsymbol{S}_4\, \boldsymbol{S}_1 \tag{2.56}$$

where

$$\boldsymbol{S}_4 = \frac{\partial \boldsymbol{R}}{\partial \boldsymbol{F}_{\text{r}}} = \begin{bmatrix} -3\dfrac{|M_{\text{r}}|}{N_{\text{r}}^2} & 3\dfrac{\rho}{N_{\text{r}}} & 0 \\ \dfrac{4}{C} - \dfrac{6b}{C^2} & -6\dfrac{\rho}{C^2} & 0 \\ \dfrac{9}{2}\dfrac{|M_{\text{r}}|Q_{\text{r}}}{N_{\text{r}}^2 C^2} & -\dfrac{9}{2}\dfrac{\rho Q_r}{N_{\text{r}} C^2} & \dfrac{3}{2C} \end{bmatrix} \tag{2.57}$$

and $\boldsymbol{f}_{\text{sen}}$ is the flexibility matrix of the normalized problem, which is defined as:

$$\boldsymbol{f}_{\text{sen}} = \frac{\partial \boldsymbol{u}_{\text{sen}}}{\partial \boldsymbol{r}} = \begin{bmatrix} \dfrac{\partial \delta_0}{\partial c} & \dfrac{\partial \delta_0}{\partial \widetilde{\sigma}_{\text{m}}} & \dfrac{\partial \delta_0}{\partial \widetilde{\tau}_{\text{m}}} \\ \dfrac{\partial \theta}{\partial c} & \dfrac{\partial \theta}{\partial \widetilde{\sigma}_{\text{m}}} & \dfrac{\partial \theta}{\partial \widetilde{\tau}_{\text{m}}} \end{bmatrix} \tag{2.58}$$

Although the analytic evaluation of this matrix is possible (Avgenakis, 2015), it will not be presented here, since the polynomial approximation method is preferred. Then, defining the polynomial derivative term vector $\boldsymbol{P}_{\text{c}}'$:

$$\boldsymbol{P}_c' = \begin{bmatrix} 6c^5 & 5c^4 & 4c^3 & 3c^2 & 2c & 1 & 0 \end{bmatrix}^T \tag{2.59}$$

the normalized problem flexibility matrix is simply given by:

$$\boldsymbol{f}_{\text{sen}} = \frac{1}{E} \begin{bmatrix} \left(\widetilde{\sigma}_{\text{m}}\, \boldsymbol{V}_\sigma^{\text{T}} + \widetilde{\tau}_{\text{m}}\, \boldsymbol{V}_\tau^{\text{T}}\right) \boldsymbol{P}_c' & \boldsymbol{V}_\sigma^{\text{T}}\, \boldsymbol{P}_c & \boldsymbol{V}_\tau^{\text{T}}\, \boldsymbol{P}_c \\ \left(\widetilde{\sigma}_{\text{m}}\, \boldsymbol{R}_\sigma^{\text{T}} + \widetilde{\tau}_{\text{m}}\, \boldsymbol{R}_\tau^{\text{T}}\right) \boldsymbol{P}_c' & \boldsymbol{R}_\sigma^{\text{T}}\, \boldsymbol{P}_c & \boldsymbol{R}_\tau^{\text{T}}\, \boldsymbol{P}_c \end{bmatrix} \tag{2.60}$$

Summary of the self-equilibrating stresses contribution

Given a vector of forces in the simply-supported beam natural system, $\boldsymbol{F}_{\mathrm{n}}$, the following steps must be followed to calculate the contribution of the self-equilibrating stresses to the member response:

1. Calculate the rocking end forces $\boldsymbol{F}_{\mathrm{r}}$ using Eq. (2.10)
2. Calculate the stress distribution parameters $\boldsymbol{R}$ using Eq. (2.12)
3. Calculate the normalized stress distribution parameters $\boldsymbol{r}$ using Eq. (2.13)
4. Calculate the normalized problem displacements $\boldsymbol{u}_{\mathrm{sen}}$ using Eq. (2.51) (or Eq. (2.48))
5. Calculate the normalized problem flexibility matrix $\boldsymbol{f}_{\mathrm{sen}}$ using Eq. (2.60)
6. Calculate the natural system displacements $\mathbf{u}_{\mathrm{se}}$ using Eq. (2.54)
7. Calculate the natural system flexibility matrix $\boldsymbol{f}_{\mathrm{se}}$ using Eq. (2.56)

2.4 Combined response of the rocking member

In order to obtain the total response of the rocking member, the contribution of the stresses according to the technical theory of bending and that of the self-equilibrating stresses have to be combined. The input required to predict the member response according to each contribution is the same vector of natural system nodal forces, $\boldsymbol{F}_{\mathrm{n}}$, meaning that the formulation of the macro-element is force-based, while each contribution produces a different natural system displacement vector, $\boldsymbol{u}_{\mathrm{n}}$, and flexibility matrix, $\boldsymbol{f}_{\mathrm{n}}$. Due to the principle of superposition, the total natural system displacement vector is the sum of the displacement vectors produced by the two contributions and consequently the total natural system flexibility matrix is also the sum of the flexibility matrices of the two contributions.

The general algorithm for the combined element is presented in Table 2.3, referring to an iteration step i of a Newton-Raphson solution strategy. Subscript *ttb* refers to the contribution of the stresses according to the technical theory of bending and *se* refers to that of the self-equilibrating stresses. As a force-based formulation is used, part of this algorithm follows the algorithm used for the geometrically nonlinear force-based beam-column element proposed by Neuenhofer and Filippou (1998).

2.5 Examples

In this section, the proposed macro-element is applied to three characteristic examples and the results are validated by comparison with the ones obtained using the commercial finite element program Abaqus.

Table 2.3: Rocking macro-element algorithm

Step description	Related equations	Eq. number in text
1. Displacements and displacement increments with respect to the last iteration	$\boldsymbol{u}_{\mathrm{n},i} = \boldsymbol{T}_i \boldsymbol{u}_{\mathrm{e},i}$ $\Delta\boldsymbol{u}_{\mathrm{n},i} = \boldsymbol{u}_{\mathrm{n},i} - \boldsymbol{u}_{\mathrm{n},i-1}$	(2.1)
2. Nodal force increments	$\Delta\boldsymbol{F}_{\mathrm{n},i} = \boldsymbol{f}_{\mathrm{n},i-1}^{-1} \Delta\boldsymbol{u}_{\mathrm{n}i}$	
3. Nodal forces estimation	$\boldsymbol{F}_{\mathrm{n},i} = \boldsymbol{F}_{\mathrm{n},i-1} + \Delta\boldsymbol{F}_{\mathrm{n},i}$	
4. Flexibility matrix and displacements according to the technical theory of bending	$\boldsymbol{u}^{*}_{\mathrm{ttb},i} = \boldsymbol{f}_{\mathrm{ttb}}\, \boldsymbol{F}_{\mathrm{n},i}$	(2.7)
5. Check whether there is rocking or not. If not, ignore steps (6)-(9) and set $\boldsymbol{u}^{*}_{\mathrm{se},i} = \boldsymbol{0}$ and $\boldsymbol{F}_{\mathrm{se},i} = \boldsymbol{0}$.	$\left\lvert \dfrac{M_{1,i}}{N_i} \right\rvert > \dfrac{b}{3} \Rightarrow$ rocking	
6. Self-equilibrating stresses contribution parameters	$\boldsymbol{F}_{\mathrm{r},i} = \boldsymbol{S}_1\, \boldsymbol{F}_{\mathrm{n},i}$ $\boldsymbol{R}_i = \boldsymbol{R}(\boldsymbol{F}_{\mathrm{r},i})$ $\boldsymbol{r}_i = \boldsymbol{S}_{2,i}\, \boldsymbol{R}_i$	(2.10) (2.12) (2.13)
7. Displacements and flexibility matrix of the semi-infinite strip problem	$\boldsymbol{u}_{\mathrm{sen},i} = \boldsymbol{u}_{\mathrm{sen}}(\boldsymbol{r}_i)$ $\boldsymbol{f}_{\mathrm{sen},i} = \boldsymbol{f}_{\mathrm{sen}}(\boldsymbol{r}_i)$	(2.51) (2.60)
8. Displacements due to the self-equilibrating stresses contribution	$\boldsymbol{u}^{*}_{\mathrm{se},i} = \boldsymbol{S}_{3,i}\, \boldsymbol{u}_{\mathrm{sen},i}$	(2.54)
9. Flexibility matrix due to the self-equilibrating stresses contribution	$\boldsymbol{f}_{\mathrm{se},i} = \boldsymbol{S}_{3,i}\, \boldsymbol{f}_{\mathrm{sen},i}\, \boldsymbol{S}_{2,i}\, \boldsymbol{S}_{4,i}\, \boldsymbol{S}_1$	(2.56)
10. Total predicted displacements	$\boldsymbol{u}^{*}_{\mathrm{n},i} = \boldsymbol{u}^{*}_{\mathrm{ttb},i} + \boldsymbol{u}^{*}_{\mathrm{se},i}$	
11. Displacement residuals	$\boldsymbol{u}^{\mathrm{r}}_{\mathrm{n},i} = \boldsymbol{u}_{\mathrm{n},i} - \boldsymbol{u}^{*}_{\mathrm{n},i}$	
12. Total flexibility matrix	$\boldsymbol{f}_{\mathrm{n},i} = \boldsymbol{f}_{\mathrm{ttb},i} + \boldsymbol{f}_{\mathrm{se},i}$	
13. Additional nodal forces	$\boldsymbol{F}^{*}_{\mathrm{n},i} = \boldsymbol{f}^{-1}_{\mathrm{n},i}\, \boldsymbol{u}^{\mathrm{r}}_{\mathrm{n},i}$	
14. Updated nodal forces	$\boldsymbol{F}^{\mathrm{old}}_{\mathrm{n},i} = \boldsymbol{F}_{\mathrm{n},i}$ $\boldsymbol{F}_{\mathrm{n},i} = \boldsymbol{F}^{\mathrm{old}}_{\mathrm{n},i} + \boldsymbol{F}^{*}_{\mathrm{n},i}$	
15. Check convergence	$\dfrac{\lvert\boldsymbol{F}^{*}_{\mathrm{n},i}\rvert}{\lvert\boldsymbol{F}^{\mathrm{old}}_{\mathrm{n},i}\rvert} >$ error $\Rightarrow$ return to step (4)	
16. Local coordinate system nodal forces and stiffness matrix	$\boldsymbol{F}_{\mathrm{e},i} = \boldsymbol{T}^{*}_i\, \boldsymbol{F}_{\mathrm{n},i}$ $\boldsymbol{K}_{\mathrm{e},i} = \boldsymbol{T}_{\mathrm{g},i} + \boldsymbol{T}^{*}_i\, \boldsymbol{f}^{-1}_{\mathrm{n},i}\, \boldsymbol{T}^{*\mathrm{T}}_i$	(2.3) (2.5)

Rocking body with constant vertical force

In this example, the response of a simple rocking body with a constant vertical force on its top side (Fig. 2.8a) is examined. The rocking body has height $H = 4$ m, width $B = 1$ m and thickness d_{w}=1 m and is loaded on its top with a vertical force $N = -2,500$ kN.

The proposed macro-element is used to model the whole rocking body, with its rocking end at the bottom. The polynomial approximation method is used for the self-equilibrating

stresses contribution, which leads to a faster and more robust analysis. Although not important for slender bodies, shear deformation effects are also taken into account. Regarding the Abaqus model, 2D plane stress elements are used with a dense mesh near the contact region (Fig. 2.8b). The contact interface is modelled with contact interactions in order to allow only compressive stresses to develop, assuming though that a horizontal slip is prevented.

In Fig. 2.8c, the pushover capacity curves (applied horizontal force, P_x, versus horizontal displacement, δ_x) produced by the proposed macro-element model are shown for various E values and $\nu = 0.2$. The theoretical rigid block case is also shown for comparison (dashed line). It can be seen that, due to the nonlinearity of the response, the maximum strength achieved and the ultimate displacement at overturning decrease with decreasing E values.

In Fig. 2.9 the $E = 30$ GPa case is examined more analytically and the results are compared to Abaqus, as well as other simplified models. More specifically, apart from the pushover capacity curve (Fig. 2.9a), the curves presenting the vertical displacement (Fig. 2.9b) and the rotation (Fig. 2.9c) at node A are shown. It can be seen that, generally, there is very good agreement between the macro-element and the Abaqus results. The only notable difference between the two models can be seen in the vertical displacement response for large displacements. This is because the geometric nonlinearity formulation used is not exact for large displacements, as explained in the relevant section.

Additional comparisons are also conducted with simplified beam-column element models. One such model consists of a beamWithHinges element, which is included in the element library of OpenSees, with a compression-only fiber section at its rocking end, assuming a plastic hinge length equal to the section width (fine dashed line in Fig. 2.9). An additional comparison is shown with a simplified model consisting of a layer of compression-only springs with stiffness $k_s = E/H$ at the base of a rigid element, modelled as a zero-length fiber section element (fine dashed-dotted line in Fig. 2.9), an idea that has been used by several researchers (e.g. Penna et al., 2014). These comparisons show that the results of the proposed macro-element are superior to those of the simplified approaches, which cannot capture the response accurately (Figs. 2.9). It is noted that the discrepancy of the results of the simplified models from the theoretically correct solution (Abaqus results) increases with the value of the axial force N, while the accuracy of the proposed model is very good independently of the applied axial force.

Tendon-restrained rocking body

In the second example, an elastic tendon with axial stiffness $E_t A_t$=1,200 MN is installed at the center of the body of the previous example (Fig. 2.10a), which imposes an initial prestressing force $N = -2500$ kN. It is noted that, in this case, the axial force of the

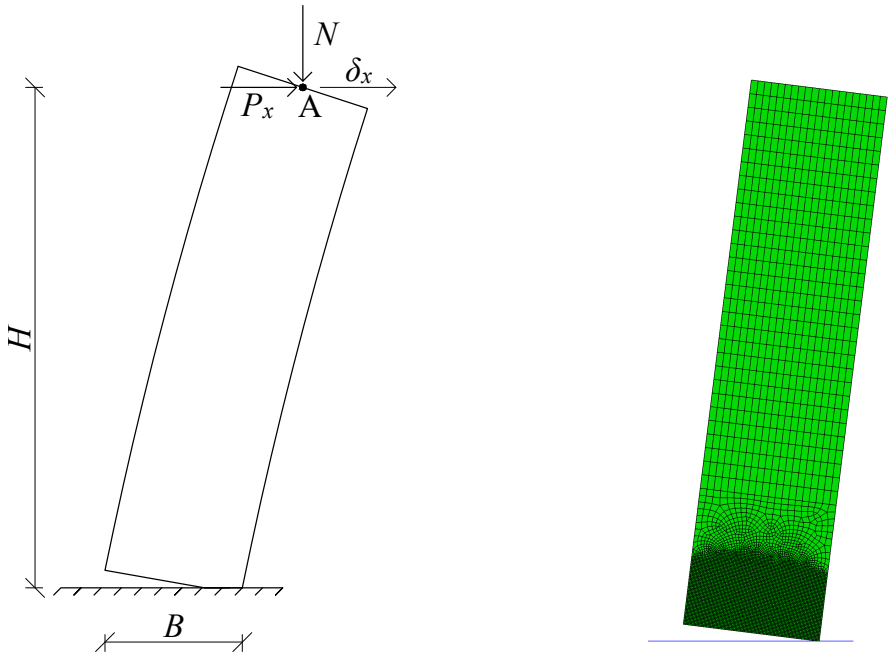

(a)

(b)

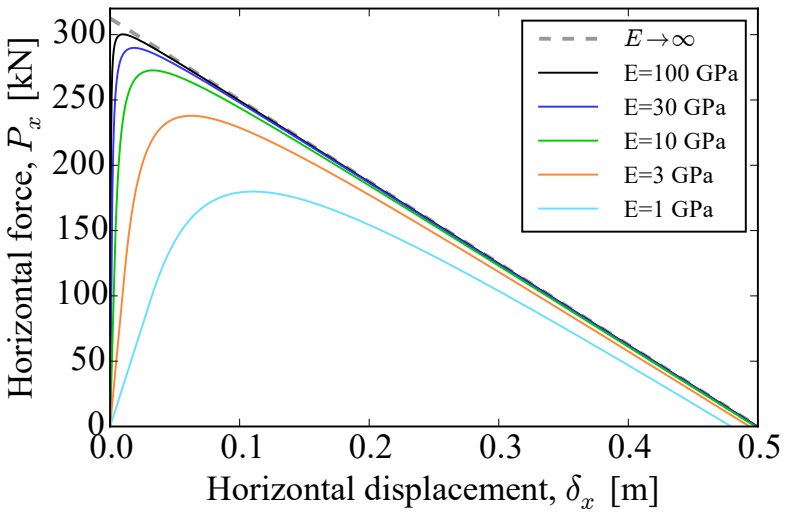

(c)

Figure 2.8: Rocking body under a vertical and a horizontal top force: (a) Model description and body deformation; (b) Corresponding Abaqus model; (c) Pushover capacity curves for different E values.

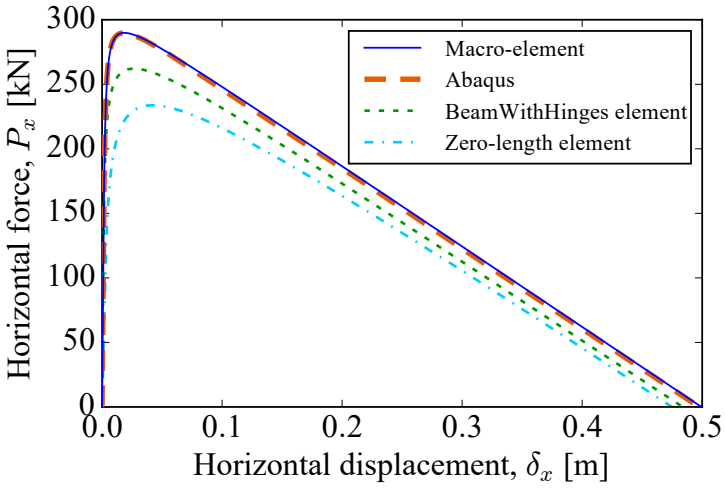

(a)

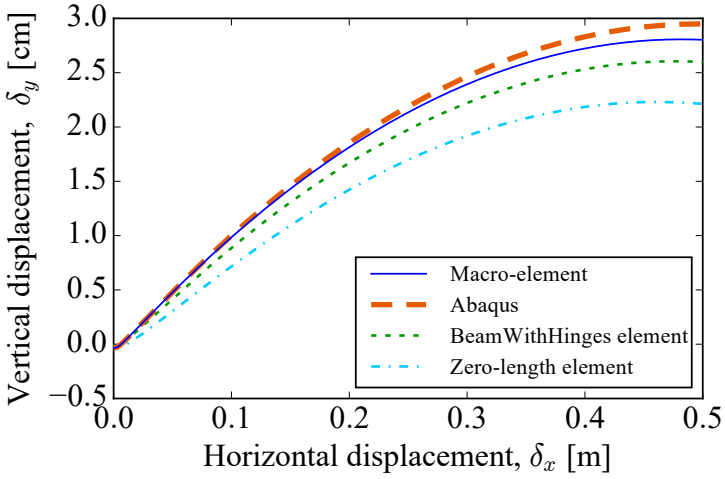

(b)

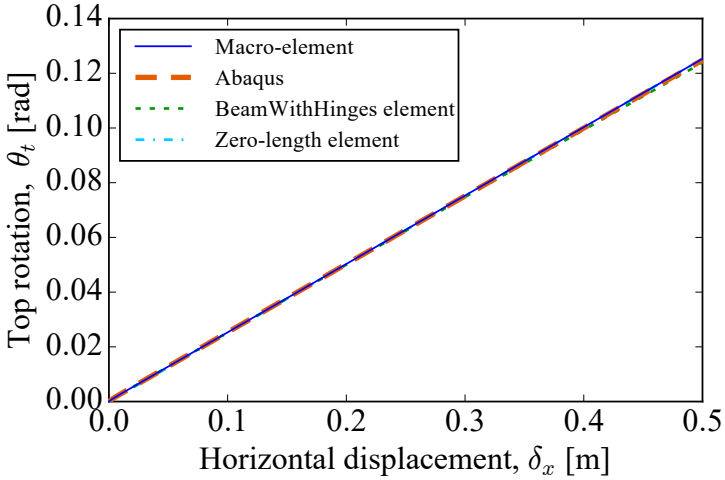

(c)

Figure 2.9: Rocking body under a vertical and a horizontal top force: (a) Pushover capacity curve; (b) Vertical displacement; (c) Top rotation for E=30 GPa. The macro-element results are compared with the corresponding Abaqus, beamWithHinges and zero-length element model results.

tendon does not remain constant, as the length of the tendon increases with the body rotation.

Regarding the modelling of the tendon, a tendon element is used for the macro-element model, which is essentially a geometrically nonlinear truss element with a pre-stressing force. In Abaqus, a truss element is used, together with a suitable predefined stress field in order to model the prestressing force (Fig. 2.10b). In both cases, the tendon element simply connects the base with the top node of the rocking body, modelling thus an unbonded tendon, which does not interact internally with the body.

The response of this system is shown in Figs. 2.10c,d. Fig. 2.10c shows the pushover capacity curve (applied horizontal force, P_x, versus the horizontal drift, d_x) and it can be seen that the post-rocking branch is ascending, as expected, since the tendon offers stability to the system. This happens, since, as the body rotates, the tendon elongates and the stabilizing force applied to the rocking body increases. The increase in the axial force of the tendon with the body drift is shown in Fig. 2.10d.

The comparison of the macro-element results with the ones obtained using Abaqus shows that the proposed macro-element is capable of modelling restrained rocking systems, in which the axial force changes during the rocking motion, as the axial degree of freedom is taken explicitly into account.

Single-bay frame containing a rocking wall

In this example, a single-bay frame containing a rocking wall, able to rock at both its ends (Fig. 2.11a), is examined. The frame dimensions are $L_{\mathrm{f}} = 6.5$ m and $H_{\mathrm{f}} = 4.5$ m, the columns have cross section 0.60 m $\times$ 0.60 m, the beam has cross section of height 0.50 m and thickness 0.25 m, while the rocking wall has width B_{w}=1.50 m and thickness d_{w}=0.20 m. The material of all elements has properties E=30 GPa and ν=0.2. A uniformly distributed vertical load $q_{\mathrm{l}} = 60.0$ kN/m is applied along the beam and a self-weight load is assumed for the rocking wall corresponding to density ρ_{w}=25.0 kN/m^3.

For the macro-element model, conventional linear elements along the centerline of the columns and the beam are used, while practically rigid elements are used to model the beam-column joints (Fig. 2.11b). Since the rocking wall is able to rock at both its ends, a rocking macro-element is considered at each end. In order to capture the deformation of the beam, the top rocking element is connected to the beam through rigid elements and hinges able to transmit the axial force of the rocking wall to an approximately correct location along the beam. The self-weight of the rocking wall is applied on its central node, so that the axial forces of both rocking ends approximately correspond to the real ones.

Regarding the modelling of the frame with Abaqus, 3D brick elements are used for the whole model (Fig. 2.11c) with practically rigid elements for the frame joints, while contact interactions are used between the bottom surface of the rocking wall and the base,

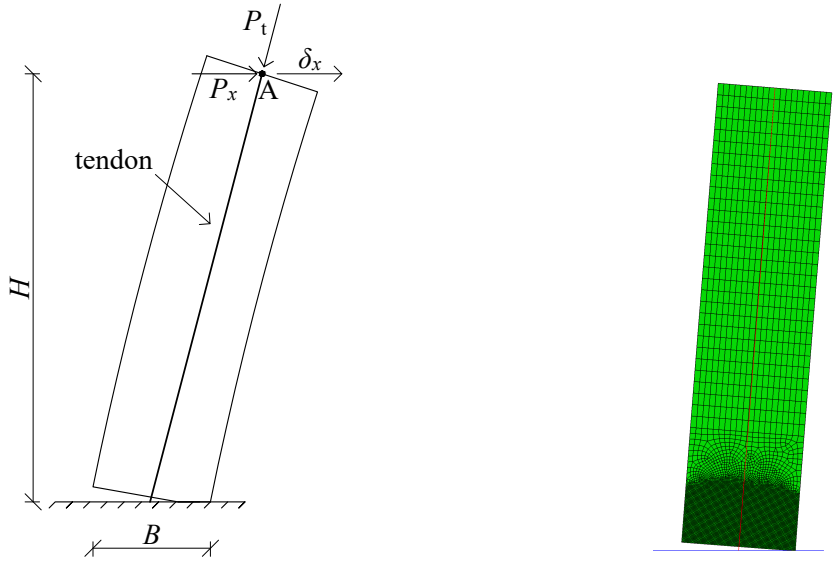

(a) (b)

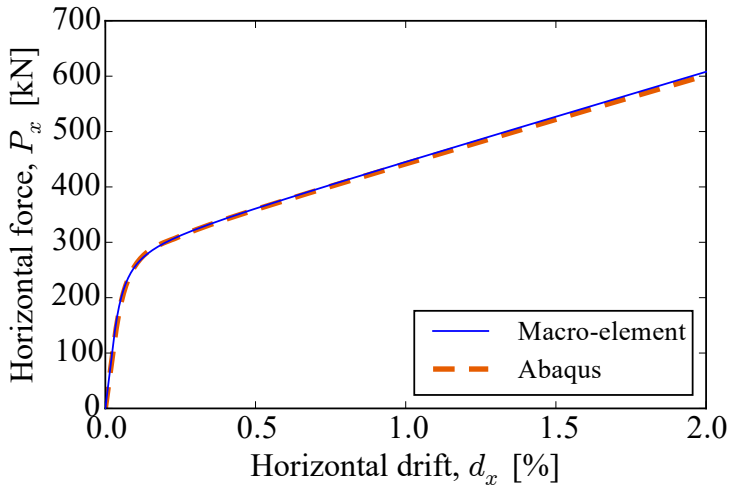

(c)

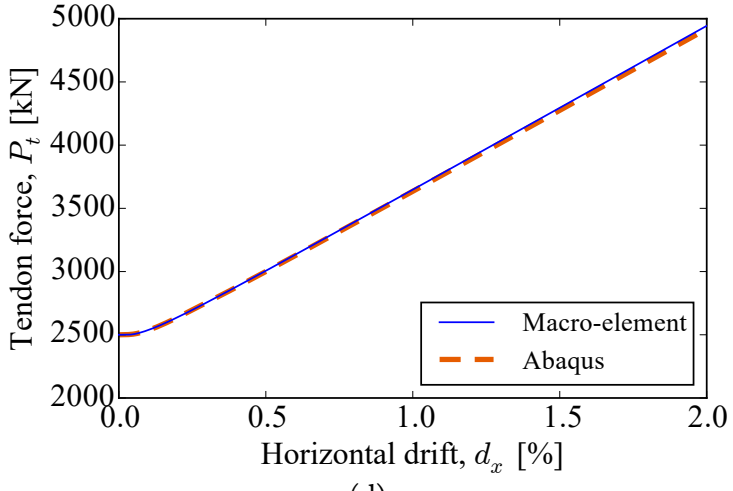

(d)

Figure 2.10: Tendon-restrained rocking body: (a) Model description and body deformation; (b) Corresponding Abaqus model; (c) Pushover capacity curve; (d) Tendon force. In plots (c), (d), the macro-element results are compared with the corresponding Abaqus results.

as well as the top surface of the rocking wall and the bottom surface of the beam, which however do not allow a relative slip between the surfaces.

The results are depicted in Fig. 2.12, where the horizontal force, P_x, and the rocking wall axial force, N_{w}, are plotted versus the horizontal drift, d_x. For comparison, the pushover capacity curve of the bare frame is also presented.

The results show that the stiffness and the lateral resistance of the frame increase with the inclusion of the rocking wall (Fig. 2.12a). As depicted in Fig. 2.12b, in which a zoom of the pushover capacity curve is shown for small drifts, the nonlinearity of the rocking response is mainly located at the beginning of the response. The increase of the stiffness and the lateral capacity of the frame is associated with the increasing axial force of the rocking wall, shown in Fig. 2.12c, which is attributed to the beam restraining of the rocking motion.

Is can be seen that the results obtained with the macro-element almost coincide with the ones produced by Abaqus. Small discrepancy is observed only in the axial force of the wall: for a horizontal drift of 2%, the error is about 6%. It should be noted though that a precise match of the results between the two models could not be achieved, even for the bare frame.

The previous examples generally show that the proposed macro-element can produce very accurate results compared with those of equivalent Abaqus models, while requiring extremely lower runtimes and showing a much more robust behavior.

2.6 Examples: Parametric investigation

In this section, the effect of various parameters on the lateral load bearing capacity of the rocking configurations presented in the examples of the previous section is examined for monotonic loading, so that the influence of member deformability on the response is investigated.

Rocking body with constant vertical force

First, a single rocking body, on which a constant vertical force is acting (Fig. 2.8a) is examined. The body has height H, base width B and thickness d_{w}, while a vertical force N is applied on its top central node, A. The body is considered to be deformable with modulus of elasticity E. The effect of the Poisson ratio ν is not taken into account, as it is not considered important. The base mat is considered rigid, thus, any deformation takes place only in the body.

The response of the body is governed by two normalized quantities:

- $\tan\alpha = \dfrac{B}{H}$, which expresses the influence of the slenderness of the body

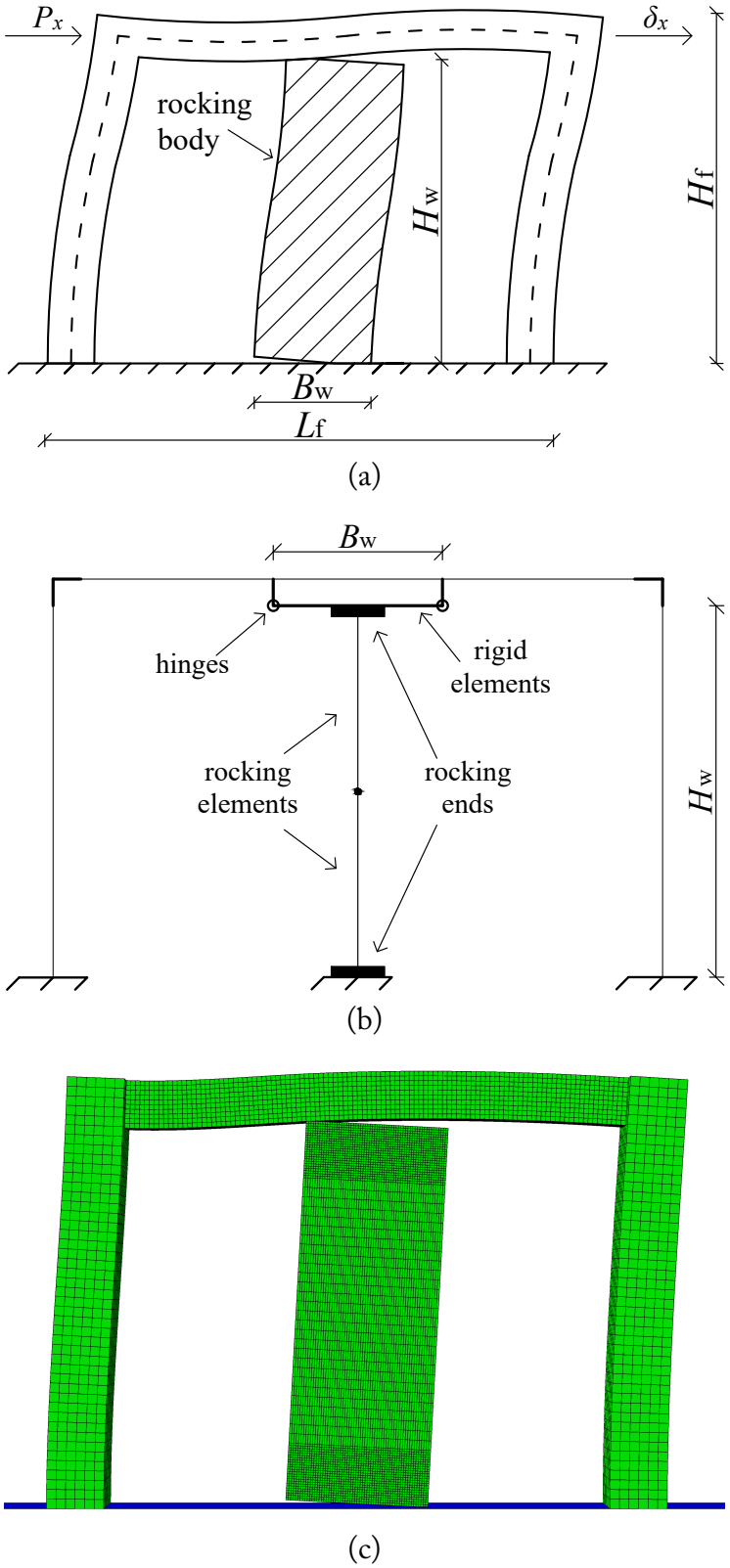

Figure 2.11: Single-bay frame containing a rocking wall: (a) Model description and deformation; (b) Numerical model with the proposed macro-elements considered at the top and bottom sides of the rocking wall; (c) Corresponding Abaqus model.

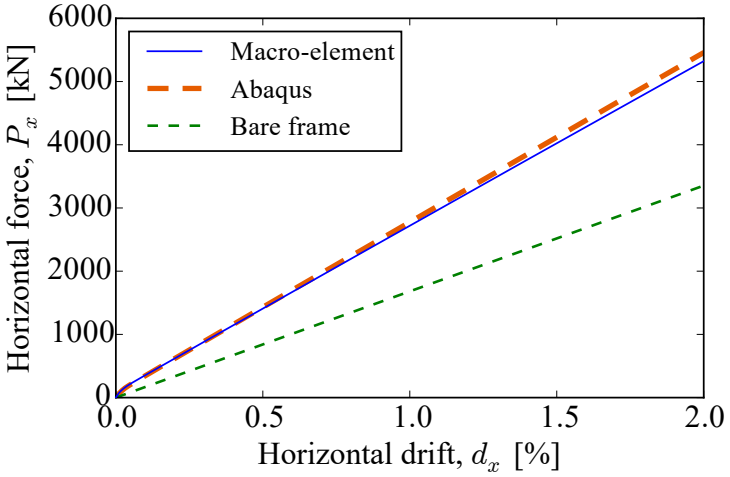

(a)

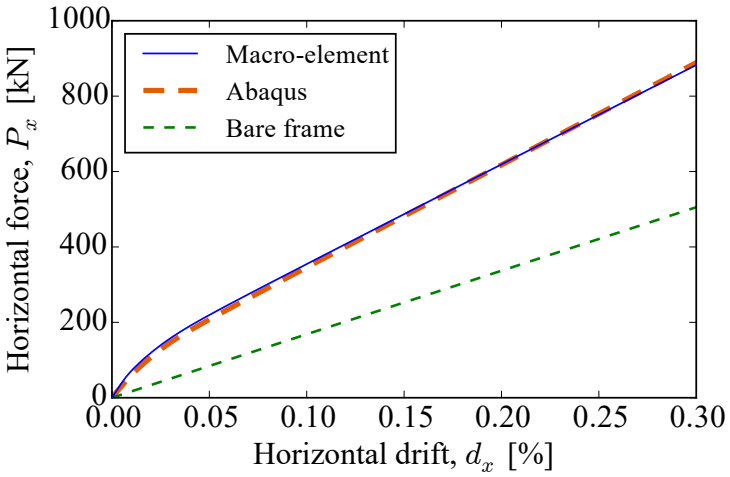

(b)

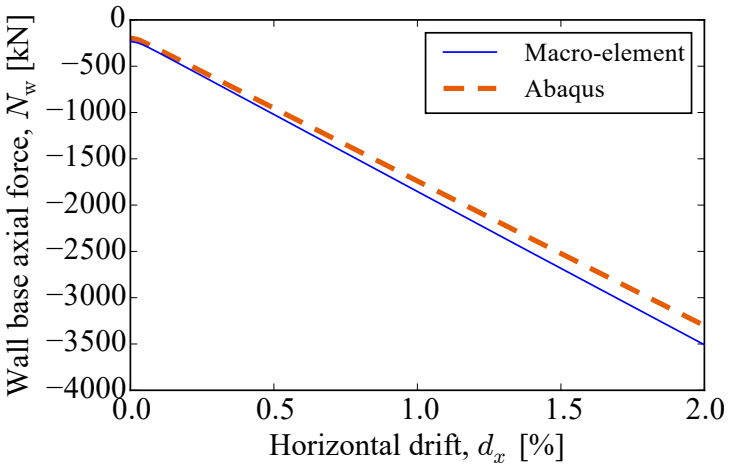

(c)

Figure 2.12: Single-bay frame containing a rocking wall: (a) Pushover capacity curve; (b) Zoom of plot (a) for small drifts; (c) Rocking wall axial force. The results of the numerical model using the proposed macro-element are compared with the corresponding Abaqus results.

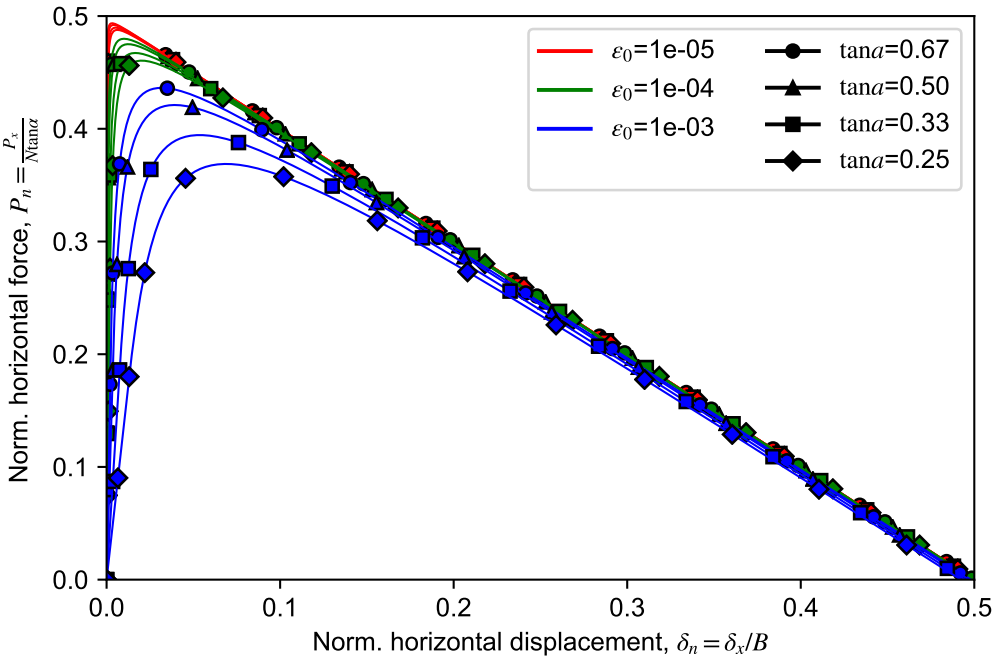

Figure 2.13: Rocking body horizontal force - horizontal displacement response curves.

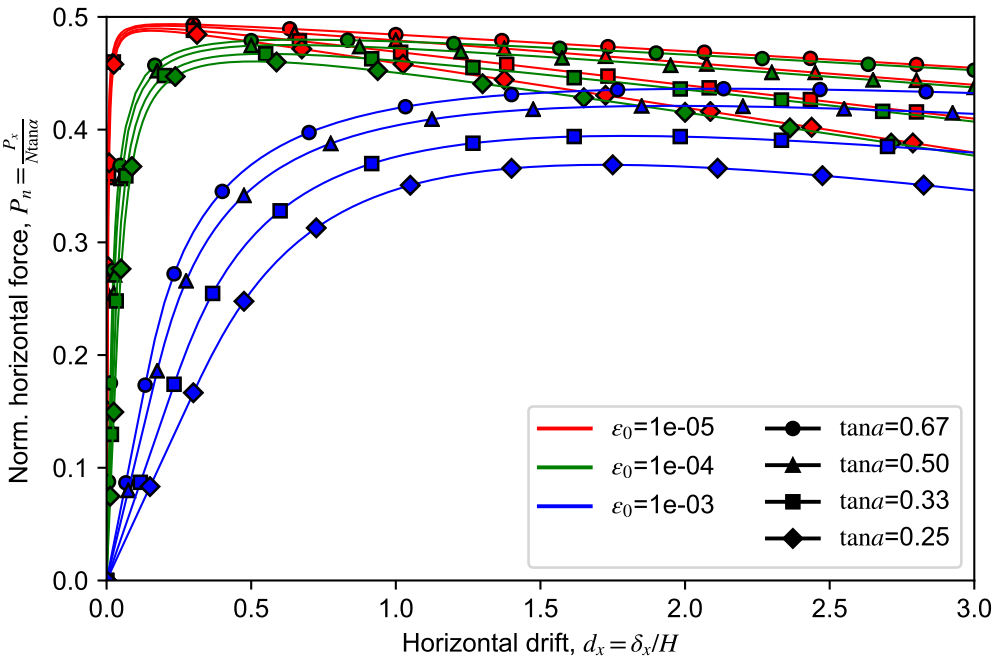

Figure 2.14: Rocking body horizontal force - horizontal drift response curves.

- $\epsilon_0 = \dfrac{N}{EBd_w}$, which corresponds to the initial axial deformation of the body due to the vertical force and measures the flexibility of the body and the magnitude of the vertical force.

Also, in the following, the results are shown normalized, specifically:

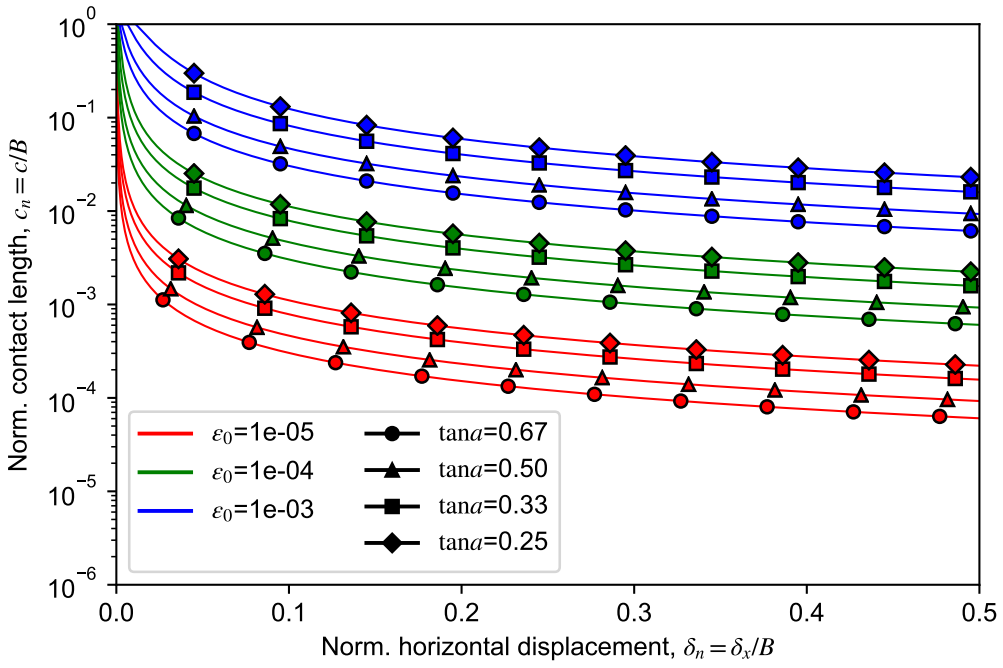

Figure 2.15: Rocking body contact length - horizontal displacement response curves.

- The horizontal force is normalized with respect to the quantity $N \tan\alpha$: $P_n = \dfrac{P_x}{N \tan\alpha}$. Thus, for the rigid block, rocking starts for $P_n = 0.5$.
- The horizontal top displacement is normalized with respect to the base width B: $\delta_n = \dfrac{\delta_x}{B}$. It is noted that, for typical cases of slender bodies in which $\tan\alpha \approx \alpha$ and $\theta \approx \dfrac{\delta_x}{H}$, $\delta_n \approx \dfrac{\theta}{\alpha}$.
- The amount of rocking is measured with the horizontal drift: $d_x = \dfrac{\delta_x}{H}$.
- The contact length is normalized with respect to the base width B: $c_n = \dfrac{c}{B}$

In Fig. 2.13, the normalized horizontal force versus the normalized horizontal top displacement is shown. Response curves are given for various values of the body slenderness α and the initial deformations ϵ_0. For comparison reasons with the models of the next sections, in Fig. 2.14 the initial region of the response is shown in terms of horizontal drift. As can be seen from these curves, the response converges to the rigid body solution (a straight descending line starting at $P_n = 0.5$) for $\epsilon_0 \to 0$, as expected.

Figures 2.13 and 2.14 show that the effect of the deformation on the response of the rocking body is noticeable. More specifically, as the body becomes more flexible or the axial force becomes larger (larger ϵ_0), the maximum normalized force that can be attained, $P_{n,max}$, reduces. Note that, for given ϵ_0, $P_{n,max}$ also reduces for smaller $\tan\alpha$, i.e. for slenderer bodies. It is reminded that $P_n = P_x/(N \tan\alpha)$, thus, for any value of P_n, the

actual horizontal resistance P_x is proportional to the vertical force N and the slenderness $\tan\alpha$.

The effect of the deformability of the base of the body on the normalized contact length c_n is shown in Fig. 2.15, in which c_n is plotted versus the normalized top horizontal displacement, δ_n. It can be observed that for slender or flexible bodies, as well as for large vertical forces, the contact region during rocking is not detrimental, so the base deformability cannot be neglected. It is interesting to note that the contact length attains a practically constant value for large displacements.

Tendon-restrained rocking body

In this case, the configuration where a prestressed unbonded elastic tendon is installed at the center of the body (Fig. 2.10b), which produces a stabilizing force, is examined. This system simulates real configurations encountered in practice, such as rocking columns and shear walls in which insertion of tendons is common. In contrast to the previous case, where the stabilizing force was constant for the whole response, the force applied to the body by the tendon constantly increases as the body rotates, due to the tendon elongation. Also, the direction of its application follows the tendon rotation.

The response is now governed by three normalized parameters which, apart from $\tan\alpha$ and ϵ_0 mentioned above, include the parameter μ, defined as:

- $\mu = \dfrac{E_t A_t}{EBd_{\mathrm{w}}}$, in which E_t and A_t are the Young's modulus and the cross section area of the tendon, respectively,

which measures the ratio of tendon to body axial stiffness. It should be noted that ϵ_0 in this case refers to the initial value of the prestressing force, N_0.

Concerning the response, the following normalized quantity is additionally used:

- $N_n = \dfrac{N - N_0}{E_t A_t \tan\alpha} = \dfrac{\epsilon_t - \epsilon_{t0}}{\tan\alpha}$

which represents the additional deformation of the tendon due to its elongation.

The response of this system, for several typical values of the nomalized parameters, is presented in Figs. 2.16 to 2.21.

In Figs. 2.16 and 2.17, the normalized horizontal force is plotted versus the drift $d_x = \delta_x/H$ for $\epsilon_0 = 5 \cdot 10^{-5}$ and $5 \cdot 10^{-4}$, respectively, and for several values of μ and $\tan\alpha$. It is seen that the prestressing tendon influences the response significantly, resulting in a positive post-rocking stiffness. It is noted that $\mu = 0$ (blue curves) corresponds to the case where no tendon exists and the vertical force maintains a constant value equal to N_0. The curves in this case correspond to the response of the constant vertical force rocking body shown in Fig. 2.14.

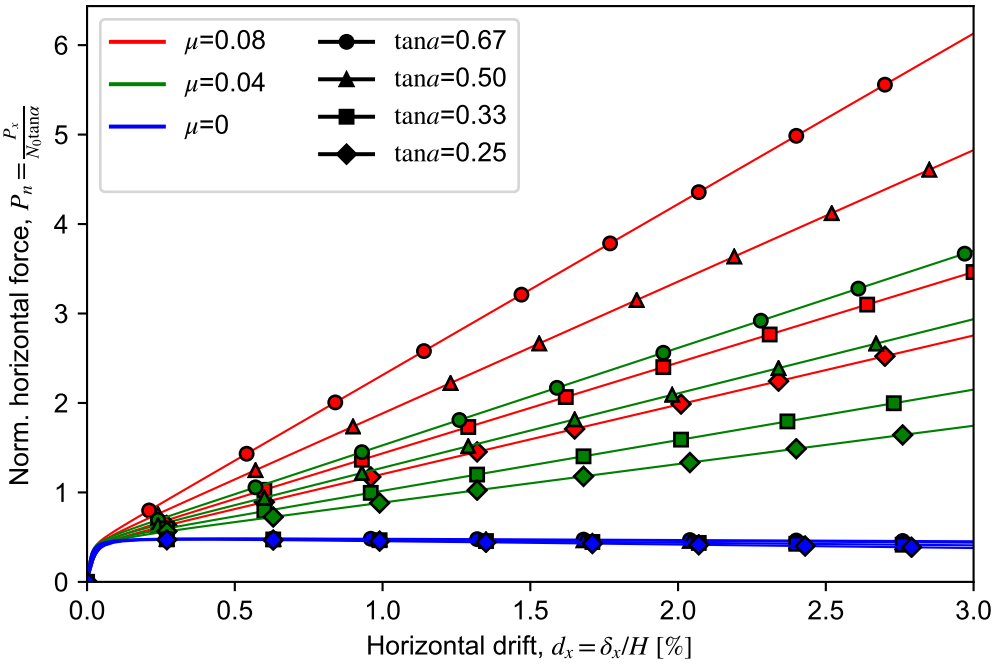

Figure 2.16: Tendon constrained body force - displacement response curves for $\epsilon_0 = 5 \cdot 10^{-5}$. The case $\mu = 0$ corresponds to a rocking body with a constant vertical force N_0 without tendon.

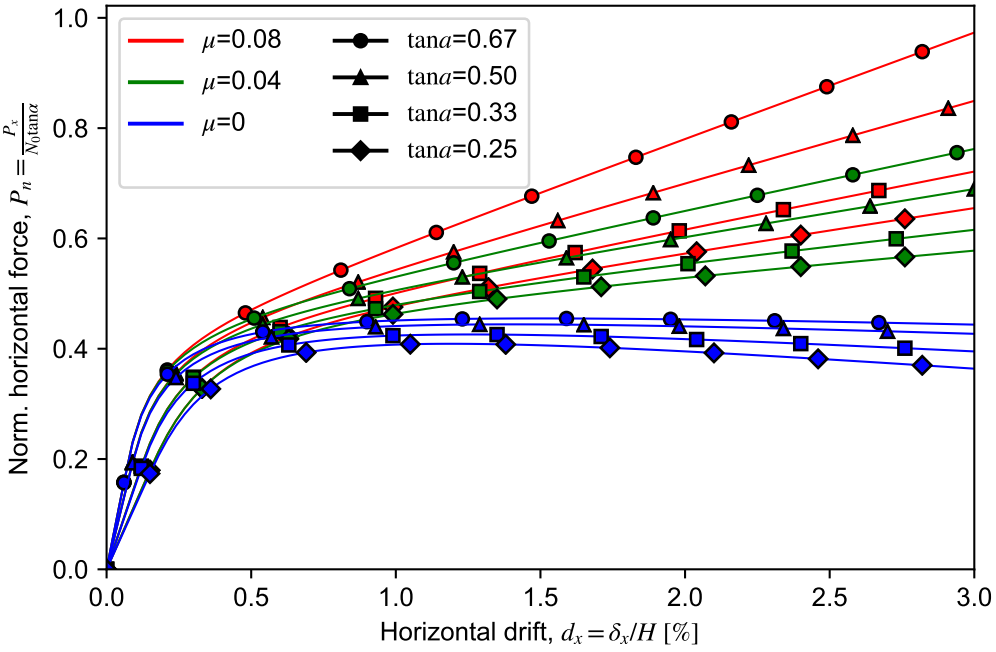

Figure 2.17: Tendon constrained body force - displacement response curves for $\epsilon_0 = 5 \cdot 10^{-4}$. The case $\mu = 0$ corresponds to a rocking body with a constant vertical force N_0 without tendon.

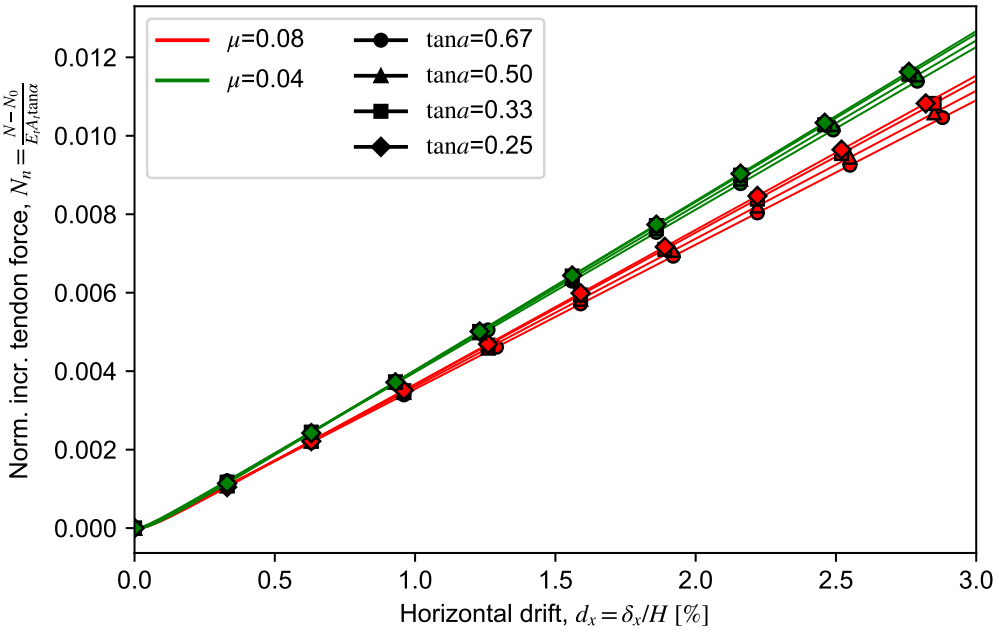

Figure 2.18: Tendon constrained body tendon force - displacement response curves for $\epsilon_0 = 5 \cdot 10^{-5}$.

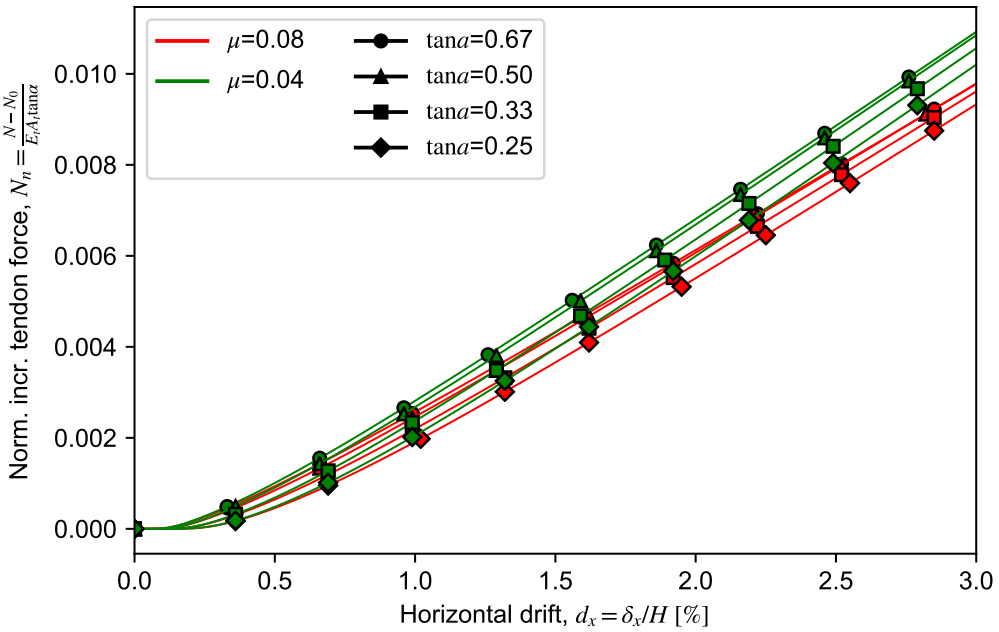

Figure 2.19: Tendon constrained body tendon force - displacement response curves for $\epsilon_0 = 5 \cdot 10^{-4}$.

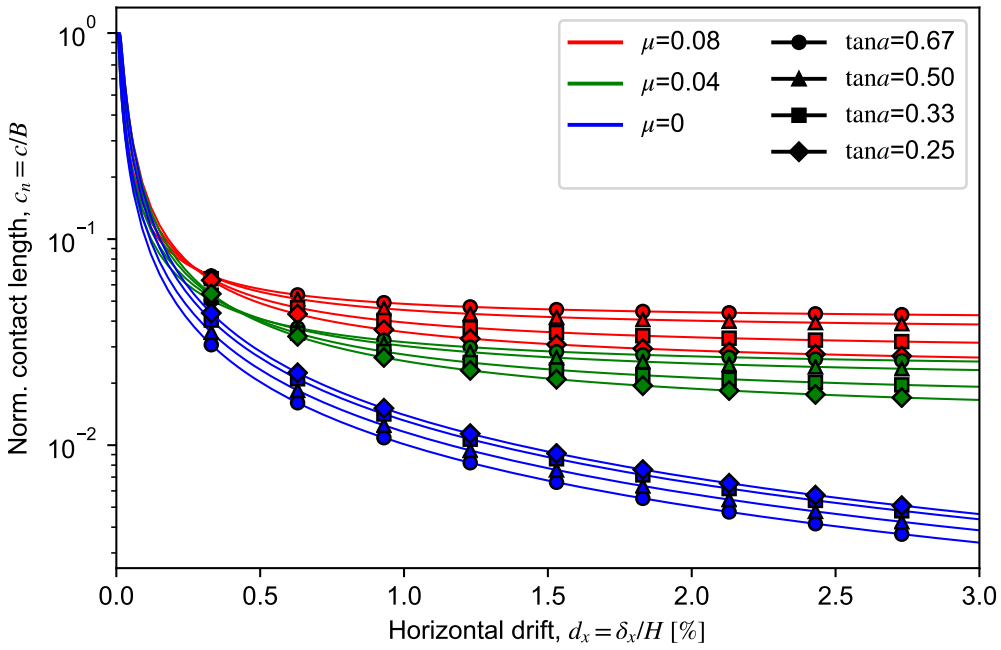

Figure 2.20: Tendon constrained body contact length - displacement response curves for $\epsilon_0 = 5 \cdot 10^{-5}$. The case $\mu = 0$ corresponds to a rocking body with a constant vertical force N_0 without tendon.

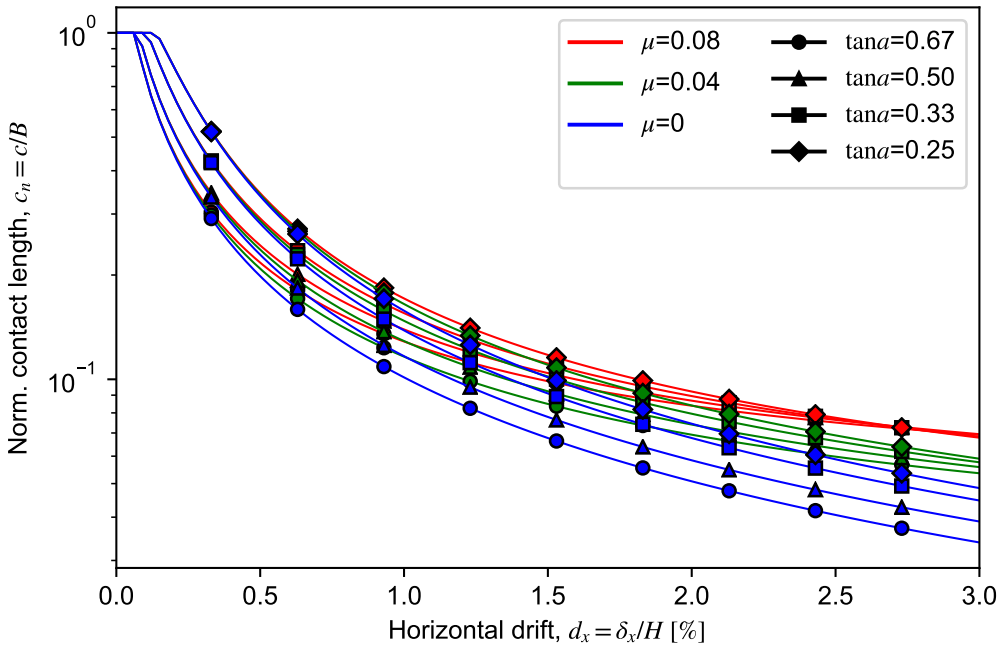

Figure 2.21: Tendon constrained body contact length - displacement response curves for $\epsilon_0 = 5 \cdot 10^{-4}$. The case $\mu = 0$ corresponds to a rocking body with a constant vertical force N_0 without tendon.

It can be seen that the normalized resistance P_n increases significantly with the drift of the body, especially for smaller values of ϵ_0. Note that ϵ_0 decreases for smaller values of the prestress force N_0 or more rigid bodies (larger E). This increase in the horizontal resistance should be attributed to the additional axial force developed in the tendon due to its elongation (Figs. 2.18, 2.19). Interestingly, the normalized additional tendon's force is almost independent of ϵ_0, μ and $\tan\alpha$, in contrast to the P_n which is significantly affected by these parameters.

Finally, Figs. 2.20 and 2.21 show the progressive reduction in the normalized contact length, c_n, during the response. Similarly to rocking bodies with constant vertical force, the contact area rapidly decreases with the drift and attains a practically constant value for large displacements, especially for relatively small ϵ_0 values, that is, for stiffer bodies. It is noticed that almost constant values of c_n are associated with constant stiffness of the system (Figs. 2.16, 2.17).

Single-bay frame containing a rocking wall

The effect of the rocking of a shear wall placed at the middle of the span of a single-story, single-bay frame (Fig. 2.11a) is examined next. The wall is rocking on both the bottom and the top sides.

Results are presented for a RC frame with columns of cross section 0.50 m x 0.60 m and beam of cross section 0.25 m x 0.50 m, while the thickness of the rocking wall perpendicular to the frame is assumed 0.25 m. The Young's modulus of the main frame is E_f=30 GPa, while the Young's modulus of the wall, E_w, is considered a varying parameter. For the structural members of the frame (columns and beam), the cracked stiffness was considered, and, according to the usually made assumption (e.g. Eurocode 8 - European Committee for Standardization (CEN), 2004) the effective stiffness was taken equal to one half of the geometric one: $EI_{\text{eff}} = 0.5EI_g$. The vertical loads acting on the system are a distributed load $q = 60$ kN/m along the beam and the self-weight of the rocking wall.

In Figs. 2.22-2.24 the response of the frame under monotonically increasing horizontal load, P, is presented for various frame height to span length, H_f/L_f, and panel width to span length, B/L_f, ratios, assuming $E_w = E_f$. Note that the case $B/L_f = 0$ corresponds to the bare frame without the wall.

In Fig. 2.22, the classical capacity curve is shown and it is evident that both the capacity and the stiffness increase with the ratio B/L_f, i.e. as the width B of the wall increases in comparison to the span length L_f. This behavior was expected, since rocking of the wall is more constrained by the beam for larger B's due the larger required vertical displacements of the beam, which also occur closer to its ends. Similarly, the capacity and the stiffness of the system increase as the ratio H_f/L_f decreases, i.e. as the frame becomes stiffer. Note that smaller ratios H_f/L_f also correspond to less slender walls for constant B

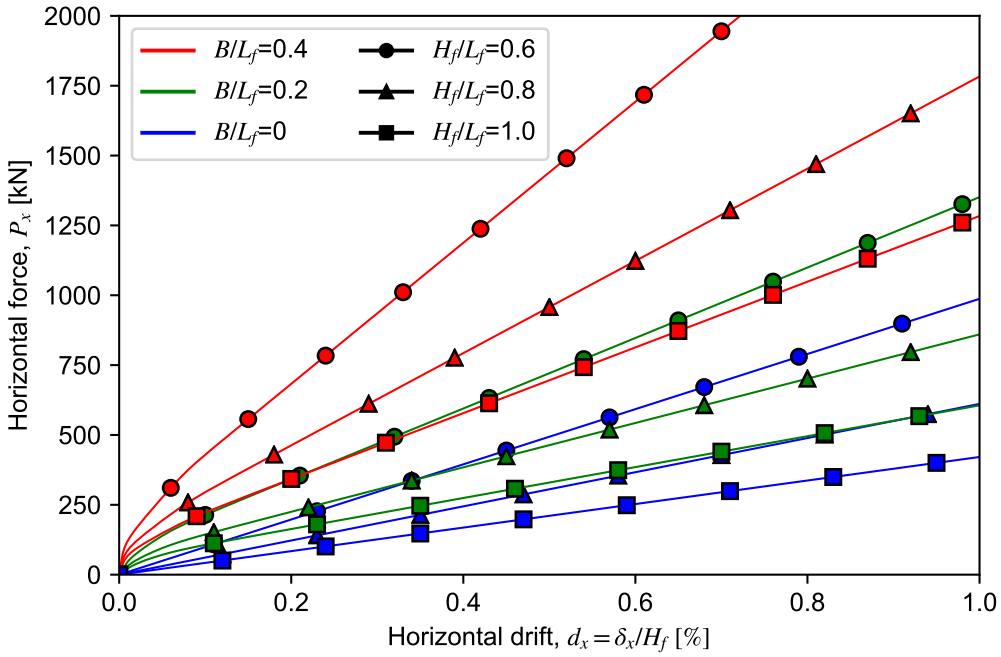

Figure 2.22: Horizontal force versus drift (capacity curves) for frames with varying B/L_f and H_f/L_f ratios ($E_w/E_f = 1$).

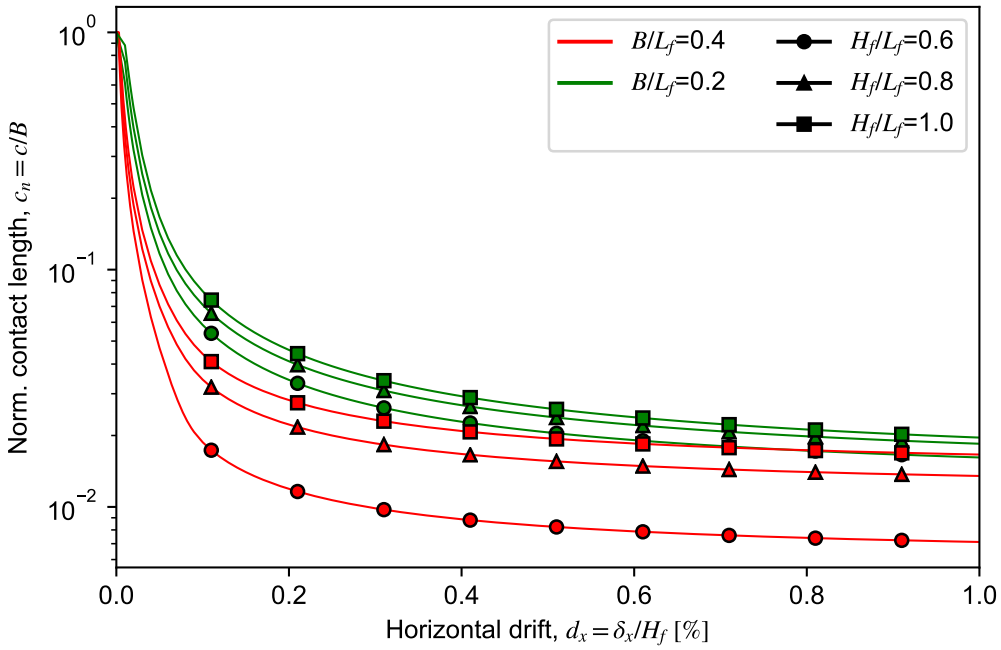

Figure 2.23: Normalized contact length at the bottom side of the rocking wall versus drift for the cases examined in Fig. 2.22. Similar are the contact lengths at the top side.

(larger $\tan\alpha$), since the height of the wall, H, is associated with the height of the frame, H_f.

It is interesting to note that the non-linearity of the response is mostly limited at the

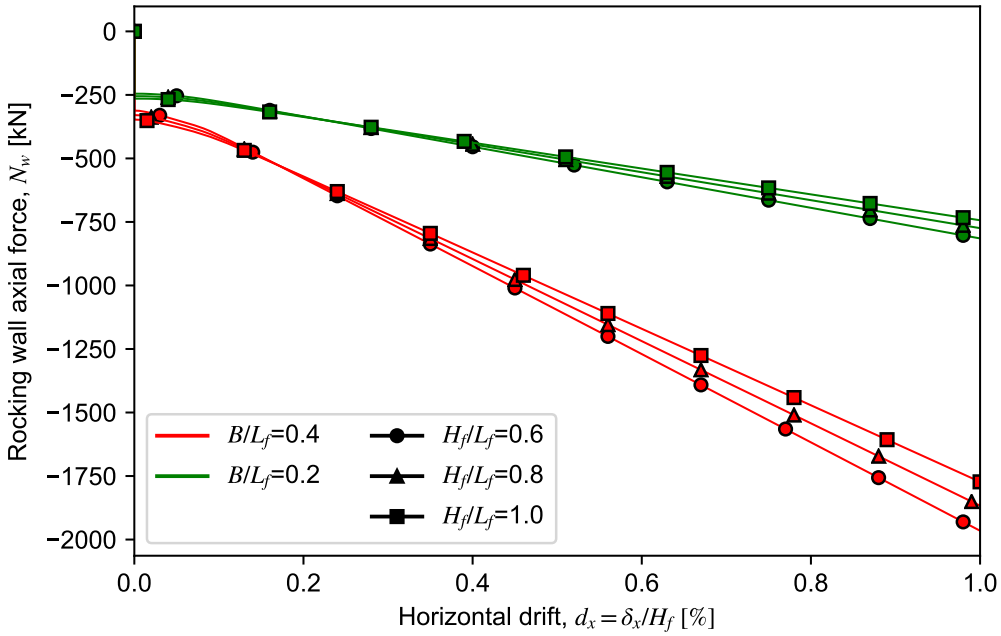

Figure 2.24: Compressive axial force of the rocking wall versus drift for the cases examined in Fig. 2.22.

beginning of the response (at small drift ratios), while the post-rocking response shows a practically constant stiffness. Thus, the overall response could, in most cases, be approximated by the response of a linear system with the post rocking stiffness. This behavior is associated with the stabilization of the contact length, as shown in Fig. 2.23.

The beneficial effect of the rocking wall to the lateral resistance of the system shown in Fig. 2.22 is accompanied by the disadvantageous development of tensile axial forces in the columns to balance the compressive axial force induced to the wall due to the kinematic constraints imposed by the beam. The axial force N_w that develops in the wall during rocking is shown in Fig. 2.24 and, as expected, it increases with B/L_f. The ratio H_f/L_f affects N_w in a much smaller degree. It is expected that, in real structures, the tensile forces induced to the columns due to the rocking wall will not increase significantly the required reinforcement, because they will be over-balanced by the gravity loads, especially at the lower stories.

In order to examine the possible benefit of the inclusion of such a rocking wall in the original frame to its seismic behavior, a response spectrum analysis is conducted, using the EC8 design spectrum for $a_g = 3.6$ m/s^2 and ground type B. The mass of the structure is derived taking into account the distributed load and half of the rocking member self-weight. In each case, the secant stiffness at the maximum displacement was used, which was derived after iterations, similarly to the procedure suggested by FEMA 440 , with the difference that no additional hysteretic damping was considered, since rocking does not produce such damping as the unloading path practically follows the loading one.

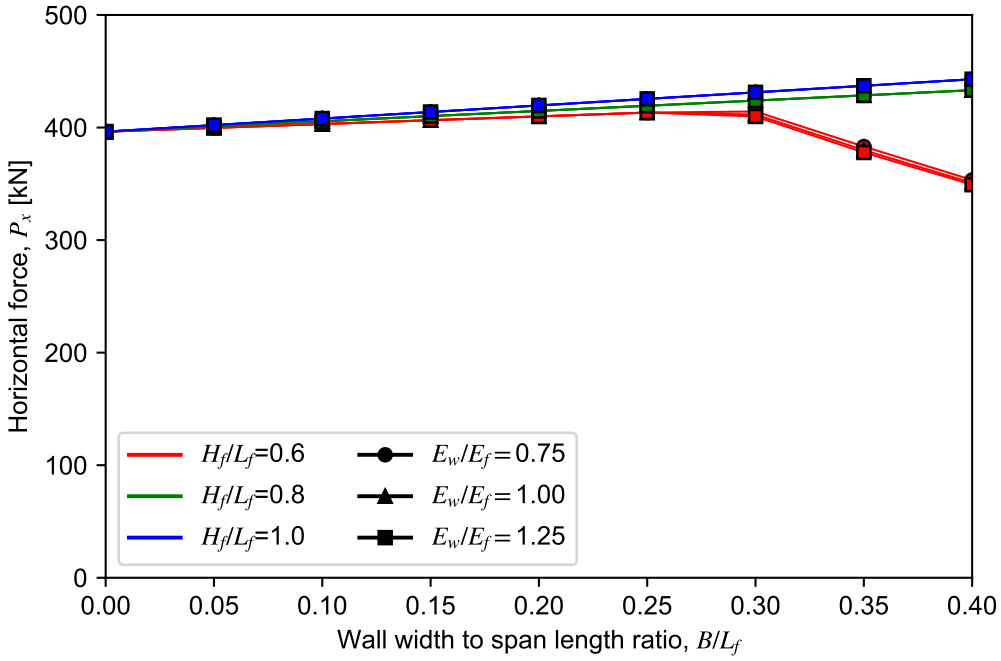

Figure 2.25: Earthquake scenario: Maximum horizontal force versus B/L_f ratios.

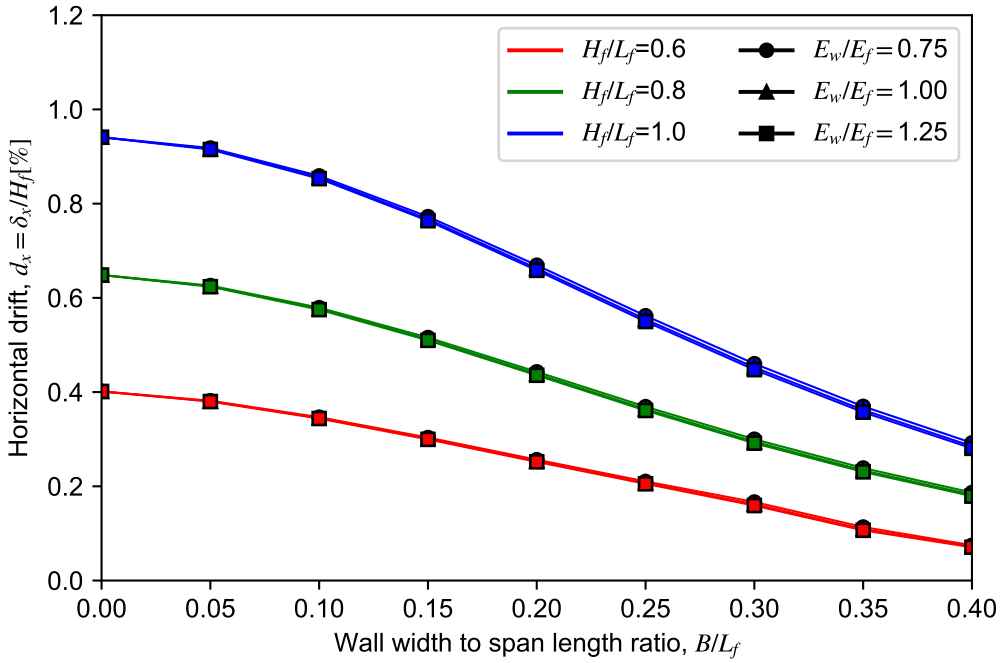

Figure 2.26: Earthquake scenario: Maximum horizontal drift versus B/L_f ratios.

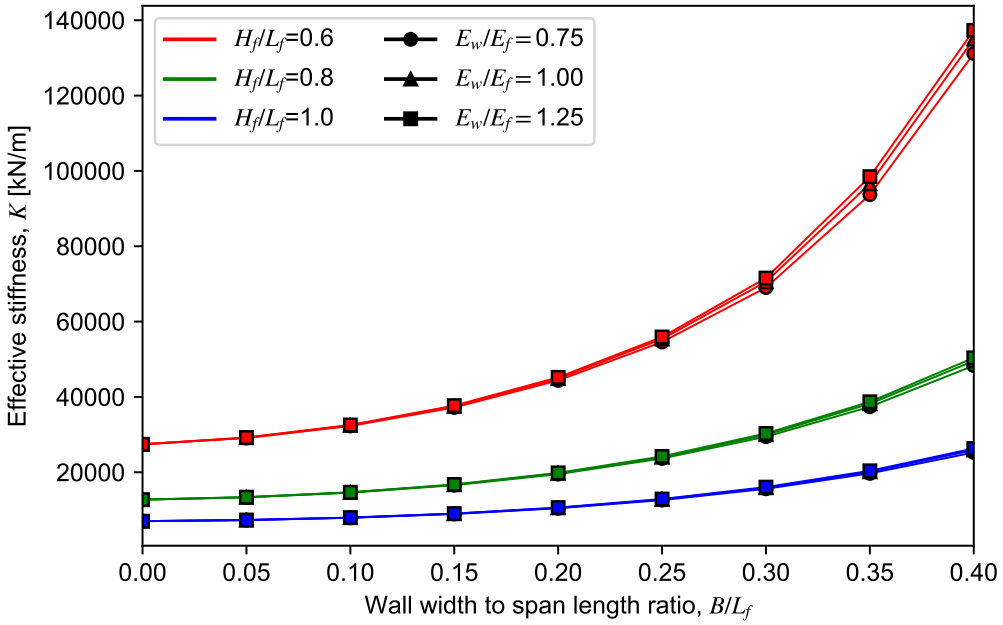

Figure 2.27: Effective system stiffness for different B/L_f ratios.

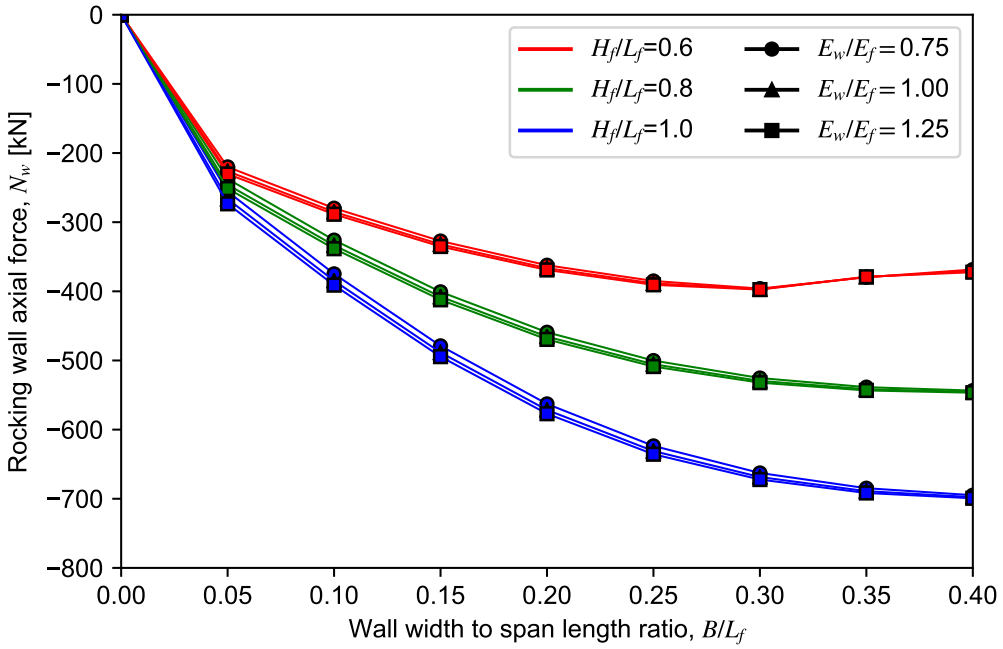

Figure 2.28: Earthquake scenario: Axial force induced to the wall versus B/L_f ratios.

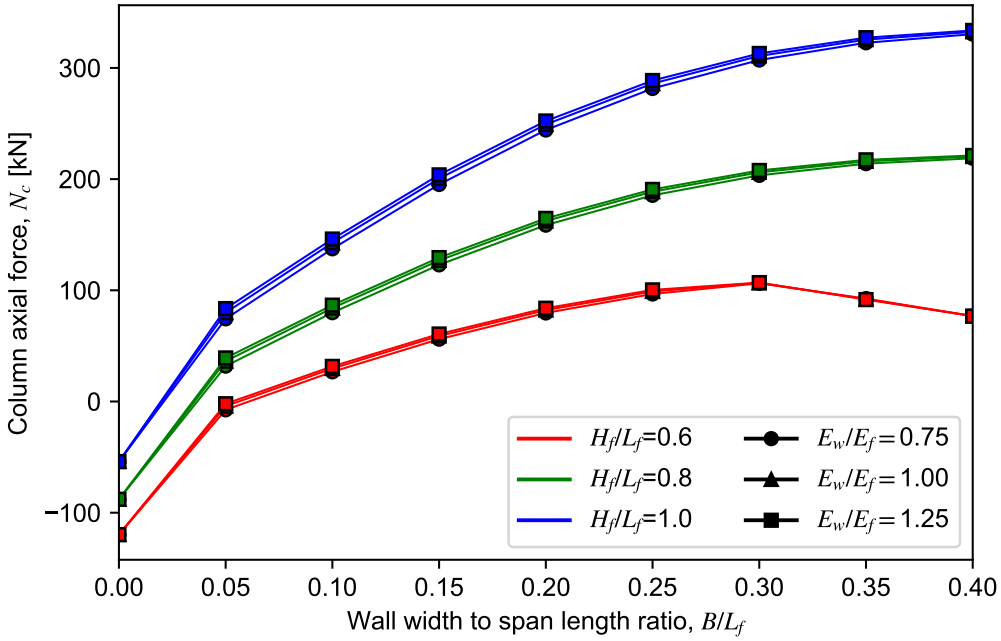

Figure 2.29: Earthquake scenario: Axial force induced to the columns versus B/L_f ratios.

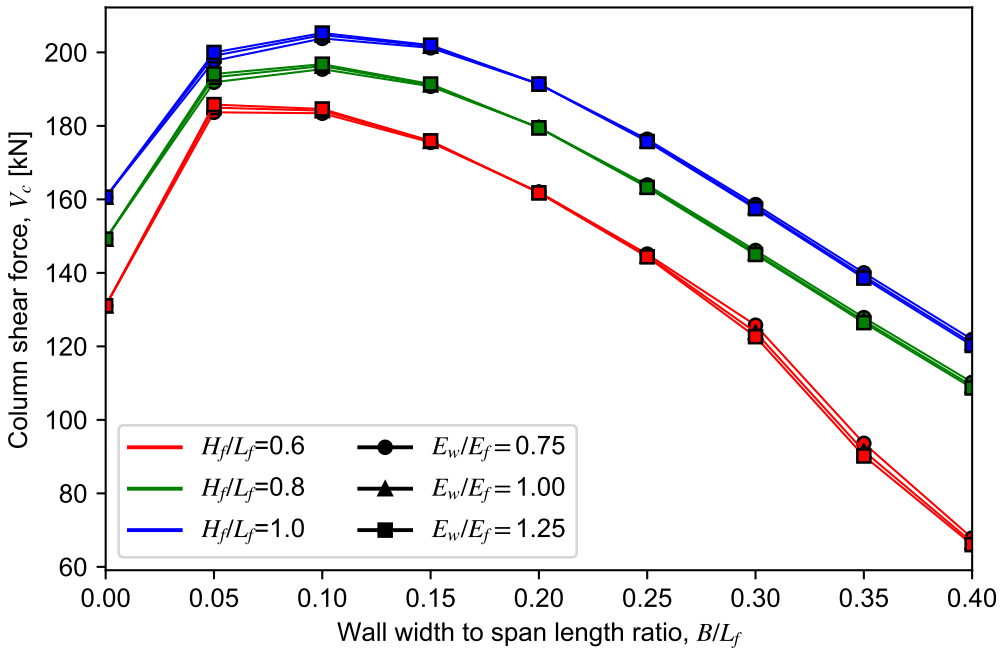

Figure 2.30: Earthquake scenario: Shear force induced to the columns versus B/L_f ratios.

In Figs. 2.25-2.30, maximum attainable values for various quantities for this earthquake scenario are presented with respect to the panel width to span length ratio, B/L_f. Various analyses have been performed for different frame height to span length ratios, H_f/L_f, and different panel to frame moduli of elasticity, E_w/E_f.

Concerning the base shear force (Fig. 2.25), it is seen that the insertion of the wall does not alter it significantly, which was expected, since the total mass is about the same in all cases examined and the periods of the structure generally fall in the constant acceleration region of the design spectrum ($T_B - T_C$). Only for very stiff configurations ($H_f/L_f = 0.6$ and $B/L_f > 0.30$), for which $T_{\text{eff}} < T_B$ a reduction is observed in the base shear (Fig. 2.25).

Concerning the horizontal displacements and the produced drifts, they significantly decrease as the width of the wall increases (larger B/L_f ratios) or the stiffness of the frame increases (smaller H_f/L_f ratios) (Fig. 2.26). This is associated with the corresponding increase in the overall effective stiffness of the system depicted in Fig. 2.27.

The axial forces induced to the wall, N_w (compressive) and the columns, N_c, (tensile) are shown in Figs. 2.28 and 2.29, respectively. Fig. 2.28 reveals that larger axial forces are imposed on wider rocking walls, due to the frame constraining their motion. Concerning the axial forces induced to the columns (Fig. 2.29), the ones of the column which is more influenced by the rocking motion are shown. It is seen that they become tensile even for relatively narrow rocking walls and increase as the width of the wall increases. They are also larger for larger H_f/L_f ratios (less stiff frames). Such tensile forces are not expected to be a problem in a real structure where the columns bear significantly large compressive loads from upper floors.

The main benefit of the inclusion of the rocking wall in the frame concerns the reduction in the shear forces induced to the columns, which is shown in Fig. 2.30. Although for a relatively narrow wall the columns' shear force is not affected significantly or can even increase, wide walls result in a significant decrease in the shear forces of the columns, which is more pronounced as the ratio B/L_f increases.

Concerning the effect of the modulus of elasticity of the wall, the results show that, in general, differences between E_w and E_f in the order of $\pm 25\%$, as the ones expected in realistic situations, do not influence the response significantly. On the contrary, H_f/L_f and especially B/L_f ratios are considered very important.

3

Modeling of inelastic rocking bodies under monotonic loading

Rocking members in structural systems are expected to behave inelastically for large seismic excitations. In this chapter, the macroelement presented in the previous chapter, which considered the element material to be elastic, is extended to also take material nonlinearity into account. It is noted, though, that only the monotonic case loading can be considered in a similar manner as the elastic case, since cyclic loading is more complex and needs a different treatment, which will be presented in Chapter 5.

3.1 Stress distributions for monotonic loading of the inelastic rocking body

For the solution of the inelastic material case, new stress distributions acting on the rocking interface have to be assumed. As a simplification, the area inside the element is considered to behave elastically, so that the existing solution of the semi-infinite strip stress problem, based on the theory of elasticity, as well as the principle of superposition hold. However, as discussed in the ensuing, this assumption does not lead to results far from the reality, since only the elongations of the elastic portion of the section are taken into account.

For the normal stresses, a trapezoidal stress distribution is assumed to act on the rocking interface, after yielding occurs (Fig. 3.1). In order to examine the response of the member under the trapezoidal loading, a new parameter μ is defined:

$$\mu = \frac{c_y}{c} \tag{3.1}$$

where c_y is the length of the contact area which has yielded.

The resultant axial force and moment can be expressed as:

$$N_{\mathrm{r}} = \frac{1}{2}(1+\mu)bc\sigma_y \tag{3.2}$$

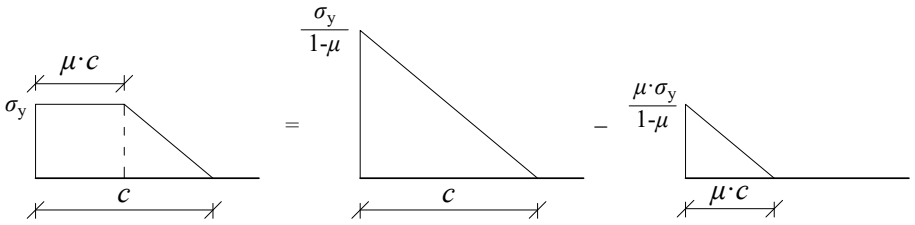

Figure 3.1: Normal stress distribution acting on the rocking interface after yielding and decomposition into triangular distributions.

$$M_{\mathrm{r}} = \rho \left[\frac{1}{2}(1+\mu)b^2 c \left(\frac{c}{3} - 1 \right) \sigma_y + \frac{1}{6}\mu^2 b^2 c^2 \sigma_y \right] \tag{3.3}$$

where ρ is the signum function of M_{r}.

The trapezoidal distribution can be expressed as the difference of the two triangular distributions with parameters $(\sigma_y/(1-\mu), c)$ and $(\mu\sigma_y/(1-\mu), \mu c)$ shown in Fig. 3.1. Assuming that the shear stress distribution results from the difference of two parabolic distributions corresponding to the aforementioned triangular normal stress distributions and that the ratio of the maximum shear stress values is the same as the maximum normal stresses ratio, the resultant shear force is

$$Q_{\mathrm{r}} = \rho \frac{2}{3}(1-\mu^2)bct \tag{3.4}$$

where t is the maximum shear stress corresponding to the distribution of contact length c.

Given a vector of resultant forces acting on the rocking interface, $\boldsymbol{F}_{\mathrm{r}}$, the load distribution parameter vector, $\boldsymbol{r}_{\mathrm{y}} = [c, \mu, t]^T$, is calculated from:

$$\boldsymbol{r}_{\mathrm{y}} = \begin{Bmatrix} c \\ \mu \\ t \end{Bmatrix} = \begin{Bmatrix} \dfrac{N_{\mathrm{r}}\omega}{\sigma_{\mathrm{y}} b} \\ \dfrac{2}{\omega} - 1 \\ \dfrac{3\rho\omega^2 Q_{\mathrm{r}}}{8(\omega-1)bc} \end{Bmatrix} \tag{3.5}$$

where

$$\omega = \sqrt{3\left(\frac{2b\sigma_{\mathrm{y}}}{N_{\mathrm{r}}} + \frac{2\rho M_{\mathrm{r}}\sigma_{\mathrm{y}}}{N_{\mathrm{r}}^2} - 1 \right)} + 1 \tag{3.6}$$

The corresponding derivative matrix of the load parameters to the rocking end forces

is

$$\boldsymbol{S}_{24\mathrm{y}} = \frac{\partial \boldsymbol{r}_{\mathrm{y}}}{\partial \boldsymbol{F}_{\mathrm{r}}} = \begin{bmatrix} \dfrac{2(c+2\mu c-3)}{(\mu-1)bc\sigma_{\mathrm{y}}} & -\dfrac{6\rho}{(\mu-1)b^2c\sigma_{\mathrm{y}}} & 0 \\ \dfrac{6(\mu+1)-4(1+\mu+\mu^2)c}{(\mu-1)bc^2\sigma_{\mathrm{y}}} & \dfrac{6\rho(\mu+1)}{(\mu-1)b^2c^2\sigma_{\mathrm{y}}} & 0 \\ \dfrac{2ct(2\mu^3+3\mu^2+6\mu+1)-6t(1+\mu)^2}{(\mu-1)^2(\mu+1)bc^2\sigma_{\mathrm{y}}} & -\dfrac{6\rho t(\mu+1)}{(\mu-1)^2b^2c^2\sigma_{\mathrm{y}}} & \dfrac{3\rho}{2bc(1-\mu^2)} \end{bmatrix} \tag{3.7}$$

It is noted that the material yields when

$$\sigma_{\mathrm{y}} > \frac{2N_{\mathrm{r}}}{3\left(b+\frac{\rho M_{\mathrm{r}}}{N_{\mathrm{r}}}\right)} \tag{3.8}$$

3.2 Additional displacements due to the self-equilibrating stresses

Similarly to the elastic material case, the self-equilibrating stress distributions originating from the previous interface stresses are examined using the semi-infinite strip problem solution. However, the additional displacements due to these self equilibrating stresses are not calculated by approximation of the whole contact area fiber elongation profile with a linear distribution, but only of the portion of the section that remains elastic, that is in the interval $[-1+\mu c, -1+c]$. This can be applied, since the fibers under this area are assumed to remain elastic, in contrast to the fibers under the yielded contact zone.

Using the aforementioned procedure, the self-equilibrating stresses normalized displacement approximation formula presented next is produced, giving very good results for $c \leq 2/(\mu+1)$, which includes most of the usual cases:

$$\boldsymbol{u}_{\text{sen,y}} = \frac{1}{E}\begin{Bmatrix} \sigma_{\mathrm{y}}\delta_{\sigma}(c,\mu) + t\delta_{\tau}(c,\mu) \\ \sigma_{\mathrm{y}}\theta_{\sigma}(c,\mu) + t\theta_{\tau}(c,\mu) \end{Bmatrix} \tag{3.9}$$

where the functions $\delta_{\sigma}(c,\mu), \theta_{\sigma}(c,\mu), \delta_{t}(c,\mu), \theta_{t}(c,\mu)$ are presented in the following.

Normal stresses Introducing a normalized contact length $c_{\mathrm{n}} = c(\mu+1)$, functions $\delta_{\sigma}(c,\mu)$ and $\theta_{\sigma}(c,\mu)$ are given by:

$$\delta_{\sigma} = \delta_A(c_{\mathrm{n}}) + \delta_B(\mu)(c_{\mathrm{n}}-2) \tag{3.10}$$

$$\theta_{\sigma} = \theta_A(c_{\mathrm{n}}) + \theta_B(\mu) + \theta_C(\mu)\theta_D(c_{\mathrm{n}}) \tag{3.11}$$

where the various functions appearing in these equations have the forms:

$$\delta_A(c_\mathrm{n}) = a_1\left[1-(c_\mathrm{n}/2)^{a_2}\right]^{a_3} \tag{3.12}$$

$$\delta_B(\mu) = a_1\tan(\frac{\pi}{2}\mu) + a_2\mu + a_3\mu^2 + a_4\mu^3 \tag{3.13}$$

$$\theta_A(c_\mathrm{n}) = a_1\left[1-(c_\mathrm{n}/2)^{a_2}\right]^{a_3}(1-c_\mathrm{n}/2)^2 \tag{3.14}$$

$$\theta_B(\mu) = a_1\tan(\frac{\pi}{2}\mu) + a_2\mu + a_3\mu^2 + a_4\mu^3 \tag{3.15}$$

$$\theta_C(\mu) = a_1\mu^4 + a_2\mu^3 + a_3\mu^2 + (-4a_1 - 3a_2 - 2a_3)\mu \tag{3.16}$$

$$\theta_D(c_\mathrm{n}) = a_1c_\mathrm{n}^6 + a_2c_\mathrm{n}^5 + a_3c_\mathrm{n}^4 + a_4c_\mathrm{n}^3 + (-16a_1 - 8a_2 - 4a_3 - 2a_4 + 0.25)c_\mathrm{n}^2 \tag{3.17}$$

The constant parameters appearing in these equations are given in Table 3.1.

Furthermore, the following derivatives are calculated, which are needed in the following:

$$\frac{\partial\delta_\sigma}{\partial c} = (\mu+1)(\frac{d\delta_A}{dc_\mathrm{n}} + \delta_B) \tag{3.18}$$

$$\frac{\partial\delta_\sigma}{\partial \mu} = c(\frac{d\delta_A}{dc_\mathrm{n}} + \delta_B) + \frac{d\delta_B}{d\mu}(c_\mathrm{n}-2) \tag{3.19}$$

$$\frac{\partial\theta_\sigma}{\partial c} = (\mu+1)(\frac{d\theta_A}{dc_\mathrm{n}} + \theta_C\frac{d\theta_D}{dc_\mathrm{n}}) \tag{3.20}$$

$$\frac{\partial\theta_\sigma}{\partial \mu} = c(\frac{d\theta_A}{dc_\mathrm{n}} + \theta_C\frac{d\theta_D}{dc_\mathrm{n}}) + \frac{d\theta_B}{d\mu} + \theta_D\frac{d\theta_C}{d\mu} \tag{3.21}$$

It is noted that for $c > 2/(\mu+1)$, due to the symmetry of the self-equilibrating normal stresses, the following equations hold:

$$\delta_\sigma(c,\mu) = -\delta_\sigma(2-\mu c, (2-c)/(2-\mu c)) \tag{3.22}$$

$$\theta_\sigma(c,\mu) = \theta_\sigma(2-\mu c, (2-c)/(2-\mu c)) \tag{3.23}$$

A comparison between the semi-infinite strip problem results and the ones predicted from the aforementioned equations can be seen in Fig. 3.2.

Shear stresses

$$\delta_\tau = \delta_1(c)\delta_2(\mu) \tag{3.24}$$

$$\theta_\tau = \theta_1(c)\theta_2(\mu) \tag{3.25}$$

where the functions appearing in these equations have the forms:

$$\delta_1(c) = a_1\left[1-(c/2)^{a_2}\right]^{a_3} \tag{3.26}$$

$$\delta_2(\mu) = (a_1\mu - 1)(\mu - 1) \tag{3.27}$$

$$\theta_1(c) = a_1\left[1-(c/2)^{a_2}\right]^{a_3} \tag{3.28}$$

$$\theta_2(\mu) = (a_1\mu - 1)(\mu - 1) \tag{3.29}$$

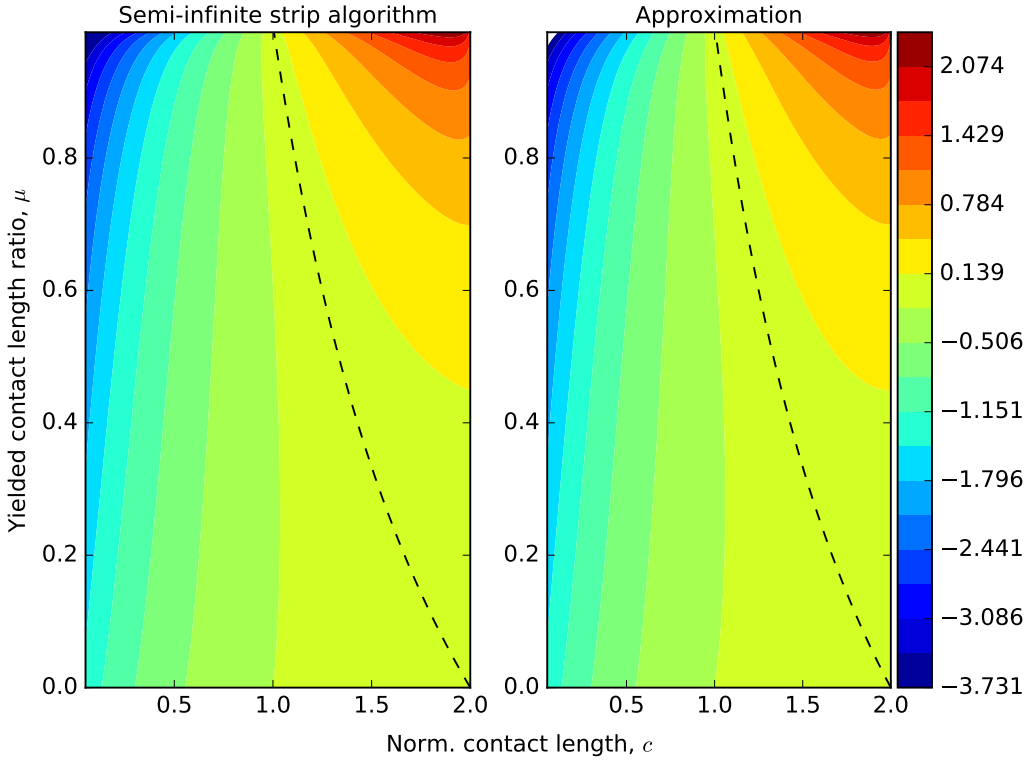

Axial elongation

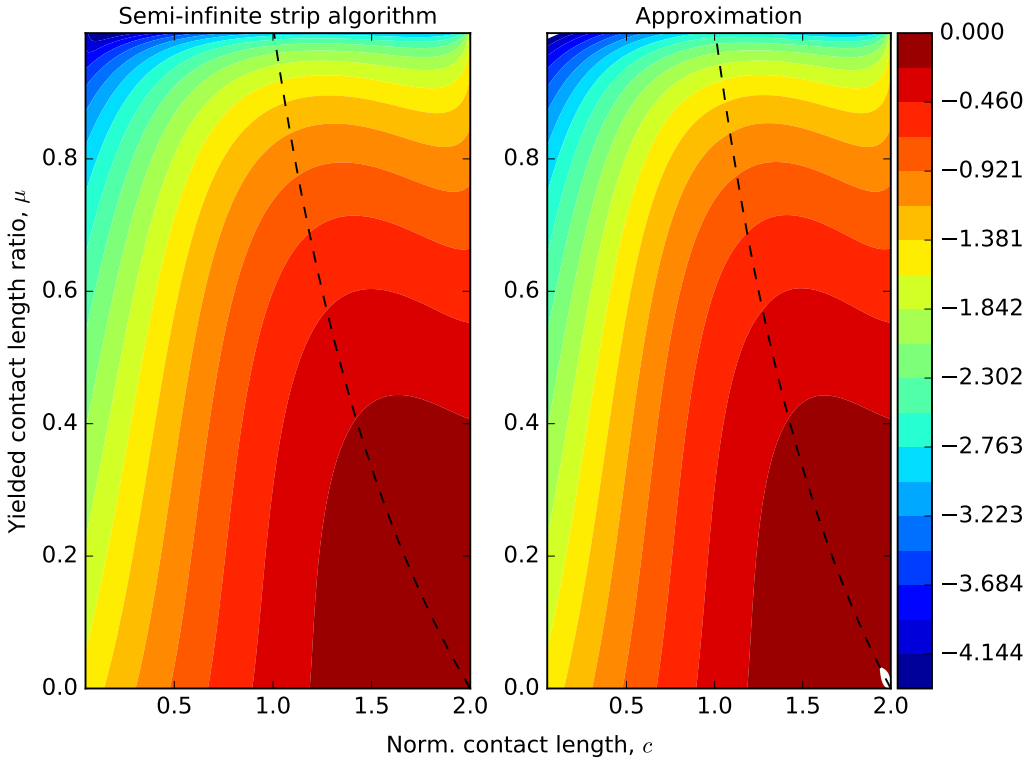

Rocking end rotation

Figure 3.2: Normalized axial elongation and rocking end rotation for $\sigma_y = 1$.

Table 3.1: Approximation functions constant term vectors

Function	a_1	a_2	a_3	a_4
δ_A	-1.61868182	0.74341712	2.38990044	
δ_B	0.02707282	0.71805567	-0.42532673	0.64748945
θ_A	-1.60601045	2.71616773	0.52133449	
θ_B	-0.05393963	-1.54431579	0.98577157	-1.35812515
θ_C	-0.4009598	1.46727493	-2.19487061	
θ_D	-0.03040586	0.15378978	-0.33644138	0.38440043
δ_1	2.48001601	0.68431159	1.80867566	
δ_2	-0.43362038			
θ_1	2.35842517	0.98635297	1.52894546	
θ_2	-0.45228844			

The constant parameters appearing in these equations are given in Table 3.1.

A comparison between the semi-infinite strip problem results and the ones predicted from the aforementioned equations can be seen in Fig. 3.3.

Derivative matrix The derivative matrix, $\boldsymbol{f}_{sen,y}$ of the normalized displacements due to the self equilibrating stresses, $\boldsymbol{u}_{\text{sen,y}}$ with respect to the normalized load parameters, $\boldsymbol{r}_{\text{y}}$ is:

$$\boldsymbol{f}_{sen,y} = \frac{\partial \boldsymbol{u}_{\text{sen,y}}}{\partial \boldsymbol{r}_{\text{y}}} = \frac{1}{E}\begin{bmatrix} \sigma_y \dfrac{\partial \delta_\sigma}{\partial c} + t\dfrac{\partial \delta_\tau}{\partial c} & \sigma_y \dfrac{\partial \delta_\sigma}{\partial \mu} + t\dfrac{\partial \delta_\tau}{\partial \mu} & \delta_\tau \\ \sigma_y \dfrac{\partial \theta_\sigma}{\partial c} + t\dfrac{\partial \theta_\tau}{\partial c} & \sigma_y \dfrac{\partial \theta_\sigma}{\partial \mu} + t\dfrac{\partial \theta_\tau}{\partial \mu} & \theta_\tau \end{bmatrix} \tag{3.30}$$

Changes in the elastic macroelement algorithm due to yielding After the calculation of the rocking interface forces, $\boldsymbol{F}_{\text{r}}$, the yielding condition of Eq. (3.8) is checked. If the material has yielded, then the following changes are performed in the original algorithm:

- The load parameter vector, $\boldsymbol{r}$, of Eq. (2.13) is substituted with $\boldsymbol{r}_y$ of Eq. (3.5).
- The derivative matrix of the load parameter vector $\boldsymbol{r}$ with respect with the rocking interface forces $\boldsymbol{F}_{\text{r}}$, that is the product $\boldsymbol{S}_2\boldsymbol{S}_4$ of Eqs. (2.14) and (2.57), is substituted with $\boldsymbol{S}_{24y}$ of Eq. (3.7).
- The normalized displacement vector due to the self-equilibrating stresses, $\boldsymbol{u}_{\text{sen}}$ (Eq. 2.51), is substituted with $\boldsymbol{u}_{\text{sen,y}}$ of Eq. (3.9).
- The corresponding derivative matrix, $\boldsymbol{f}_{sen}$, of Eq. (2.60) is substituted with $\boldsymbol{f}_{sen,y}$ of Eq. (3.30).

The rest of the algorithm steps remain the same as in the original elastic material algorithm.

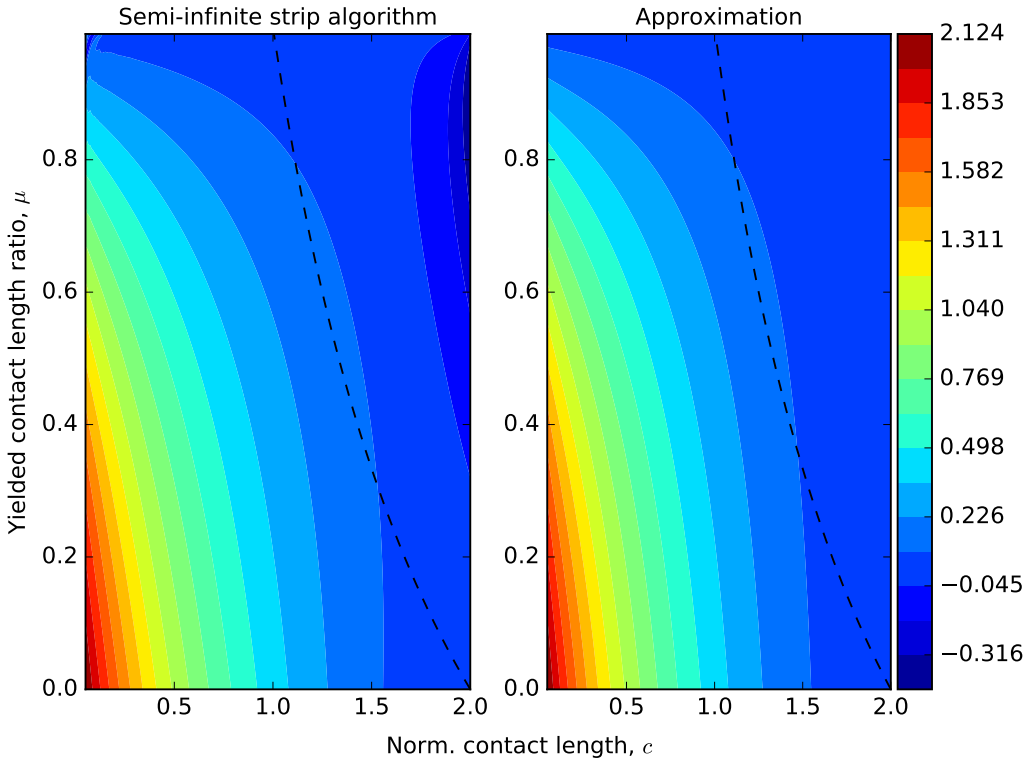

Axial elongation

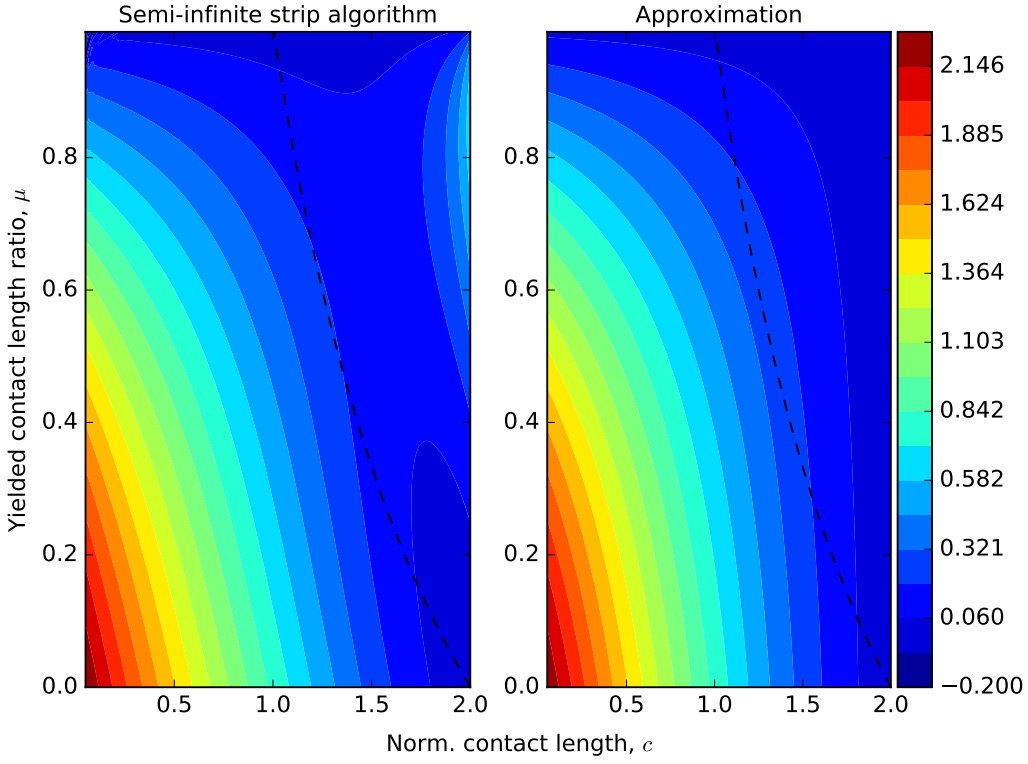

Rocking end rotation

Figure 3.3: Normalized axial elongation and rocking end rotation for $t = 1$. The approximation is accurate enough for $c \leq 2/(\mu + 1)$.

3.3 Examples

Rocking body with constant vertical force and varying yield stress

In this example, a simple rocking body is examined, with height $H = 4$ m, width $B = 1$ m and depth $d = 1$ m and Young's modulus $E = 30$ GPa. The body is loaded on its top central node with a constant vertical force, $N = -2500$ kN (Fig. 3.4a).

Fig. 3.4b shows the pushover capacity curves (horizontal force versus horizontal displacement) of this body for varying yield stress values. It can be seen that the maximum strength and the ultimate displacement decrease for decreasing yield stress values.

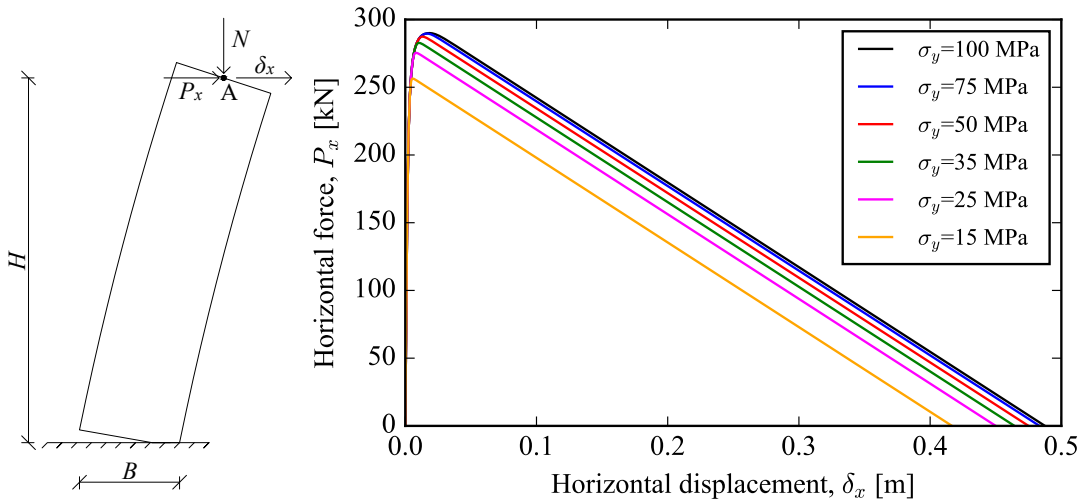

(a) (b)

Figure 3.4: (a) Rocking body with constant vertical force model and (b) pushover capacity curves for varying stress yield values.

Comparison of results with Abaqus

In the following, the results produced with the macroelement are compared to those of the commercial software Abaqus . Unfortunately, pushover capacity curves for rocking bodies are very difficult to obtain with Abaqus for a yielding material due to convergence problems. For this reason, comparisons are performed for a simply supported beam with a rocking end, which corresponds to the macroelement natural coordinate system (Fig. 3.5).

The simply supported beam examined has length $L = 8$ m, width $B = 2$ m, depth $d = 1$ m, Young's modulus $E = 30$ GPa, yield stress $\sigma_y = 20$ MPa and is loaded with a constant axial force $N = -1000$ kN.

In Figs. 3.6 and 3.7, the axial elongation and the rocking end rotation are shown for increasing values of the applied moment on the rocking end of the simply supported

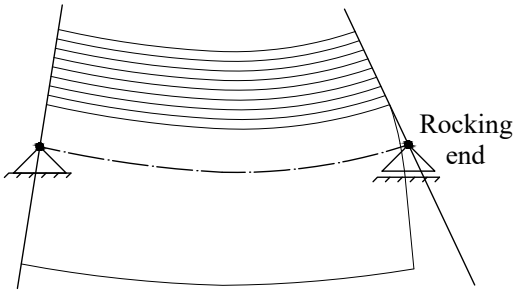

Figure 3.5: Simply supported beam with rocking end.

beam. Fig. 3.6 refers to the case of a beam with equal applied moments on both its ends, meaning that there is no shear force along the beam, while 3.7 refers to the case of an applied moment only on the rocking end of the beam, leading to the development of shear forces. In both cases, it can be seen that the results of the macroelement are very close to the ones obtained using equivalent Abaqus models.

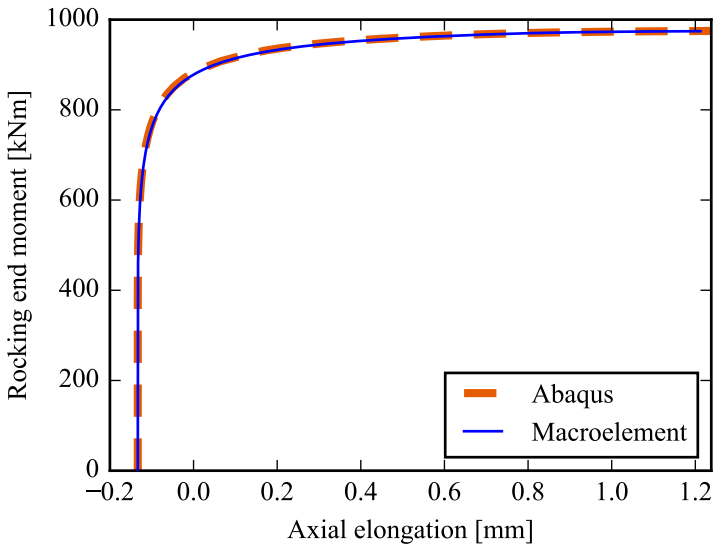

(a)

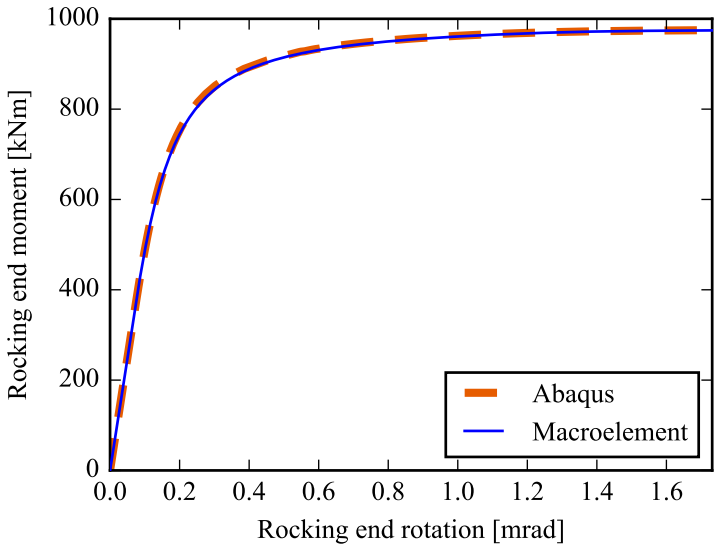

(b)

Figure 3.6: (a) Axial elongation and (b) rocking end rotation of a rocking simply supported beam loaded with equal increasing moments on both its ends (no development of shear) and comparison with Abaqus.

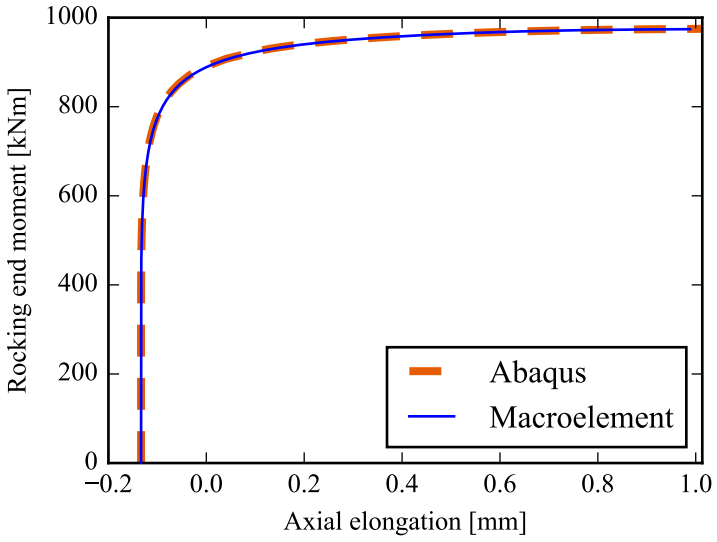

(a)

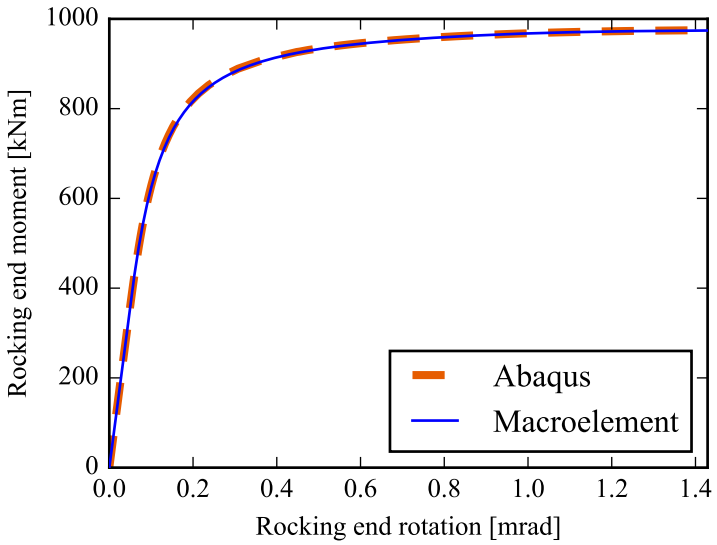

(b)

Figure 3.7: (a) Axial elongation and (b) rocking end rotation of a rocking simply supported beam loaded with an increasing moment only on its rocking end and comparison with Abaqus.

4 The nonlinear displacement distribution of the semi-infinite strip

In this chapter, the problem of the semi-infinite strip with traction-free lateral sides is revisited, in order to examine the displacement profile across the semi-infinite strip under an arbitrary normal load distribution on its end. Although the solution of this problem is important even for practical applications (e.g. the prediction of the rocking motion of deformable bodies), only numerical solutions exist until now, which are cumbersome to implement for such cases.

The displacement profile of the semi-infinite strip under a concentrated normal load is approximated with analytical functions, which must exhibit specific properties. These results are then extended to arbitrary normal load distributions and characteristic cases are presented. Finally, the problem of the determination of the stress distribution across the interface between a deformable rocking body and its base is solved based on the previous derivations.

4.1 Introduction

The determination of the stresses of a semi-infinite strip ($x \geq 0$, $-1 \leq y \leq 1$) with traction-free lateral sides ($y = \pm 1$), for any admissible combination of given tractions or displacements applied on its free end ($x = 0$) (Fig. 4.1) has been a topic of interest for many decades among engineers. Unlike similar problems for the semi-infinite space for which analytical solutions exist, the problem of the semi-infinite strip presents additional mathematical difficulties which do not allow for closed-form analytical solutions, especially in what concerns the determination of stresses for given normal and shear tractions.

Many approaches for the solution of the problem have been proposed over the decades, such as those of Horvay (1957), Theocaris (1959), Benthem (1963), Gaydon and Shepherd (1964), Johnson Jr and Little (1965), Bogy (1975) and Gregory (1980). Most of these

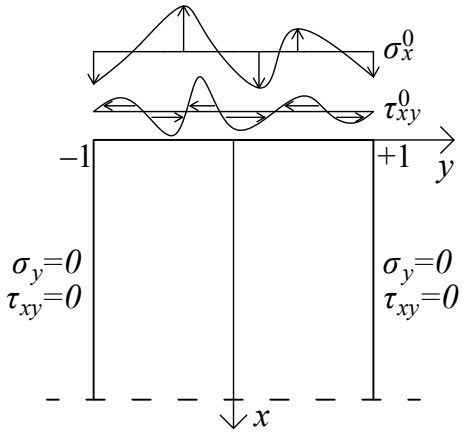

Figure 4.1: The semi-infinite strip

involve solving singular integral equations or infinite systems of coupled linear equations which result from the expansion of the stress function to the Papkovich-Fadle eigenfunctions (Papkovich, 1940; Fadle, 1940), which are not orthogonal.

Although this problem is particularly interesting for the theoretical analysis of structural members, it has lost attention during the last decades, since the technical theory of bending, which assumes that the element's cross section remains plane, is considered sufficient for conventional elastic structural analyses. However, there are practical cases where the technical theory of bending is inadequate. One such case is the prediction of the response of deformable rocking members.

Rocking members cannot develop tensile stresses across the interface with the rocking base and as such, nonlinear stress distributions develop near the contact area where member sections do not remain plane, phenomena which cannot be captured by the technical theory of bending. In the previous chapters, it was proven that for the prediction of the response of such members, the solution of the semi-infinite strip problem can be used. The numerical solution of the semi-infinite strip problem proposed by Gaydon and Shepherd (1964) is utilized in order to calculate approximate additional nodal displacements due to the partial loading of the rocking interface.

It is evident that the calculation of the displacement profile of the fibers of the semi-infinite strip is necessary for practical cases like this. However, the aforementioned existing numerical solutions are cumbersome to use in practical applications. The objective of this chapter is to provide analytical expressions which can be used for the determination of the displacement profile of the semi-infinite strip in practical engineering applications. First, the basic case of a concentrated normal load applied at an arbitrary point on the semi-infinite strip end is examined. Having solved this problem, the displacement distribution due to an arbitrary normal load can be calculated, since any load distribution can be expressed as the integral of concentrated loads across the end section of the strip.

4.2 Decomposition of the problem

The method proposed by Gaydon and Shepherd (1964) for the determination of the stresses inside the element for given semi-infinite strip end loads is based on the decomposition of the applied stress distribution in two parts: (i) the contribution of the resultant forces and (ii) a self-equilibrating stress distribution (Fig. 4.2). For the calculations, only the self-equilibrating part of the load distributions needs to be examined thoroughly, as the contribution of the resultant forces can be calculated according to the technical theory of bending.

More specifically, given an arbitrary stress distribution $[\sigma_0]$ (Fig. 4.2a), the resultant normal force and moment are calculated. According to the technical theory of bending, these give rise to a linear stress distribution which acts across the whole member section, $[\sigma_{\text{ttb}}]$ (Fig. 4.2b) and for which the stresses induced inside the element can be calculated. The difference between the original stress distribution and the resultant forces contribution is a self-equilibrating stress distribution, $[\sigma_{\text{se}}]$ (Fig. 4.2c). Since the resultant force and moment of this distribution is zero, its effect far from the loaded area is negligible, according to the Saint-Venant's principle. However, its effect near the loaded area on the stresses and the displacements is significant. In order to employ the aforementioned methodology, these self-equilibrating stresses are decomposed into a symmetric and an antisymmetric part, for which different stress functions are used.

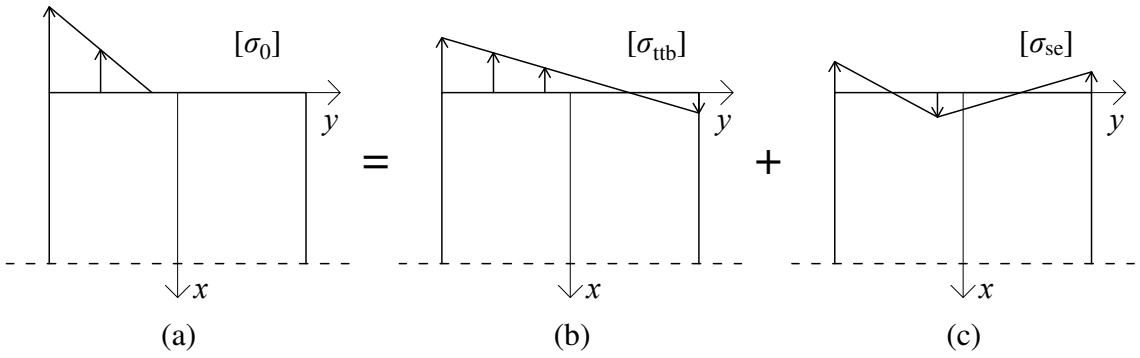

Figure 4.2: Stress distribution decomposition: (a) Original distribution; (b) Resultant forces contribution and (c) remaining self-equilibrating stresses.

This methodology enables us to examine the local effects of a self-equilibrating stress load on the semi-infinite strip. Apart from the determination of the stress distribution near the loaded end, the methodology by Gaydon and Shepherd (1964) can be easily extended for the calculation of the fiber displacements across the semi-infinite strip due to the self-equilibrating stresses, as the integral of the corresponding fiber strains. The extended methodology for the determination of the fiber displacements is rather involved and not repeated here, but can be found in Chapter 2.

For the evaluation of the displacement profiles across the ends of a finite member

length due to an arbitrary nonlinear normal load distribution applied at one of its ends, the same decomposition presented above is applied: The displacement distributions due to the resultant forces contribution is linear and calculated according to the technical theory of bending for given resultant forces at the member ends. Regarding the displacement profiles due to the self-equilibrating stresses contribution, since their effect is local to the end with the nonlinear load distribution, the solution produced for the semi-infinite strip displacements can be used for this end even for a member with finite length and no additional displacements are produced for the linearly loaded member end, given that the length of the member is sufficient (Chapter 2). Finally, the results of the two previous contributions need to be superimposed.

4.3 Displacement function for a concentrated load

Problem statement

In order to calculate the displacements due to an arbitrary stress load applied at the semi-infinite strip end, the concentrated load problem is solved first (Fig. 4.3a), since any load distribution can be considered as a summation of concentrated loads across the strip end. As mentioned previously, only the displacements due to the self-equilibrating stresses corresponding to the concentrated load need to be thoroughly examined in the ensuing.

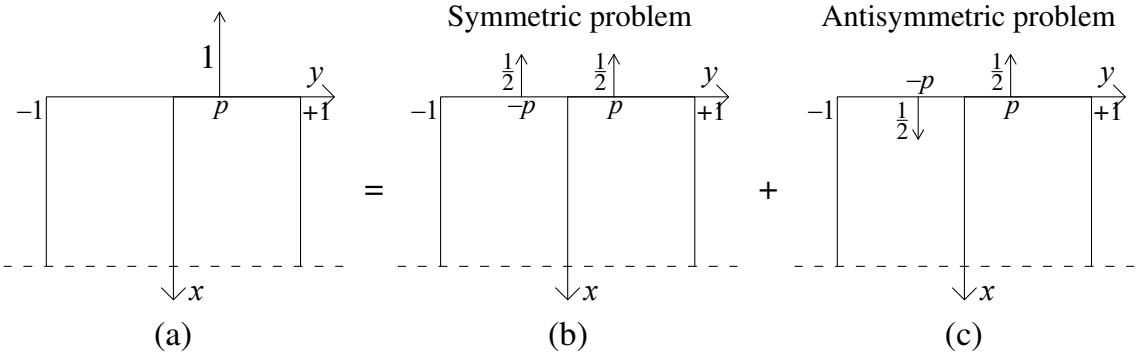

Figure 4.3: (a) Unit point load acting at location p of the semi-infinite strip end; Decomposition into (b) the Symmetric problem and (c) the Antisymmetric one.

A concentrated load at the strip end can be considered as a Dirac delta function for the calculation of the necessary load parameters of the methodology used (Gaydon and Shepherd, 1964). Although the concentrated load introduces a singularity which does not guarantee convergence of the solution (Gregory, 1980), the produced results regarding the fiber displacement distributions exhibit convergent response. A large number of expansion functions are used in order to produce results that are as accurate as possible, however small inaccuracies persist for concentrated loads applied near the corner of the semi-infinite

strip and for the displacements at locations close to this area, which however do not create notable problems.

The results produced for various values of the location p across the strip end for a unit concentrated load (Fig. 4.3a) and location y at which the displacement is measured, and for the normalized case of unit Young's modulus, $E = 1$, are shown in Fig. 4.4. It is noted that, for $E \neq 1$, the displacement values shown have to be divided by E. Furthermore, the displacement at y, considering plane stress conditions, is

$$u(y) = \int_0^\infty \varepsilon(x, y)\, \mathrm{d}x = \frac{1}{E}\left(\int_0^\infty \sigma_x(x, y)\, \mathrm{d}x - \nu \int_0^\infty \sigma_y(x, y)\, \mathrm{d}x\right) \tag{4.1}$$

However, since no shear loading is considered at the strip end and, also, the shear stresses are zero at an infinite distance from the strip end, the integral of the transverse normal stresses along the x-axis of any fiber is zero due to equilibrium in the y-axis. Therefore,

$$\int_0^\infty \sigma_y(x, y)\, \mathrm{d}x = 0 \tag{4.2}$$

which implies that the results are independent of Poisson's ratio, ν.

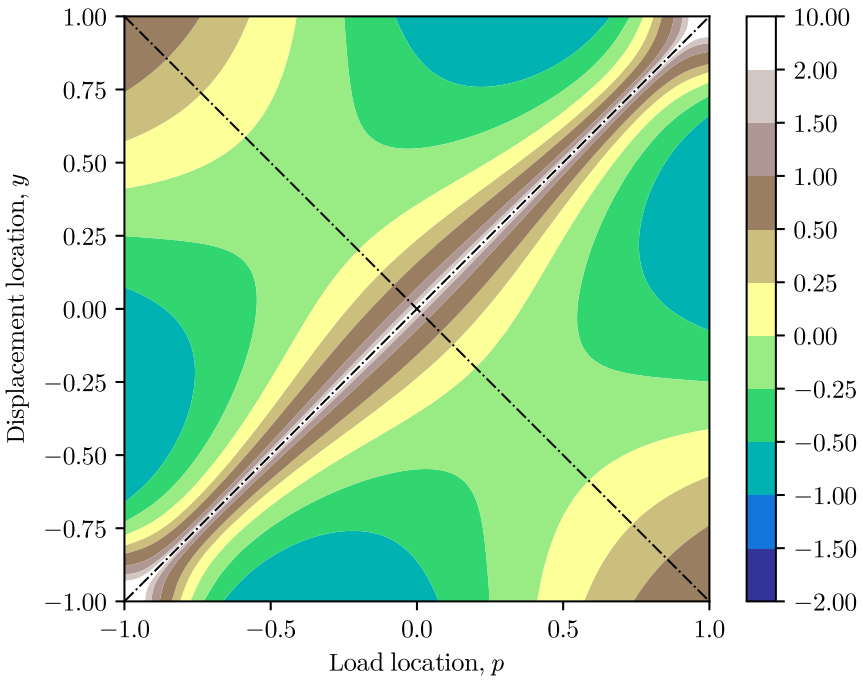

Figure 4.4: Displacement at location y for a concentrated load at location p

As can be seen in Fig. 4.4, the displacement function, U, is doubly symmetric with respect to the two diagonals. The symmetry about the main diagonal means that the displacement at y for a load applied at location p is equal to the displacement at p for a load applied at location y, which is equivalent to the Maxwell-Betti reciprocal work

theorem used in structural analysis (e.g. Timoshenko and Goodier, 1951). Furthermore, symmetry about (0,0) exists, since the displacement at $-y$ for a load at $-p$ is equal to the displacement at y for a load at p. These two symmetries produce a doubly symmetric function, meaning that only one of the four quarters can be examined.

For the approximation of the displacement function, apart from the aforementioned symmetries, the following condition must also hold: Since this displacement function refers to displacements produced by the self-equilibrating part of the loading, the zeroth and first moment of the displacement distribution for a given load location p must be zero:

$$\int_{-1}^{1} U(y,p)\ \mathrm{d}y = 0 \tag{4.3}$$

$$\int_{-1}^{1} y\ U(y,p)\ \mathrm{d}y = 0 \tag{4.4}$$

In order to facilitate the implementation of the aforementioned conditions, it is preferable to examine the symmetric and the antisymmetric problem individually, which refer to the calculation of the displacement distribution for half concentrated loads at locations p and $-p$ with the same and the opposite sign, respectively (Figs. 4.3b and 4.3c). The displacement functions produced for the symmetric and the antisymmetric problem are shown in Fig. 4.5. It is evident that, due to the additional symmetries, only one eighth of these two functions is unique.

Approximation of the symmetric displacement function

The symmetric displacement function, U_s, depicted in Fig. 4.5(a), is symmetric about both main axes and both diagonals. As such, the following condition must hold for the approximating function:

$$\begin{aligned} U_\mathrm{s}(y,p) &= U_\mathrm{s}(-y,p) = U_\mathrm{s}(-y,-p) = U_\mathrm{s}(y,-p) \\ &= U_\mathrm{s}(p,y) = U_\mathrm{s}(-p,y) = U_\mathrm{s}(-p,-y) = U_\mathrm{s}(p,-y) \end{aligned} \tag{4.5}$$

Although only one eighth of the domain can be examined, it is more convenient to examine a quarter of the domain, namely $0 \leq y \leq 1$, $0 \leq p \leq 1$. For this region, the following condition must also hold due to Eq. (4.3) and the symmetry about the y-axis:

$$\int_{0}^{1} U_s(y,p)\ \mathrm{d}y = 0 \tag{4.6}$$

It is noted that Eq. 4.4 is satisfied by default due to symmetry about the y-axis.

As can be seen from Fig. 4.5(a), there is a singularity along the diagonals, with the values of the displacements approaching infinity. After more careful examination and trying various functions, this singularity seems to be logarithmic in nature. This is consistent

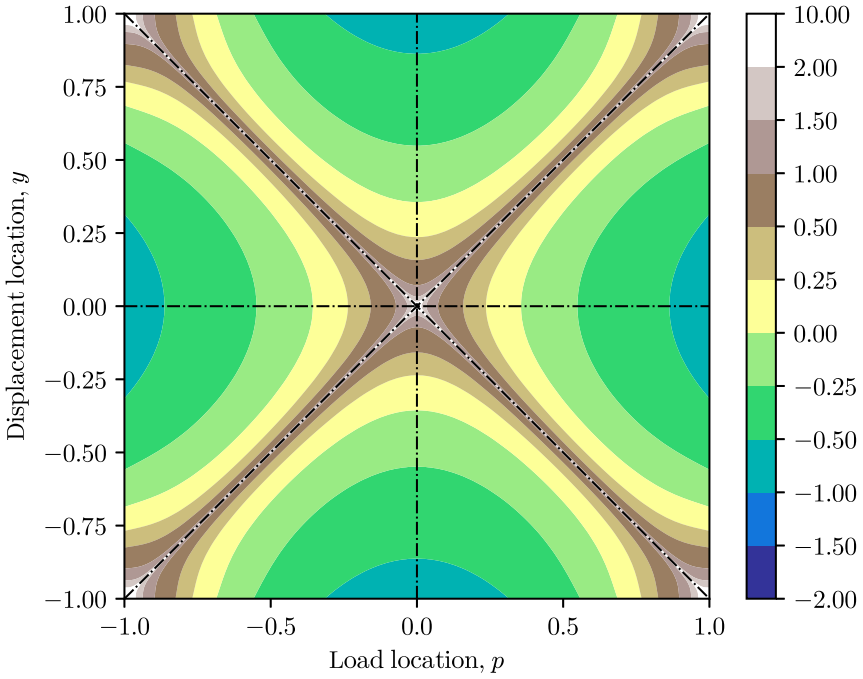

(a)

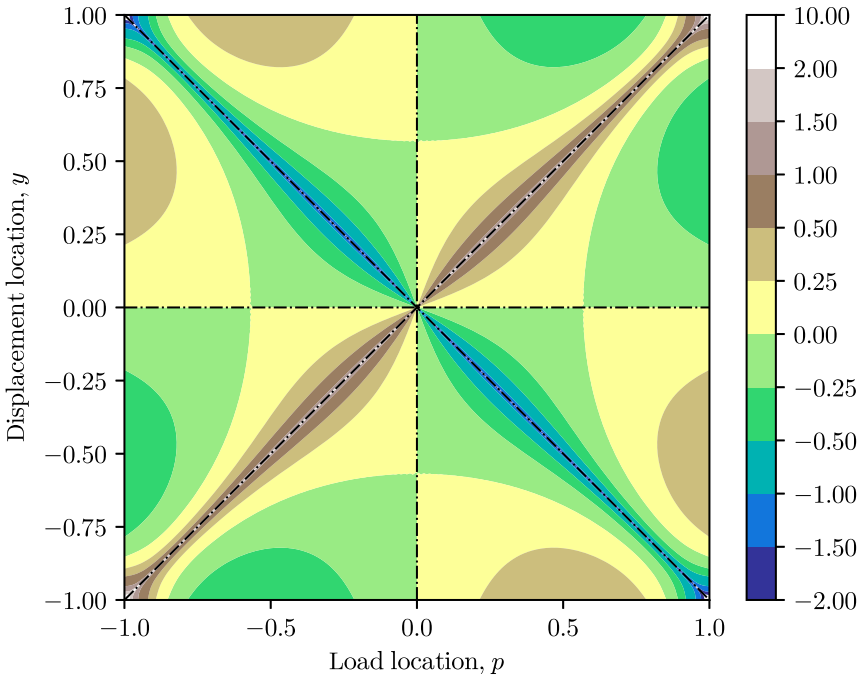

(b)

Figure 4.5: Displacement functions for (a) the symmetric and (b) the antisymmetric problem.

with the result regarding the displacement distribution produced by a unit concentrated load on a semi-infinite space (e.g. Das, 2013):

$$u^*(y,p) = 2A \ln|p-y| + C \tag{4.7}$$

where $E = 1$ and $\nu = 0$ are considered, $A = -1/\pi$ and C is a constant.

Considering the symmetric problem which refers to symmetric loading about 0 with point loads equal to $1/2$ and ignoring the constant term C, the corresponding function is

$$U_{\text{sA1}}(y,p) = A \ln|p-y| + A \ln|p+y| \tag{4.8}$$

By trying to approximate the logarithmic singularities of the symmetric displacement function with a function of the form of Eq. (4.8), it was found that the best approximation was attained by keeping the coefficient $A = -1/\pi$, as in the theoretical solution of the semi-infinite space. The difference between the original symmetric function, U_{s}, and the function U_{sA1}, is depicted in Fig. 4.6, where only one quarter is shown for clarity. It can be seen that the remaining function is now smooth across the diagonal.

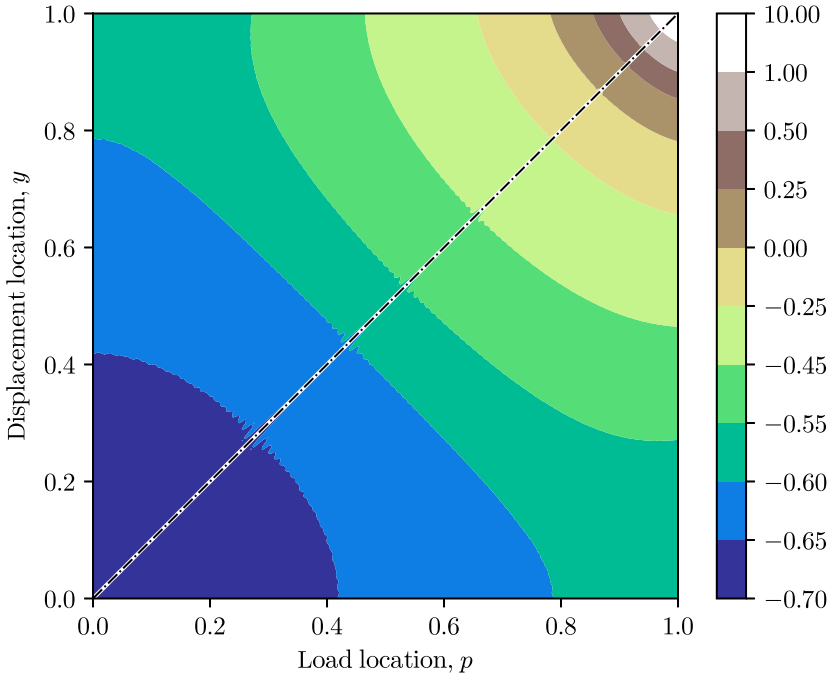

Figure 4.6: Symmetric displacement function after removal of diagonal logarithmic singularities.

Although this function satisfies Eq. (4.5), Eq. (4.6) is not satisfied, as:

$$\int_0^1 U_{\text{sA1}}(y,p)\, \mathrm{d}y = A\left[(\ln(1+p)-1)(1+p) + (\ln(1-p)-1)(1-p)\right] \tag{4.9}$$

Furthermore, it can be seen that a singularity remains at (1,1). For these reasons, a new function is sought, which eliminates the non-zero integral introduced by Eq. (4.8) and includes a singularity at (1,1). A function that satisfies these conditions, as well as the symmetry conditions of Eq. (4.5), is:

$$U_{\mathrm{sA2}}(y,p) = -A\left[\ln(1-yp)(1-2yp) + \ln(1+yp)(1+2yp) - 2\right] \tag{4.10}$$

The difference between U_{s} and $U_{\mathrm{sA1}} + U_{\mathrm{sA2}}$ can be seen in Fig. 4.7. This function has significantly smaller values than U_{s}, however further approximation is considered necessary. Furthermore, it can be seen that the singularity at (1,1) remains, but now extends in a small circular area around (1,1).

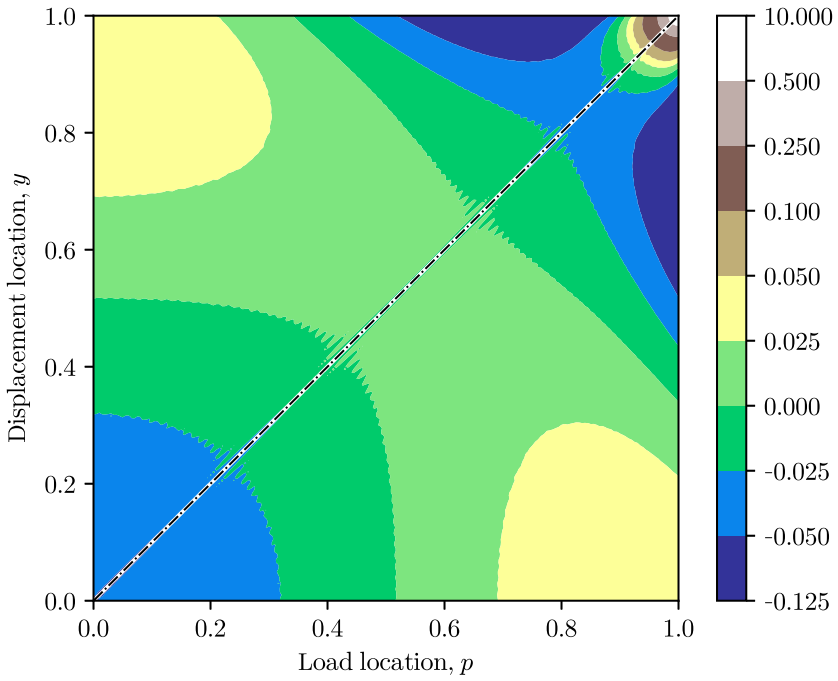

Figure 4.7: Symmetric displacement function after removal of diagonal logarithmic singularities and corresponding integral equilibrating function.

In order to eliminate this remaining singularity, a function of the form

$$\begin{aligned} U_{\mathrm{sB1}} = B\Big[&\ln((1-y)^2+(1-p)^2) + \ln((1-y)^2+(1+p)^2) \\ &+ \ln((1+y)^2+(1+p)^2) + \ln((1+y)^2+(1-p)^2)\Big] \end{aligned} \tag{4.11}$$

is introduced, which satisfies Eq. (4.5). However, again, Eq. (4.6) is not satisfied. For this reason, the following function which satisfies Eq. (4.5) and negates the non-zero integral

is also used:

$$\begin{aligned} U_{\mathrm{sB2}} = B\,\big[&-2\ln((1-y)^2+4) - 2\ln((1+y)^2+4) \\ &- 2\ln((1-p)^2+4) - 2\ln((1+p)^2+4) \\ &+ 2(1-y)\arctan((1-y)/2) + 2(1+y)\arctan((1+y)/2) \\ &+ 2(1-p)\arctan((1-p)/2) + 2(1+p)\arctan((1+p)/2) \\ &- 2\pi + 12\ln(2) + 4\big] \end{aligned} \tag{4.12}$$

The coefficient B in Eqs. (4.11) and (4.12) is defined in the ensuing.

Finally, a polynomial function satisfying Eqs. (4.5) and (4.6) is introduced, which has the form:

$$\begin{aligned} U_{\mathrm{sP}} = {} & q_{22}/9 + 2q_{42}/15 + q_{44}/25 + 2q_{62}/21 + 2q_{64}/35 \\ & + q_{66}/49 + 2q_{82}/27 + 2q_{84}/45 + 2q_{86}/63 + q_{88}/81 \\ & + q_{22}y^2p^2 + q_{44}y^4p^4 + q_{66}y^6p^6 + q_{88}y^8p^8 \\ & + q_{42}y^2p^2(y^2+p^2) + q_{62}y^2p^2(y^4+p^4) + q_{82}y^2p^2(y^6+p^6) \\ & + q_{64}y^4p^4(y^2+p^2) + q_{84}y^4p^4(y^4+p^4) + q_{86}y^6p^6(y^2+p^2) \\ & - (y^2+p^2)(q_{22}/3 + q_{42}/5 + q_{62}/7 + q_{82}/9) \\ & - (y^4+p^4)(q_{42}/3 + q_{44}/5 + q_{64}/7 + q_{84}/9) \\ & - (y^6+p^6)(q_{62}/3 + q_{64}/5 + q_{66}/7 + q_{86}/9) \\ & - (y^8+p^8)(q_{82}/3 + q_{84}/5 + q_{86}/7 + q_{88}/9) \end{aligned} \tag{4.13}$$

The coefficients q in this function are defined in the following. Powers up to 8 have been used in this function in order to achieve sufficient accuracy.

In order to determine coefficients B and q of the aforementioned functions, a least squares approach is employed which minimizes the difference of the function shown in Fig. 4.7 with respect to functions U_{sB1}, U_{sB2} and U_{sP}. This is achieved using the *curve_fit* tool of the *SciPy Python* package, which can implement least squares fitting for functions of higher dimensions. The resultant coefficients which match the target function in the best way are given in Table 4.1 and the correponding approximation is shown in Fig. 4.8.

Finally, the resultant approximation of the symmetric displacement function is defined as:

$$U_{\mathrm{s}} = U_{\mathrm{sA1}} + U_{\mathrm{sA2}} + U_{\mathrm{sB1}} + U_{\mathrm{sB2}} + U_{\mathrm{sP}} \tag{4.14}$$

Approximation of the antisymmetric displacement function

The procedure followed for the approximation of the antisymmetric displacement function is similar to the one described above. As can be seen in Fig. 4.5(b), the antisymmetric

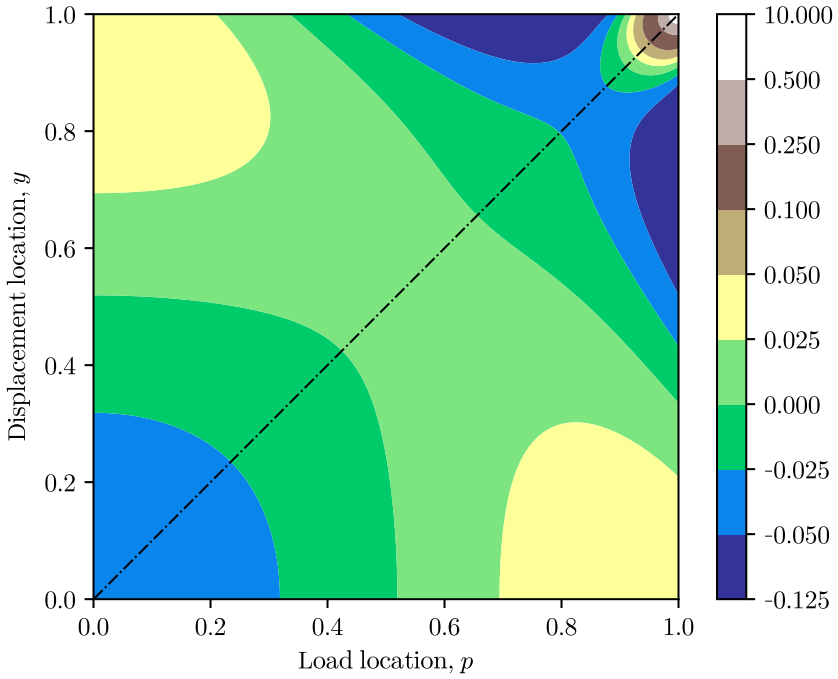

Figure 4.8: Approximation of the symmetric displacement function after removal of diagonal logarithmic singularities and corresponding integral equilibrating function.

displacement function is symmetric about both diagonals and antisymmetric about both main axes. As such, the following condition must hold for the approximating function:

$$\begin{aligned} U_{\mathrm{a}}(y,p) &= -U_{\mathrm{a}}(-y,p) = U_{\mathrm{a}}(-y,-p) = -U_{\mathrm{a}}(y,-p) \\ &= U_{\mathrm{a}}(p,y) = -U_{\mathrm{a}}(-p,y) = U_{\mathrm{a}}(-p,-y) = -U_{\mathrm{a}}(p,-y) \end{aligned} \tag{4.15}$$

Examining again the domain $0 \leq y \leq 1$, $0 \leq p \leq 1$, the following condition must also hold due to Eq. (4.4) and antisymmetry about the y-axis:

$$\int_0^1 y\, U_a(y,p)\, \mathrm{d}y = 0 \tag{4.16}$$

It is noted that Eq. (4.3) is satisfied by default due to the antisymmetry about the y-axis.

The solution of the corresponding antisymmetric semi-infinite space problem has the form

$$U_{\mathrm{aA1}}(y,p) = A \ln|p-y| - A \ln|p+y| \tag{4.17}$$

with $A = -1/\pi$. The difference between the original symmetric function, U_{a}, and the function $U_{\mathrm{a}A1}$, is depicted in Fig. 4.9, where only one quarter is shown for clarity. It can be seen that the remaining function is now smooth across the diagonal.

Although this function satisfies Eq. (4.15), Eq. (4.16) is not satisfied, as:

$$\int_0^1 y\, U_{\mathrm{aA1}}(y,p)\, \mathrm{d}y = A\left[-p + (\ln(1-p) - \ln(1+p))(1-p^2)/2\right] \tag{4.18}$$

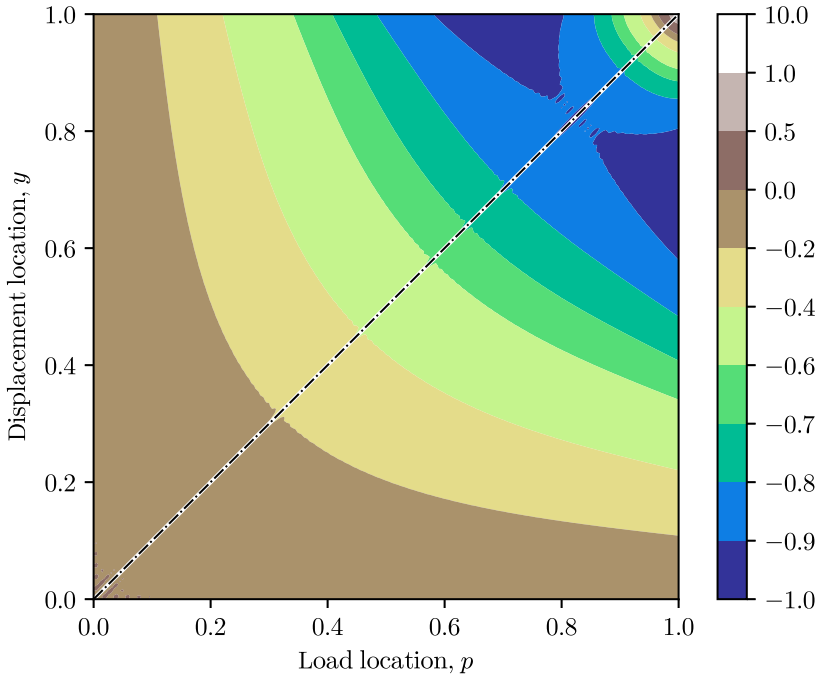

Figure 4.9: Antisymmetric displacement function after removal of diagonal logarithmic singularities.

Furthermore, it can be seen that again a singularity remains at (1,1). For these reasons, a new function is sought, which eliminates the non-zero integral introduced by Eq. (4.17) and includes a singularity at (1,1). A function that satisfies these conditions, as well as the symmetry conditions of Eq. (4.15), is:

$$U_{\mathrm{aA2}}(y,p) = -A\left[(\ln(1-yp) - \ln(1+yp))\,(1-2y^2p^2) - 4yp\right] \tag{4.19}$$

The difference between U_{a} and $U_{\mathrm{aA1}} + U_{\mathrm{aA2}}$ can be seen in Fig. 4.10. Again, a singularity extending in a small circular area around (1,1) remains, but the remaining values of the antisymmetric problem are lower than the corresponding ones of the symmetric case. Nevertheless, the same procedure is followed again in order to approximate the remaining function.

The singularity at (1,1) should be captured using a similar function as the one used for the symmetric problem, since it can be shown that these singularities cancel out if they are subtracted. This also means that the coefficient of this function should be common between the symmetric and the antisymmetric problem. The corresponding function used for the antisymmetric problem is

$$\begin{aligned} U_{\mathrm{aB1}} = B\,\big[&\ln((1-y)^2+(1-p)^2) - \ln((1-y)^2+(1+p)^2) \\ &+ \ln((1+y)^2+(1+p)^2) - \ln((1+y)^2+(1-p)^2)\big] \end{aligned} \tag{4.20}$$

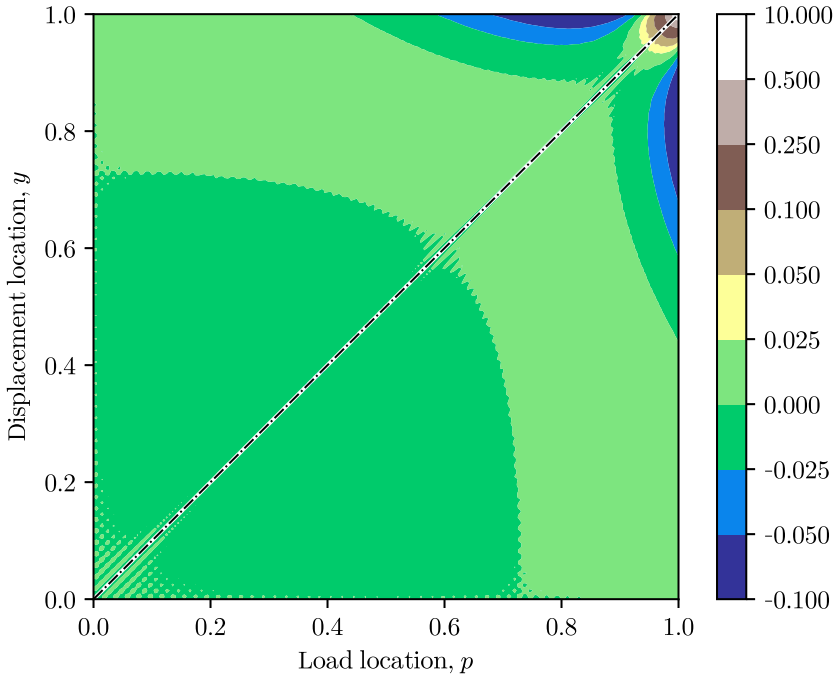

Figure 4.10: Antisymmetric displacement function after removal of diagonal logarithmic singularities and corresponding integral equilibrating function.

which satisfies Eq. (4.15). Eq. (4.16) is not satisfied, so the following function satisfying Eq. (4.15) which negates the non-zero integral is used:

$$\begin{aligned} U_{\mathrm{aB2}} = B\Big[&\frac{3}{2}p((1-y)^2\ln((1-y)^2+4) - (1+y)^2\ln((1+y)^2+4)) \\ &+ \frac{3}{2}y((1-p)^2\ln((1-p)^2+4) - (1+p)^2\ln((1+p)^2+4)) \\ &+ 3p((1+y)^2\ln(1+y) - (1-y)^2\ln(1-y)) \\ &+ 3y((1+p)^2\ln(1+p) - (1-p)^2\ln(1-p)) \\ &+ 6p((1-y)\arctan((1-y)/2) - (1+y)\arctan((1+y)/2)) \\ &+ 6y((1-p)\arctan((1-p)/2) - (1+p)\arctan((1+p)/2)) \\ &+ 6yp(\pi + 2\ln(2) + 1)\Big] \end{aligned} \tag{4.21}$$

The polynomial function of the antisymmetric problem, which satisfies Eqs. (4.15) and (4.16) is

$$\begin{aligned} U_{\mathrm{aP}} = &\, q_{31}yp(y^2+p^2) + q_{51}yp(y^4+p^4) + q_{71}yp(y^6+p^6) \\ &+ q_{53}y^3p^3(y^2+p^2) + q_{73}y^3p^3(y^4+p^4) + q_{75}y^5p^5(y^2+p^2) \\ &- 3yp(q_{31}/5 + q_{51}/7 + q_{71}/9) - 5y^3p^3(q_{31}/3 + q_{53}/7 + q_{73}/9) \\ &- 7y^5p^5(q_{51}/3 + q_{53}/5 + q_{75}/9) - 9y^7p^7(q_{71}/3 + q_{73}/5 + q_{75}/7) \end{aligned} \tag{4.22}$$

Similarly to the symmetric case, in order to determine coefficients B and q of the aforementioned functions, a least squares approach is employed which minimizes the difference of the function shown in Fig. 4.10 with respect to functions U_{aB1}, U_{aB2} and U_{aP}.

In reality, as mentioned above, the coefficient B of the symmetric and antisymmetric problem must be the same. By approximating the functions of the symmetric and antisymmetric problem individually, the values for B are close to each other, but not exactly equal. So, its value is fixed to the average of the two aforementioned results and then a least squares fitting is performed again in order to determine the remaining coefficients q of the polynomial functions. The resultant coefficients which match the target function in the best way are given in Table 4.1 and the correponding approximation is shown in Fig. 4.11.

Finally, the resultant approximation of the antisymmetric displacement function is defined as:

$$U_{\text{a}} = U_{\text{aA1}} + U_{\text{aA2}} + U_{\text{aB1}} + U_{\text{aB2}} + U_{\text{aP}} \tag{4.23}$$

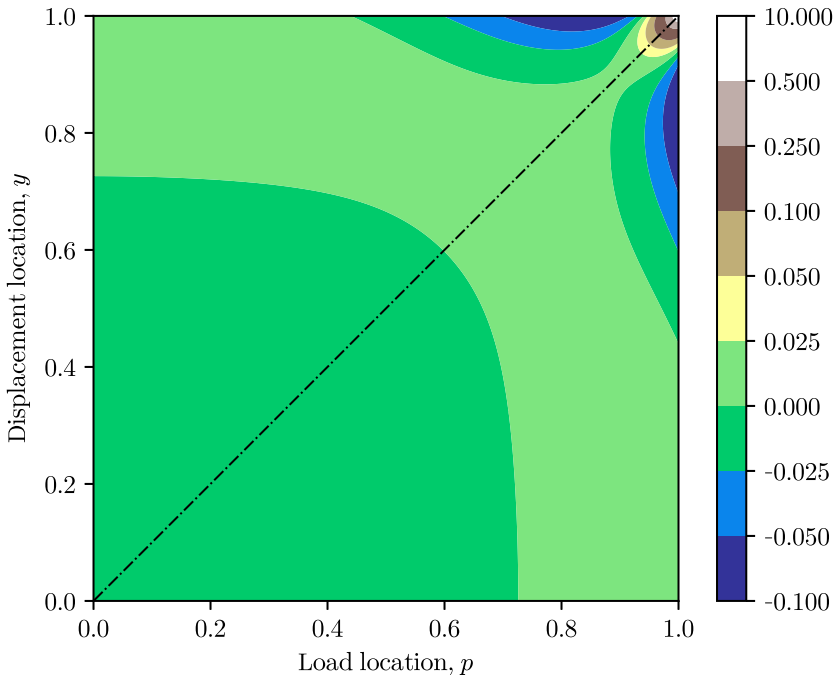

Figure 4.11: Approximation of the antisymmetric displacement function after removal of diagonal logarithmic singularities and corresponding integral equilibrating function.

Total displacement function

Adding the symmetric and antisymmetric displacement functions, the total displacement function is as follows:

$$U(y,p) = A\,U_{\text{A}} + B\,U_{\text{B}} + U_{\text{sP}} + U_{\text{aP}} \tag{4.24}$$

Coeff.	Value	Coeff.	Value	Coeff.	Value
A	-1/π	q_{64}	18.273236	q_{31}	0.74952005
B	-0.19532775	q_{66}	-38.99971412	q_{51}	-0.08175407
q_{22}	-1.23991592	q_{82}	0.74180336	q_{53}	5.10578057
q_{42}	1.08897876	q_{84}	-9.64366612	q_{71}	0.04700608
q_{44}	-9.7265530	q_{86}	22.03387365	q_{73}	-2.9709584
q_{62}	-1.50465044	q_{88}	-13.05630027	q_{75}	9.15391675

Table 4.1: Approximation function coefficients

where

$$\begin{aligned} U_{\mathrm{A}} = {} & 2\ln|p-y| + 2\ln(1-yp)(y^2p^2+yp-1) \\ & - 2\ln(1+yp)(y^2p^2+yp) + 2(2yp+1) \end{aligned} \tag{4.25}$$

$$\begin{aligned} U_{\mathrm{B}} = {} & 2\ln((1-y)^2+(1-p)^2) + 2\ln((1+y)^2+(1+p)^2) \\ & + 3p((1+y)^2\ln(1+y) - (1-y)^2\ln(1-y)) \\ & + 3y((1+p)^2\ln(1+p) - (1-p)^2\ln(1-p)) \\ & + (3p/2 - 3yp + 3y^2p/2 - 2)\ln((1-y)^2+4) \\ & + (-3p/2 - 3yp - 3y^2p/2 - 2)\ln((1+y)^2+4) \\ & + (3y/2 - 3yp + 3yp^2/2 - 2)\ln((1-p)^2+4) \\ & + (-3y/2 - 3yp - 3yp^2/2 - 2)\ln((1+p)^2+4) \\ & + 2(1-y+3p-3yp)\arctan((1-y)/2) \\ & + 2(1+y-3p-3yp)\arctan((1+y)/2) \\ & + 2(1-p+3y-3yp)\arctan((1-p)/2) \\ & + 2(1+p-3y-3yp)\arctan((1+p)/2) \\ & + 6yp(\pi + 2\ln(2) + 1) - 2(\pi - 6\ln(2) - 2) \end{aligned} \tag{4.26}$$

and U_{sP}, U_{aP} given by Eqs. (4.13) and (4.22), respectively.

It is noted that the following limits hold:

$$\lim_{x\to 1}(1-x)\ln(1-x) = \lim_{x\to -1}(1+x)\ln(1+x) = 0 \tag{4.27}$$

so function U_{B} has a removable singularity at $y = \pm 1$ or $p = \pm 1$ if $y \neq p$.

In Fig. 4.12, a comparison between the displacement distribution of the numerical solution and the proposed approximation is presented for various values of the location of the load, p. Only cases $0 \leq p < 1$ are presented for clarity, since the opposite sign cases are symmetrical to the ones presented. This figure shows that the proposed approximation predicts very well the numerical values.

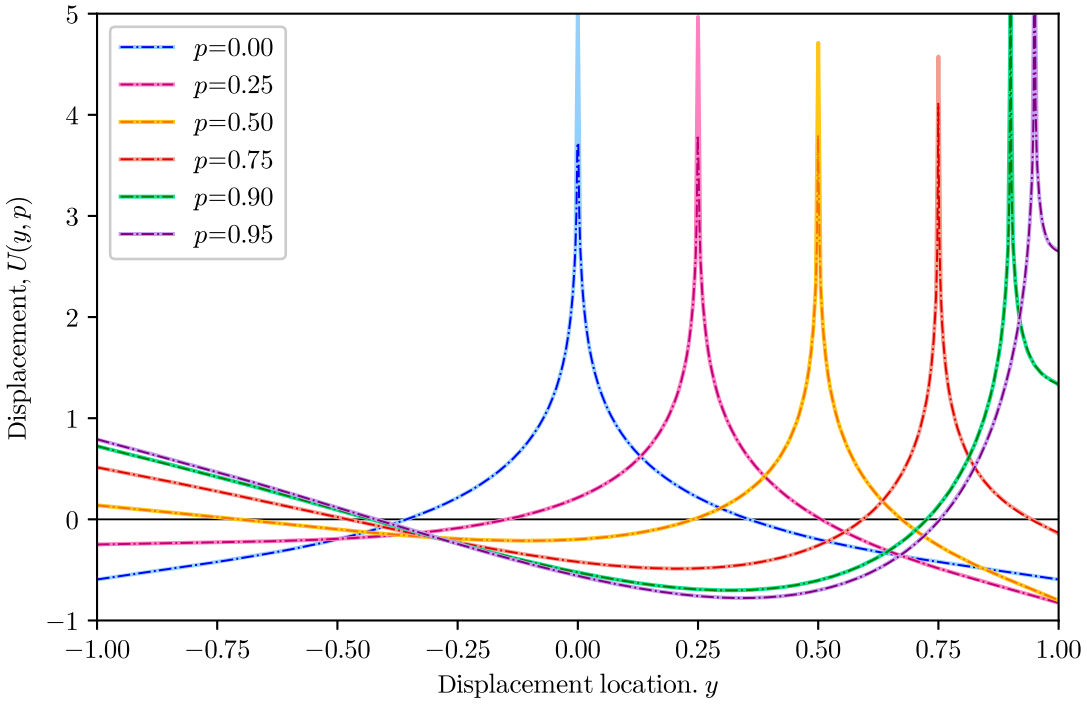

Figure 4.12: Displacement distributions for various values of the location of the load: Comparison of numerical results (solid lines) and proposed approximation (dashed lines).

4.4 Extension to rectangular and triangular normal load distributions

After the determination of the displacement distribution for the self-equilibrating stresses of a concentrated load applied at an arbitrary location on the semi-infinite strip end, the displacement profile due to the self-equilibrating stresses of any normal load distribution can be calculated, since an arbitrary load can be considered as the superposition of concentrated loads across the the semi-infinite strip end. Thus, if the normal load distribution is $\sigma(y)$, the displacements across the strip are calculated as:

$$u(y) = \int_{-1}^{1} \sigma(p)\, U(y,p)\, \mathrm{d}p \tag{4.28}$$

In this section, two characteristic cases are considered: a rectangular load (Fig. 4.13a) and a triangular load (Fig. 4.13b).

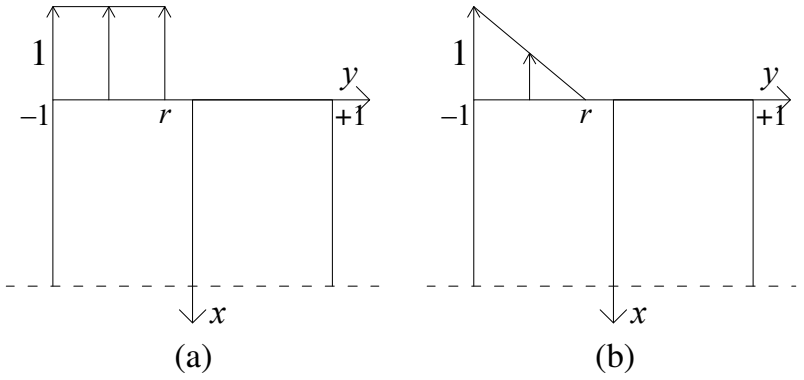

Figure 4.13: (a) Rectangular load and (b) Triangular load cases examined

Rectangular load

The displacement distribution due to the self-equilibrating stresses of a rectangular load with unit stress value in the region $[-1, r]$ of the strip end (Fig. 4.13a) is calculated as:

$$U_{\mathrm{R}}(y, r) = \int_{-1}^{r} U(y, p)\ \mathrm{d}p \tag{4.29}$$

This integral is easy to calculate given the function U (Eq. 4.24). The analytical expressions of the non-polynomial terms are given in 4.A. The displacement distributions for various r values are shown in Fig. 4.14, where both the numerical results according to the method by Gaydon and Shepherd (1964) and the approximation of the aforementioned integral are presented. It can be seen that there is very good agreement between the proposed approximation and the numerical results.

In Fig. 4.14, only results for $r \geq 0$ are presented for clarity, however the conclusions of this comparison are easily extended to cases $r < 0$, due to the following property:

Since only the self-equilibrating stresses are considered, a rectangular load in the region $[-1, r]$ is equivalent to a rectangular load spanning the whole section, which does not give rise to self-equilibrating stresses, and an opposite sign rectangular load in the region $[r, 1]$. Thus, further taking the symmetry about $y = 0$ into account, the following symmetry holds for the rectangular load displacement distribution:

$$U_{\mathrm{R}}(-y, -r) = -U_{\mathrm{R}}(y, r) \tag{4.30}$$

It is noted that although the value of function U does not exist for $y = p$, the integral of Eq. (4.29) does have a finite limit at $y = r$. The displacement at the load tip ($y = r$) is presented in Fig. 4.15, for both the numerical solution and the proposed approximation.

Triangular load

Similarly, the displacement distribution due to the self-equilibrating stresses of a triangular load in the region $[-1, r]$ of the end section with unit maximum stress at $y = -1$ (Fig.

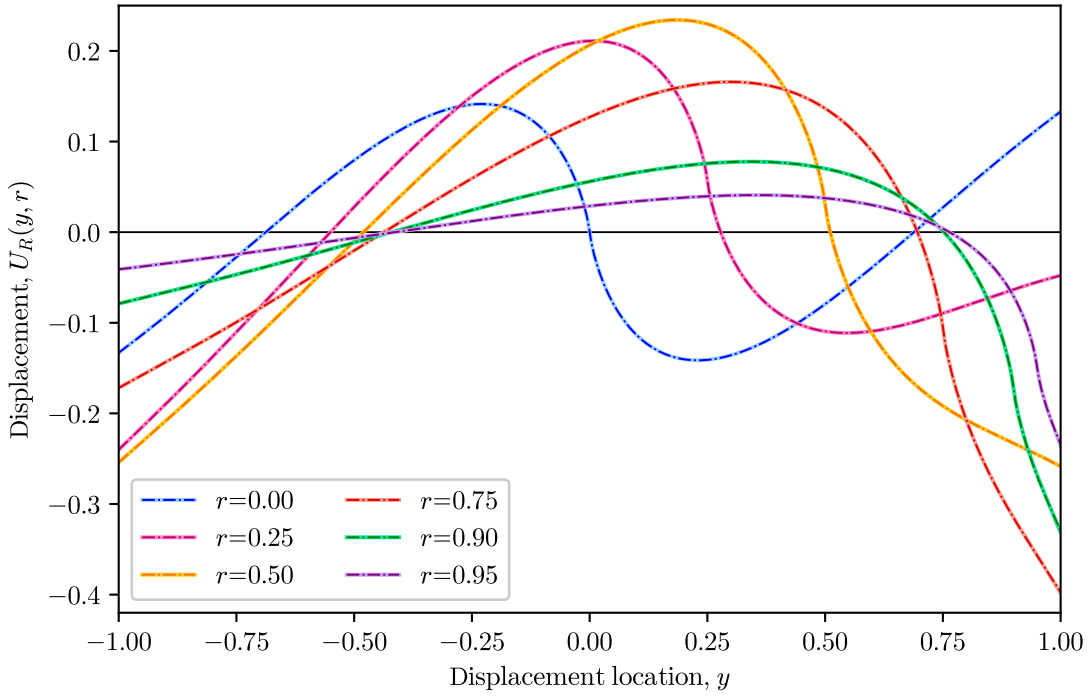

Figure 4.14: Displacement distributions due to rectangular loading for various r values: Comparison of numerical results (solid lines) and proposed approximation (dashed lines).

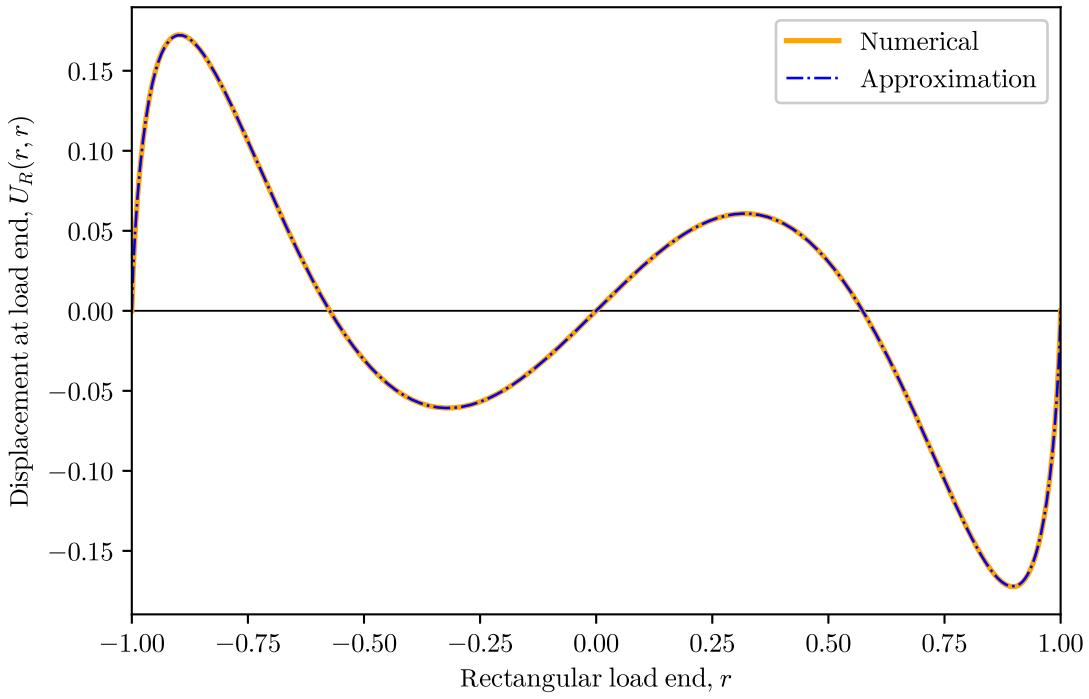

Figure 4.15: Displacement due to rectangular loading at $y = r$ for various r values: Comparison between numerical results and proposed approximation.

4.13b) is calculated as:

$$U_{\mathrm{T}}(y,r) = \frac{r}{r+1}\int_{-1}^{r} U(y,p)\,\mathrm{d}p - \frac{1}{r+1}\int_{-1}^{r} p\,U(y,p)\,\mathrm{d}p \tag{4.31}$$

The analytical expression of the non-polynomial terms of both integrals can be found in 4.A. The displacement distributions for various values of r are given in Fig. 4.16, where both the numerical results according to the method by Gaydon and Shepherd (1964) and the approximation of the aforementioned integral are presented, again showing very good agreement with each other.

Similarly to the rectangular loading, the following symmetry holds for the triangular loading displacement distribution:

$$U_{\mathrm{T}}(-y,-r) = \frac{1+r}{1-r}\,U_{\mathrm{T}}(y,r) \tag{4.32}$$

So, although only cases with $r \geq 0$ are presented, the aforementioned identity implies that the depicted comparison of the results also holds for cases with $r < 0$.

Again, Eq. (4.31) does have a finite limit for $y = r$ and the displacement at the load tip ($y = r$) is presented in Fig. 4.17, for both the numerical solution and the proposed approximation.

4.5 Application to the elastic rocking body

One important practical application of the semi-infinite strip results is the prediction of the response of rocking bodies. In contrast to conventional members, rocking bodies cannot develop tensile stresses at the rocking interfaces, but only compressive stresses acting partially on the rocking end sections. Due to this partial loading, nonlinear stress distributions develop near the contact areas (Fig. 1.5). This also influences the displacement distributions across rocking body sections near the contact area, which are nonlinear.

As explained in Section 4.2, in order to examine the influence of the nonlinear stress distributions, the stresses at the rocking interfaces must be decomposed into stresses according to the technical theory for the respective resultant forces and self-equilibrating stresses. Since the effect of the latter is negligible far from the rocking interfaces, the displacement distribution at sections far from the contact areas is almost linear across the element, as predicted by the technical theory of bending.

For a body rocking on a rigid surface, since the rocking interface is planar, the displacement distribution of the fibers corresponding to the contact region must be linear also at the rocking end. Since the displacements according to the technical theory are linear across the whole section by default, this means that the displacements due to the self-equilibrating stresses must also be linear for this contact region (Fig. 4.18).

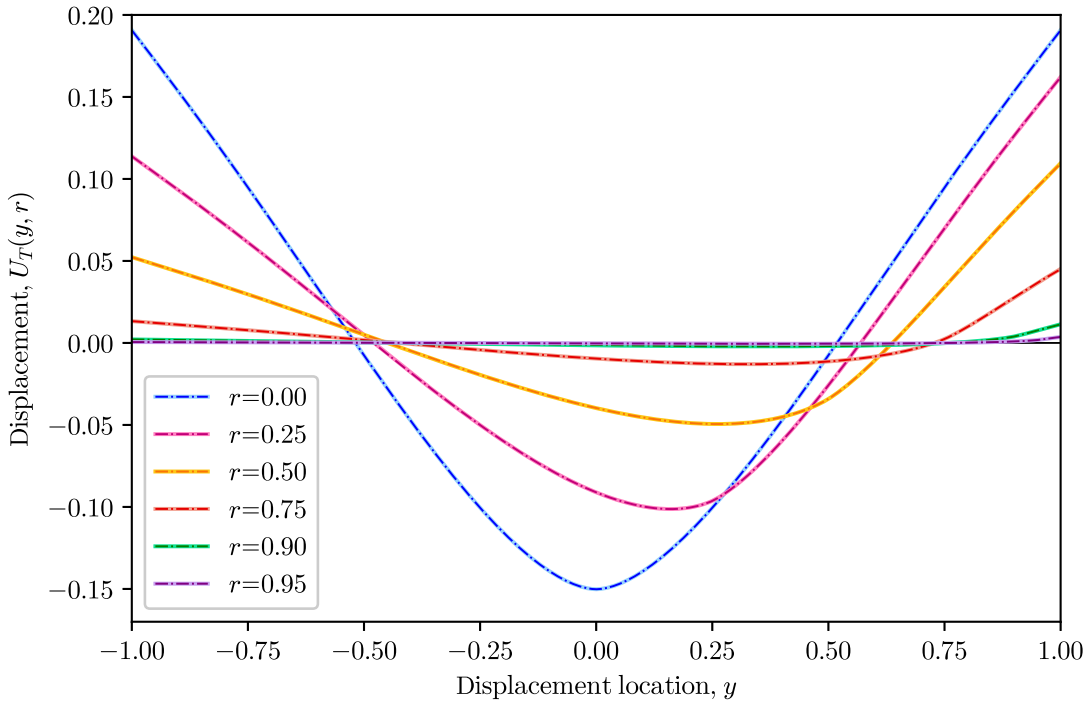

Figure 4.16: Displacement distributions due to triangular loading for various r values: Comparison of numerical results (solid lines) and proposed approximation (dashed lines).

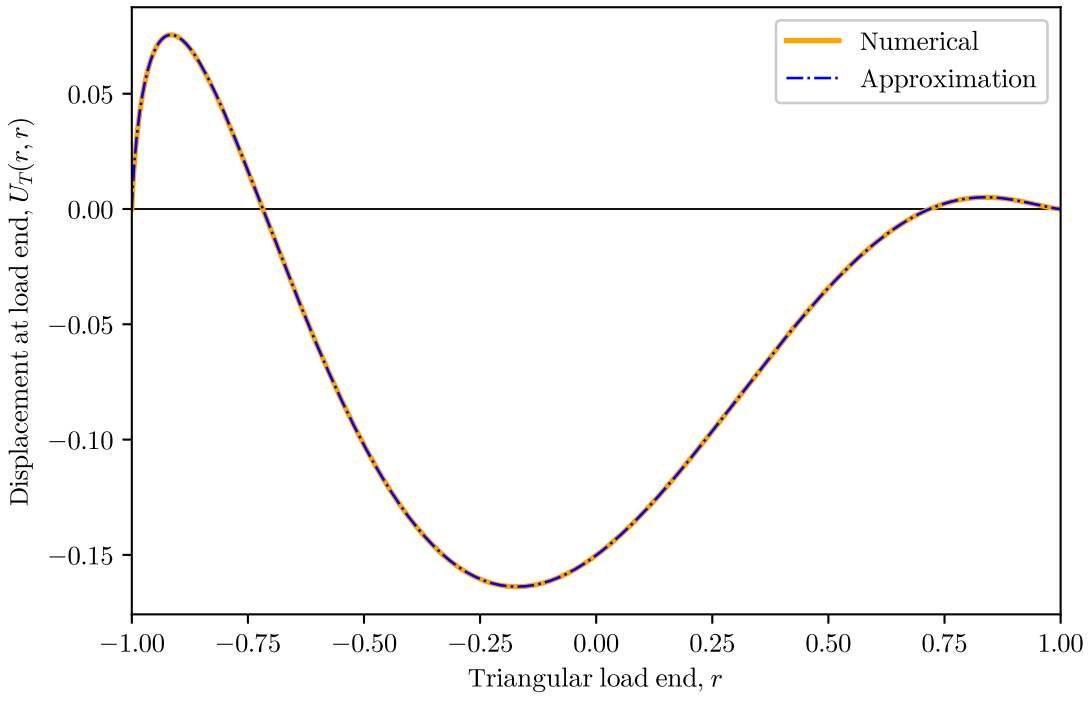

Figure 4.17: Displacement due to triangular loading at $y = r$ for various r values: Comparison between numerical results and proposed approximation.

Considering that the effect of the self-equilibrating stresses vanishes at sections far from the contact area, their contribution can be equivalently examined using the semi-infinite strip model, which is much easier to solve. In terms of the semi-infinite strip problem, and assuming that the contribution of the shear stresses on the normal displacements is negligible compared to the one of the normal stresses (e.g. relatively slender bodies), this means that a suitable normal stress distribution must be found, so that the produced displacement distribution under the corresponding semi-infinite strip end loading is linear.

The aforementioned problem can be stated mathematically as follows: Given a contact length, c of the normal load (meaning that $\sigma = 0$ at $y = -1+c$) and n control points across the contact region, assuming without loss of generality that the stress value at $y = -1$ is $\sigma = 1$, the stresses at the intermediate $n - 2$ points must be determined, so that

$$\frac{u_{i+1} - u_i}{y_{i+1} - y_i} = \frac{u_i - u_{i-1}}{y_i - y_{i-1}} \tag{4.33}$$

for $i = 2, ..., n - 1$, where u_i are the displacements at the control points y_i (Fig. 4.18). This gives us $n - 2$ equations with $n - 2$ unknowns. It is noted that in order for the calculated stresses to be meaningful, they should all have the same sign as the one assumed for $y = -1$.

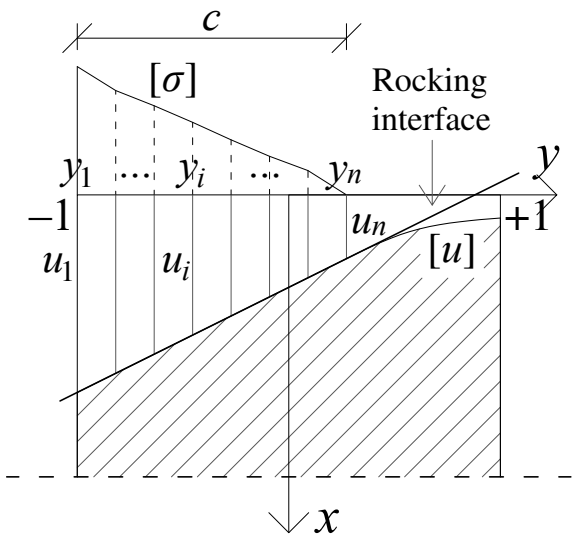

Figure 4.18: Stress distribution acting across the rocking interface, $[\sigma]$, and induced displacement distribution, $[u]$. The displacement distribution under the load must be linear. Only deformations parallel to the load are shown for clarity.

The respective displacements can be calculated numerically in many ways. The numerical method used must take into account that the displacement under the concentrated load is not finite. However, it is helpful that these singularities regarding the displacements do not exist for the rectangular and triangular load cases. The easiest integration scheme is

to consider a rectangular load which has its center at each point y_i and extends until the middle of the distance between neighboring points.

Here, the more accurate decomposition of the stress distribution into a sum of triangular loads is used with the corresponding displacements calculated as stated in Section 4.4. The singularities of the displacement distributions due to a triangular load are removable, thus no problems arise in the numerical solution of the problem.

The first step is to decompose the unknown stress distribution (Fig. 4.19a) into "hat" functions, $H(y)$, that is n functions, each one of which has unit value at a point y_j and zero values everywhere else, with linear transition inside the intervals $[y_{j-1}, y_j]$ and $[y_j, y_{j+1}]$ (Fig. 4.19b). In this way, any piecewise linear stress distribution can be expressed as

$$\sigma(y) = \sum_j \sigma_j H_j(y) \tag{4.34}$$

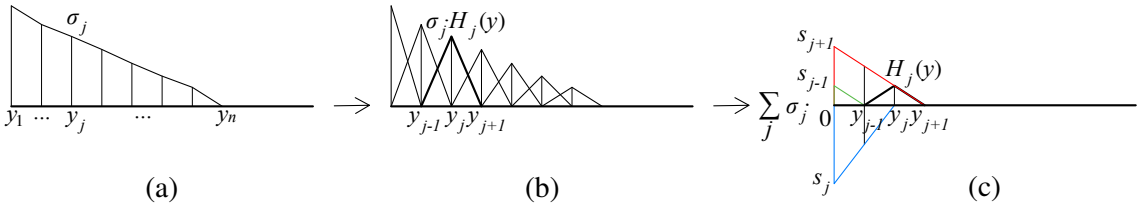

(a) (b) (c)

Figure 4.19: Decomposition of the stress distribution: (a) Original distribution; (b) Decomposition into hat functions; (c) Decomposition of the hat function around y_j into three triangular distributions starting at $y = -1$.

A hat function $H_j(y)$ around point y_j is composed of three linear parts in the interval $[-1, y_{j+1}]$ and thus can be decomposed into three triangular distributions starting at $y = -1$ (Fig. 4.19c). The vector containing the maximum stresses, $\mathbf{S}$, of the triangular distributions ending at points y_j can be proven that is connected to the stress values at points y_j, $\boldsymbol{\sigma}$, through the relationship:

$$\mathbf{S} = \mathbf{H}\,\boldsymbol{\sigma} \tag{4.35}$$

where $\mathbf{H}$ is a $n \times n$ matrix with zero values except for the following entries:

$$\begin{aligned} H_{j-1,j} &= \frac{1 + y_{j-1}}{y_j - y_{j-1}} \\ H_{j,j} &= -\frac{y_j + 1}{y_j - y_{j-1}} - \frac{1 + y_j}{y_{j+1} - y_j} \\ H_{j+1,j} &= \frac{y_{j+1} + 1}{y_{j+1} - y_j} \end{aligned} \tag{4.36}$$

for $j = 1, ..., n$, where fractions containing y_0 or y_{n+1} are ignored.

A new $n \times n$ matrix $\mathbf{U}_t$ is formulated next, whose entry $U_{t,ij}$ refers to the displacement at y_i due to a triangular load with its tip at y_j (meaning a load length of $1 + y_j$) and unit

maximum stress, using the formulas found in Section 4.4. The first column referring to a triangular load with tip at $y = -1$ is set to zero. Then, a new matrix $\mathbf{U}_\sigma$ is produced, whose entry $U_{\sigma,ij}$ refers to the displacement at y_i due to the stress at y_j, which is given by:

$$\mathbf{U}_\sigma = \mathbf{U}_\mathrm{t}\,\mathbf{H} \tag{4.37}$$

Afterwards, a $(n-2)\times n$ matrix $\mathbf{K}$ is formulated, whose entry K_{ij} gives the contribution of the stress at y_j on the difference between the slopes of the intervals $[y_{i+1}, y_{i+2}]$ and $[y_i, y_{i+1}]$, given by

$$K_{ij} = \frac{U_{\sigma,i+2,j} - U_{\sigma,i+1,j}}{y_{i+2} - y_{i+1}} - \frac{U_{\sigma,i+1,j} - U_{\sigma,i,j}}{y_{i+1} - y_i} \tag{4.38}$$

The stress at point $y = -1 + c$ is equal to zero, thus the final column of $\mathbf{K}$ is removed. Furthermore, the stress at the leftmost point, $y = -1$, is assumed to have a unit value. Thus, if the first column of $\mathbf{K}$ is denoted as $\mathbf{K}_0$ and the $n-2$ remaining columns form the matrix $\mathbf{K}_n$, the stresses $\boldsymbol{\sigma}_n$ at the intermediate $n-2$ locations are calculated as the solution of the linear system:

$$\mathbf{K}_n\,\boldsymbol{\sigma}_n = -\mathbf{K}_0 \tag{4.39}$$

After the calculation of the stress distribution, the displacements $\mathbf{u}$ at various locations y_i^* across the whole section due to the self-equilibrating stresses can be calculated as

$$\mathbf{u} = \mathbf{U}_\mathrm{t}^*\,\mathbf{H}\,\boldsymbol{\sigma} \tag{4.40}$$

where $\boldsymbol{\sigma} = [1, \boldsymbol{\sigma}_n, 0]^T$ and $\mathbf{U}_\mathrm{t}^*$ is a matrix whose entry $U_{\mathrm{t},ij}^*$ refers to the displacement at y_i^* due to a triangular load with its tip at y_j and unit maximum stress at $y = -1$, as previously.

Applying this procedure for many values of the contact length, c, the stress distributions shown in Fig. 4.20 are produced, where the corresponding linear stress distributions are also presented in dashed lines. It can be seen that the stress distributions produced are nonlinear and may in reality even contain singularities at points $y = -1$ and $y = -1 + c$. For the limiting case $c = 2$, corresponding to full contact at the base interface, a linear stress distribution develops, as expected, since the technical theory of bending can be used, which predicts linear stresses and displacements across the section by default.

The lever arms produced by exact stress distributions shown in Fig. 4.20 with respect to the center of the section are presented in Fig. 4.22. In the same figure, the lever arm corresponding to a triangular load with the same contact length, c, is also shown for comparison. It can be seen that, generally, the lever arm produced by the exact stress load is lower than the one for triangular load.

Regarding the displacement distribution across the rocking section, the previous stress distributions were calculated so that the displacement profile under the load is linear.

There is, however, no constraint regarding the displacement distribution across the (uplifted) non-contact region of the rocking section, which is nonlinear. This is due to the nonlinearity of the displacements produced by the self-equilibrating stresses, which influence the whole section (Fig. 4.18). The deviation of the displacement distribution of the non-contact region from the linear distribution for various contact lengths, c, is presented in Fig. 4.21, where the distributions have been normalized so that the displacement deviation at $y = 1$ is equal to unity. The shapes of these distributions correspond to the shape of the gap formed between the rocking interface and the body (e.g. across the uplifted non-contact regions at the top and bottom rocking interfaces of Fig. 1.5).

It can be seen that the displacement distribution across the non-contact region is indeed nonlinear, so the assumption of a bilinear displacement distribution composed of two linear segments across the contact and non-contact regions of the rocking interface would be only approximate. This approximation neglects that the displacement distribution must be first-order continuous across the whole section, which is accounted for in the methodology presented in this thesis and reflected on the derived displacement deviation distributions of Fig. 4.21. Interestingly, though, as $c \to 0$, meaning that the rocking body can be considered almost rigid and contact takes place almost at the corner of the rocking body, the displacements across the non-contact region are essentially linear, which agrees with the assumption of non-deformability of a rigid rocking body.

The central displacement, δ_0, and the slope, θ, of the linear displacement distributions under the load produced by the exact stress loadings (Fig. 4.20) are presented in Fig. 4.23. In the same figure, the predictions according to the formulas proposed in Chapter 2 are also presented for comparison. As explained in that chapter, δ_0 and θ are the parameters of the best-fit line that approximates the displacement distribution under a triangular load. It is noted that for a triangular load, the contact length, c_t, and the maximum stress, s_t, for given axial force, N_n, and moment, M_n, at the end section of the semi-infinite strip are:

$$c_\mathrm{t} = 3 \left(1 + \frac{M_n}{N_n}\right) \tag{4.41}$$

$$s_\mathrm{t} = \frac{2N_n}{c_t} = \frac{2}{3} \frac{N_n}{1 + M_n/N_n} \tag{4.42}$$

For compatibility reasons, the results of the two methods are compared for the same axial force and moment acting on the rocking section and the results are presented in terms of parameters c_t and s_t.

It can be seen that the assumption made in Chapter 2 gives very good results. The only discrepancy between the results can be observed for small values of the equivalent contact length, c_t. For such small contact lengths, the numerical solution by Gaydon and Shepherd (1964) does not converge well even for a fairly large number of eigenfunctions used, so the results in Chapter 2 have been extrapolated to cover this area. Furthermore, the

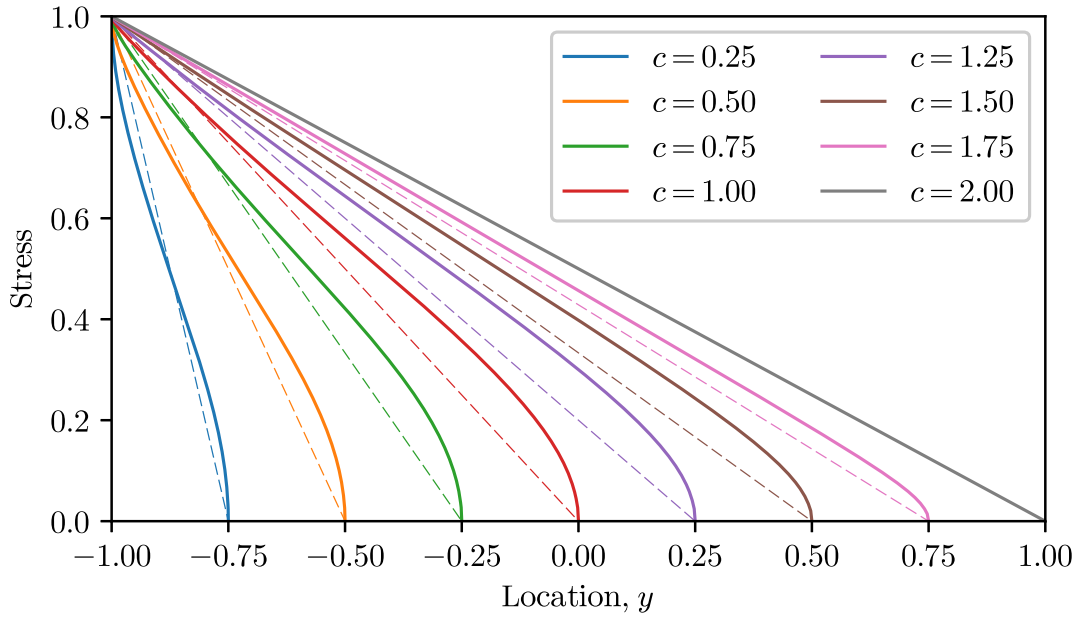

Figure 4.20: Stress distributions for various contact lengths, c, which produce linear displacement distributions under the load. The corresponding linear stress distribution for each contact length is shown with a dashed line.

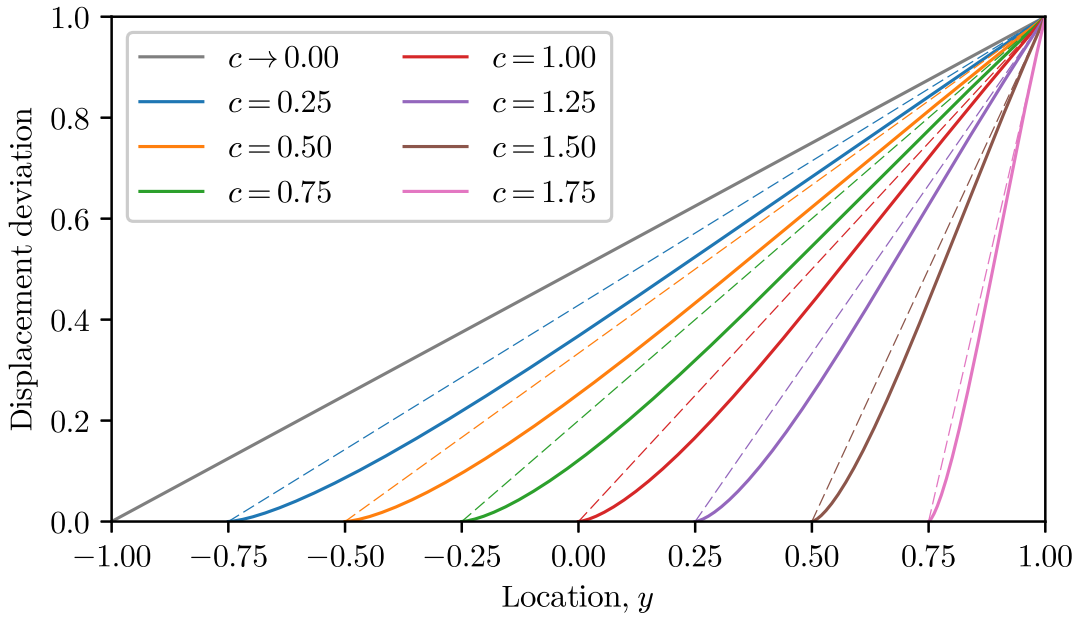

Figure 4.21: Deviation of the displacement distribution across the non-contact region from the linear displacement distribution of the contact region for various contact lengths, c, normalized so that the displacement at $y = 1$ is equal to one. The corresponding linear distribution for each contact length is shown with a dashed line.

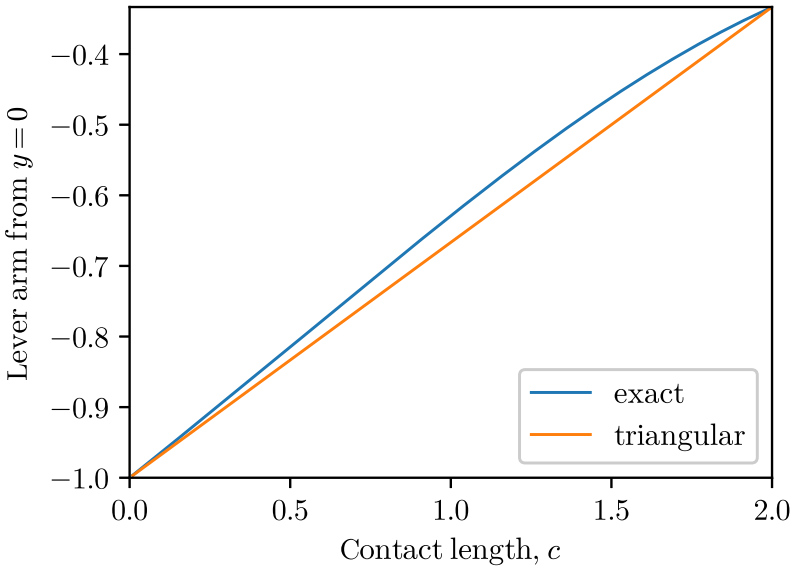

Figure 4.22: Lever arm of exact stress distributions with respect to the center of the section and comparison with that of triangular loads with the same contact length, c.

respective values of the results obtained using the methodology proposed in the present chapter ("exact" distributions) might be sensitive to even small errors included in the proposed approximation functions. Thus, it is difficult to decide on which values are more accurate. Nevertheless, the discrepancy between them is not expected to have a significant effect on practical applications.

It is expected that the establishment of an analytical function for the displacement distribution of the semi-infinite strip under a point load will provide significant help in future works regarding the prediction of the response of deformable rocking bodies.

4.A Analytical expressions for the non-polynomial terms of the displacement integrals

The polynomial terms of Eq. (4.24), that is functions U_{sP} and U_{aP}, are easy to integrate for the derivation of the displacement due to a rectangular or triangular load. The indefinite integrals regarding U_{A} and U_{B} are given here.

$$\begin{aligned} I_{\mathrm{A}} = \int U_{\mathrm{A}}(y,p)\,\mathrm{d}p = 2\,f_1(y,p) - (2y^2p^2 + 5yp - 1)\,p\,f_2(yp)/3 \\ + (1+yp)\,(2yp-1)\,p\,f_2(-yp)/3 + 4yp^2/3 \end{aligned} \tag{4.43}$$

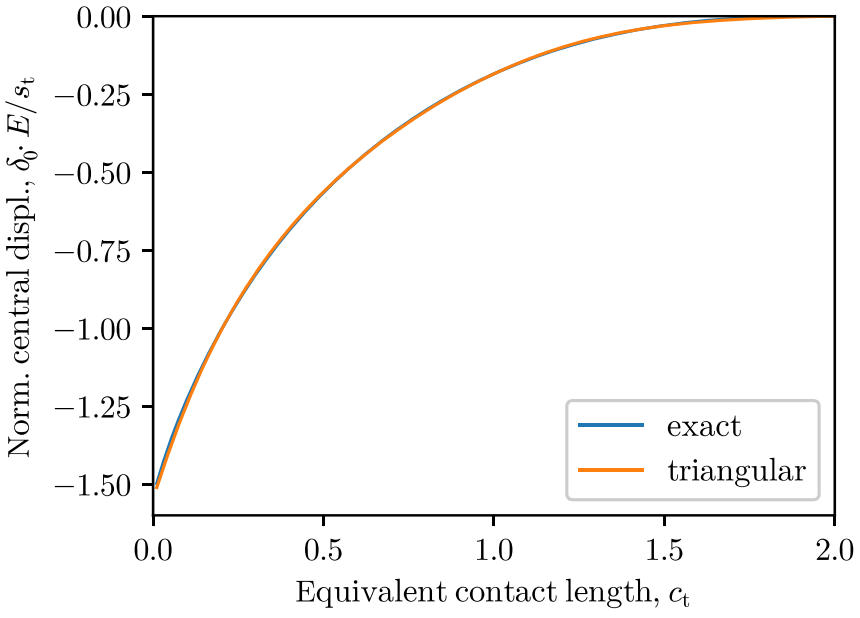

(a)

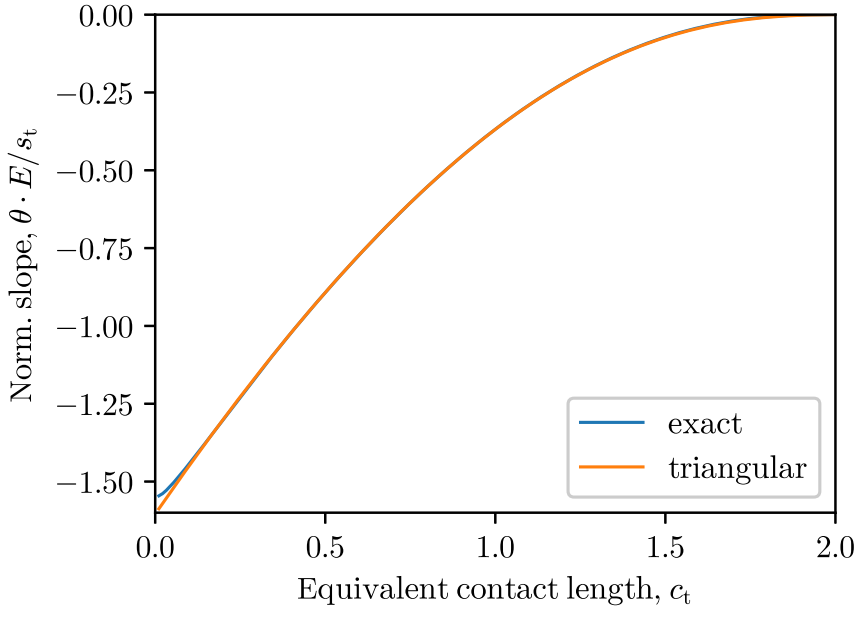

(b)

Figure 4.23: (a) Normalized central displacement and (b) normalized slope of the linear displacement distributions under the load produced by the "exact" stress loads and comparison with the results of equivalent triangular loads with the same axial force and moment. c_t and s_t are the contact length and maximum stress of the equivalent triangular load, respectively, while E is the modulus of elasticity of the member.

$$J_{\mathrm{A}} = \int p\, U_{\mathrm{A}}(y,p)\, \mathrm{d}p = (p+y)\; f_1(y,p) - [(3yp+7) f_1(yp,1) + f_2(yp) + f_3(yp)]\; p^2/6 \\ - [(3yp+1)\; f_1(-yp,1) + f_2(-yp) + f_3(-yp)]\; p^2/6 + yp^3 + p^2/3 - yp \tag{4.44}$$

$$I_{\mathrm{B}} = \int U_{\mathrm{B}}(y,p)\, \mathrm{d}p = -4f_4(y,p) - 2f_5(y,p) + 4f_4(-y,-p) + 2f_5(-y,-p) \\ + 3\,[(1+y)f_1(-y,1) - (1-y)f_1(y,1)]\; p^2/2 + [(1+p)^2 f_1(-p,1) + (1-p)^2 f_1(p,1)]\; y \\ + \ln[(1-y)^2+4]\; (3y^2p - 6yp + 3p - 8)\; p/4 \\ - \ln[(1+y)^2+4]\; (3y^2p + 6yp + 3p + 8)\; p/4 \\ + \ln[(1-p)^2+4]\; (2 - y/2 - 2p + 3yp/2 - 3yp^2/2 + yp^3/2) \\ - \ln[(1+p)^2+4]\; (2 + y/2 + 2p + 3yp/2 + 3yp^2/2 + yp^3/2) \\ + \arctan(y/2 - 1/2)\; (3p+2)\; (y-1)\; p - \arctan(y/2+1/2)\; (3p-2)\; (y+1)\; p \\ - \arctan(p/2 - 1/2)\; [(3y+1)\; (-5 + 2p - p^2) + 8\; (1+y)] \\ - \arctan(p/2 + 1/2)\; [(3y-1)\; (5 + 2p + p^2) + 8\; (1-y)] \\ + 2\; (6\ln(2) - \pi)\; p + 3\; (2\ln(2) + \pi + 1)\; yp^2 \tag{4.45}$$

$$J_{\mathrm{B}} = \int p\, U_{\mathrm{B}}(y,p)\, \mathrm{d}p = -4f_4(y,p) + (1-y)f_5(p,y) - (1+p)f_5(y,p) \\ - 4f_4(-y,-p) + (1+y)f_5(-p,-y) - (1-p)f_5(-y,-p) \\ + [(1+y)\; f_1(-y,1) - (1-y)\; f_1(y,1)]\; p^3 \\ + [(3p-1)\; (1+p)^2\; f_1(-p,1) + (3p+1)\; (1-p)^2\; f_1(p,1)]\; y/4 \\ + \ln[(1-y)^2+4]\; (y^2p - 2yp + p - 2)\; p^2/2 \\ - \ln[(1+y)^2+4]\; (y^2p + 2yp + p + 2)\; p^2/2 \\ + \ln[(1-p)^2+4]\; (-1/3 - p^2 + 15y/8 + 3yp^2/4 - yp^3 + 3yp^4/8) \\ + \ln[(1+p)^2+4]\; (-1/3 - p^2 - 15y/8 - 3yp^2/4 - yp^3 - 3yp^4/8) \\ + \arctan(y/2 - 1/2)\; (2p+1)(y-1)\; p^2 - \arctan(y/2+1/2)\; (2p-1)(y+1)\; p^2 \\ - \arctan(p/2 - 1/2)\; [(y+1/3)\; (-13 + 3p^2 - 2p^3) + 8(1+y)] \\ - \arctan(p/2 + 1/2)\; [(y-1/3)\; (-13 + 3p^2 + 2p^3) - 8(1-y)] \\ + 2\; (2\ln(2) + \pi + 1)\; yp^3 + (6\ln(2) - \pi + 2/3)\; p^2 - 2yp \tag{4.46}$$

The functions $f_1, ..., f_5$ are given in Table 4.2. These functions contain removable singularities at the points given in the table, for which the corresponding limits are given.

Function	Definition	Singularity point	Limit
f_1	$f_1(x,z) = (z-x)\ln\lvert z-x\rvert$	$x = z$	0
f_2	$f_2(x) = \dfrac{(1-x)\ln(1-x)}{x}$	$x = 0$	-1
		$x = 1$	0
f_3	$f_3(x) = \dfrac{1+f_2(x)}{x}$	$x = 0$	$\dfrac{1}{2}$
		$x = 1$	1
f_4	$f_4(x,z) = (1-x)\arctan\left(\dfrac{1-z}{1-x}\right)$	$x = 1$	0
f_5	$f_5(x,z) = (1-z)\ln\left[(1-x)^2+(1-z)^2\right]$	$x = z = 1$	0

Table 4.2: Functions for the calculation of the displacement integrals containing removable singularities.

4.B Incorporation of the rocking interface stress determination procedure into the macroelement algorithm of Chapter 2

In Chapter 2, a macroelement formulation for the prediction of the response of elastic deformable rocking bodies was proposed. In this formulation, the normal stresses developing across the rocking interface are assumed to have a triangular distribution. Since a triangular load does not produce linear displacements (Section 4.4), a best-fit linear approximation of the induced displacements is performed, so that there is compatibility with the observation that the displacement distribution across the loaded region of the rocking interface is linear.

As explained in Section 4.5, this approximation does indeed give very good results (Fig. 4.23). More specifically, given a set of an axial force and moment acting on the rocking end, the central displacement and rotation produced by the equivalent triangular load, whose parameters are calculated using Eqs. (4.41) and (4.42), are in very good agreement with the ones produced by the exact nonlinear stress distribution.

This means, that the macroelement procedure proposed in Chapter 2 does not need to be altered regarding the calculation of the additional displacements produced by the partial loading of the rocking interface. However, if one wants to determine the exact stress distribution acting on the rocking interface at the end of a converged step, the procedure presented in Section 4.5 can be incorporated as follows:

For given axial force, N_{r}, and moment, M_{r}, acting on the rocking end of a member with semi-width b, normalized with respect to the width d, and for n control points across the contact region:

- Calculate the normalized forces referring to the semi-infinite strip dimensions, $N_n = N_{\mathrm{r}}/b$ and $M_n = M_{\mathrm{r}}/b^2$.

- Calculate the lever arm for a stress distribution acting on the left side of the semi-infinite strip end, $r = -|M_n/N_n|$. If $|r| \leq 1/3$, the whole section is loaded with a linear stress distribution and the technical theory of bending applies, otherwise continue to the next steps.
- Estimate the normalized contact length, c, from Fig. 4.22, or from the following approximation:

$$c = 3(r+1) + (10.49 + 41.93r + 74.22r^2 + 63.13r^3 + 20.79r^4)(r+1)(r+1/3) \quad (4.47)$$

- Calculate the coordinates of the control points, $y_j = -1 + c\ (j-1)/(n-1)$, $j = 1, ..., n$.
- Formulate matrix $\mathbf{U}_{\mathrm{t}}$, whose entry $U_{\mathrm{t},ij}$ refers to the displacement at y_i due to a triangular load with its tip at y_j, using Eq. (4.31).
- Formulate matrix $\mathbf{H}$ using Eq. (4.36).
- Formulate matrix $\mathbf{U}_\sigma$ using Eq. (4.37).
- Formulate matrix $\mathbf{K}$ using Eq. (4.38).
- Formulate and solve Eq. (4.39) to determine $\boldsymbol{\sigma}_n$.
- The vector of stresses corresponding to points y_j is $\boldsymbol{\sigma} = [1, \boldsymbol{\sigma}_n, 0]^T$.
- Calculate the axial force of the calculated stress distribution:

$$N_1 = \sum_{j=1}^{n-1} \frac{1}{2}(y_{j+1} - y_j)(\sigma_{j+1} + \sigma_j) \quad (4.48)$$

- Scale the calculated stresses to match the given normalized axial force:

$$\hat{\boldsymbol{\sigma}} = \frac{N_n}{N_1}\, \boldsymbol{\sigma} \quad (4.49)$$

  The stresses corresponding to the normalized semi-infinite strip have the same value as the ones corresponding to the original member with arbitrary semi-width b.
- If $\rho = \mathrm{sign}(M_{\mathrm{r}}/N_{\mathrm{r}})$, the points of action of stresses $\hat{\boldsymbol{\sigma}}$ on the original member rocking end section are $Y_j = -b\ \rho\ y_j$, while the contact length is $C = b\ c$.
- The additional displacements due to the self equilibrating normal stresses at points Y_i^* across the rocking interface are calculated using Eq. (4.40) for $y_i^* = -(\rho/b)\ Y_i^*$ and $\hat{\boldsymbol{\sigma}}$ instead of $\boldsymbol{\sigma}$, which additionally need to be multiplied with (b/E).

It is noted that the determination of the stress distribution inside the member for the calculated stress distribution at the rocking interface is a much more involved process. In order to do so, the maximum stresses of the triangular loads, $\boldsymbol{S}$, are needed, which are calculated using Eq. (4.35) with $\hat{\boldsymbol{\sigma}}$ instead of $\boldsymbol{\sigma}$. Afterwards, the procedure described in

detail in Chapter 2 must be followed for the determination of the stresses inside the body of the member induced by each individual triangular load, all of which must be finally superimposed with the stress distribution predicted by the technical theory of bending for the given resultant forces at the member ends.

5

Modeling of inelastic rocking bodies under cyclic loading

In this chapter, the macroelement formulation for inelastic rocking bodies under cyclic loading is presented. In contrast to the monotonic loading examined in Chapter 3, cyclic loading, which is examined herewith, is much more complex and needs a different treatment.

It should be noted that the formulation presented in this chapter is developed for static analyses. The dynamic motion of rocking members, though, is more complex, since it also involves other motion modes (sliding and upthrow) and requires a suitable treatment of damping, especially during impacts. The proposed formulation herein can serve as the basis for the extension of the macroelement for dynamic analyses; however, the necessary modifications to incorporate the aforementioned phenomena are considerable and will be presented in the following chapter.

5.1 Problem statement

The material of the rocking body is assumed to be elastic-perfectly plastic with Young's modulus E, Poisson's ratio ν and yield stress σ_y, while the same modulus of elasticity is assumed during unloading. As usual practice in beam-column elements, material yielding is assumed only for the normal stresses, due to the increased difficulty of implementing another yielding criterion combining all stresses.

As will be explained in the ensuing, a stress - strain material relationship is not directly used, because inelasticity is introduced in the form of inelastic displacements under constant yield stress. It is also noted that, modifications to account for more complicated material laws are difficult to implement with the proposed formulation, as they would require additional assumptions for the calculation of the inelastic strains.

The main characteristic of rocking bodies is that, in contrast to conventional structural

members, tensile stresses cannot develop across the rocking interface. As a result, little tensile stresses can develop inside the body close to its rocking end. This means that the plastic deformations developing in this area cannot be reversed by sufficient tensile stresses, so they can be considered almost irreversible for the formulation presented herein.

Since tensile stresses cannot develop across the rocking interface, the stress distribution across this interface is nonlinear. However, the technical theory of bending used in usual structural analyses cannot predict such response, meaning that this theory cannot be used for rocking members. As extensively described in Chapter 2, the following approach, based on the more general theory of elasticity, is used instead, which is considered an invaluable tool for the accurate prediction of deformable rocking bodies.

It is reminded that the displacements produced by the nonlinear stress distribution across the rocking interface can be examined by decomposing it into two distributions: (i) A stress distribution according to the technical theory of bending for the given rocking end resultant forces and (ii) Self-equilibrating distributions, which influence the local displacements but do not produce resultant forces and moments (Fig. 4.2).

The self-equilibrating stresses developing near the contact area have no resultant forces and moment, so, according to the Saint-Venant principle, their effect far from the contact area is negligible. This means that the displacement distribution across member sections far from the contact area is almost linear across the element, as predicted by the technical theory of bending (Fig 1.5). Furthermore, the additional displacements induced to the rocking body across the rocking interface by the self-equilibrating stresses can be equivalently calculated as those corresponding to a semi-infinite strip (Fig. 4.1), since this problem is much more easily solved. The semi-infinite strip examined is loaded with self-equilibrating normal and shear stresses across its end ($x = 0, -1 \leq y \leq 1$) and, in contrast to the well-known semi-infinite space, is stress-free at its sides ($y = \pm 1$). The results for the semi-infinite strip loaded with self-equilibrating normal and shear stresses can be easily translated into ones referring to the rocking body, as it will be shown in the ensuing.

Although the theory of elasticity used to solve the aforementioned semi-infinite strip problem can only be rigorously applied to elastic bodies, it would be useful to use it appropriately also for inelastic ones. To this end, the following assumptions are made: (i) The behavior defined previously for the inelastic material is considered as is for the rocking interface, where, however, only compressive stresses can develop (Fig. 5.1). (ii) The stress distributions on the rocking interface produce elastic displacements, $[u_{\text{el}}]$, which are calculated according to the elastic theory of the semi-infinite strip. (iii) Fibers with inelastic behavior or fibers which are stress-free at the rocking interface may develop additional displacements, $[u_{\text{a}}]$, beyond the aforementioned elastic ones. In the case of inelastic behaviour, these additional displacements are negative ($u_{\text{a}} < 0$) and correspond to the additional plastic displacements that develop during the current step, while in the case

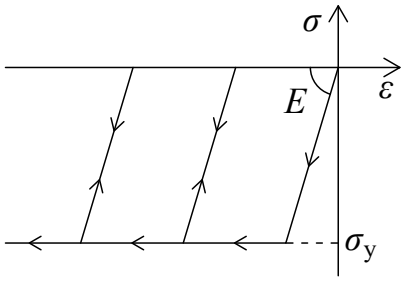

Figure 5.1: Elastic-perfectly plastic material law assumed for the rocking body at the rocking interface, where only compressive stresses can develop.

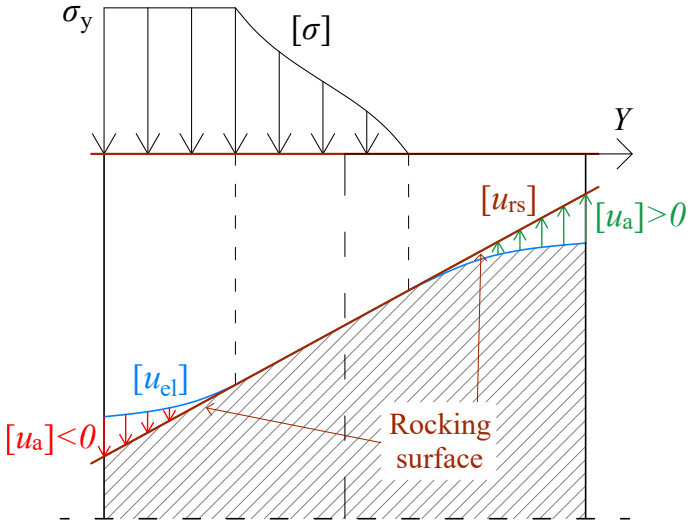

Figure 5.2: Stress distribution acting across the rocking interface and displacements produced across the yielded, elastic and non-contact regions, which match the displacements of the rocking surface.

of stress-free fibers at the rocking interface, which do not belong to the contact region, additional displacements are positive ($u_a > 0$) and correspond to the gaps formed between the body and the rocking interface (Fig. 5.2). It should be noted that, in addition to all of the aforementioned displacements, each fiber may also have a preexisting plastic displacement, $u_{pl,pr}$, from previous steps, which is almost irreversible, as explained above.

For a given linear displacement distribution across the rocking end, $u_{rs}(Y)$, which corresponds to the planar rocking surface (Fig. 5.2) and is determined from the displacements at node j of the element, the stress distribution at the rocking interface has to be determined, so that the following condition holds for each fiber located at Y:

$$u_{el}(Y) + u_a(Y) + u_{pl,pr}(Y) = u_{rs}(Y) \tag{5.1}$$

with

$$\begin{aligned} &u_a(Y) \geq 0, \text{ for regions which are stress-free } (\sigma(Y) = 0) \\ &u_a(Y) = 0, \text{ for regions with elastic response } (\sigma_y < \sigma(Y) < 0) \\ &u_a(Y) \leq 0, \text{ for regions with inelastic response } (\sigma(Y) = \sigma_y) \end{aligned} \tag{5.2}$$

where $u_{\text{el}}(Y)$ is the elastic displacement at Y induced by the normal and shear stresses, $u_{\text{a}}(Y)$ is the additional plastic or gap displacement at Y, depending on the response of the respective fiber at the rocking interface as defined above, $u_{\text{pl,pr}}(Y)$ is the preexisting plastic displacement at Y from previous steps and $\sigma(Y)$ is the normal stress of the fiber located at Y at the rocking end.

Fig. 5.2 shows the original and deformed position of the rocking body and the rocking surface. The shaded area corresponds to the deformed rocking body, where only deformations of the body parallel to the loading are shown for clarity. The normal stresses, $[\sigma]$, as well as the shear stresses, acting across the rocking interface produce elastic displacements, $[u_{\text{el}}]$, which develop across the whole section (in blue), while negative additional (plastic) displacements $[u_{\text{a}}]$ develop across the yielded area (in red) and positive additional ("gap") displacements $[u_{\text{a}}]$ form between the rocking surface and the body across the non-loaded area (in green), so that the total displacements match those of the rocking surface (node j of the element), $[u_{\text{rs}}]$ (in brown). Preexisting plastic displacements are not considered in the figure for simplification.

It should be mentioned that this problem statement does not make the assumption of linear strain distribution across the contact region, which has been proven to be incorrect even for elastic bodies (Chapter 4). As also shown in the next section, this is because such a linear strain distribution produces nonlinear displacements across the contact region, which comes in contrast to the assumption of a planar rocking surface (Fig. 5.2).

In addition, it is evident that only displacements parallel to the deformed member axis are considered in the proposed formulation, while small relative displacements of the individual control points perpendicular to the member axis, for example due to Poisson's phenomenon, are neglected, as is the usual practice in beam-column formulations. Nevertheless, and despite the fact that a planar rocking surface is assumed, some kind of stress singularity may still exist at the corners of the rocking body, as shown in Chapter 4, but does not affect the solution convergence.

Elastic strain and additional displacement distributions

For the numerical solution of the aforementioned problem, the rocking interface is examined in the same coordinate system as the one used for the semi-infinite strip, $-1 \leq y \leq 1$, meaning that coordinates Y of the actual rocking end section are normalized with respect to the semi-width of the member section, b, and is discretized into a number of control points with fixed normalized coordinates, $\mathbf{Y}_w$.

Each of these control points is assigned a stress value, σ, or more conveniently an elastic strain of the rocking body at the rocking interface, $\varepsilon_{\text{el}} = \sigma/E$, as well as an additional displacement, the normalized value of which, with respect to b, is denoted with $\tilde{u}_{\text{a}}$. Eq. 5.2 suggests that these quantities cannot take values independently from each other. Although

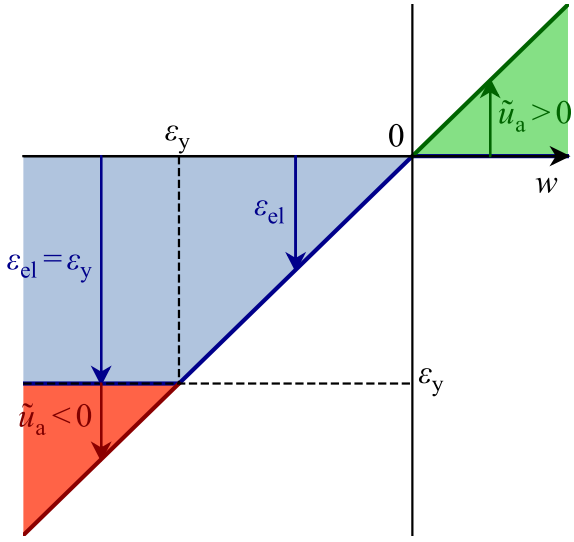

Figure 5.3: Unified representation of both the elastic strain, ε_{el}, (in blue) and the normalized additional displacement, $\tilde{u}_a$, (positive values in green and negative values in red) under variable w: For $w \leq \varepsilon_y$, $\varepsilon_{el} = \varepsilon_y$ and $\tilde{u}_a = w - \varepsilon_y \leq 0$; for $\varepsilon_y < w \leq 0$, $\varepsilon_{el} = w$ and $\tilde{u}_a = 0$, while for $w > 0$, $\varepsilon_{el} = 0$ and $\tilde{u}_a = w > 0$.

the dimensionless quantities ε_{el} and $\tilde{u}_a$ are not directly comparable with each other, a new dimensionless variable

$$w = \varepsilon_{el} + \tilde{u}_a \tag{5.3}$$

is introduced for algorithmic reasons, which represents the sum of the elastic strains and the normalized additional displacements. This variable is able to represent the whole allowable range of ε_{el} and $\tilde{u}_a$ values at each fiber as follows (Fig. 5.3):

$$\varepsilon_{el} = \begin{cases} 0 & \text{, if } w > 0 \\ w & \text{, if } \varepsilon_y < w \leq 0 \\ \varepsilon_y & \text{, if } w \leq \varepsilon_y \end{cases} \tag{5.4}$$

and

$$\tilde{u}_a = \begin{cases} w & \text{, if } w > 0 \\ 0 & \text{, if } \varepsilon_y < w \leq 0 \\ w - \varepsilon_y & \text{, if } w \leq \varepsilon_y \end{cases} \tag{5.5}$$

where $\varepsilon_y = \sigma_y / E$.

The previous relationships express the assumptions in Eq. (5.2) and more specifically (Fig. 5.3):

- if $w > 0$, the fiber does not come in contact with the rocking surface and does not develop an elastic strain ($\varepsilon_{el} = 0$), but only a positive additional ("gap") displacement, $\tilde{u}_a = w > 0$.

- if $\varepsilon_{\mathrm{y}} < w \leq 0$, the fiber behaves elastically, so an elastic strain at the interface develops with $\varepsilon_{\mathrm{y}} < \varepsilon_{\mathrm{el}} \leq 0$ and the additional displacement is zero, $\tilde{u}_{\mathrm{a}} = 0$.
- if $w \leq \varepsilon_{\mathrm{y}}$, the fiber behaves inelastically, so it develops an elastic strain equal to the yield strain, $\varepsilon_{\mathrm{el}} = \varepsilon_{\mathrm{y}}$, and an additional plastic displacement, $\tilde{u}_{\mathrm{a}} = w - \varepsilon_{\mathrm{y}} \leq 0$.

If n_w is the number of control points used, $\mathbf{W}$ is a vector with length n_w, which contains all of the w values and $\mathbf{S}_w$ and $\mathbf{U}_{\mathrm{a}}$ are the same length vectors containing the elastic strains and additional displacements for all control points, respectively. In addition, $\mathbf{U}_{\mathrm{pl,pr}}$ is the vector containing the normalized plastic displacements at the control points retained from previous steps.

5.2 Prediction of elastic displacements for given stress distributions across the rocking interface

Before continuing with the problem treatment, the displacements induced by the self-equilibrating stresses that develop across the rocking interface are derived in this section, which are used next in the proposed algorithm.

Normal stresses

After uplift, the stress distribution across the rocking interface is nonlinear due to its partial loading. As previously mentioned, the effect of such nonlinear loading can be considered by decomposing it into (i) a linear loading as predicted by the technical theory of bending for the resultant forces produced and into (ii) a self-equilibrating load. Regarding the displacements produced by the self-equilibrating part of the normal stresses, the displacement distribution across the rocking interface for an arbitrary stress distribution has to be determined.

This displacement distribution can be more easily calculated for an equivalent semi-infinite strip, as mentioned before. The solution of this problem is presented in Chapter 4, where an analytic expression for the displacements across the member for a concentrated load at an arbitrary location is given, by approximating the numerical results of the methodology proposed by Gaydon and Shepherd (1964). Function $U(y, p)$ (Eq. 4.24), refers to the displacement of the semi-infinite strip at location y for a unit concentrated load at p, normalized with respect to the modulus of elasticity of the body, E.

In the proposed formulation, the normal loads across the rocking interface are decomposed into triangular or trapezoidal loads. As any stress distribution can be considered as the integral of concentrated loads across the load surface, the displacements due to a triangular load with unit negative slope, maximum value at $y = -1$ and load tip at r (Fig.

5.4a) are given by:

$$U_{\text{tr}}(y,r) = r\int_{-1}^{r} U(y,p)\,dp - \int_{-1}^{r} p\,U(y,p)\,dp \tag{5.6}$$

The integrals required in the previous equation are given in Appendix 4.A. Furthermore, the displacements due to a trapezoidal load with constant value between $y = -1$ and $y = r_{\text{l}}$ and unit negative slope between $y = r_{\text{l}}$ and $y = r_{\text{r}}$ (Fig. 5.4b) are given by:

$$U_{\text{trapz}}(y, r_{\text{l}}, r_{\text{r}}) = U_{\text{tr}}(y, r_{\text{r}}) - U_{\text{tr}}(y, r_{\text{l}}) \tag{5.7}$$

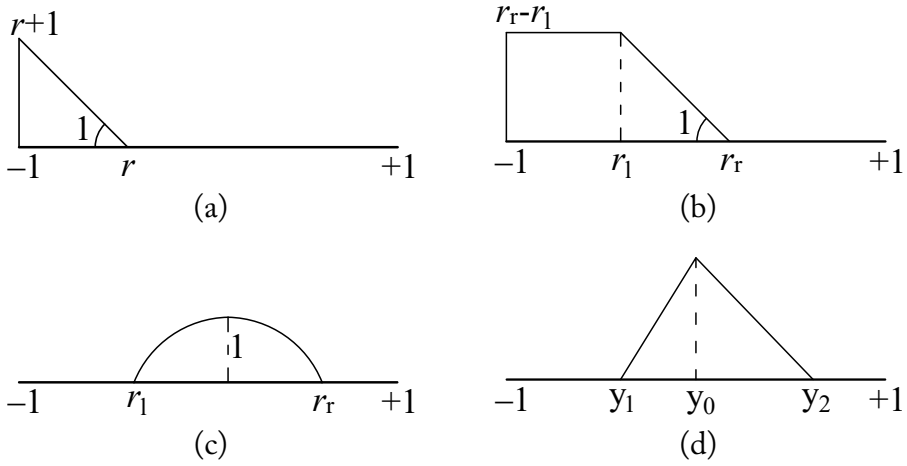

Figure 5.4: (a) Triangular normal load with maximum value at $y = -1$ and slope equal to -1; (b) Trapezoidal normal load with elastic stress boundaries at r_{l} and r_{r} and stress slope between them equal to -1; (c) Parabolic shear load with unit maximum value and boundaries r_{l} and r_{r}; (d) Triangular normal load with maximum value at y_0 and boundaries at y_1 and y_2.

Shear stresses

The real distribution of the shear stresses is unknown, since in reality there is an interaction with the normal stresses and an accurate prediction of its shape requires special solution methods based on the theory of elasticity. However, the contribution of the shear stresses is assumed here to be that of an equivalent parabolic distribution (Fig. 5.4c), independently of the exact normal stress distribution. The normal stress distribution determines the boundaries of the contact region across the rocking interface, r_{l} and r_{r}, which coincide with the the boundaries assumed for the parabolic shear distribution.

Generally, the displacement profile produced by a parabolic shear loading is nonlinear. Nevertheless, for simplicification, this distribution is linearized across the contact region, as in Chapter 2.

In order to calculate the linearized displacements for the self-equilibrating part of the parabolic shear stress distribution, the methodology presented in Chapter 2 is followed,

with the difference that both parabolic distribution boundaries, r_l and r_r, corresponding to the contact region boundaries, need to be considered. For this loading, if τ_m is the maximum shear stress, the shear stress distribution is:

$$\tilde{\tau}(y) = \begin{cases} 0, & \text{for } y \leq r_l \\ \dfrac{4\tau_m}{(r_r - r_l)^2}(r_r - y)(y - r_l), & \text{for } r_l \leq y \leq r_r \\ 0, & \text{for } y \geq r_r \end{cases} \tag{5.8}$$

The terms β_i associated with this distribution, which are necessary for the calculation of the elongation integrals as in Chapter 2 are:

For the symmetric problem (antisymmetric shear distribution):

$$\begin{aligned}\beta_i =& \frac{2\sqrt{2}\tau_m}{\lambda_i^4\,(r_r - r_l)^2}\left[\lambda_i\,(r_r - r_l)\,\left(\frac{\sinh(\lambda_i\,r_r)}{\cosh\lambda_i} + \frac{\sin(\lambda_i\,r_r)}{\cos\lambda_i} + \frac{\sinh(\lambda_i\,r_l)}{\cosh\lambda_i} + \frac{\sin(\lambda_i\,r_l)}{\cos\lambda_i}\right)\right. \\ &\left. - 2\left(\frac{\cosh(\lambda_i\,r_r)}{\cosh\lambda_i} - \frac{\cos(\lambda_i\,r_r)}{\cos\lambda_i} - \frac{\cosh(\lambda_i\,r_l)}{\cosh\lambda_i} + \frac{\cos(\lambda_i\,r_l)}{\cos\lambda_i}\right)\right]\end{aligned} \tag{5.9}$$

and for the antisymmetric problem (symmetric shear distribution):

$$\begin{aligned}\beta_i =& \frac{2\sqrt{2}\tau_m}{\mu_i^4\,(r_r - r_l)^2}\left[\mu_i\,(r_r - r_l)\,\left(\frac{\cosh(\mu_i\,r_r)}{\sinh\mu_i} - \frac{\cos(\mu_i\,r_r)}{\sin\mu_i} + \frac{\cosh(\mu_i\,r_l)}{\sinh\mu_i} - \frac{\cos(\mu_i\,r_l)}{\sin\mu_i}\right)\right. \\ &\left. - 2\left(\frac{\sinh(\mu_i\,r_r)}{\sinh\mu_i} - \frac{\sin(\mu_i\,r_r)}{\sin\mu_i} - \frac{\sinh(\mu_i\,r_l)}{\sinh\mu_i} + \frac{\sin(\mu_i\,r_l)}{\sin\mu_i}\right)\right]\end{aligned} \tag{5.10}$$

The parameters of the derived best-fit line according to this methodology correspond to the central displacement and rotation of the rocking end due to the self-equilibrating shear stress loading.

The results are produced for a unit value of $t = \tau_\mathrm{m}/E$, where τ_m is the maximum shear stress and E is the modulus of elasticity. It is noted that, for simplification of the approximation of the results, only the results for Poisson's ratio $\nu = 0$ are derived here, meaning that only the contribution of the normal stresses inside the element parallel to the member axis on the displacements is considered, since the results for $\nu \neq 0$ do not differ significantly from the ones presented here.

For the approximation of the results, the following two parameters were found to produce a good fit:

$$q = 1 + \frac{r_\mathrm{l} + r_\mathrm{r}}{2} \tag{5.11}$$

$$p = \frac{1 + r_\mathrm{l}}{1 + r_\mathrm{r}} \tag{5.12}$$

which correspond to the distance of the center of the parabolic distribution from $y = -1$ and to the ratio of the distances of the parabolic distribution edges from $y = -1$, respectively. Results are presented only for the cases where $-1 \leq (r_\mathrm{l} + r_\mathrm{r})/2 \leq 0$, or

equivalently $0 \leq q \leq 1$, since the results for $0 < (r_\mathrm{l} + r_\mathrm{r})/2 \leq 1$ are antisymmetric to the former ones, as explained below.

The central displacement and the rocking end rotation are approximated by

$$\delta_{t\mathrm{n}}(r_\mathrm{l}, r_\mathrm{r}) = a_t(p)\left(1 - q^{b_t(p)}\right)^{c_t(p)} \tag{5.13}$$

$$\theta_{t\mathrm{n}}(r_\mathrm{l}, r_\mathrm{r}) = d_t(p)(1-q)^{e_t(p)} + f_t(p) \tag{5.14}$$

respectively, where the individual functions are:

$$\begin{aligned}
a_t(p) &= a_1 + a_2 p + a_3 p^2 \\
b_t(p) &= a_1 + a_2 p + a_3 p^2 + a_4 p^3 + a_5 p^4 \\
c_t(p) &= a_1 (1-p)^{a_2} + 1 \\
d_t(p) &= (1-p)(a_1 + a_2 p + a_3 p^2) \\
e_t(p) &= a_1 + a_2 (1-p)^{a_3} + a_4 p \\
f_t(p) &= a_1 p + a_2 p^2 + a_3 p^3 + a_4 p^4 + a_5 p^5
\end{aligned} \tag{5.15}$$

The aforementioned functions were chosen to approximate the numerical results as well as possible and do not have any physical meaning, while the respective coefficients are given in Table 5.1.

Coeff.	$a_t(p)$	$b_t(p)$	$c_t(p)$	$d_t(p)$	$e_t(p)$	$f_t(p)$
a_1	2.43622225	0.69820019	0.81346044	2.34041769	1.40432262	0.43434583
a_2	-2.38180594	-1.09830807	3.77005753	-1.95923561	0.13024245	3.10747649
a_3	0.70789987	1.92667568		0.89142605	3.65641634	-6.96783698
a_4		-1.12706668			-0.05492961	6.5017201
a_5		0.68886705				-2.28427661

Table 5.1: Coefficients of shear stress loading displacement functions.

In Fig. 5.5, a comparison between the values produced by the numerical solution by Gaydon and Shepherd (1964) and the proposed approximation are presented, showing that the latter gives practically indistinguishable differences in the results.

For the case $0 < (r_\mathrm{l} + r_\mathrm{r})/2 \leq 1$, the displacements are calculated due to antisymmetry from equations:

$$\delta_{t\mathrm{n}}(r_\mathrm{l}, r_\mathrm{r}) = -\delta_{t\mathrm{n}}(-r_\mathrm{r}, -r_\mathrm{l}) \tag{5.16}$$

$$\theta_{t\mathrm{n}}(r_\mathrm{l}, r_\mathrm{r}) = \theta_{t\mathrm{n}}(-r_\mathrm{r}, -r_\mathrm{l}) \tag{5.17}$$

where the parameters $q = 1 - (r_\mathrm{l} + r_\mathrm{r})/2$ and $p = (1 - r_\mathrm{r})/(1 - r_\mathrm{l})$ are used.

5.3 Approximate determination of region boundaries

By assigning a value w at each control point across the rocking interface , elastic strain, $\varepsilon_{\mathrm{el}}$, or additional normalized displacement, $\tilde{u}_\mathrm{a}$, values are assigned to each one. Connecting

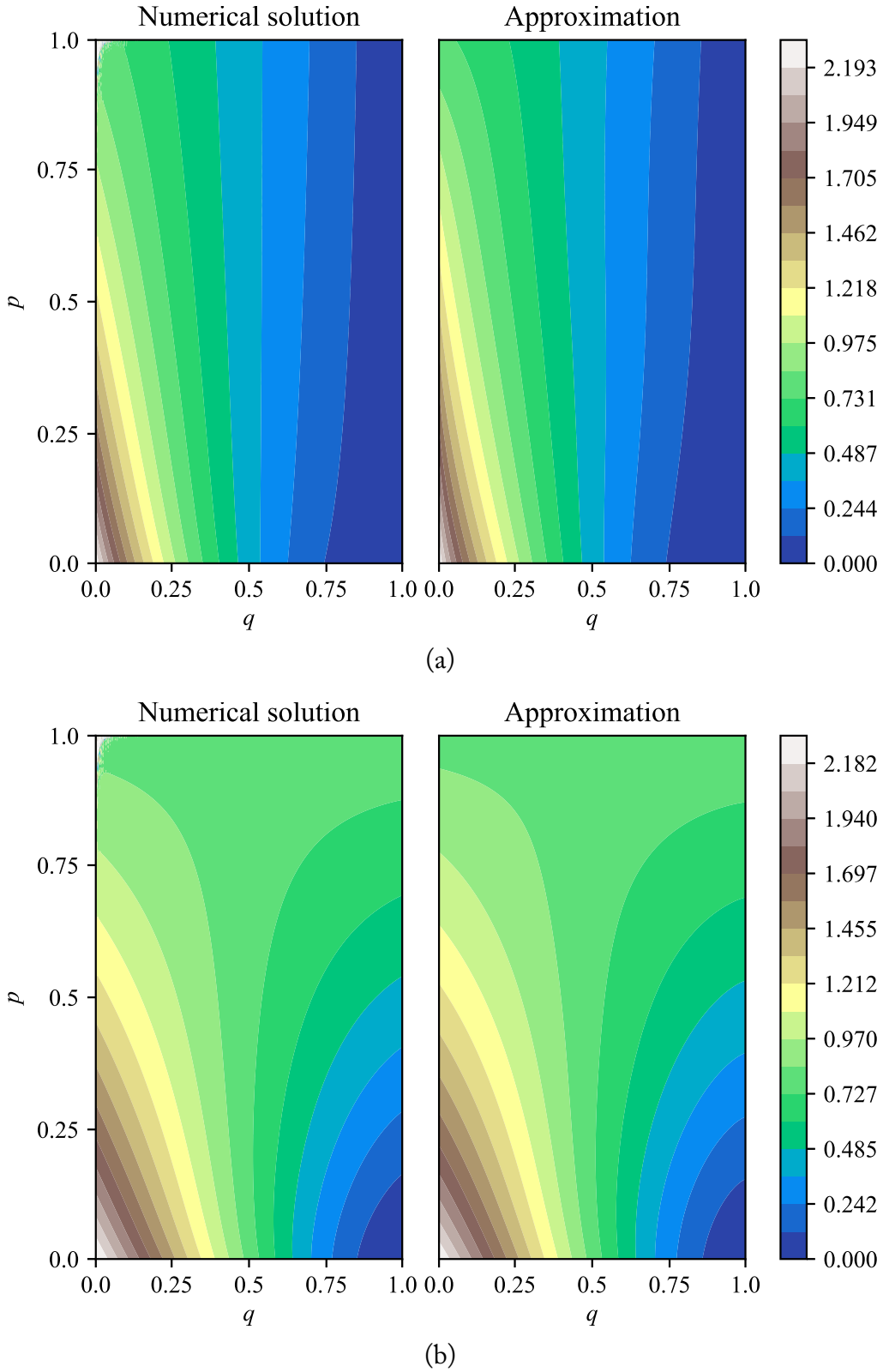

Figure 5.5: Comparison of (a) the central displacement and (b) the rocking end rotation due to the self-equilibrating shear stresses, as given by the numerical solution and the proposed approximation.

these values with linear segments, the corresponding elastic strain and additional displacement distributions across the rocking interface are created (Fig. 5.6). However, it can be seen that this procedure creates regions that develop both elastic strains ($\epsilon_y < \epsilon_{el} < 0$) and additional displacements, which violates the assumptions described previously.

This is why specific points between the respective control points must be chosen, corresponding to boundaries of regions with different behavior, where the additional displacements become zero and the elastic strains become either zero or equal to the yield strain. If such boundary points between regions are not explicitly considered (Fig. 5.6), the accuracy and continuity of the produced forces for given continuous displacements is not ensured, leading for example to non-smooth force-displacement curves, even for dense control point locations and to discontinuous function for the contact zone of the body with the base, leading to numerical problems. In addition, region boundaries may exist between two control points, even though these two points have the same elastic or inelastic response, since existing plastic displacements between them influence the shape of the produced stress distribution.

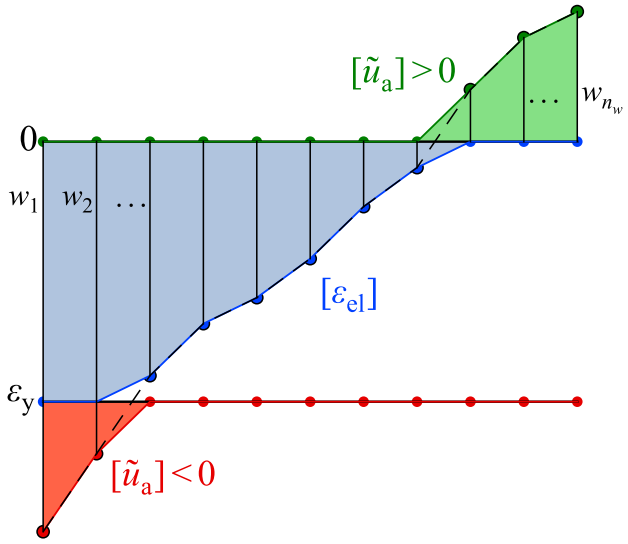

Figure 5.6: Creation of distributions $[\tilde{u}_a]$ and $[\varepsilon_{el}]$ from **W** values. It can be seen that, if explicit region boundaries between control points are not considered, some intervals may develop both elastic strains ($\epsilon_y < \epsilon_{el} < 0$) and normalized additional displacements, $\tilde{u}_a$.

The exact determination of such points is difficult and computationally inefficient, often leading to numerical problems. It should be noted that if the crossings of the linear segments created by the w values with the horizontal lines $w = 0$ and $w = \varepsilon_y$ are used, significant errors are introduced, since the strains and the additional normalized displacements are incomparable quantities, which are unified together under variable w for numerical purposes only.

The accuracy of results between the control points is not of main concern, so an approximate methodology may be chosen, as long as it ensures the consistency and continuity of the produced results. To this end, the region boundaries between two control points are determined on the basis that the total displacement distribution, that is, the sum of the elastic, the additional and the preexisting plastic displacements, is linear inside the interval. The nonlinearities in the displacement distribution in this interval are assumed to be mainly caused by the nonlinearities of the normal stress and the additional displacement distributions in the same interval, while the contribution of the shear stress distribution is assumed to be insignificant.

In order to examine the displacement nonlinearities produced by a nonlinear normal load, let us first consider the extreme case of a concentrated load at a location p with $-1 < p < 1$. For this load, Eq. (4.24) presents a displacement singularity at $y = p$, which originates from the first term of the expression, $U_1 = -2/\pi \cdot \ln|p - y|$, while the rest of the expression is continuous at this point. In fact, U_1 is symmetric about $y = p$, meaning that for symmetric ys about $y = p$, the slopes are opposite, attaining infinitely large values as $y \to p$.

Let us now consider the triangular normal load shown in Fig. 5.4d, with maximum value at y_0 and load boundaries at y_1 and y_2. The displacements produced by this load can be calculated by considering the triangular load as the integral of concentrated loads over the loaded area. This integration removes the singularities of the concentrated load described above. However, as $y_1 \to y_0$ and $y_2 \to y_0$, this triangular load approximates a concentrated load at y_0. So, even for a triangular load, for small $y_1 - y_0$ and $y_2 - y_0$ values, U_1 is considered to be the crucial function for the determination of the displacement nonlinearities in this region.

Taking only the aforementioned function into account, it can be shown that the ratio between the difference of the displacement slopes in the intervals $[y_0, y_2]$ and $[y_1, y_0]$, ΔK_u, and the difference of the elastic strain slopes in the respective intervals, ΔK_ε, is

$$\frac{\Delta K_u}{\Delta K_\varepsilon} = -\frac{2}{\pi}\,\Delta y\;\left[\beta\;\ln(\beta) + (1-\beta)\ln(1-\beta)\right] \tag{5.18}$$

where $\Delta y = y_2 - y_1$ and $\beta = (y_0 - y_1)/\Delta y$. The plot of the function in brackets is shown in Fig. 5.7. It is obvious that parameter β, which practically determines the location of the peak of the triangular load with respect to the total loaded region, influences the result. However, as an approximation, the mean value of the aforementioned function for $\beta \in [0, 1]$, equal to $-1/2$, can be assumed, regardless of the exact location of the maximum elastic strain, therefore:

$$\Delta K_u \approx \frac{\Delta y}{\pi}\,\Delta K_\varepsilon \tag{5.19}$$

The previous equation practically means, that, for a triangular load profile in any interval $[y_1, y_2]$ with zero strain values at the boundaries, the deviation of the shape of the

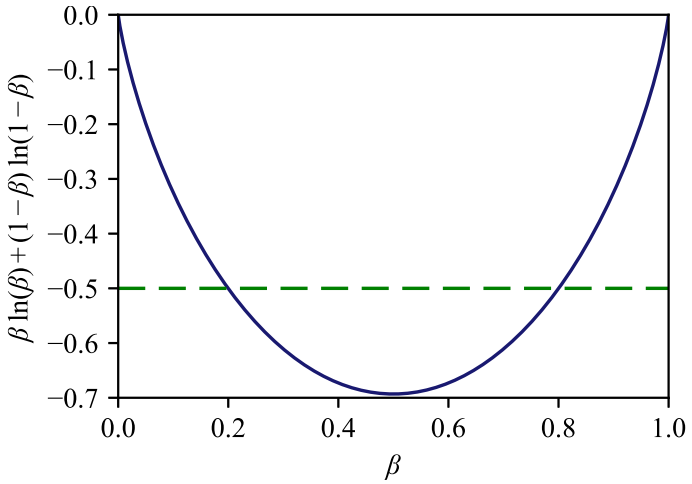

Figure 5.7: Function $\beta\ln(\beta) + (1-\beta)\ln(1-\beta)$ (solid blue line) and its mean value (dashed green line), equal to $-1/2$.

induced displacements from the linear displacement distribution (ΔK_u) can be obtained by multiplying the load profile with $\Delta y/\pi$. By further assuming that the previous remark can be extended to a strain distribution of any shape, a direct relationship between the deviations of the strain and the displacement distributions from the corresponding linear distributions can be established. More specifically, if the values of the strain distribution are multiplied with $\Delta y/\pi$ (Eq. 5.19), the shape of the modified strain distribution inside the interval, $[\varepsilon'_{\text{el}}]$, equals the one of the induced elastic displacements, making the modified strain and additional and plastic displacement distributions directly comparable. Equivalently, modified w' values at the interval boundaries are defined as follows:

$$w' = \begin{cases} w & \text{, if } w > 0 \\ w\dfrac{\Delta y}{\pi} & \text{, if } \varepsilon_{\text{y}} < w \leq 0 \\ w + \varepsilon_{\text{y}}\left(\dfrac{\Delta y}{\pi} - 1\right) & \text{, if } w \leq \varepsilon_{\text{y}} \end{cases} \tag{5.20}$$

so that modified strains are immediately produced for $\varepsilon_{\text{y}} < w \leq 0$, while the additional displacements remain the same for the other two cases.

Let us now consider an interval $[y_1, y_2]$ with values w'_1 and w'_2 at the interval boundaries (Fig. 5.8a), which has no preexisting plastic displacements. For the case shown in Fig. 5.8a, $w'_1 > 0$ and $\varepsilon'_{\text{y}} < w'_2 < 0$, so the left boundary develops a positive additional displacement (gap) and the right boundary develops an elastic strain, meaning that a region boundary must exist between them, for which $w' = 0$. The line connecting the values w'_1 and w'_2 at the interval boundaries crosses the horizontal line $w' = 0$ at y_0. The vertical orange lines in Fig. 5.8a represent the deviation from the linear modified strain distribution (red line). As previously mentioned, it is considered that the linear strain distribution does not produce significant nonlinearities inside the interval; therefore, since modified

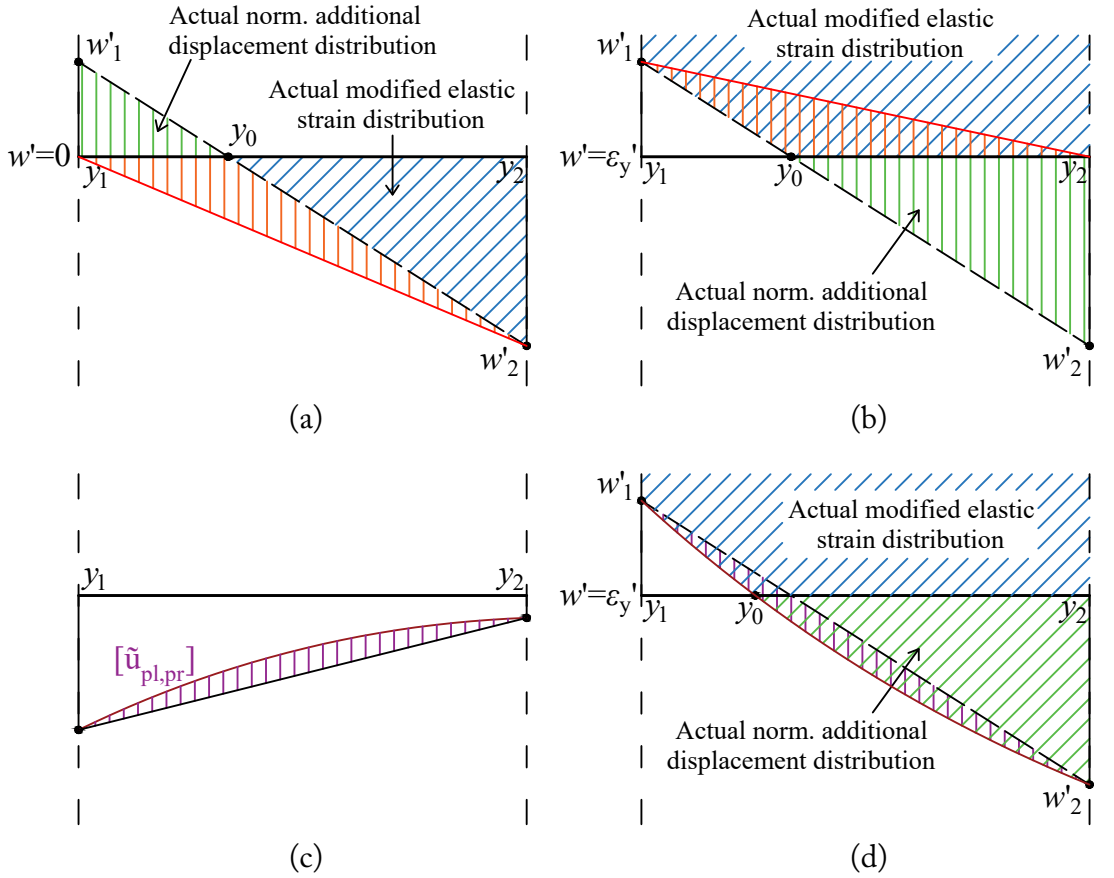

Figure 5.8: Schematic representation of the methodology used to estimate region boundary points and correct region distributions: (a) Interval with $w'_1 > 0$ and $\varepsilon'_y < w'_2 < 0$; (b) Interval with $\varepsilon'_y < w'_1 < 0$ and $w'_2 < \varepsilon'_y$; (c) Preexisting plastic displacement distribution; and (d) modification to account for the preexisting plastic displacements.

strain values are used, the shape produced by the vertical orange lines corresponds to the deviation of the elastic displacements from the linear elastic displacement distribution. However, additional displacements also exist, shown with vertical green lines. The sum of the orange and green displacement distributions is linear, implying that this procedure does not create any deviation of the displacements from a linear distribution. This means that y_0 is indeed the correct region boundary and the distributions shown in Fig. 5.8a with vertical green and slanted blue lines are the actual additional displacement and modified strain distributions, respectively. The same procedure can be applied to any w' combinations at the interval boundaries, such as the case presented in (Fig. 5.8b), where $\varepsilon'_y < w'_1 < 0$ and $w'_2 < \varepsilon'_y$.

If a plastic displacement distribution exists inside the interval from previous steps (Fig. 5.8c), a modification is necessary to account for it. In such a case, the deviant plastic displacement distribution is calculated (vertical purple lines in Fig. 5.8c) and its opposite is then added to the line connecting the interval boundary values to create a new curve (brown curve in Fig. 5.8d), so that the summation of the elastic, the additional and the

preexisting plastic displacements produces a linear displacement distribution. In order to locate the region boundaries and the actual distributions inside the interval, the procedure described previously is applied again, but the aforementioned curve is used instead of the linear one to determine y_0.

From this procedure, it follows that the elastic strain distribution inside each interval is generally nonlinear. The actual elastic strain distribution is calculated by dividing the modified strain distribution found with the previous procedure with $\Delta y/\pi$ (Eq. 5.20). Applying the previous procedure for all intervals across the rocking interface, vectors $\mathbf{S}$ and $\mathbf{Y}_s$ are created, containing the values and coordinates of the actual elastic strain distribution, respectively, for the whole section. Furthermore, the difference between this strain distribution and the linear segment connecting the strain values at the interval boundaries defines additional loads which must be taken into account (e.g. the distribution in vertical orange lines in Fig 5.8a, divided by $\Delta y/\pi$). The opposite of the slopes of this distribution difference, as well as their left and right boundaries are stored in vectors $\mathbf{K}_s$, $\mathbf{Y}_{Ksl}$ and $\mathbf{Y}_{Ksr}$, respectively.

To summarize, the necessary region boundaries and correct elastic strain and additional displacement distributions inside each interval are calculated as follows:

1. Calculate w' at the region boundaries using Eq. (5.20).
2. Draw the line connecting the aforementioned values.
3. Calculate the differences between all linear segments of the plastic displacement distribution with the line connecting the plastic displacement values at the interval boundaries.
4. Add the opposite of the aforementioned deviant distribution to the line of step 2.
5. Determine the region boundaries from the points of the crossings of this curve with the horizontal lines corresponding to $w' = \varepsilon'_{\mathrm{y}} = \varepsilon_{\mathrm{y}}(\Delta y/\pi)$ and $w' = 0$.
6. The regions between the aforementioned horizontal lines correspond to the correct modified strain or additional displacement distributions. The additional loads due to the nonlinearity of the strain distribution are calculated as the difference between the modified strain distribution, divided by $\Delta y/\pi$ (Eq. 5.19), from the line connecting the strain values at the interval boundaries.

It it noted here that due to the existence of plastic displacements, a new region may form inside an interval, although none of the interval boundaries suggests that such a region exists. For example, a common phenomenon during unloading is that decompression does not happen uniformly across the contact region, as one would intuitively think, but

the yielded region remains and translates towards the center of the element. The procedure described above is able to predict such a response, even if this yielded region is formed between two control points behaving elastically.

Furthermore, the ratio between displacement and strain slopes derived above, equal to $\Delta y/\pi$ on average, is much less than unity. On the contrary, if the crossings of the $[w]$ distribution with $w = 0$ and $w = \varepsilon_{\mathrm{y}}$ were used as region boundaries, meaning that the aforementioned ratio would be assumed equal to one, the introduced error would be significant, even if no plastic displacements were present.

5.4 Calculation of displacements for given W values

As described previously, convergence of the algorithm is achieved when the sum of the elastic, the additional and the preexisting plastic displacements equals the values of the given target linear displacement distribution. This equality is checked explicitly only at the control points, $\mathbf{Y}_w$, and implicitly between them, with the procedure described in the previous section for the determination of the region boundaries.

For given $\mathbf{W}$ vector, containing the w values for all control points (Eq. 5.3), the aforementioned displacement contributions are determined. The contribution of the elastic displacements induced by the loading is the most difficult to calculate and originates from three sources: The resultant forces at the rocking interface, the self-equilibrating normal stresses and the self-equilibrating shear stresses. Regarding the other contributions, vector $\mathbf{U}_{\mathrm{a}}$, calculated using Eq. (5.5) for each control point, contains the normalized additional displacements at the control points, while $\mathbf{U}_{\mathrm{pl,pr}}$ contains the normalized plastic displacements induced at the control points from previous steps.

Elastic displacements due to the resultant forces

As already explained, the element is examined in a corotational coordinate system of a simply supported beam. For a conventional elastic member, the relationship between nodal displacements and nodal forces in this coordinate system is (e.g. Przemieniecki, 2012):

$$\mathbf{u}_{\mathrm{r}} = \begin{bmatrix} \dfrac{L}{EA} & 0 & 0 \\ 0 & \dfrac{L}{3EI} + \dfrac{\alpha}{GAL} & -\dfrac{L}{6EI} + \dfrac{\alpha}{GAL} \\ 0 & -\dfrac{L}{6EI} + \dfrac{\alpha}{GAL} & \dfrac{L}{3EI} + \dfrac{\alpha}{GAL} \end{bmatrix} \mathbf{F}_{\mathrm{n}} \tag{5.21}$$

where $\mathbf{u}_{\mathrm{r}} = [\delta_{\mathrm{rf}}, \theta_{1\mathrm{rf}}, \theta_{2\mathrm{rf}}]^T$ is the vector containing the central elongation and the rotations at the two member ends due to the resultant forces, $\mathbf{F}_{\mathrm{n}} = [N, M_1, M_2]^T$ is the vector containing the axial force and moments at the two member ends, E is Young's modulus, G is the shear modulus, A is the area of the member section, I is the moment of inertia

of the member section and α is the shear shape factor with $\alpha \approx 1.2$ for rectangular cross sections (the shear deformations contribution can be neglected by setting $\alpha = 0.0$).

The forces at the rocking end, normalized with respect to the semi-width, b, and the thickness, d, as well as the modulus of elasticity, E, are:

$$N_{\mathrm{n}} = \frac{N}{bdE} \tag{5.22}$$

$$M_{\mathrm{n}} = \frac{M_1}{b^2 dE} \tag{5.23}$$

$$Q_{\mathrm{n}} = \frac{Q}{bdE} = -\frac{M_1 + M_2}{bdLE} \tag{5.24}$$

These normalized forces, $\mathbf{F}_{\mathrm{nn}} = [N_{\mathrm{n}}, M_{\mathrm{n}}, Q_{\mathrm{n}}]^T$, are introduced, so that compatibility with the resultant forces produced by the stresses acting on the coordinate system of the semi-infinite strip ($b = d = 1$) is achieved, where the stresses are also normalized with respect to E.

Using these quantities, the nodal displacements at the member ends due to the normalized resultant forces on the rocking end are calculated as:

$$\mathbf{u}_{\mathrm{r}} = \mathbf{f}_{\mathrm{r}}\, \mathbf{F}_{\mathrm{nn}} \tag{5.25}$$

with

$$\mathbf{f}_{\mathrm{r}} = \begin{bmatrix} \frac{L}{2} & 0 & 0 \\ 0 & \frac{3L}{4b} & \frac{L^2}{4b^2} - \alpha(1+\nu) \\ 0 & -\frac{3L}{4b} & -\frac{L^2}{2b^2} - \alpha(1+\nu) \end{bmatrix} \tag{5.26}$$

Normalized axial force and moment at the rocking end Given the vectors $\mathbf{S}$ and $\mathbf{Y}_s$ of length n_s, containing the values of the elastic strain distribution at the respective coordinates, including those between the control points, the normalized axial force and the normalized moment are given by:

$$N_{\mathrm{n}} = \frac{1}{2} \sum_{i=1}^{n_s - 1} (y_{i+1} - y_i)(s_{i+1} + s_i) \tag{5.27}$$

$$M_{\mathrm{n}} = \frac{1}{6} \sum_{i=1}^{n_s - 1} (y_{i+1} - y_i)(2 s_i y_i + s_i y_{i+1} + s_{i+1} y_i + 2 s_{i+1} y_{i+1}) \tag{5.28}$$

where s_i and y_i are the elements of vectors $\mathbf{S}$ and $\mathbf{Y}_s$.

Normalized shear force at the rocking end Since the self-equilibrating stresses have a local influence on the area near the rocking end according to the Saint-Venant principle, the rotation at node i of the element (Fig. 1.5), which corresponds to the non-rocking end, is unaffected by the self-equilibrating stresses formed at the rocking end. As a result, rotation θ_2 is determined only from the resultant forces of the member ends. Given θ_2, the normalized shear force is calculated from

$$Q_{\mathrm{n}} = \frac{\theta_2 - f_{\mathrm{r},32} M_n}{f_{\mathrm{r},33}} \tag{5.29}$$

where $f_{\mathrm{r},32} = -(3L)/(4b)$ and $f_{\mathrm{r},33} = -L^2/(2b^2) - \alpha(1+\nu)$.

After the calculation of Q_{n}, the first two rows of Eq. (5.25) are used to determine the contribution of the resultant forces to the rocking end displacements, δ_{rf} and $\theta_{1\mathrm{rf}}$. Alternatively, the value of the shear force calculated using Eq. (5.29) can be condensed into Eq. (5.25), so vector $\mathbf{u}_{\mathrm{rf}} = [\delta_{\mathrm{rf}}, \theta_{1\mathrm{rf}}]^T$ can be directly calculated from

$$\mathbf{u}_{\mathrm{rf}} = \begin{bmatrix} f_{\mathrm{r},11} & 0 \\ 0 & f_{\mathrm{r},22} - \dfrac{f_{\mathrm{r},23} \cdot f_{\mathrm{r},32}}{f_{\mathrm{r},33}} \end{bmatrix} \begin{Bmatrix} N_{\mathrm{n}} \\ M_{\mathrm{n}} \end{Bmatrix} + \begin{Bmatrix} 0 \\ \dfrac{f_{\mathrm{r},23}}{f_{\mathrm{r},33}} \theta_2 \end{Bmatrix} \tag{5.30}$$

where additionally, $f_{\mathrm{r},11} = L/2$, $f_{\mathrm{r},22} = (3L)/(4b)$ and $f_{\mathrm{r},23} = L^2/(4b^2) - \alpha(1+\nu)$.

Elastic displacements due to the self-equilibrating shear stresses

If y_{cl} and y_{cr} are the boundaries of the contact zone, as determined by the approximate calculation of the region boundaries, since an equivalent parabolic shear stress distribution is considered between them, the maximum shear stress, normalized with respect to the modulus of elasticity, E, is:

$$t = \frac{3Q_{\mathrm{n}}}{2(y_{\mathrm{cr}} - y_{\mathrm{cl}})} \tag{5.31}$$

For given shear stress distribution boundaries, the parameters $\mathbf{u}_{t\mathrm{n}} = [\delta_{t\mathrm{n}}, \theta_{t\mathrm{n}}]^T$ of the linearized displacements induced to the contact region of the rocking end with normalized semi-width $b = 1$ by a parabolic distribution with $t = 1$ are given by Eqs. (5.13) and (5.14) or Eqs. (5.16) and (5.17). For the value of t calculated using Eq. (5.31), the respective vector containing the displacement parameters due to the self-equilibrating shear stresses is:

$$\mathbf{u}_t = t\ \mathbf{u}_{t\mathrm{n}} \tag{5.32}$$

It is noted here that, using the aforementioned methodology, the contribution of the self-equilibrating shear stresses can be approximately considered for slender rocking bodies only. For squat rocking bodies, e.g. bodies with length approximately equal to their width, the self-equilibrating shear stresses contribution becomes important and, since it usually produces displacements which are of opposite sign to the normal self-equilibrating stresses, convergence problems may occur.

Elastic displacements due to primary self-equilibrating normal stresses

The primary normal strain distribution is the one formed by linear segments between the elastic strains $\mathbf{S}_w$ located at points $\mathbf{Y}_w$. This stress distribution differs from the actual one formed by taking into account the nonlinearities between the control points; however, it is examined separately because the control points remain fixed across the rocking interface. As a result, the following formulation remains unaltered throughout the analysis, meaning that the respective matrices need to be formulated only once, at the beginning of the analysis.

The purpose of the following derivations is to formulate a matrix $\mathbf{V}$, whose entry (i, j) is the elastic displacement induced at location y_i due to a unit elastic strain at location y_j, with the elastic strains at the other control points being equal to zero. In order to derive this matrix, the elastic strain distribution (Fig. 5.9a) is first decomposed into triangular hat loads (Fig. 5.9b). Then, each hat load is decomposed into three triangular loads with maximum values at $y = -1$ (Fig. 5.9c), for which the displacements induced across the section can be easily calculated.

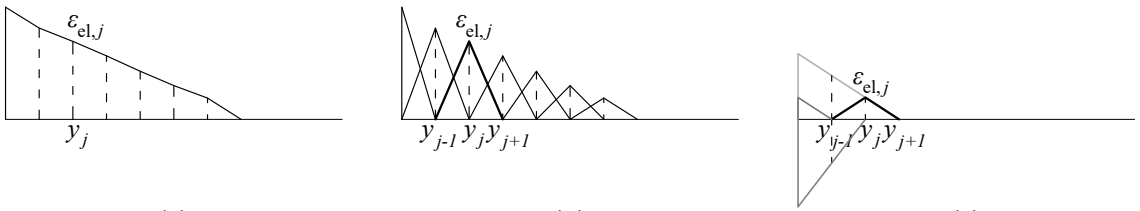

Figure 5.9: (a) Elastic strain distribution; (b) Decomposition into hat triangular loads; (c) Decomposition of each hat load into triangular loads with maximum value at $y = -1$.

More specifically, matrix $\mathbf{H}$ is formulated, whose entry (k, j) refers to the contribution of the elastic strain at y_j to the opposite of the slope of the triangular load with maximum value at $y = -1$ and load tip at y_k. It can be proven that the non-zero entries of this matrix are given by the following expressions:

$$\begin{aligned} H_{j-1,j} &= \frac{1}{y_j - y_{j-1}} \\ H_{j,j} &= -\frac{1}{y_j - y_{j-1}} - \frac{1}{y_{j+1} - y_j} \\ H_{j+1,j} &= \frac{1}{y_{j+1} - y_j} \end{aligned} \tag{5.33}$$

for each $j = 1, ..., n_w$, where fractions containing y_0 and y_{n_w+1} in their denominator are ignored.

In addition, matrix $\mathbf{G}$ is formulated, whose entry (i, k) is the displacement induced at location y_i due to a triangular load of maximum value at $y = -1$ and unit negative

slope (Fig. 5.4a) with load tip at y_k. This matrix is formulated using Eq. (5.6). It is worth noting, that, since the aforementioned triangular loads are produced from the elastic strains and not the corresponding stresses, the displacements of Eq. (5.6), which generally correspond to $E = 1$, are produced directly for the correct modulus of elasticity of the rocking body, E.

Finally, matrix $\mathbf{V}$ is given by

$$\mathbf{V} = \mathbf{G}\ \mathbf{H} \tag{5.34}$$

which remains constant throughout the analysis.

Vector $\mathbf{U}_{e1}$, which contains the displacements at the control points due to the primary normal stresses, is formed during each iteration as:

$$\mathbf{U}_{e1} = \mathbf{V}\ \mathbf{S}_w \tag{5.35}$$

Elastic displacements due to secondary self-equilibrating normal stresses

Apart from the primary normal stress distribution, which is linear between control points, secondary normal stresses need to be taken into account, expressing the nonlinearities of the normal stress distribution between the control points due to region transitions or nonlinear plastic displacements between them.

As mentioned above, vectors $\mathbf{K}_s$, $\mathbf{Y}_{Ksl}$ and $\mathbf{Y}_{Ksr}$ are created during the procedure of the approximate determination of the region boundaries, which contain the opposite of the slopes of the deviant strain distribution, as well as the corresponding left and right interval boundaries.

The displacements induced across the rocking end section for each one of these segments is calculated by multiplying the slope of each segment, k_s, with the displacements at the control points produced by a trapezoidal load with negative unit slope in the elastic region (Fig. 5.4b), which has boundaries y_{ksl} and y_{ksr}, calculated using Eq. (5.7).

Adding the contributions of all elements of vector $\mathbf{K}_s$ on the control point displacements, vector $\mathbf{U}_{e2}$ is created, which contains the displacements at the control points due to the secondary normal stresses.

Target displacements

If $\mathbf{u}_n = [\delta, \theta_1, \theta_2]^T$ is the vector containing the element displacements in the corotational coordinate system, namely the axial elongation, the chord rotation at the rocking end and the chord rotation at the other end, then a new vector $\mathbf{u}_{rs} = [\delta, \theta_1]^T$ is formed, which contains the two first elements of $\mathbf{u}_n$. These are the parameters of the target linear displacement distribution of the rocking surface, which must match the displacements produced by all aforementioned displacement contributions. It may be recalled that the third

element of $\mathbf{u}_{\mathrm{n}}$, which is the chord rotation at the non-rocking end, is satisfied by default, since Eq. (5.29) is used to calculate Q_{n}.

Combination of the control point displacements

Until now, the following vectors regarding displacements have been derived:

- $\mathbf{U}_{\mathrm{e1}}$ and $\mathbf{U}_{\mathrm{e2}}$, which refer to the contribution of the self-equilibrating normal stresses on the displacements of the control points across the semi-infinite strip end.
- $\mathbf{U}_{\mathrm{a}}$ and $\mathbf{U}_{\mathrm{pl,pr}}$, which contain the normalized additional and preexisting plastic displacements of the control points across the semi-infinite strip end.
- $\mathbf{u}_t$, which refers to the contribution of the self-equilibrating shear stresses on the central displacement and rotation of the semi-infinite strip end.
- $\mathbf{u}_{\mathrm{rf}}$, which refers to the contribution of the resultant forces on the central displacement and rotation of the member rocking end.
- $\mathbf{u}_{\mathrm{rs}}$, which refers to the central displacement and rotation of the planar rocking surface.

It is clear that various incompatibilities exist between the aforementioned vectors. First of all, vectors $\mathbf{U}_{\mathrm{e1}}$, $\mathbf{U}_{\mathrm{e2}}$, $\mathbf{U}_{\mathrm{a}}$ and $\mathbf{U}_{\mathrm{pl,pr}}$ contain values referring to the control points, while $\mathbf{u}_t$, $\mathbf{u}_{\mathrm{rf}}$ and $\mathbf{u}_{\mathrm{rs}}$ contain only two values, referring to the central displacement and rotation of the rocking end. In addition, vectors $\mathbf{U}_{\mathrm{e1}}$, $\mathbf{U}_{\mathrm{e2}}$, $\mathbf{U}_{\mathrm{a}}$, $\mathbf{U}_{\mathrm{pl,pr}}$ and $\mathbf{u}_t$ refer to normalized displacements of the semi-infinite strip ($b = 1$), while $\mathbf{u}_{\mathrm{rf}}$ and $\mathbf{u}_{\mathrm{rs}}$ to displacements of the actual member rocking section.

The displacements of the semi-infinite strip due to the self-equilibrating stresses have to be multiplied with b to derive the displacements of the actual member at the respective points (Chapter 2). However, it is more convenient here to examine all displacements in the semi-infinite strip normalized coordinate system, thus, all actual member displacements are divided by b, instead.

Coordinate Y_i across the actual member rocking end section, corresponding to normalized coordinate y_i of the semi-infinite strip, is determined by:

$$Y_i = b\, y_i \tag{5.36}$$

Also, given a central displacement, δ, and a rotation, θ_1, of the rocking end of the actual member, the displacement at point Y_i of the rocking end is given by:

$$U(Y_i) = \delta + Y_i\, \theta_1 = \delta + b\, y_i\, \theta_1 \tag{5.37}$$

Since the conversion of the actual member rocking end displacements into ones compatible with the semi-infinite strip displacements demands that $U(Y_i)$ be divided by b, this is achieved by dividing the term referring to the central displacement by b and leaving the rotation unchanged, while using the normalized coordinates contained in $\mathbf{Y}_w$. Using the previous remark, new vectors $\mathbf{U}_t$, $\mathbf{U}_{\text{rf}}$ and $\mathbf{U}_{\text{rs}}$ are formed, containing displacements for the control points across the normalized rocking end section:

$$\mathbf{U}_t = \mathbf{C}\ \mathbf{u}_t \tag{5.38}$$

$$\mathbf{U}_{\text{rf}} = \mathbf{C}\ \mathbf{B}\ \mathbf{u}_{\text{rf}} \tag{5.39}$$

$$\mathbf{U}_{\text{rs}} = \mathbf{C}\ \mathbf{B}\ \mathbf{u}_{\text{rs}} \tag{5.40}$$

with

$$\mathbf{C} = \begin{bmatrix} 1 & y_{w1} \\ 1 & y_{w2} \\ & \dots \\ 1 & y_{w,n_w} \\ & \end{bmatrix} \tag{5.41}$$

and

$$\mathbf{B} = \begin{bmatrix} 1/b & 0 \\ 0 & 1 \end{bmatrix} \tag{5.42}$$

Finally, the difference between the resultant and the target displacement vectors is defined:

$$\mathbf{U}_{\text{d}} = \mathbf{U}_{\text{e1}} + \mathbf{U}_{\text{e2}} + \mathbf{U}_{\text{a}} + \mathbf{U}_{\text{pl,pr}} + \mathbf{U}_t + \mathbf{U}_{\text{rf}} - \mathbf{U}_{\text{rs}} \tag{5.43}$$

As a sidenote, it is understood that a modification of the macroelement to consider an arbitrary rocking surface displacement distribution instead of a linear one that corresponds to a rigid base surface that remains planar, is a rather simple task: instead of using Eq. (5.40) referring to a linear target displacement distribution, vector $\mathbf{U}_{\text{rs}}$ may be formed using the actual target displacements at each control point across the rocking surface, divided by b.

5.5 Algorithm convergence

The algorithm converges if the norm of $\mathbf{U}_{\text{d}}$ is less than a convergence limit defined by the user. Usually, an iteration procedure is needed, in which a better estimation of $\mathbf{W}$ is derived in each step so that $\mathbf{U}_{\text{d}}$ ultimatelly fulfills the convergence criterion. To this end, the derivatives of all quantities mentioned in the previous section with respect to $\mathbf{W}$ are needed.

These derivatives are not presented here for space reasons, but can be easily derived using the chain rule on every quantity dependent explicitly or implicitly on $\mathbf{W}$. This way, matrix $\partial \mathbf{U}_{\mathrm{d}}/\partial \mathbf{W}$ is formed and a better estimation of $\mathbf{W}$ is given by:

$$\mathbf{W}_{\text{new}} = \mathbf{W}_{\text{prev}} - \left(\frac{\partial \mathbf{U}_{\mathrm{d}}}{\partial \mathbf{W}}\right)^{-1} \mathbf{U}_{\mathrm{d}} \tag{5.44}$$

It is worth noting that, due to the high nonlinearity of the problem, the increment prediction of $\mathbf{W}$ denoted by the second term of the right-hand side of Eq. (5.44) might be so large that the solution is not approached. Thus, if the algorithm does not converge after some iterations, in order for the update of $\mathbf{W}$ to follow better the nonlinearity around the solution, this increment can be reduced using a parameter λ, with $0 < \lambda < 1$, so the previous equation then reads:

$$\mathbf{W}_{\text{new}} = \mathbf{W}_{\text{prev}} - \lambda \cdot \left(\frac{\partial \mathbf{U}_{\mathrm{d}}}{\partial \mathbf{W}}\right)^{-1} \mathbf{U}_{\mathrm{d}} \tag{5.45}$$

After convergence is achieved, the forces and the respective stiffness matrix in the corotational coordinate system are calculated as follows:

The produced forces in the corotational coordinate system, $\mathbf{F}_{\mathrm{n}}$, are calculated by inverting Eqs. (5.22), (5.23) and (5.24):

$$\mathbf{F}_{\mathrm{n}} = bdE \begin{bmatrix} 1 & 0 & 0 \\ 0 & b & 0 \\ 0 & -b & -L \end{bmatrix} \mathbf{F}_{\mathrm{nn}} \tag{5.46}$$

where $\mathbf{F}_{\mathrm{nn}} = [N_{\mathrm{n}}, M_{\mathrm{n}}, Q_{\mathrm{n}}]^T$ is the vector containing the normalized rocking end forces.

The corresponding stiffness matrix is defined as $\partial \mathbf{F}_{\mathrm{n}}/\partial \mathbf{u}_{\mathrm{n}}$. The force vector, $\mathbf{F}_{\mathrm{n}}$, though, is not dependent only on $\mathbf{u}_{\mathrm{n}}$, but also on $\mathbf{W}$, which also changes when vector $\mathbf{u}_{\mathrm{n}}$ does. In order to calculate $\partial \mathbf{W}/\partial \mathbf{u}_{\mathrm{n}}$, it is necessary to calculate $\partial \mathbf{U}_{\mathrm{d}}/\partial \mathbf{u}_{\mathrm{n}}$ by derivating all the quantities using again the chain rule. Then, since the value of $\mathbf{U}_{\mathrm{d}}$ should remain close to zero with a change in $\mathbf{u}_{\mathrm{n}}$, the following equation holds:

$$\frac{\partial \mathbf{W}}{\partial \mathbf{u}_{\mathrm{n}}} = -\left(\frac{\partial \mathbf{U}_{\mathrm{d}}}{\partial \mathbf{W}}\right)^{-1} \frac{\partial \mathbf{U}_{\mathrm{d}}}{\partial \mathbf{u}_{\mathrm{n}}} \tag{5.47}$$

So, finally, the stiffness matrix in the corotational coordinate system is derived as:

$$\mathbf{K}_{\mathrm{n}} = \frac{D\mathbf{F}_{\mathrm{n}}}{D\mathbf{u}_{\mathrm{n}}} = \frac{\partial \mathbf{F}_{\mathrm{n}}}{\partial \mathbf{u}_{\mathrm{n}}} + \frac{\partial \mathbf{F}_{\mathrm{n}}}{\partial \mathbf{W}} \frac{\partial \mathbf{W}}{\partial \mathbf{u}_{\mathrm{n}}} \tag{5.48}$$

Iteration procedure for given nodal displacements The input given to the macroelement by the global finite element framework is the vector of local system displacements, $\mathbf{u}_{\mathrm{e}}$. These are converted to corotational system displacements, $\mathbf{u}_{\mathrm{n}}$, using Eq. (2.1). Afterwards, iterations of the procedure presented above are performed, in order to find the

vector $\mathbf{W}$ that satisfies the convergence criterion, $\mathbf{U}_{\mathrm{d}} \approx \mathbf{0}$. Specifically, given the corotational system displacements of the last committed step, $\mathbf{u}_{\mathrm{n,prev}}$ and the corresponding matrix $\partial\mathbf{W}/\partial\mathbf{u}_{\mathrm{n}}$ (Eq. 5.47), the new estimate of vector $\mathbf{W}$ for the next step is given by:

$$\mathbf{W}_{\mathrm{new}} = \mathbf{W}_{\mathrm{prev}} + \frac{\partial \mathbf{W}_{\mathrm{n}}}{\partial \mathbf{u}_{\mathrm{n}}} \left(\mathbf{u}_{\mathrm{n}} - \mathbf{u}_{\mathrm{n,prev}}\right) \tag{5.49}$$

After convergence of $\mathbf{W}$ is achieved, the force vector $\mathbf{F}_{\mathrm{n}}$, and the stiffness matrix, $\mathbf{K}_{\mathrm{n}}$, in the corotational coordinate system are calculated using Eqs. (5.46) and (5.48), respectively. The output of the macroelement to the general finite element framework are the local system forces, $\mathbf{F}_{\mathrm{e}}$ (Eq. 2.3), and the local system stiffness matrix, $\mathbf{K}_{\mathrm{e}}$ (Eq. 2.5).

After convergence of the whole model containing the rocking macroelement when a condition demanded by the finite element framework is achieved (e.g. the displacement at a node equals a given value), the current state of all the elements contained in the model is saved. For the rocking macroelement, this means that the normalized additional plastic displacement distribution across the rocking interface, $[\tilde{u}_{\mathrm{a}}] < 0$, calculated during the determination of the region boundaries (e.g. Figs. 5.8b and d) at the current step, must be added to the existing normalized plastic displacement distribution, $[\tilde{u}_{\mathrm{pl,pr}}]$, so that the next step begins with the actual plastic displacements induced to the element until then.

5.6 Examples

In this section, the response of three rocking body configurations is examined using the proposed macroelement formulation.

Rocking body with constant vertical force

The response of a solitary rocking body with a constant vertical force on its top side (Fig. 5.10) is examined in this example. The rocking body has height $H = 4$ m, width $B = 1$ m and thickness $d = 1$ m, modulus of elasticity $E = 30$ GPa and yield stress $\sigma_{\mathrm{y}} = 20$ MPa and is loaded on its top with a vertical force $N = -2500$ kN. The whole body is modeled using one macroelement with its rocking end (node *j*) at the bottom.

In Fig. 5.11, the loading - unloading curves (horizontal displacement, δ_x, versus applied horizontal force, P_x) are shown for varying number of control points, n_w, used in the analysis. It can be seen that even the model with only 11 control points (red line) produces results that are very close to more dense control point configurations, meaning that the proposed algorithm can capture well the actual stress and displacement distributions between control points.

In Fig. 5.12, the elastic strains (blue curves) and plastic displacements (red curves) at the base of the member at several steps during loading - unloading of the first half-cycle are presented. It can be seen that gradually the element yields, starting to develop plastic

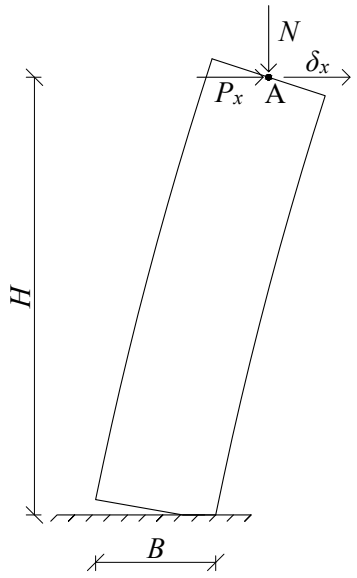

Figure 5.10: Rocking body with constant vertical force.

displacements, before reaching the maximum displacement of the quarter-cycle, where the elastic strain distribution becomes almost rectangular.

Interesting to note that, contrary to what one would imagine, i.e. that the whole contact region would decompress during motion reversal, the actual response is totally different: The element continues to yield while returning to its original position, with the yield strains gradually moving towards the center of the element, before becoming elastic again. This means that the formation of plastic displacements does not stop at the maximum displacement, but continues during unloading at regions a little further from the base edge. This can be seen more clearly in Fig. 5.13, where the plastic displacement distributions that develop across the rocking interface at characteristic quarter-cycles during the cyclic loading are presented. The formation of the plastic displacements described in Fig. 5.12 is also presented in the first two plots of Fig. 5.13. In a similar manner, plastic displacements continue to develop for the remaining cycles of the analysis.

Structural configurations with restrained rocking members

The ability of the proposed macroelement to predict realistically the response of restrained rocking bodies is discussed in the ensuing.

First, a rocking concrete wall which is tendon restrained is examined and more specifically the model SRW-B examined in Twigden et al. (2017). In brief, the rocking wall has height $H = 2.86$ m, width $B = 0.8$ m and thickness $d = 0.125$ m and is restrained with three prestressed tendons located at the center and about 0.2 m from the center. Regarding the material properties, concrete strength is $f_c = 35.0$ MPa, its modulus of elasticity is assumed $E_c = 4700\sqrt{f_c} = 27.8$ GPa, while each tendon has stiffness $EA_t = 28529.0$

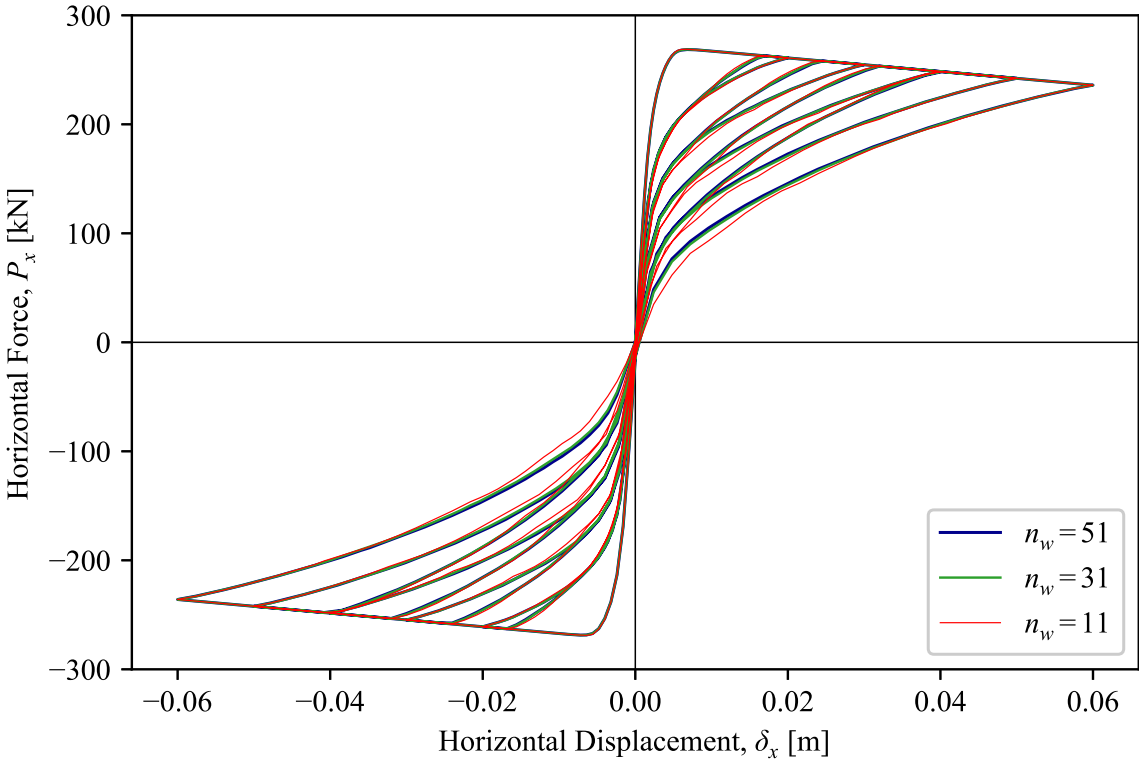

Figure 5.11: Rocking body with constant vertical force: Horizontal displacement versus applied horizontal force curves for various number of control points, n_w, used.

kN/m and initial prestress 96.1 kN, which is reduced to 89.1 kN due to prestress losses equal to 7.3%. As mentioned in the paper, the sum of the tendon forces is further reduced with respect to the expected value, approximately following the simplified analysis by Aaleti and Sritharan (2009), as the lateral displacement increases. For this reason, in the present analysis, the tendon stiffness is calibrated so that the sum of the tendon forces at the maximum lateral displacement matches the one measured at the experiment (about 440 kN). Additional weight is added on top of the wall equal to 31.35 kN, while the self-weight of the wall equals 7.15 kN. In order to apply the self-weight at the center of the wall, the wall is modeled using two elements: one rocking macroelement for the lower part, with its rocking end (node *j*) at the bottom, and one conventional element for the upper part.

The experimental response of wall SRW-B is presented in Fig. 5.14a*, while the results produced by the model which includes the proposed macroelement with the aforementioned properties is shown in Fig. 5.14b. It can be seen that the results obtained with the proposed algorithm match very well the experimental backbone curve. A notable discrepancy between the results can be seen during unloading for large displacements, where the experimental curve does not pass close to (0,0) as in the numerical analysis and contrary to what one would expect for typical rocking systems. According to Twigden et al. (2017),

*The author would like to thank Prof. R. Henry for providing the experimental data.

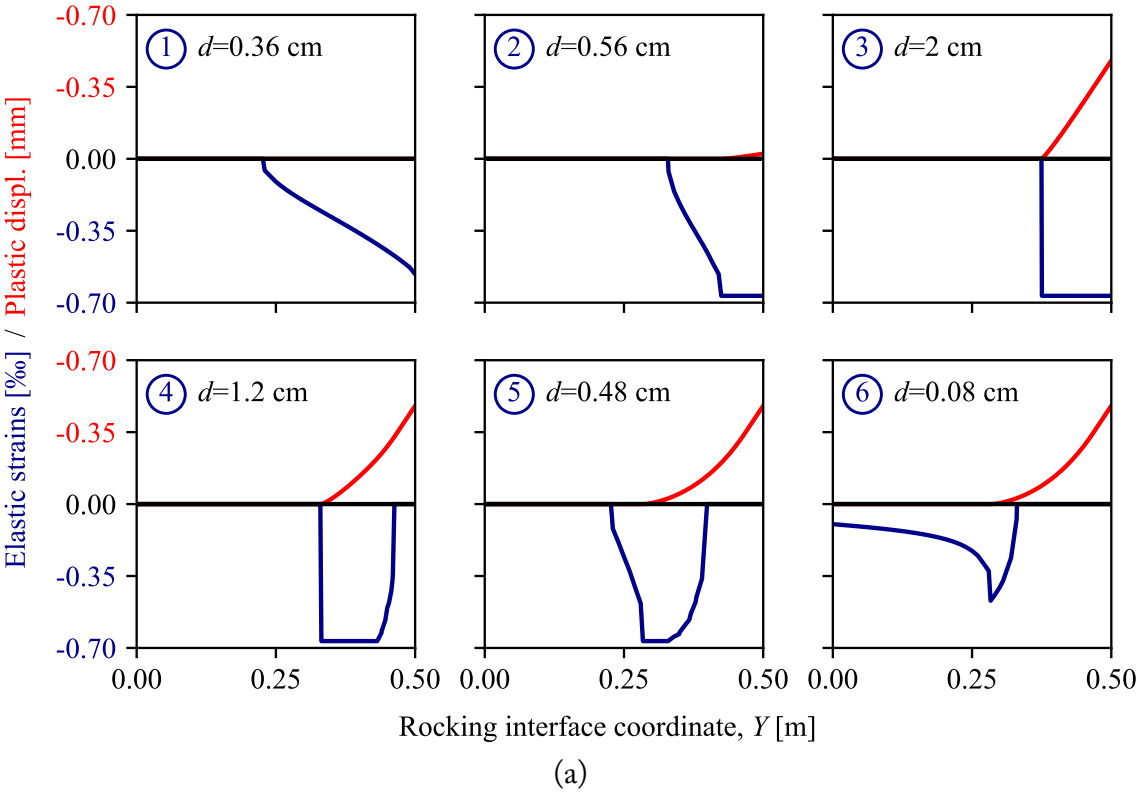

(a)

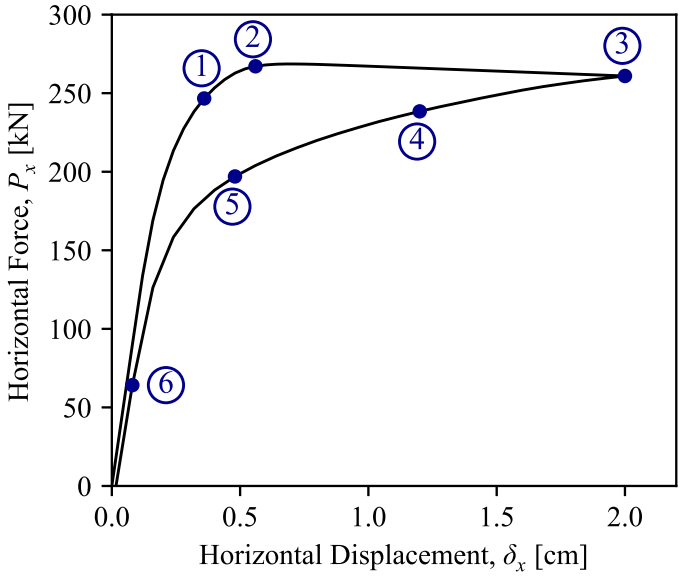

(b)

Figure 5.12: (a) Elastic strains (blue curves) and plastic displacements (red curves) developing on the rocking interface before the end of the first half-cycle, where yielding occurs. The right half of the element section is shown. (b) Corresponding points on the loading - unloading curve.

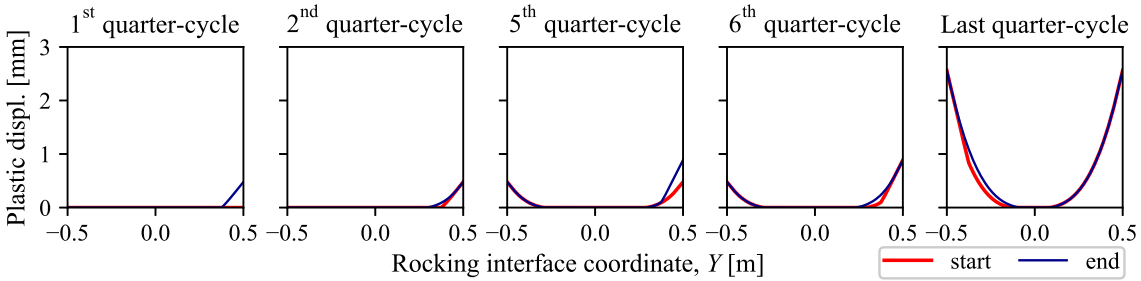

Figure 5.13: Plastic displacement distributions across the rocking interface at characteristic quarter-cycles during the cyclic loading. The distribution at the beginning of each quarter-cycle is shown in red and at the end in blue. Different scales are used for the horizontal and the vertical axes.

this can be attributed to several reasons, such as prestress loss, debris underneath the wall or damage near the wall toes. It should be also noted that an armouring steel base frame was positioned under the wall and foam strips were used under the concrete rocking edges, so that local concrete spalling could be avoided, influencing the wall response.

The second restrained rocking member configuration examined is the calcium-silicate brick masonry wall EC COMP 1 investigated experimentally in Graziotti et al. (2016), which exhibited mainly flexural behaviour. The masonry wall specimen under consideration has height $H = 2.75$ m, width $B = 1.1$ m and thickness $d = 0.102$ m. Regarding material properties, accoring to the paper, the masonry ultimate strength, f_{m}, was equal to 6.20 MPa. However, a smaller value is used here for the yield strength, $f_{\mathrm{y}} = 4.0$ MPa, as a mean value for the bilinearized material response. The modulus of elasticity of masonry is taken equal to $E_{\mathrm{m}} = 4.2$ GPa. An applied vertical load equal to 58.34 kN is considered, while the self weight is taken equal to 5.71 kN. The rotation of the wall is restrained at its top edge, but no restraining along the vertical axis is applied according to the paper; however, some kind of such restraining should exist, as evident from the ascending post-rocking backbone curve. A vertical spring with $k_{\mathrm{s}} = 3500$ kN/m is assumed in order to model this behavior. It should be noted that, since both ends of the member are expected to detach from their bases and develop damage in this configuration, the specimen is modeled using two macroelements, with their rocking ends (nodes j) at the top and the bottom of the specimen and their non-rocking ends (nodes i) joined in the middle.

The experimental results of wall EC COMP 1 are shown in Fig. 5.15a[†], while the results produced with the proposed macroelements are plotted in Fig. 5.15b. The experimental response, however, shows a large hysteresis at later cycles that cannot be explained for purely rocking response and, evidently, cannot be captured by the proposed macroelements. Fig. 5.15 shows that, in general, the model with the proposed macroelements can predict the response adequately, with discrepancies concerning the reloading-unloading curves, especially at later cycles, due to the aforementioned unexpected hysteretic be-

[†]The author would like to thank Prof. F. Graziotti for providing the experimental data.

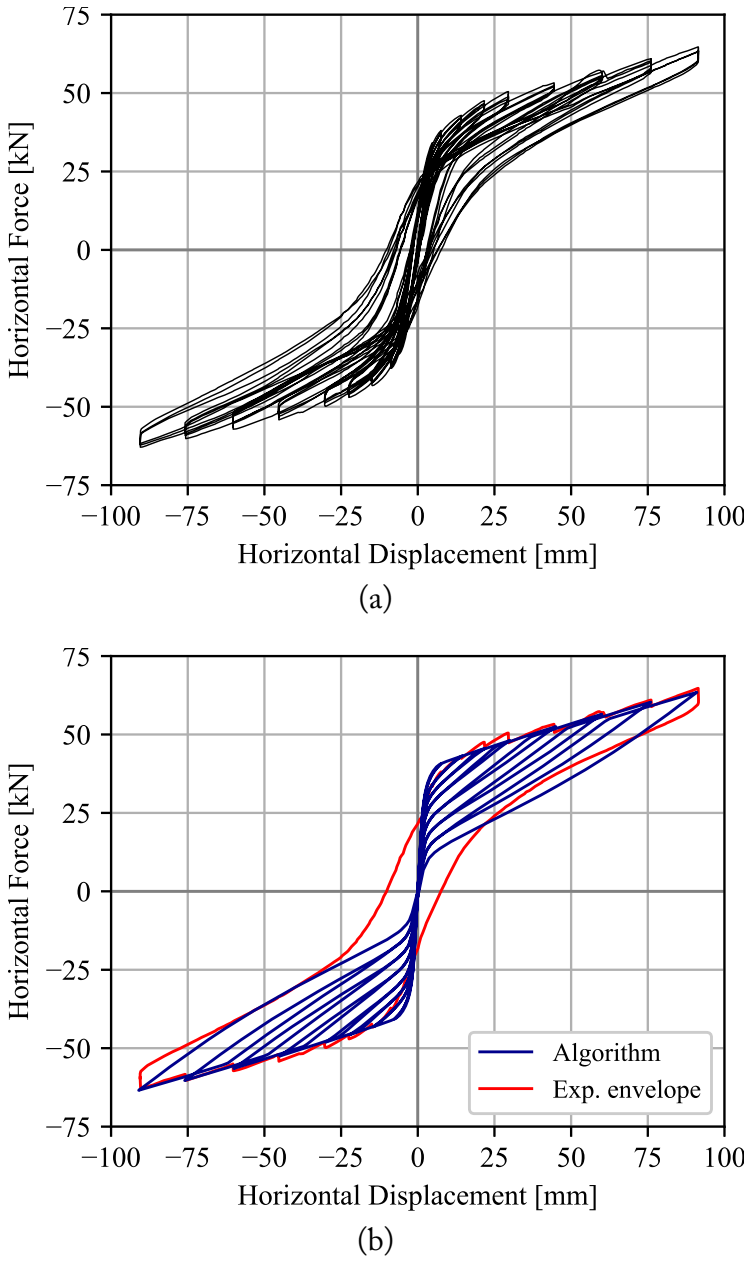

Figure 5.14: (a) Experimental loading - unloading (force - displacement) curves for cyclic response of member SRW-B (Twigden et al., 2017); (b) Response according to the proposed algorithm (in blue) and comparison with the envelope of the experimental response at the last cycle (in red).

haviour observed during the tests.

From the previous examples it can be seen that, although the bilinear material model assumed for the macroelement cannot account for the precise material response, such as that of concrete or masonry, the main characteristics of the cyclic response can be adequately predicted. Thus, the proposed macroelement can be used for a quick and adequately accurate estimation of the response of structural systems with rocking members.

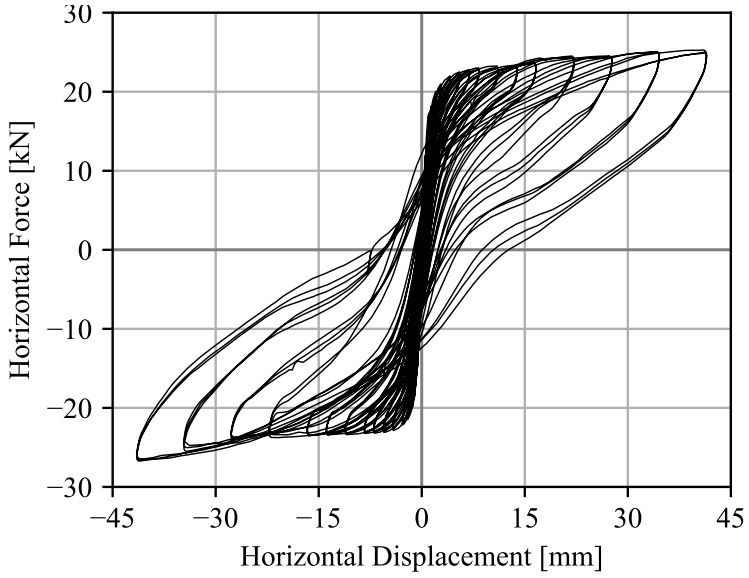

(a)

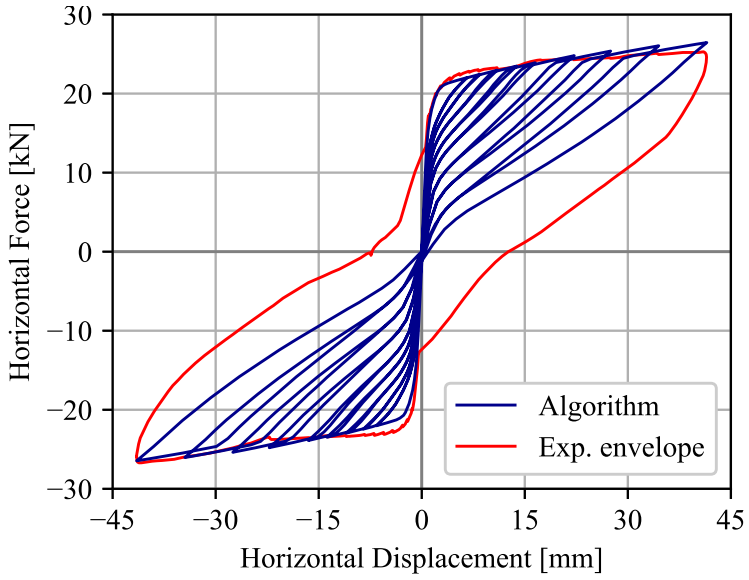

(b)

Figure 5.15: (a) Experimental loading - unloading (force - displacement) curves for cyclic response of member EC COMP 1 (Graziotti et al., 2016); (b) Response according to the proposed algorithm (in blue) and comparison with the envelope of the experimental response at the last cycle (in red).

Comparison with corresponding models containing elastic or rigid rocking bodies

In order to assess the implications of not considering the material inelasticity of the rocking body or even the rocking body deformability altogether, the results produced by the macroelement for the previous examples are compared with results for corresponding models considering the rocking body to be elastic (by setting a very large σ_y value) or

the rocking body to be rigid (by additionally setting a very large E value).

The results are presented in Fig. 5.16, where it can be seen that, apart from the fact that the elastic and rigid models do not present any hysteresis, there are also notable differences between the backbone curves produced for an inelastic, an elastic and a rigid rocking body. Regarding the differences between the inelastic and the elastic response, it can be seen that the inelastic one may attain considerably lower force values in the post-rocking branch, as expected, especially for larger displacements. However, there are also noteworthy differences between the responses of the elastic and the rigid body. Obviously, these differences are larger at the pre-rocking branch of the elastic body response, however in the case of restrained rocking bodies (cases (b) and (c) in Fig. 5.16), this discrepancy continues even after rocking initiates.

The previous comparisons underline the importance of appropriately taking into account the deformability and inelasticity of the rocking body in applications where large axial forces are expected, such as tendon- or beam-restrained rocking body configurations. The proposed macrolement is particularly suitable for the analysis of such cases, whose accurate analytical modeling is very difficult.

5.A Appendix: Alternative method based on quadratic programming optimization

In this Appendix, an alternative formulation is presented for the solution of the problem of the determination of vector $\mathbf{W}$, that is the elastic strains and additional displacements at the rocking interface. Instead of considering region boundary points between control points as a function of $\mathbf{W}$, these boundary points are considered the main variables of the problem, while the values of the stresses or additional displacements in between are considered secondary ones, instead. These stresses or additional displacements need to obey specific inequalities as before, depending on the region they belong to. In fact, given the region boundaries, the calculation of the region internal values can be formulated as a quadratic programming optimization problem, which can be easily solved using existing algorithms: The values of the stresses and additional displacements inside the regions need to be determined, adhering to the respective constraints, which minimize the distance between the produced and the linear target displacement distributions.

Despite the mathematical convenience of such a formulation, it is not chosen as the main formulation of the proposed algorithm, since it leads to many problems: Firstly, it is computationally taxing, since it requires the calculation of second order derivatives and additionally all the quantities involved need to be first-order continuous, which is difficult to implement for the plastic displacements. Secondly, whether the points where the stresses or additional displacements are calculated are considered fixed across the section or

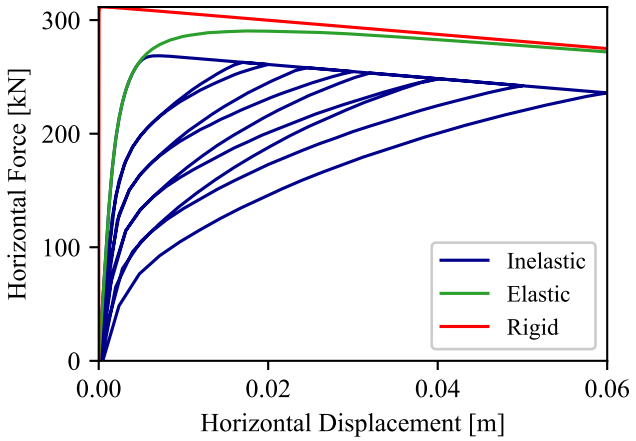

(a)

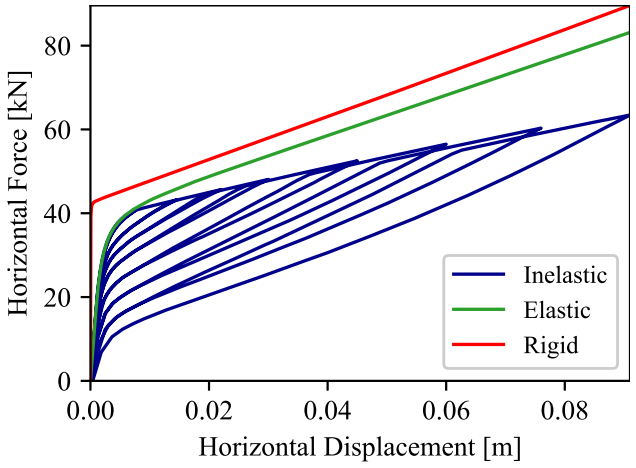

(b)

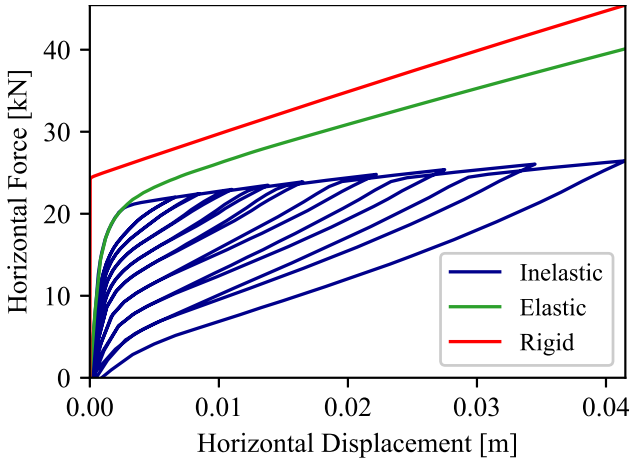

(c)

Figure 5.16: Comparison of the force - displacement curves for cyclic response produced by the macroelement for the (a) constant vertical force, (b) SRW-B and (c) EC COMP 1 models (in blue) with results for respective models considering the rocking body to be elastic (in green) and rigid (in red). Only the positive semi-axes are shown for clarity.

moving together with the region boundaries, numerical problems arise when the distance between any of the points becomes very small. Thirdly, the creation of new regions during yielding or uplift or removal of existing ones is not straightforward and the continuity of the solution is not always guaranteed. Finally, even when all of the aforementioned problems are addressed, the solution may get stuck inside a local minimum instead of the global one, so random steps are sometimes needed to overcome them. However, it is presented here as a suggestion for future research.

The determination of the stress distribution at the rocking interface is divided into two steps: The first step is the determination of the elastic, inelastic and compression-free regions and the respective boundaries across the rocking interface and the second step is the calculation of the stresses or additional elongations of the internal points. As will be seen, the first step is a nonlinear problem, while the second is one is a simpler one.

Assuming that the rocking interface has been divided into non-contact, elastic and inelastic regions, the boundaries between regions are gathered in a vector $\mathbf{R}$. Points $\mathbf{Y}_w$, which have no fixed locations for the current formulation, are inserted inside the regions, including the points at the edges of the section, where the stresses and additional displacements are controlled. Vector $\mathbf{Y}$ contains both $\mathbf{R}$ and $\mathbf{Y}_w$ in ascending order. A vector $\mathbf{q}$ is introduced that contains the corresponding region identifier ("0" for a non-contact region, "1" for an elastic region and "2" for an inelastic one) for each point in $\mathbf{Y}$ (region boundaries are considered either "0" or "2"). The unknown stresses or additional elongations are expressed in a vector $\mathbf{W}$ for each of the points in $\mathbf{Y}_w$. For formula simplification and computational reasons, the stresses and additional elongations are normalized with respect to the modulus of elasticity, E.

Stresses

The elastic strains $\mathbf{S}$ at points $\mathbf{Y}$ can be expressed as linear functions of $\mathbf{W}$:

$$\mathbf{S} = \mathbf{B}_s \mathbf{W} + \mathbf{b}_s \tag{5.50}$$

where $\mathbf{B}_s$ is a $n_y \times n_w$ matrix and $\mathbf{b}_s$ is a n_y vector (n_y being the length of vector $\mathbf{Y}$), with zero entries everywhere except for the following entries:

- $B_{s,ij} = 1$ for $j = 1, ..., n_w$ if $q_i = 1$ where i is the index of $\mathbf{Y}$ that corresponds to $Y_{w,j}$.
- $b_{s,i} = \epsilon_y$ for $i = 1, ..., n_y$ if $q_i = 2$.

Since stresses are constant for non-contact and inelastic regions, it can be concluded that the whole stress distribution can be described using the boundaries of these regions, as well as internal points of the elastic ones (point vector $\mathbf{Y}_{\mathrm{m}}$), so the calculation of all

entries of $\mathbf{S}$ is not necessary. The stresses at these main locations $\mathbf{Y}_{\mathrm{m}}$ are given by:

$$\mathbf{S}_{\sigma} = \mathbf{B}_{\sigma}\mathbf{W} + \mathbf{b}_{\sigma} \tag{5.51}$$

where $\mathbf{B}_{\sigma}$ and $\mathbf{b}_{\sigma}$ are the reduced $\mathbf{B}_S$ matrix and $\mathbf{b}_S$ vector, keeping only the rows corresponding to points contained in $\mathbf{Y}_{\mathrm{m}}$.

Additional elongations

Similarly to the stresses, additional displacements are expressed as linear functions of $\mathbf{W}$:

$$\mathbf{U}_a = \mathbf{B}_a\mathbf{W} \tag{5.52}$$

where $\mathbf{B}_a$ is a $n_y \times n_w$ matrix, with zero entries everywhere except for the following entries: $B_{a,ij} = 1$ for $j = 1, ..., n_w$ if $q_i \neq 1$ where i is the index of $\mathbf{Y}$ that corresponds to $Y_{w,j}$.

Additional elongations at region boundaries $\mathbf{R}$ are considered equal to 0.

Resultant forces at the rocking interface

Having expressed the stresses at locations $\mathbf{C}$ as linear functions of $\mathbf{W}$, the nomalized resultant axial force N_n and moment M_n at the rocking interface are expressed as:

$$N_n = \mathbf{B}_N\mathbf{W} + \mathbf{b}_N \tag{5.53}$$

$$M_n = \mathbf{B}_M\mathbf{W} + \mathbf{b}_M \tag{5.54}$$

Regarding the axial force calculation,

$$\mathbf{B}_N = \mathbf{A}_N^T\,\mathbf{B}_{\sigma} \tag{5.55}$$

$$b_N = \mathbf{A}_N^T\,\mathbf{b}_{\sigma} \tag{5.56}$$

where $\mathbf{A}_N$ is a vector with length n_c with:

$$\mathbf{A}_{N,i} = \frac{y_{\mathrm{m},i+1} - y_{\mathrm{m},i-1}}{2} \tag{5.57}$$

for $i = 1, ..., n_m$, where n_m is the length of vector $\mathbf{Y}_{\mathrm{m}}$, $y_{\mathrm{m},0} = y_{\mathrm{m},1}$ and $y_{\mathrm{m},n_m+1} = y_{\mathrm{m},n_m}$.

Regarding the moment calculation,

$$\mathbf{B}_M = \mathbf{A}_M^T\,\mathbf{B}_{\sigma} \tag{5.58}$$

$$b_M = \mathbf{A}_M^T\,\mathbf{b}_{\sigma} \tag{5.59}$$

where $\mathbf{A}_M$ is a vector with length n_c with:

$$\mathbf{A}_{M,i} = \frac{y_{\mathrm{m},i+1} - y_{\mathrm{m},i-1}}{6}\left(y_{\mathrm{m},i+1} + y_{\mathrm{m},i} + y_{\mathrm{m},i-1}\right) \tag{5.60}$$

for $i = 1, ..., n_m$, where $y_{\mathrm{m},0} = y_{\mathrm{m},1}$ and $y_{\mathrm{m},n_m+1} = y_{\mathrm{m},n_m}$.

Contribution of the resultant forces on the rocking end displacements

According to Eq. (5.30), the displacements due to the resultant forces are functions of $\mathbf{W}$ as follows:

$$\mathbf{u}_{\text{rf}} = \begin{bmatrix} f_{\text{r,11}} & 0 \\ 0 & f_{\text{r,22}} - f_{\text{r,32}}\dfrac{f_{\text{r,23}}}{f_{\text{r,33}}} \end{bmatrix} \begin{Bmatrix} N_n \\ M_n \end{Bmatrix} + \begin{Bmatrix} 0 \\ \dfrac{f_{\text{r,23}}}{f_{\text{r,33}}}\theta_2 \end{Bmatrix} = \mathbf{B}_{\text{rf}}\mathbf{W} + \mathbf{b}_{\text{rf}} \tag{5.61}$$

where

$$\mathbf{B}_{\text{rf}} = \begin{bmatrix} f_{\text{n11}} & 0 \\ 0 & f_{\text{r,22}} - f_{r,32}\dfrac{f_{\text{r,23}}}{f_{\text{r,33}}} \end{bmatrix} \begin{bmatrix} \mathbf{B}_N \\ \mathbf{B}_M \end{bmatrix} \tag{5.62}$$

and

$$\mathbf{b}_{\text{rf}} = \begin{bmatrix} f_{\text{n11}} & 0 \\ 0 & f_{\text{r,22}} - f_{\text{r,32}}\dfrac{f_{\text{r,23}}}{f_{\text{r,33}}} \end{bmatrix} \begin{Bmatrix} b_N \\ b_M \end{Bmatrix} + \begin{Bmatrix} 0 \\ \dfrac{f_{\text{r,23}}}{f_{\text{r,33}}}\theta_2 \end{Bmatrix} \tag{5.63}$$

Maximum shear stress

Using Eqs. (5.29) and (5.31), the normalized maximum shear stress, t, can be expressed as

$$t = \mathbf{B}_t\mathbf{W} + b_t \tag{5.64}$$

where

$$\mathbf{B}_t = -\frac{f_{\text{r,32}}}{f_{\text{r,33}} \cdot \gamma_Q}\mathbf{B}_M \tag{5.65}$$

$$b_t = \frac{\theta_2}{f_{\text{r,33}} \cdot \gamma_Q} - \frac{f_{\text{r,32}}}{f_{\text{r,33}} \cdot \gamma_Q}b_M \tag{5.66}$$

and

$$\gamma_Q = \frac{2}{3}\left(y_{\text{cr}} - y_{\text{cl}}\right) \tag{5.67}$$

Contribution of self-equilibrating shear stresses on the rocking end displacements

If $\mathbf{u}_{tn} = [\delta_{tn}, \theta_{tn}]^T$, the additional displacements induced to the contact region are expressed as linear functions of $\mathbf{W}$ as follows:

$$\mathbf{u}_t = \mathbf{B}_{ut}\mathbf{W} + \mathbf{b}_{ut} \tag{5.68}$$

with

$$\mathbf{B}_{ut} = \begin{bmatrix} \delta_{tn} & 0 \\ 0 & \theta_{tn} \end{bmatrix} \begin{bmatrix} \mathbf{B}_t \\ \mathbf{B}_t \end{bmatrix} \tag{5.69}$$

and

$$\mathbf{b}_{ut} = b_t \cdot \mathbf{u}_{tn} \tag{5.70}$$

Contribution of self-equilibrating normal stresses on the rocking end displacements

The contribution of the self-equilibrating normal stresses is taken into account with a formula similar to Eq. (5.35):

$$\mathbf{U}_{\mathrm{e}} = \mathbf{V}_{w}\, \mathbf{S}_{\sigma} \tag{5.71}$$

where $\mathbf{S}_{\sigma}$ contains the stresses at the main locations $\mathbf{Y}_{\mathrm{m}}$ and matrix $\mathbf{V}_{w}$ is formulated in the same manner as matrix $\mathbf{V}$ of the original formulation (Eq. 5.34), but is not constant in this case and is formed using the elements of $\mathbf{Y}_{\mathrm{m}}$ at each instant.

Combining the previous equation with Eq. (5.51), the following equations are formed:

$$\mathbf{U}_{\mathrm{e}} = \mathbf{B}_{\mathrm{e}}\mathbf{W} + \mathbf{b}_{\mathrm{e}} \tag{5.72}$$

with

$$\mathbf{B}_{\mathrm{e}} = \mathbf{V}_{w}\, \mathbf{B}_{\sigma} \tag{5.73}$$

$$\mathbf{b}_{\mathrm{e}} = \mathbf{V}_{w}\, \mathbf{b}_{\sigma} \tag{5.74}$$

Difference between target and predicted elongations

Similarly to Eq. (5.43), the difference between the target and the predicted elongations is given by

$$\mathbf{U}_{\mathrm{d}} = \mathbf{B}_{\mathrm{d}}\mathbf{W} + \mathbf{b}_{\mathrm{d}} \tag{5.75}$$

with

$$\mathbf{B}_{\mathrm{d}} = \mathbf{B}_{\mathrm{e}} + \mathbf{B}_{\mathrm{a}} + \mathbf{C}\,\mathbf{B}_{t} + \mathbf{C}\,\mathbf{B}\,\mathbf{B}_{\mathrm{rf}} \tag{5.76}$$

and

$$\mathbf{b}_{\mathrm{d}} = \mathbf{b}_{\mathrm{e}} + \mathbf{U}_{\mathrm{pl,pr}} + \mathbf{C}\,\mathbf{b}_{t} + \mathbf{C}\,\mathbf{B}\,\mathbf{b}_{\mathrm{rf}} - \mathbf{C}\,\mathbf{B}\,\mathbf{u}_{\mathrm{rs}} \tag{5.77}$$

with matrices $\mathbf{C}$ and $\mathbf{B}$ given by Eqs. (5.41) and (5.42), respectively.

It it noted that vector $\mathbf{U}_{\mathrm{pl,pr}}$ in this formulation does not refer to constant points, but to the locations corresponding to $\mathbf{Y}_{w}$.

Convex Quadratic Problem formulation

Since matrix $\mathbf{B}_{\mathrm{d}}$ is not square, meaning that the number of equations is greater than the number of unknowns, $\mathbf{W}$, the problem cannot be solved directly. Furthermore, the inequalities regarding the unknown stresses and additional displacements, depending on the regions of the corresponding locations, must be taken into account for the values in $\mathbf{W}$ to have meaning.

One possible solution would be to reduce $\mathbf{B}_{\mathrm{d}}$ and $\mathbf{b}_{\mathrm{d}}$ to include only elongation differences on points not being region boundaries, and the elongation differences at region

boundaries could be checked at a later stage. However, the problem regarding the aforementioned inequalities would persist.

This is why a more elegant solution to the problem is to express it as a convex quadratic minimization problem. More specifically, the convex quadratic minimization problem is defined as:

$$\text{minimize } f = \frac{1}{2}\mathbf{W}^T\mathbf{G}\mathbf{W} - \mathbf{a}^T\mathbf{W} \ \ (+d) \tag{5.78}$$

subject to

$$\mathbf{D}^T\mathbf{W} \geq \mathbf{b} \tag{5.79}$$

where matrix $\mathbf{G}$ is a positive definite symmetric matrix[‡].

Here, the function that has to be minimized, f, is half the sum of squares of the elements of $\mathbf{U}_\mathrm{d}$:

$$f = \frac{1}{2}\mathbf{U}_\mathrm{d}^T \ \mathbf{U}_\mathrm{d} = \frac{1}{2}\mathbf{W}^T \ \mathbf{B}_\mathrm{d}^T \ \mathbf{B}_\mathrm{d} \ \mathbf{W} + \mathbf{B}_\mathrm{d}^T \ \mathbf{b}_\mathrm{d} \ \mathbf{W} + \frac{1}{2}\mathbf{b}_\mathrm{d}^T \ \mathbf{b}_\mathrm{d} \tag{5.80}$$

meaning that

$$\mathbf{G} = \mathbf{B}_\mathrm{d}^T \ \mathbf{B}_\mathrm{d} \tag{5.81}$$

$$\mathbf{a} = -\mathbf{B}_\mathrm{d}^T \ \mathbf{b}_\mathrm{d} \tag{5.82}$$

while the constant term (with respect to $\mathbf{W}$)

$$d = \frac{1}{2}\mathbf{b}_\mathrm{d}^T \ \mathbf{b}_\mathrm{d} \tag{5.83}$$

can be dropped for the minimization procedure. Eq. (5.81) shows that $\mathbf{G}$ is indeed a positive semidefinite symmetric matrix as a product of the transpose of a matrix with itself. It turns out that $\det(\mathbf{B}_\mathrm{d}) \neq 0$, so $\mathbf{G}$ is positive definite.

Furthermore, each column of $\mathbf{D}$ and entry of $\mathbf{b}$ refer to an inequality constraint, so for each element $y_{w,i}$ in $\mathbf{Y}_w$, new columns and entries are added in $\mathbf{D}$ and $\mathbf{b}$ respectively, as follows:

- $D_{ik} = 1$, $b_k = 0$ for points with $q_i = 0$
- $D_{ik} = -1$, $b_k = 0$ and $D_{i,k+1} = 1$, $b_{k+1} = \epsilon_y$ for points with $q_i = 1$
- $D_{ik} = -1$, $b_k = 0$ for points with $q_i = 2$

where k is the current column/entry to be added.

Convex quadratic optimization problems are quick and easy to solve, for example with the *quadprog* package for Python, which uses the algorithm by Goldfarb and Idnani (1983).

[‡]This symbol is widely used in the respective literature and should not be confused with the matrix used in Eq. (5.34).

Apart from finding the optimal solution $\mathbf{W}$ and the minimum of the objective function, $\hat{f}$, the algorithm also returns the inequality constraints that are active, that is, they hold as equalities at the optimal solution. It is evident that the minimum of the original function, f is

$$f = \hat{f} + d \tag{5.84}$$

where $\hat{f}$ is the minimum of the function without the constant term. The minimum value of f should be close to zero in order to consider the result the solution to the problem under examination.

Changing the region boundaries

Throughout the previous analysis, the region boundaries, $\mathbf{R}$, are kept constant, so that all the quantities are linearly dependent on $\mathbf{W}$ and a quadratic programming problem is formulated, since by changing $\mathbf{R}$ and as a result $\mathbf{Y}_{\mathrm{m}}$, the problem is nonlinear. However, the minimum value of f resulting from this approach is in the initial steps not zero. The next step in order to further minimize f is to change $\mathbf{R}$.

If f has a minimum value with respect to $\mathbf{R}$, this means that $\dfrac{\partial f}{\partial \mathbf{R}}$ is an array with n_r zero entries. If that is not the case, vector $\mathbf{R}$ must be updated with the addition of $\Delta\mathbf{R}$ given by solving:

$$\frac{\partial^2 f}{\partial \mathbf{R}^2}\,\Delta\mathbf{R} = -\frac{\partial f}{\partial \mathbf{R}} \tag{5.85}$$

It should be noted that since entries in $\mathbf{R}$ have a specific order, special attention should be paid that the addition of $\Delta\mathbf{R}$ does not alter this order. A suitable fraction of $\Delta\mathbf{R}$ can be used instead for the new step to ensure this.

The aforementioned procedure of course requires the calculation of matrices $\dfrac{\partial^2 f}{\partial \mathbf{R}^2}$ and $\dfrac{\partial f}{\partial \mathbf{R}}$, which is not an easy task, considering that most quantities used are dependent on $\mathbf{R}$. However, by sequentially differentiating all quantities used as presented in the previous steps, these matrices can be calculated successfully.

Listing all the necessary calculations would be cumbersome, however the general approach is as follows. Since most quantities are expressed with matrix calculations, matrix differentiations must be applied with respect to vector $\mathbf{R}$, which produces new matrices with one extra dimension for first order differentiation and two extra dimensions for second order differentiation. This way, matrices up to the fourth dimension are created. In order to calculate the derivative of a product of matrices, the chain rule is used as in usual calculus, but paying special attention that the rows and columns multiplied between matrices are the correct ones. To aid in this task, a very helpful function is the "einsum" function provided by the *NumPy* python package, which describes the multiplication of matrices using matrix axis indices, along which matrix multiplications take place. By fol-

lowing the aforementioned procedure, one can arrive at matrices $\frac{\partial \mathbf{G}}{\partial \mathbf{R}}$, $\frac{\partial^2 \mathbf{G}}{\partial \mathbf{R}^2}$, $\frac{\partial \mathbf{a}}{\partial \mathbf{R}}$, $\frac{\partial^2 \mathbf{a}}{\partial \mathbf{R}^2}$, $\frac{\partial d}{\partial \mathbf{R}}$ and $\frac{\partial^2 d}{\partial \mathbf{R}^2}$.

Knowing the active constraints of the QP problem at the optimal solution, matrix $\mathbf{D}_s$ can be constructed, which contains all columns of $\mathbf{D}$ that refer to active constraints. The derivatives of the optimal solution, $\mathbf{W}$ with respect to matrix $\mathbf{G}$ and vector $\mathbf{a}$ are given by (e.g. Boot, 1963):

$$\frac{\partial \mathbf{W}}{\partial \mathbf{a}} = \mathbf{G}^{-1} - \mathbf{G}^{-1}\ \mathbf{D}_s\ \left(\mathbf{D}_s^T\ \mathbf{G}^{-1}\ \mathbf{D}_s\right)^{-1}\ \mathbf{D}_s^T\ \mathbf{G}^{-1} \tag{5.86}$$

and

$$\frac{\partial w_k}{\partial G_{ij}} = -\frac{\partial w_k}{\partial a_i} w_j \tag{5.87}$$

Therefore,

$$\frac{\partial w_i}{\partial r_j} = \sum_k \frac{\partial w_i}{\partial a_k}\ \frac{\partial a_k}{\partial r_j} + \sum_k \sum_l \frac{\partial w_i}{\partial G_{kl}}\ \frac{\partial G_{kl}}{\partial r_j} \tag{5.88}$$

and by calculating

$$\frac{\partial^2 w_i}{\partial r_j\ \partial a_k} = -\frac{\partial w_i}{\partial a_l}\ \frac{\partial G_{lm}}{\partial r_j}\ \frac{\partial w_m}{\partial a_k} \tag{5.89}$$

and $\frac{\partial^2 \mathbf{W}}{\partial \mathbf{R}\ \partial \mathbf{G}}$ from applying the chain rule to Eq. (5.87) respectively, the second order derivative $\frac{\partial^2 \mathbf{W}}{\partial \mathbf{R}^2}$ can be calculated from Eq. (5.88).

Finally, derivatives $\frac{\partial f}{\partial \mathbf{R}}$ and $\frac{\partial^2 f}{\partial \mathbf{R}^2}$ can be calculated by differentiation of Eq. (5.78), so Eq. (5.85) can then be used.

A similar procedure can be used for the calculation of the derivative $\frac{\partial \mathbf{R}}{\partial \mathbf{u}_\mathrm{n}}$, where $\mathbf{u}_\mathrm{n}$ is the vector of target displacements at member ends, which is needed for the formulation of the stiffness matrix of the element. The following derivatives are calculated for a change only in $\mathbf{u}_\mathrm{n}$: $\frac{\partial \mathbf{W}}{\partial \mathbf{u}_\mathrm{n}}$, $\frac{\partial^2 \mathbf{W}}{\partial \mathbf{u}_\mathrm{n} \partial \mathbf{G}}$, $\frac{\partial^2 \mathbf{W}}{\partial \mathbf{u}_\mathrm{n} \partial \mathbf{R}}$ and finally $\frac{\partial^2 f}{\partial \mathbf{u}_\mathrm{n} \partial \mathbf{R}}$.

Since by changing $\mathbf{u}_\mathrm{n}$, the minimum value of f needs to remain close to 0, the following equation holds:

$$\frac{\partial^2 f}{\partial \mathbf{R}^2}\ \frac{\partial \mathbf{R}}{\partial \mathbf{u}_\mathrm{n}} = -\frac{\partial^2 f}{\partial \mathbf{u}_\mathrm{n} \partial \mathbf{R}} \tag{5.90}$$

from which $\frac{\partial \mathbf{R}}{\partial \mathbf{u}_\mathrm{n}}$ is calculated.

6 Modeling of inelastic rocking bodies under dynamic loading

In this chapter, the cyclic inelastic macroelement formulation is extended, in order to take into account phenomena associated with the dynamic rocking motion. To this end, a suitable treatment of damping is introduced, which does not violate the physical contraint of compressive-only stresses at the rocking interface and other motion modes usually observed together with the rocking motion, namely sliding and upthrow, are predicted by introducing a new internal variable regarding the sliding of the member on the rocking surface. Thus, a macroelement is created, which is able to take into account the interaction between rocking, deformability, inelasticity, damping, energy loss during impacts, sliding and upthrow in a uniform manner.

6.1 Macroelement coordinate systems

Usually, finite element frameworks demand the forces, $\mathbf{F}_e$, and stiffness matrix, $\mathbf{K}_e$, of an element for given displacements, $\mathbf{u}_e$, in the element local coordinate system, which is the system aligned with the initial position of the member and has 6 degrees of freedom (Fig. 6.1a).

The static formulation proposed in previous chapters, like other nonlinear finite element formulations, uses internally a corotational (natural) coordinate system (Fig. 6.1c), from which the rigid body motion of the element as a whole has been removed. This coordinate system, which is associated with the deformation of the member, is aligned with the deformed position of the element and has three independent degrees of freedom (forces $\mathbf{F}_n$ and displacements $\mathbf{u}_n$).

In order to account for sliding in the dynamic marcoelement formulation, another indermediate coordinate system is considered, from which the sliding motion has been removed (Fig. 6.1b). This intermediate coordinate system has six degress of freedom (forces

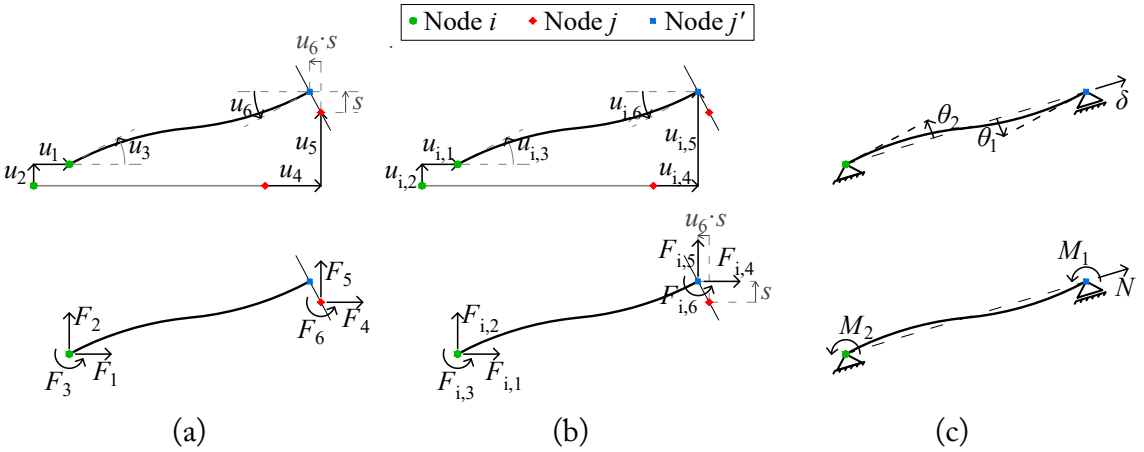

Figure 6.1: Displacements and Forces in the (a) Local; (b) Intermediate and (c) Corotational coordinate systems. Node *j* corresponds to the initial position of the rocking end of the body on the rocking surface, while node *j'* corresponds to the displaced position of the projection of the rocking end on the rocking surface due to sliding and upthrow.

$\mathbf{F}_{\mathrm{i}}$ and displacements $\mathbf{u}_{\mathrm{i}}$), which are aligned with the local coordinate system of the body. It can be understood that the usual conversions between the local and the corotational coordinate systems applied when no sliding is present now apply between the intermediate and the corotational coordinate systems, instead.

For the introduction of sliding, a new internal variable s is introduced, which is the displacement of the rocking end of the element perpendicular to the original member axis due to sliding, with respect to the initial reference node of the member end (Fig. 6.1). This means that the conversion of the local displacements, $\mathbf{u}_{\mathrm{e}}$, to the intermediate displacements, $\mathbf{u}_{\mathrm{i}}$ is performed as follows:

$$\mathbf{u}_{\mathrm{i}} = \mathbf{u}_{\mathrm{e}} + s \cdot [0, 0, 0, -u_6, 1, 0]^T \tag{6.1}$$

where u_6 is the rotation of the rocking end (Node *j*) in the local coordinate system.

Correspondingly, the forces in the intermediate coordinate system, $\mathbf{F}_{\mathrm{i}}$ are converted into local coordinate system forces, $\mathbf{F}_{\mathrm{e}}$, as follows:

$$\mathbf{F}_{\mathrm{e}} = \mathbf{F}_{\mathrm{i}} + s \cdot [0, 0, 0, 0, 0, -F_{\mathrm{i},4} - u_6\, F_{\mathrm{i},5}]^T \tag{6.2}$$

where $F_{\mathrm{i},4}$ and $F_{\mathrm{i},5}$ are the forces parallel and perpendicular to the undeformed member axis in the intermediate coordinate system without sliding. It can be seen that only the moment at the rocking end differs between the intermediate and the local coordinate systems.

This formulation is considered adequate when sliding is small considered with the other dimensions of the member. As will be later explained, since additional displacements ("gaps") may develop between the rocking end of the member and the rocking surface, the node at the rocking surface (Node *j'*), which is translated with respect to the

original position of the rocking end on the rocking surface (Node *j*), does not necessarily correspond to the base of the member, but to its projection to the rocking surface if the body has completely detached from this surface (upthrow).

For moderately small deformation-induced displacements, the following formulas can be used for the corotational system displacements and the intermediate system forces respectively (Fig. 6.1):

$$\mathbf{u}_{\mathrm{n}} = \begin{Bmatrix} \delta \\ \theta_1 \\ \theta_2 \end{Bmatrix} = \begin{Bmatrix} u_{\mathrm{i},4} - u_{\mathrm{i},1} + \frac{1}{2}(u_{\mathrm{i},5} - u_{\mathrm{i},2})^2/L \\ u_{\mathrm{i},6} - (u_{\mathrm{i},5} - u_{\mathrm{i},2})/L \\ u_{\mathrm{i},3} - (u_{\mathrm{i},5} - u_{\mathrm{i},2})/L \end{Bmatrix} \tag{6.3}$$

$$\mathbf{F}_{\mathrm{i}} = \begin{Bmatrix} F_{\mathrm{i},1} \\ F_{\mathrm{i},2} \\ F_{\mathrm{i},3} \\ F_{\mathrm{i},4} \\ F_{\mathrm{i},5} \\ F_{\mathrm{i},6} \end{Bmatrix} = \begin{Bmatrix} -N \\ -N \cdot (u_{\mathrm{i},5} - u_{\mathrm{i},2})/L + (M_1 + M_2)/L \\ M_2 \\ N \\ N \cdot (u_{\mathrm{i},5} - u_{\mathrm{i},2})/L - (M_1 + M_2)/L \\ M_1 \end{Bmatrix} \tag{6.4}$$

6.2 Treatment of damping

Of main interest for the dynamic analysis of rocking bodies is the treatment of damping, since damping generated during impacts plays a significant role on the predicted response. Although Rayleigh damping is well-documented for linear systems only, it has also been used for rocking systems (e.g. Barthes, 2012; Wiebe et al., 2012; Belleri et al., 2013, among others). Both mass- and tangent-stiffness-proportional formulations have been used, however there are drawbacks to each one (e.g. *Abaqus/CAE: User's Manual (6.11)* 2011): The former greatly affects the rigid-body motion, which corresponds to lower frequencies, while the latter reduces the theoretical time-step required for convergence, since it mainly influences higher frequency motion components.

Another promising approach (Barthes, 2012; Vassiliou et al., 2016), which is also used in commercial finite element software (e.g. *Abaqus/CAE: User's Manual (6.11)* 2011), is the use of the HHT integration scheme, which introduces numerical damping to damp high frequency components. The results produced for rigid blocks are in excellent agreement with Housner's damping model. However, the damping introduced is numerical, with no physical meaning and, furthermore the experiments generally show that Housner's damping model generally overestimates the actual damping of rocking blocks as mentioned above. Thus, a more flexible damping mechanism would be preferable, especially for deformable bodies. In order to implement Housner's damping, another option is to introduce an equivalent Dirac-like damping force (Prieto et al., 2004; Prieto and Lourenço, 2005) or, regarding finite element analyses, to perform an "event-based" analysis (Dia-

mantopoulos and Fragiadakis, 2019), where such damping is explicitly introduced when the algorithm detects impact, similarly to analytical formulations. For typical harmonic excitations, damping can be also introduced using a continuous viscous damper, which is calibrated, so that it provides the same loss of energy as the one expected theoretically (Vassiliou et al., 2014).

It is observed that most of the aforementioned approaches do not have a direct physical meaning and may, in fact, violate the assumption of a compression-only rocking interface. In this dissertation, an approach similar to tangent-stiffness-proportional damping is employed, which regards damping as a material property and which complies with the previous fundamental assumption of the compression-only rocking interface. The damping considered in the proposed formulation is defined first at stress level. More specifically, in order to incorporate damping in the macroelement, a damping stress equal to

$$\sigma_{\mathrm{d}} = \beta \cdot \dot{\sigma} \tag{6.5}$$

is applied at each point of the member, which is proportional to the rate of change of the corresponding point stress. Such damping stresses are commonly used in finite element frameworks instead of resultant damping forces.

An advantage of using the previous damping model is that by applying and integrating the damping stresses corresponding to the rate of change of the normal stresses across the two member ends, an equivalent expression for the resultant damping forces in the corotational coordinate system is produced:

$$\mathbf{F}_{\mathrm{d}} = \beta \cdot \dot{\mathbf{F}}_{\mathrm{n}} \tag{6.6}$$

The previous damping model, when applied to a linear elastic system, is equivalent to stiffness-proportional damping. When applied to nonlinear systems, it corresponds to stiffness-proportional damping based on the current stiffness of the system instead of the initial one, which is commonly used in finite element software (e.g. *OpenSees*, Mazzoni et al., 2006).

Although this damping model is easy to implement for linear systems, a physically consistent implementation for rocking bodies is not straightforward. The main characteristic of rocking bodies is that tensile stresses cannot be transmitted through the rocking interface with the base. However, the stresses applied to the rocking interface are actually the sum of the deformation-inducing and the damping stresses, so both contributions have to be taken into account in this limitation. This means that, at each point at location y across the rocking interface, the following inequality must hold:

$$\sigma_{\mathrm{s}}(y) + \sigma_{\mathrm{d}}(y) \leq 0 \tag{6.7}$$

where $\sigma_{\mathrm{s}}(y)$ and $\sigma_{\mathrm{d}}(y)$ are the deformation-inducing and damping stress at y, respectively. By incorporating Eq. (6.5), the previous equation becomes:

$$\sigma_{\mathrm{s}}(y) + \beta \cdot \dot{\sigma}_{\mathrm{s}}(y) \leq 0 \tag{6.8}$$

The exact calculation of the stress rate, $\dot{\sigma}_{\mathrm{s}}$, appearing in Eq. (6.8), through the velocities at the element ends is difficult and computationally inefficient. So, the stress rate is approximated by the following relationship:

$$\dot{\sigma}_{\mathrm{s}} \approx \frac{\sigma_{\mathrm{s}} - \sigma_{\mathrm{s,pr}}}{\Delta t} \tag{6.9}$$

where $\sigma_{\mathrm{s,pr}}$ is the stress at the previous step and Δt is the time step. This backward difference numerical approximation of the derivative is widely used, as for example in the backward Euler method for the solution of differential equations. The drawback of using such an approximation is that Δt needs to be sufficiently small during the analysis, especially when rapid changes in stresses occur, e.g. during impacts.

By substituting Eq. (6.9) into Eq. (6.8), the stress inequality becomes:

$$\sigma_{\mathrm{s}} \leq \gamma \cdot \sigma_{\mathrm{s,pr}} \tag{6.10}$$

with

$$\gamma = \frac{\beta/\Delta t}{1 + \beta/\Delta t} \tag{6.11}$$

The previous inequality means, that, for the dynamic problem, the deformation-inducing stress must not only be negative, but also lower than $\gamma \cdot \sigma_{\mathrm{s,pr}} \leq 0$. For the limiting case of $\Delta t \to \infty$, meaning that the problem is almost static, $\gamma \to 0$, so the condition of Eq. (6.10) reduces to $\sigma_{\mathrm{s}} \leq 0$, as normally used for a static analysis.

In order to account for the previous condition, a modification in the calculation of $\varepsilon_{\mathrm{el}}$ and $\tilde{u}_{\mathrm{a}}$ is performed compared with the static formulation (Chapter 5):

$$\varepsilon_{\mathrm{el}} = \begin{cases} \varepsilon_{\mathrm{lim}} & \text{, if } w > \varepsilon_{\mathrm{lim}} \\ w & \text{, if } \varepsilon_{\mathrm{y}} < w \leq \varepsilon_{\mathrm{lim}} \\ \varepsilon_{\mathrm{y}} & \text{, if } w \leq \varepsilon_{\mathrm{y}} \end{cases} \tag{6.12}$$

and

$$\tilde{u}_{\mathrm{a}} = \begin{cases} w - \varepsilon_{\mathrm{lim}} & \text{, if } w > \varepsilon_{\mathrm{lim}} \\ 0 & \text{, if } \varepsilon_{\mathrm{y}} < w \leq \varepsilon_{\mathrm{lim}} \\ w - \varepsilon_{\mathrm{y}} & \text{, if } w \leq \varepsilon_{\mathrm{y}} \end{cases} \tag{6.13}$$

where $\varepsilon_{\mathrm{lim}} = \gamma \cdot \varepsilon_{\mathrm{el,pr}}$.

The previous definition ensures that the maximum value of attainable elastic strain at the control points is $\varepsilon_{\mathrm{lim}}$, and when that holds, a gap may form between the rocking body and the rocking surface ($\tilde{u}_a > 0$). In order to satisfy the previous conditions also between control points, an approximate procedure is applied, similar to the one used in the static formulation (Chapter 5). This procedure uses modified w' values at the control points at

the boundaries of each interval, which for the dynamic case are defined as:

$$w' = \begin{cases} w + \varepsilon_{\text{lim}} \left(\frac{\Delta y}{\pi} - 1\right) & \text{, if } w > \varepsilon_{\text{lim}} \\ w \dfrac{\Delta y}{\pi} & \text{, if } \varepsilon_{\text{y}} < w \leq \varepsilon_{\text{lim}} \\ w + \varepsilon_{\text{y}} \left(\frac{\Delta y}{\pi} - 1\right) & \text{, if } w \leq \varepsilon_{\text{y}} \end{cases} \tag{6.14}$$

where Δy is the distance between the control points.

A new distribution $[w']$ is created inside the interval by adding the linear distribution formed by connecting the aforementioned values at the interval boundaries with the opposite of the deviation of the preexisting plastic displacements from the corresponding linear plastic displacement distribution (purple line in Fig. 6.2a). For the static case, the boundaries of the non-contact and the yielded region, as well as the respective modified elastic strain distributions, $[\varepsilon_{\text{el,n}}]$ and additional displacement distributions, $[\tilde{u}_{\text{a}}]$, are determined by the intersections of distribution $[w']$ with the horizontal lines $w' = 0$ and $w' = \varepsilon'_{\text{y}} = \varepsilon_{\text{y}} \, (\Delta y / \pi)$, respectively (Fig. 6.2a). It is noted that, in order to obtain the elastic strain distribution, $[\varepsilon_{\text{el}}]$, the modified elastic strain distribution $[\varepsilon_{\text{el,n}}]$ has to be divided by $(\Delta y / \pi)$.

For the dynamic case, though, the maximum values of modified elastic strains are determined by the distribution $[\varepsilon_{\text{lim,n}}]$:

$$[\varepsilon_{\text{lim,n}}] = \gamma \cdot \frac{\Delta y}{\pi} \cdot [\varepsilon_{\text{el,pr}}] \tag{6.15}$$

So, for regions where $w' > \varepsilon_{\text{lim,n}}$, these develop both the maximum elastic strains

$$[\varepsilon_{\text{lim}}] = \gamma \cdot [\varepsilon_{\text{el,pr}}] \tag{6.16}$$

and additional displacements $\tilde{u}_{\text{a}} > 0$, meaning that, although the body has detached from the rocking surface, it still maintains deformation-inducing stresses in these areas, which however cancel out with the damping stresses; thus the externally applied stresses from the rocking surface are indeed zero.

After the determination of the elastic strain distribution with the aforementioned procedure for the whole rocking interface, the normalized deformation-inducing axial force, N_{n}, and moment, M_{n}, at the rocking end can be calculated by numerical integration of this distribution, which are defined as:

$$N_{\text{n}} = \frac{N}{bdE} \tag{6.17}$$

$$M_{\text{n}} = \frac{M_1}{b^2 dE} \tag{6.18}$$

where b is the semi-width, d is the thickness and E is the modulus of elasticity of the body. Since Eq. (6.9) equivalently holds for the elastic strains and both N_{n} and M_{n} are linearly related to the elastic strains, similar equations also hold for $\dot{N}_{\text{n}}$ and $\dot{M}_{\text{n}}$.

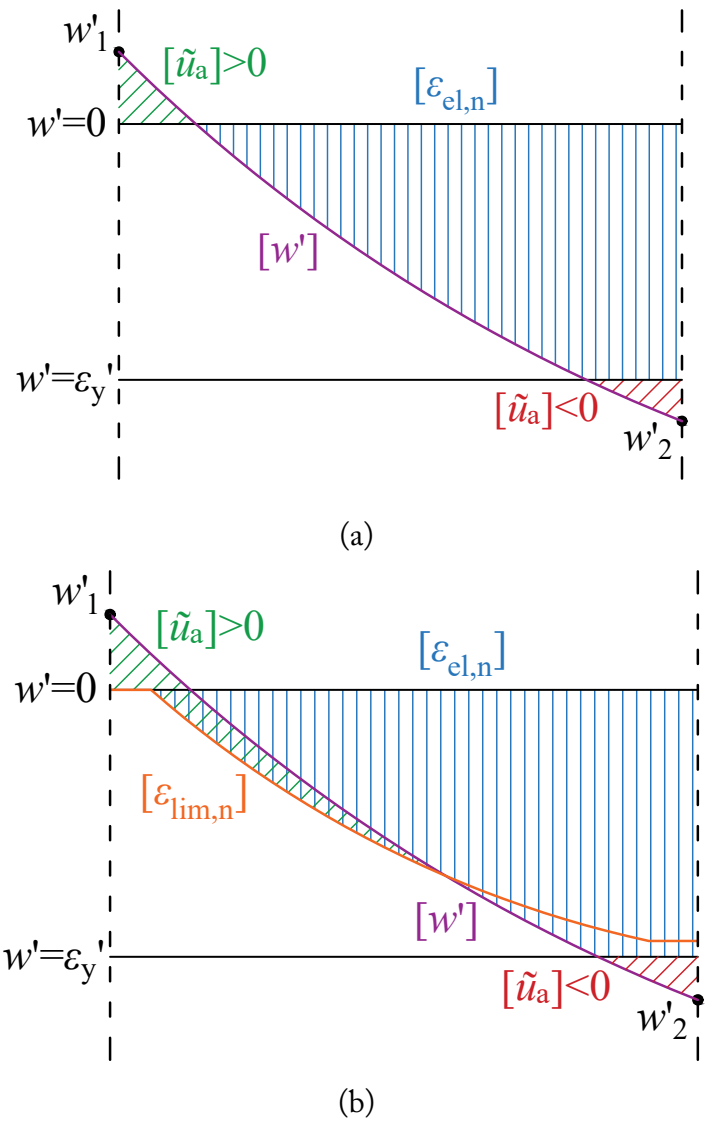

Figure 6.2: Determination of region boundaries and the corresponding modified elastic strain distributions, $[\varepsilon_{\mathrm{el,n}}]$, and normalized additional displacement distributions, $[\tilde{u}_{\mathrm{a}}]$ for the (a) static case and (b) the dynamic case.

The normalized shear force, Q_{n}, defined as:

$$Q_{\mathrm{n}} = \frac{Q}{bdE} = -\frac{M_1 + M_2}{bdLE} \tag{6.19}$$

is calculated for given rotation of the non-rocking end, θ_2, from

$$Q_{\mathrm{n}} = \frac{\theta_2 - f_{\mathrm{r},32} M_n}{f_{\mathrm{r},33}} \tag{6.20}$$

with $f_{\mathrm{r},32} = -(3L)/(4b)$ and $f_{\mathrm{r},33} = -L^2/(2b^2) - \alpha(1+\nu)$, where L is the original length of the member and α is the shear shape factor with $\alpha \approx 1.2$ for rectangular cross sections. By assuming that the approximation of Eq. (6.9) also holds for $\dot{\theta}_2$, which is the rate of change of the chord rotation of the non-rocking end, it follows from Eq. (6.20)

that this approximation also holds for the rate of change of the normalized shear force at the rocking end, $\dot{Q}_{\mathrm{n}}$. So, the rate of change of the normalized forces at the rocking end, $\mathbf{F}_{\mathrm{nn}} = [N_{\mathrm{n}}, M_{\mathrm{n}}, Q_{\mathrm{n}}]^T$, is

$$\dot{\mathbf{F}}_{\mathrm{nn}} \approx \frac{1}{\Delta t}\left(\mathbf{F}_{\mathrm{nn}} - \mathbf{F}_{\mathrm{nn,pr}}\right) \tag{6.21}$$

Finally, the sum of the deformation-inducing and the damping normalized forces at the rocking end is

$$\mathbf{F}_{\mathrm{nn,tot}} = \mathbf{F}_{\mathrm{nn}} + \beta \cdot \dot{\mathbf{F}}_{\mathrm{nn}} = \left(1 + \frac{\beta}{\Delta t}\right)\mathbf{F}_{\mathrm{nn}} - \frac{\beta}{\Delta t}\mathbf{F}_{\mathrm{nn,pr}} \tag{6.22}$$

6.3 Treatment of upthrow and sliding

The dynamic response of rocking bodies usually also involves other motion modes, namely upthrow, which is the complete detachment of the rocking body from the rocking surface, and sliding, which results in a translation of the rocking body with respect to the rocking surface.

In this formulation, upthrow is considered as a special case of sliding where the resultant axial force is zero, that is when the whole rocking interface develops positive additional displacements (gaps with respect to the rocking surface), $[\tilde{u}_{\mathrm{a}}] > 0$, so these two phenomena are treated in a uniform manner as described in the following. It is noted that the variable s introduced above measures the displacement of the projection of the rocking end of the element (Node *j'*) perpendicular to the original member axis with respect to its initial position on the rocking surface (Node *j*), and as a result also takes into account the corresponding body displacement during upthrow, while displacements perpendicular to the rocking end section during upthrow are taken into account using the additional ("gap") displacements, $\tilde{u}_{\mathrm{a}} > 0$ (Fig. 6.3).

A Coulomb friction law is implemented, which demands that

$$|F_{\mathrm{p,rs}}| \leq \mu\,|F_{\mathrm{n,rs}}| \tag{6.23}$$

where μ is the friction coefficient and $F_{\mathrm{p,rs}}$ and $F_{\mathrm{n,rs}}$ are the forces parallel and perpendicular to the rocking surface, respectively.

The aforementioned forces are related to the element forces with the relationships:

$$F_{\mathrm{n,rs}} = F_{\mathrm{4,tot}} + F_{\mathrm{5,tot}} \cdot u_6 \tag{6.24}$$

$$F_{\mathrm{p,rs}} = F_{\mathrm{5,tot}} - F_{\mathrm{4,tot}} \cdot u_6 \tag{6.25}$$

where $F_{\mathrm{4,tot}}$ and $F_{\mathrm{5,tot}}$ are the sum of the deformation-inducing and damping forces in the local coordinate system of the element parallel and perpendicular to the undeformed member axis and u_6 is the rotation of the rocking surface.

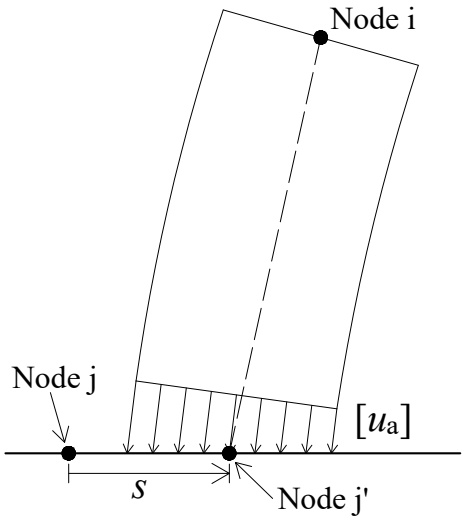

Figure 6.3: Description of the translation of the body in space during upthrow using sliding, s, and the additional displacements ("gaps"), $[u_a] > 0$.

By introducing variables:

$$\rho = (u_5 - u_2)/L \tag{6.26}$$

$$\tilde{s} = s/L \tag{6.27}$$

it follows from Eqs. (6.2), (6.4) and Eqs. (6.17), (6.19) that

$$F_{4,\text{tot}} = b\, dE N_{\text{n,tot}} \tag{6.28}$$

$$F_{5,\text{tot}} = b\, dE \left[Q_{\text{n,tot}} + (\rho + \tilde{s})\, N_{\text{n,tot}}\right] \tag{6.29}$$

Using also that

$$Q_{\text{n,tot}} = (1 + \beta/\Delta t)\, Q_{\text{n}} - (\beta/\Delta t)\, Q_{\text{n,pr}} \tag{6.30}$$

and due to Eq. (6.20),

$$Q_{\text{n}} = k_1\, (u_3 - \rho) - k_2\, M_n - k_1\, \tilde{s} \tag{6.31}$$

where $k_1 = 1/f_{\text{r,33}}$ and $k_2 = f_{\text{r,32}}/f_{\text{r,33}}$, it follows that

$$F_{5,\text{tot}} = b\, dE\, (A + B \cdot \tilde{s}) \tag{6.32}$$

where

$$A = (1 + \beta/\Delta t)\ [k_1\, (u_3 - \rho) - k_2\, M_{\text{n}}] - (\beta/\Delta t)\, Q_{\text{n,pr}} + \rho\, N_{\text{n,tot}} \tag{6.33}$$

$$B = N_{\text{n,tot}} - k_1\, (1 + \beta/\Delta t) \tag{6.34}$$

If one assumes that $F_{\text{n,rs}} \leq 0$, Ineq. (6.23) translates to

$$\mu\, F_{\text{n,rs}} \leq F_{\text{p,rs}} \leq -\mu\, F_{\text{n,rs}} \tag{6.35}$$

For $u_6 = 0$, it is evident from Eq. (6.24) that the assumption $F_{\text{n,rs}} \leq 0$ holds, since $F_{\text{n,rs}} = F_{4,\text{tot}} = b\,dE N_{\text{n,tot}}$ and $N_{\text{n,tot}}$ is always nonpositive as the integral of nonpositive strains. For $u_6 > 0$, it can be proven that if the right part of Ineq. (6.35) holds, it follows that

$$F_{\text{n,rs}} \leq F_{4,\text{tot}} \frac{1 + u_6^2}{1 + \mu\, u_6} \leq 0 \tag{6.36}$$

Similarly, for $u_6 < 0$, it can be proven that if the left part of Ineq. (6.35) holds, it follows that

$$F_{\text{n,rs}} \leq F_{4,\text{tot}} \frac{1 + u_6^2}{1 - \mu\, u_6} \leq 0 \tag{6.37}$$

From the previous remarks, it is clear that if Ineq. (6.35) holds, the assumption $F_{\text{n,rs}} \leq 0$ always holds as a consequence.

For the usual case $|u_6\,\mu| < 1$, Ineq. (6.35) can be alternatively expressed as follows:

$$L_1 \leq A + B \cdot \tilde{s} \leq L_2 \tag{6.38}$$

where

$$L_1 = N_{\text{n,tot}} \frac{u_6 + \mu}{1 - u_6 \mu} \tag{6.39}$$

$$L_2 = N_{\text{n,tot}} \frac{u_6 - \mu}{1 + u_6 \mu} \tag{6.40}$$

Ineq. (6.38) is checked at each iteration for the value of $\tilde{s}$ of the last committed step. If the friction inequality holds, then $\tilde{s}$ remains the same. Otherwise, $\tilde{s}$ is redetermined, so that, out of the two inequalitites, the one that does not initially hold, holds as an equality. After the value of $\tilde{s}$ is established, Eqs. (6.31) and (6.30) are used to calculate Q_{n} and $Q_{\text{n,tot}}$, respectively. It is noted that the rather extreme case $B = 0$, which means that the aforementioned inequalities may not be satisfiable, corresponds to $(N_{\text{n}} - k_1) = \gamma N_{\text{n,pr}} < N_{\text{n,pr}}$, which can emerge when $N_{\text{n}} - N_{\text{n,pr}} < k_1$ with $k_1 < 0$, but such a large change in the axial force can be prevented by using a smaller time step if necessary.

For the special case $u_6 = 0$, meaning that the rocking surface does not rotate, and for a very large value of μ approaching infinity, Ineq. (6.38) may not hold only if $N_{\text{n,tot}} = 0$, meaning that the rocking body has completely detached from the rocking surface, and $\tilde{s} = -A/B$ corresponds to the horizontal displacement of the body from its initial position during free-flight.

6.4 Calculation of displacements

As mentioned above, the elastic displacements induced to the member generally originate from three sources: The resultant forces at the member ends, the self-equilibrating normal stresses and the self-equilibrating shear stresses.

For the static formulation (Chapter 5), the contribution of the self-equilibrating shear stresses was taken into account using proposed approximate formulas and some further assumptions, which however are not suitable for the dynamic formulation and may lead to computational problems. For this reason, the contribution of the self-equilibrating shear stresses is neglected here, which nevertheless is not considered important for slender rocking bodies.

Contribution of resultant forces

As explained in the static formulation (Chapter 5), given the normalized axial force, N_{n}, and the normalized moment, M_{n} at the rocking end, as well as the chord rotation of the non-rocking end, θ_2, the linear displacement distribution parameters of the actual member rocking end are calculated as

$$\mathbf{u}_{\mathrm{rf}} = \begin{bmatrix} f_{\mathrm{r},11} & 0 \\ 0 & f_{\mathrm{r},22} - \dfrac{f_{\mathrm{r},23} \cdot f_{\mathrm{r},32}}{f_{\mathrm{r},33}} \end{bmatrix} \begin{Bmatrix} N_{\mathrm{n}} \\ M_{\mathrm{n}} \end{Bmatrix} + \begin{Bmatrix} 0 \\ \dfrac{f_{\mathrm{r},23}}{f_{\mathrm{r},33}} \theta_2 \end{Bmatrix} \tag{6.41}$$

where $f_{\mathrm{r},11} = L/2$, $f_{\mathrm{r},22} = (3L)/(4b)$ and $f_{\mathrm{r},23} = L^2/(4b^2) - \alpha(1+\nu)$, $f_{\mathrm{r},32} = -(3L)/(4b)$ and $f_{\mathrm{r},33} = -L^2/(2b^2) - \alpha(1+\nu)$.

These correspond to normalized displacements at the control points located at normalized coordinates y_w across the rocking interface, which are contained in vector $\mathbf{U}_{\mathrm{rf}}$:

$$\mathbf{U}_{\mathrm{rf}} = \mathbf{C}\ \mathbf{B}\ \mathbf{u}_{\mathrm{rf}} \tag{6.42}$$

with

$$\mathbf{C} = \begin{bmatrix} 1 & y_{w1} \\ 1 & y_{w2} \\ & \cdots \\ 1 & y_{w,n_w} \end{bmatrix} \tag{6.43}$$

and

$$\mathbf{B} = \begin{bmatrix} 1/b & 0 \\ 0 & 1 \end{bmatrix} \tag{6.44}$$

Contribution of self-equilibrating normal stresses

Given the elastic strain distribution across the rocking interface, the displacements due to the corresponding self-equilibrating distribution can be calculated similarly to the static formulation (Chapter 5), which involves the decomposition of the elastic strain distribution into basic geometric shapes (triangles, trapezoids) at every step, for which the displacements produced are calculated using proposed analytical expressions. However, this procedure is rather inefficient for dynamic analyses, due to the increased number of steps

and the complexity of the elastic strain distributions created due to damping. This is why a simpler procedure is proposed here:

The generally nonlinear strain distribution inside each interval between control points is approximated with a linear distribution with the same normalized axial force, N_i, and the moment, M_i, as the original elastic strain distribution of the interval. The values of this linear distribution at the left, y_l, and right boundary, y_r, of each interval are respectively:

$$s_\text{l} = 2\frac{N_i\,(y_\text{l} + 2y_\text{r}) - 3\,M_i}{(y_\text{r} - y_\text{l})^2} \tag{6.45}$$

$$s_\text{r} = -2\frac{N_i\,(2y_\text{l} + y_\text{r}) - 3\,M_i}{(y_\text{r} - y_\text{l})^2} \tag{6.46}$$

Similarly to the procedure followed in previous chapters, in order to calculate the additional displacements due to the self-equilibrating stresses originating from such a linear distribution, it is decomposed into primary shapes, for which the calculation of displacements has been established. More specifically, analytical expressions regarding the nonlinear displacement distribution of the semi-infinite strip are used, since the area of the rocking body near the contact region can be equivalently examined using the semi-infinite strip with what regards the effect of the self-equilibrating stresses, as explained in previous chapters.

If $U(y,p)$ is the function giving the displacement at fiber y for a unit concentrated load at p, which has been previously derived in Chapter 4, the displacements induced by a rectangle with unit value in the interval $[-1,r]$ and a triangle with maximum value at $y=-1$ and unit negative slope in the interval $[-1,r]$ are respectively:

$$U_\text{rect}(y,r) = \int_{-1}^{r} U(y,p)\;\mathrm{d}p \tag{6.47}$$

$$U_\text{tr}(y,r) = r\int_{-1}^{r} U(y,p) - \int_{-1}^{r} p\,U(y,p)\;\mathrm{d}p \tag{6.48}$$

The integrals required for the calculation of the previous expressions can be found in Chapter 4.

It can be proven that the displacements due to the self-equilibrating stresses corresponding to a linear distribution in the interval $[y_\text{l}, y_\text{r}]$ with values at the boundaries equal to s_l and s_r, respectively, can be calculated as

$$U_\text{lin}\,(y, y_\text{l}, y_\text{r}, s_\text{l}, s_\text{r}) = -\frac{s_\text{r} - s_\text{l}}{y_\text{r} - y_\text{l}}\,[U_\text{tr}(y, y_\text{r}) - U_\text{tr}(y, y_\text{l})] + s_\text{r}\,U_\text{rect}(y, y_\text{r}) - s_\text{l}\,U_\text{rect}(y, y_\text{l}) \tag{6.49}$$

Combining Eqs. (6.45) and (6.46) with Eq. (6.49), it follows that the displacement at y due to a unit normalized axial force, N_i, or moment, M_i, at the interval $[y_\text{l}, y_\text{r}]$ is equal

to:

$$U_N\left(y, y_{\text{l}}, y_{\text{r}}\right) = 6\frac{y_{\text{r}} + y_{\text{l}}}{\left(y_{\text{r}} - y_{\text{l}}\right)^3}\left[U_{\text{tr}}(y, y_{\text{r}}) - U_{\text{tr}}(y, y_{\text{l}})\right] - 2\frac{y_{\text{r}} + 2y_{\text{l}}}{\left(y_{\text{r}} - y_{\text{l}}\right)^2}U_{\text{rect}}(y, y_{\text{r}}) - 2\frac{2y_{\text{r}} + y_{\text{l}}}{\left(y_{\text{r}} - y_{\text{l}}\right)^2}U_{\text{rect}}(y, y_{\text{l}}) \tag{6.50}$$

$$U_M\left(y, y_{\text{l}}, y_{\text{r}}\right) = -\frac{12}{\left(y_{\text{r}} - y_{\text{l}}\right)^3}\left[U_{\text{tr}}(y, y_{\text{r}}) - U_{\text{tr}}(y, y_{\text{l}})\right] + \frac{6}{\left(y_{\text{r}} - y_{\text{l}}\right)^2}\left[U_{\text{rect}}(y, y_{\text{r}}) + U_{\text{rect}}(y, y_{\text{l}})\right] \tag{6.51}$$

respectively.

Using Eqs. (6.50) and (6.51), two $n_w \times (n_w - 1)$ matrices, $\mathbf{U}_N$ and $\mathbf{U}_M$, are formed, the element (i, j) of which refers to the induced displacement at the i-th control point, due to a unit normalized axial force or moment at the j-th interval, respectively.

If $\mathbf{N}_i$ and $\mathbf{M}_i$ are the vectors containing the normalized axial forces and moments at all intervals, respectively, then the induced displacements at the control points due to the self-equilibrating normal stresses are given by:

$$\mathbf{U}_{\text{e}} = \mathbf{U}_N\,\mathbf{N}_i + \mathbf{U}_M\,\mathbf{M}_i \tag{6.52}$$

The main benefit of this approach is that matrices $\mathbf{U}_N$ and $\mathbf{U}_M$ are constant and are formulated at the beginning of the analysis, greatly reducing computational times. Another benefit is that the induced displacements are now dependent only on the resultant forces of each interval, meaning that the elastic strain distributions may be simplified in order to further reduce computational times, as long as their resultant forces remain the same to ensure the continuity of the solution. For example, after every step convergence, the elastic strain and the plastic displacement distributions may be bilinearized between control points and in different behaviour regions (non-contact, elastic or inelastic).

Target displacements

Similarly to the static formulation (Chapter 5), iterations are performed with respect to $\mathbf{W}$, which is the vector containing the w values at all control points, for given local displacement vector, $\mathbf{u}_{\text{e}}$, until vector $\mathbf{U}_{\text{d}}$, containing the differences between the achieved and the target displacements of the rocking surface:

$$\mathbf{U}_{\text{d}} = \mathbf{U}_{\text{rf}} + \mathbf{U}_{\text{e}} + \mathbf{U}_{\text{a}} + \mathbf{U}_{\text{pl,pr}} - \mathbf{U}_{\text{rs}} \tag{6.53}$$

is almost zero, where $\mathbf{U}_{\text{rf}}$ is the vector of elastic displacements induced by the resultant forces (Eq. 6.42), $\mathbf{U}_{\text{e}}$ is the contribution of the elastic displacements induced by the self-equilibrating normal stresses (Eq. 6.52), $\mathbf{U}_{\text{a}}$ is the vector containing the additional displacements at the control points (positive for "gap" displacements in non-contact regions and negative for additional normalized plastic displacements in inelastic regions,

Eq. 6.13), $\mathbf{U}_{\text{pl,pr}}$ is the vector of preexisting normalized plastic displacements at the control points and $\mathbf{U}_{\text{rs}}$ is the vector of the normalized target displacements of the contact surface given by:

$$\mathbf{U}_{\text{rs}} = \mathbf{C}\ \mathbf{B}\ \mathbf{u}_{\text{rs}} \tag{6.54}$$

where $\mathbf{C}$ and $\mathbf{B}$ are the matrices given by Eqs. (6.43) and (6.44), respectively and $\mathbf{u}_{\text{rs}} = [\delta, \theta_1]^T$ (Eqs. 6.1 and 6.3).

After convergence has been achieved, the local force vector $\mathbf{F}_{\text{e}}$ is returned to the finite element framework (Eqs. 6.4 and 6.2), as well as the respective stiffness matrix $\mathbf{K}_{\text{e}} = \partial\mathbf{F}_{\text{e}}/\partial\mathbf{u}_{\text{e}}$, which is obtained though successive differentiation of all involved quantities.

6.5 Validation of the predicted response for rigid rocking bodies

In order to assess the capacity of the prosposed macroelement to predict the response of rigid rocking bodies accurately, the results produced by the macroelement are compared with existing analytical or numerical solutions.

First, the response of free-standing blocks under free oscillations is examined. Three rocking blocks are considered with width $B = 1$ m, thickness $d = 1$ m and heights H, which correspond to slenderness ratios $\alpha = 0.1$, 0.2 and 0.3, with $\tan\alpha = B/H$ [*]. In order to model these with finite elements, each block is modelled using two parts, with the lower part being the proposed macroelement and the upper part being a conventional elastic element. Very large values are considered for the modulus of elasticity, E, and the damping parameter, β, in order to model the perfectly inelastic impacts assumed by Housner (1963). The mass of the body is assumed concentrated at the center of the body, together with the moment of inertia corresponding to that point. It should be noted here that the inclusion of distributed mass in the macroelement is difficult, while the division of the mass and the respective moment of inertia into more nodes is not obvious and not necessarily more correct, since the rocking node of the macroelement corresponds to the rocking surface and not the rocking end of the element. However, in the case of almost rigid bodies the concentrated mass approach is considered accurate, due to the very small deformation of the bodies. Furthermore, the friction coefficient between the rocking body and the rocking surface is assumed infinite, which means that as long as a non-zero axial force exists between the rocking body and the rocking surface, there is no slip between them.

The results produced for an initial rotation θ_0 corresponding to $\theta_0/\alpha = 0.5$ by the linear solution by Housner (1963) and the respective results by the macroelement are given

[*]Not to be confused with the shear shape factor.

in Figs. 6.5, 6.6 and 6.7 for $\alpha = 0.1$, 0.2 and 0.3 respectively. It can be seen that, generally, there is very good agreement between the analytical solution and the one produced by the macroelement model for very large E and β values. The only notable discrepancy regards the rotational velocity at the end of the rocking response in Fig. 6.7, which may be attributed to the very large β value used (overcritical damping in the dynamic analysis of conventional structures) or numerical inaccuracies due to the very large parameter values used, which may require extremely small timesteps to capture the rigid body response accurately for such small oscillations. Similar numerical problems also exist in rigid body solutions and assumptions regarding the end of the rocking motion may be used to overcome them. It should be emphasized that the produced energy loss seen in Figs. 6.5, 6.6 and 6.7 is determined automatically during the response for these very large E and β values and an energy loss ratio, such as the one used in analytical solutions, is nowhere used in the finite element model. In addition, in order to capture the response during impacts as accurately as possible, the timestep is greatly reduced when abrupt axial force changes are detected.

The rigid body solution and the response produced by the macroelement for a rocking body with $\alpha = 0.2$ are also compared for ground excitations. Two ground excitation cases are considered: (a) a sinusoidal pulse with angular frequency $\omega_p = 6p$ and maximum acceleration $a_p = 2\alpha g$ (Fig. 6.8) and (b) the Castaic North Ridge Route (CDMG Station 24278) ground motion from the 1994 Northridge earthquake (Fig. 6.4).

Regarding the sinusoidal pulse response, generally there is very good agreement between the two solutions, especially at the beginning of the reponse. It should be noted that small rotations have been assumed for the formulation of the macroelement, which may demand smaller rotations than the linearization performed by Housner (1963), so a small discrepancy regarding the maximum attained rotations and oscillation periods exists, which accumulates during the response. Regarding the recorded earthquake ground motion, very good agreement exists during the strong ground motion duration, however discrepancies begin to show when the ground motion subsides, possibly again due to the very large value of β used or numerical problems due to the very small timesteps needed for such extreme parameter values, which cannot be practically used.

From the previous examples, it can be understood that in the limiting case of very large E and β values, the energy loss produced by the macroelement matches very well the one predicted by Housner (1963). It would be interesting to examine the energy loss produced by the macroelement for the cases where not both these parameters have very large values. In order to examine such cases, two dimensionless quantities are introduced:

$$\epsilon_0 = \frac{\rho g H}{E} \tag{6.55}$$

which is the initial strain at the rocking surface due to the self-weight of the body ($\epsilon_0 =$

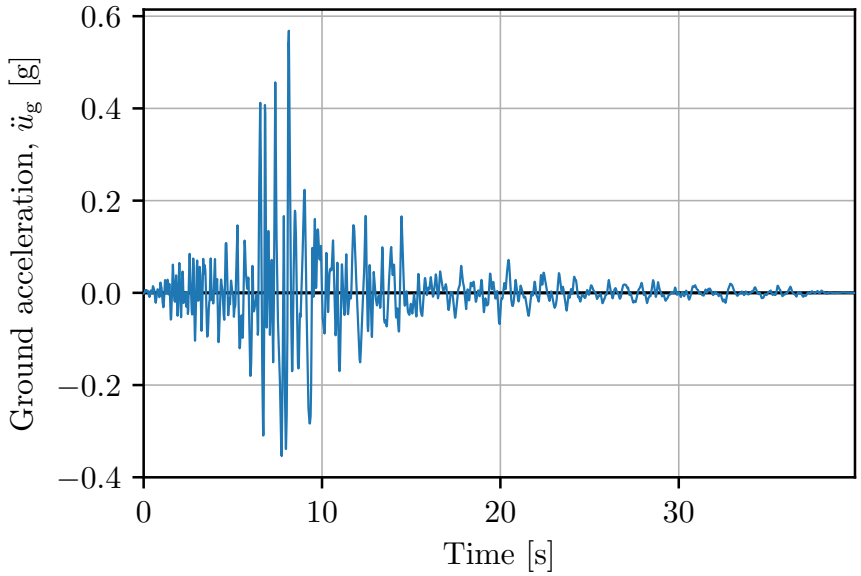

Figure 6.4: The Castaic North Ridge Route (CDMG Station 24278) ground motion from the 1994 Northridge earthquake.

10^{-6} was assumed for the rigid bodies of the previous examples) and

$$\zeta = \frac{\beta\omega}{2} \tag{6.56}$$

which is the damping ratio, as used in conventional dynamic analyses implementing stiffness-proportional damping, where the first angular eigenfrequency of the fixed body, ω, is used ($\zeta = 10000\%$ was assumed for the previous examples).

Two cases for rocking body free oscillations are examined here: (a) A rigid body ($\epsilon_0 = 10^{-6}$) with varying ζ values and (b) very large damping ($\zeta = 10000\%$) with varying ϵ_0 values. In these cases, a modified (kinetic energy) coefficient of restitution, r, is determined, so that when used in conjunction with the rigid body solution by Housner (1963), the same displacement is attained at the end of the first half-cycle. In Figs. 6.10, 6.11, 6.12, the ratio of this modified coefficient of restitution with respect to Hounser's original coefficient of restitution, r_{H}, is shown for three slenderness ratios $\alpha = 0.1$, 0.2 and 0.3, respectively, and three initial rotation cases, $\theta_0/\alpha = 0.25$, 0.50 and 0.75.

Regarding the rigid body with the varying damping ratio values, it is interesting to note that the energy loss is not monotonic with respect to ζ and it is lower than the one predicted by Housner for realistic ζ values, which is in agreement with most experimental results showing that Housner overestimates the energy loss. Regarding the almost infinitely damped body with varying ϵ_0 values, it can be seen that elastic bodies (larger ϵ_0 values) present a complicated response, where the energy loss can be either lower or larger than the one predicted by Housner. It is clear that in all cases, as $\epsilon_0 \to 0$ and $\zeta \to \infty$, the modified energy loss ratio matches the one by Housner.

6.6 Effect of parameters on the deformable rocking body response

In this section, a deformable body with width $B = 1$ m, depth $d = 1$ m and slenderness ratio $\alpha = 0.2$ is considered. The basic model examined has $\epsilon_0 = 5 \cdot 10^{-6}$ and $\zeta = 5\%$, while it is considered elastic ($\sigma_y \to -\infty$) and the friction coefficient between the rocking body and the rocking surface is assumed infinite. For simplification, the concentrated mass approach is followed again, as in the rigid body cases examined previously, since the deformations are still small enough, so that the mass distribution is not altered significantly.

The response of the aforementioned rocking body to free oscillations with $\theta_0/\alpha = 0.5$ (the rotations are measured at the center of the element), a sine pulse with $\omega_p = 6p$ and $a_p = 2\alpha g$ and the Northridge excitation are shown in Figs. 6.13, 6.14 and 6.15, respectively. In the same figure, the response of a rigid body with Housner's coefficient of restitution, $r_{\mathrm{H}} = 0.8851$, is shown, as well as the response when a modified coefficient of restitution $r_{\mathrm{m}} = 0.9256$ is used, so that the rotation at the end of the first half-cycle of the free oscillations is matched.

From Figs. 6.13, 6.14, 6.15 it is clear that, although the rigid body solution cannot fully match the response produced by the macroelement, it is much closer than the rigid body solution with Housner's coefficient of restitution. As mentioned above, small discrepancies between the macroelement and the modified rigid body solution are also expected due to the linearizations performed in the macroelement formulation. It should be also noted that due to the more realistic values used for ϵ_0 and ζ in this model, the rotational velocity becomes almost zero at the end of the earthquake excitation (Fig. 6.15), in contrast to the infinitely damped rigid body response (Fig. 6.9).

In Fig. 6.16, 6.17 and 6.18, the response of the deformable rocking body under the same excitations is shown for different ϵ_0 and ζ values than the ones used for the basic model described above. It is evident that generally both parameters have an effect on the response. Regarding the parameter ϵ_0, it is interesting to note that, regarding the earthquake excitation, higher values (more flexible bodies) may either lead to larger rotation values ($\epsilon_0 = 5 \cdot 10^{-5}$) or even a much different response, where the body stops rocking and sticks to the rocking surface ($\epsilon_0 = 10^{-4}$). Is is noted that the transition between rocking and sticking is determined automatically by the macroelement and does not need an additional assumption usually used in literature (e.g. Oliveto et al., 2003; Acikgoz and DeJong, 2012). Regarding the damping ratio ζ, it can be seen that the energy loss is not always monotonic with respect to ζ, a phenomenon was also mentioned earlier regarding the curves of Figs. 6.10, 6.11, 6.12. Furthermore, it can be seen in the earthquake excitation that the (not practically used) cases $\zeta = 1000\%$ and $\zeta = 10000\%$ (overcritical damping in the dynamic analysis of conventional structures) present a response that

cannot be fully damped at the end of the response, just like in Figs. 6.7 and 6.9.

In Figs. 6.19, 6.20 and 6.21, the response of the rocking body is shown for different yield stress values, which are presented using the dimensionless parameter σ_{r}:

$$\sigma_{\mathrm{r}} = -\frac{\rho g H}{\sigma_y} \tag{6.57}$$

which is the ratio of the initial stress at the contact interface due to the self-weight of the body to the yield stress. In addition to the rotation at the center of the rocking body, the plastic displacement distributions at the base of the rocking body at the last time of the response shown is also presented. It can be seen that, although inelasticity does not significantly alter the rotation of the body, at least for the free rocking and sine pulse cases, the induced plastic displacements are different. It should be noted that the plastic displacement distributions are bilinearized between control points as explained previously for computational reasons.

The effect of the friction coefficient, μ, is examined next. The cases examined until now correspond to $\mu \to \infty$, meaning that relative displacement between the rocking body and the rocking surface is allowed only during complete separation (upthrow), when no axial force develops between them. The central rotation, as well as the horizontal slip of the body, which also includes its horizontal displacement in mid-air, are presented in Figs. 6.22, 6.23 and 6.24 for different values of the friction coefficient, μ. Generally, it can be seen that complete detachment of the body from the rocking surface happens during impacts, since horizontal slips are present even for $\mu \to \infty$, which allows slips only during upthrow. Furthermore, the response corresponding to $\mu = 0.2$ is interesting, since a large horizontal slip due to friction is evident at the beginning of the sine pulse and earthquake excitations, changing its response, which continues to diverge from the other responses until the end.

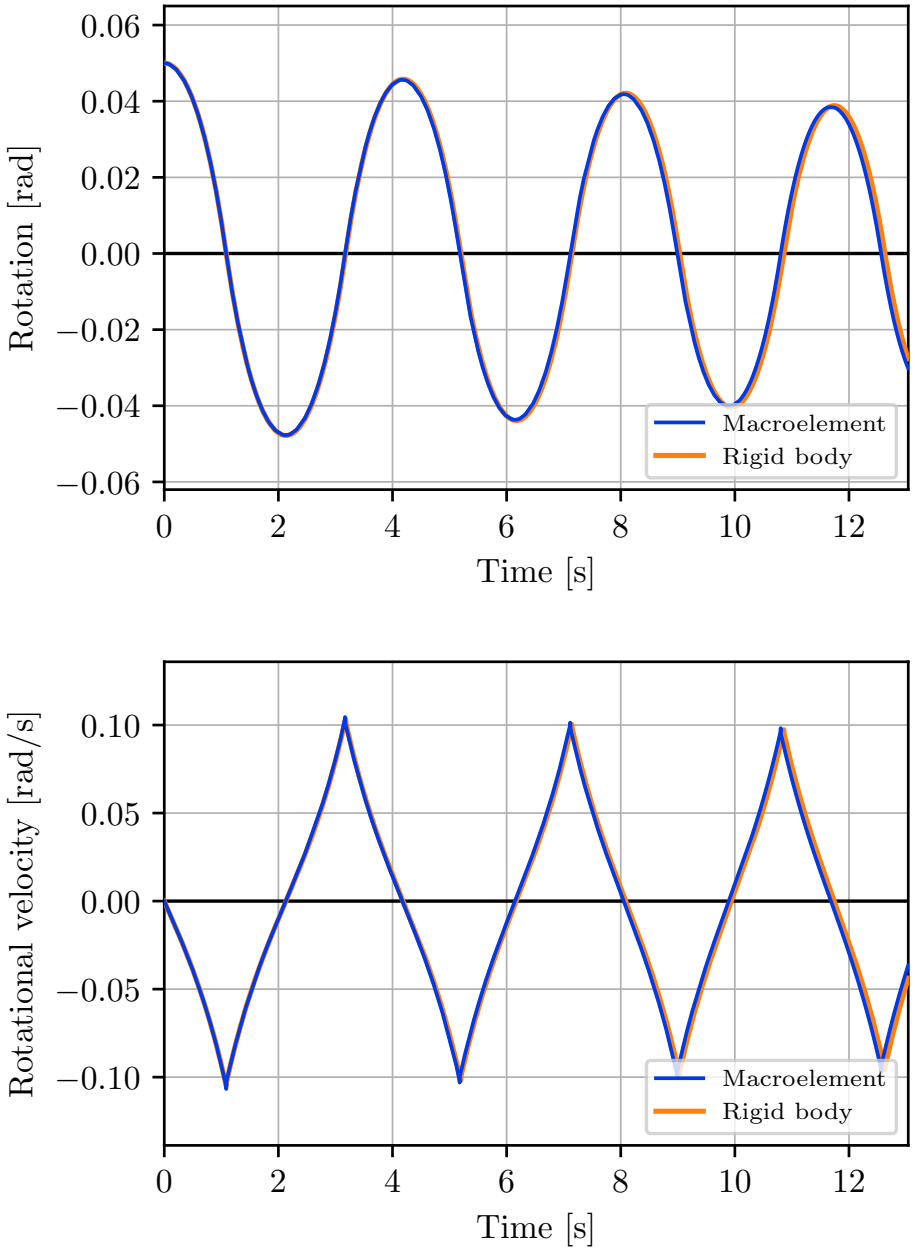

Figure 6.5: Rotation and rotational velocity for free oscillations of rigid rocking blocks with $\theta_0/\alpha = 0.5$ for $\alpha = 0.1$, as given by the macroelement (blue lines) and the analytical solution (orange lines).

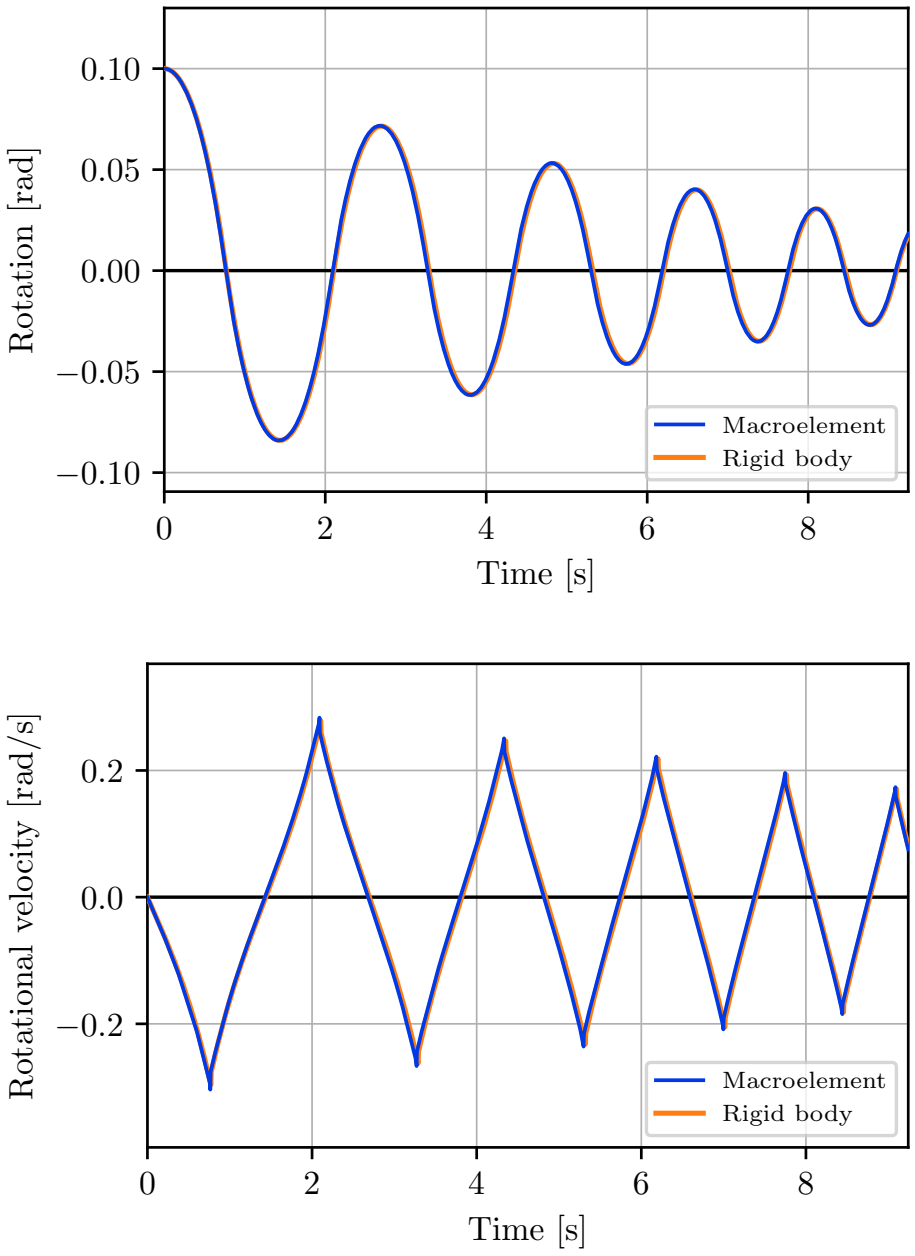

Figure 6.6: Rotation and rotational velocity for free oscillations of rigid rocking blocks with $\theta_0/\alpha = 0.5$ for $\alpha = 0.2$, as given by the macroelement (blue lines) and the analytical solution (orange lines).

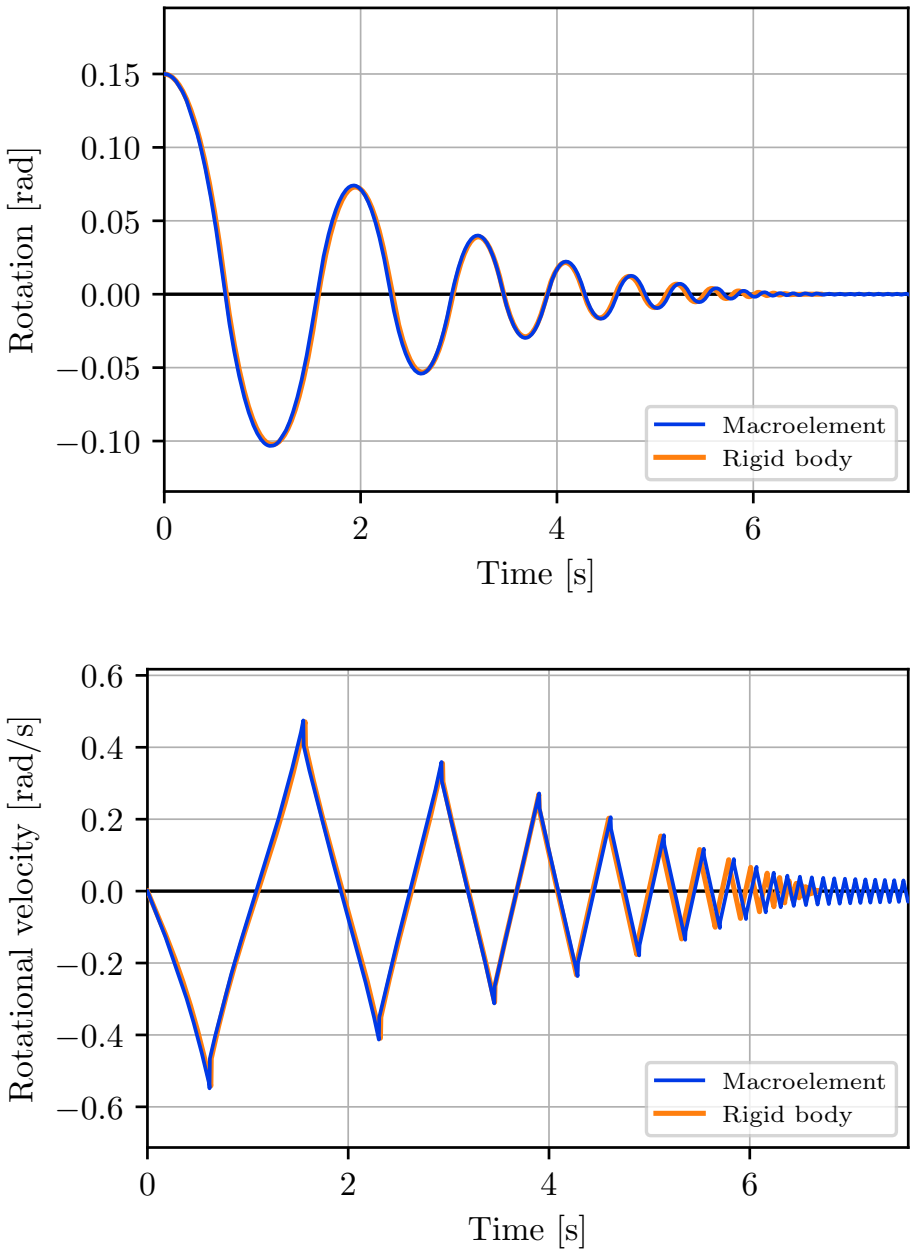

Figure 6.7: Rotation and rotational velocity for free oscillations of rigid rocking blocks with $\theta_0/\alpha = 0.5$ for $\alpha = 0.3$, as given by the macroelement (blue lines) and the analytical solution (orange lines).

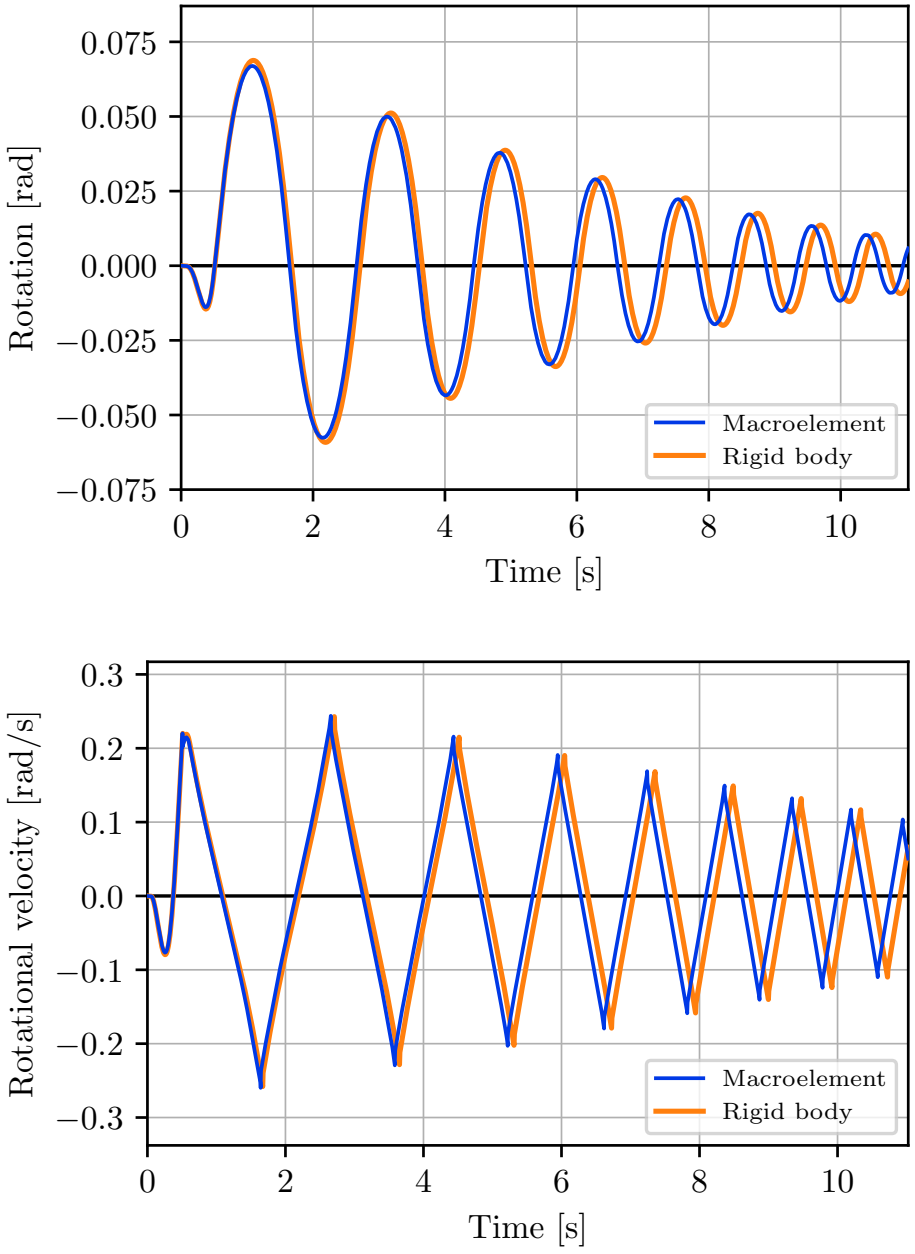

Figure 6.8: Rotation and rotational velocity of a rigid rocking block with $\alpha = 0.2$ for a sinusoidal excitation with $\omega_p = 6p$ and $a_p = 2\alpha g$, as given by the macroelement (blue lines) and the rigid body solution (orange lines).

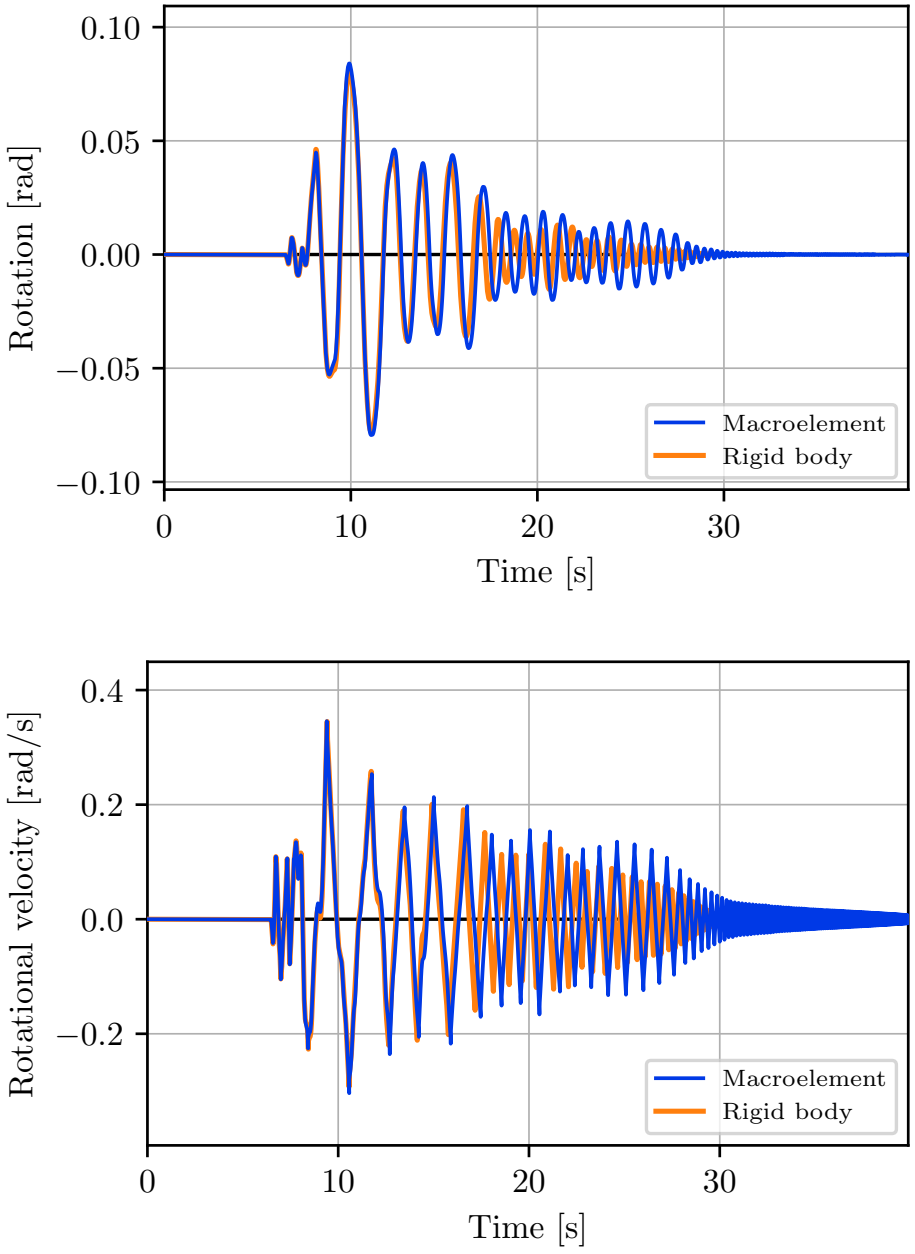

Figure 6.9: Rotation and rotational velocity of a rigid rocking block with $\alpha = 0.2$ for the 1994 Northridge ground motion, as given by the macroelement (blue lines) and the rigid body solution (orange lines).

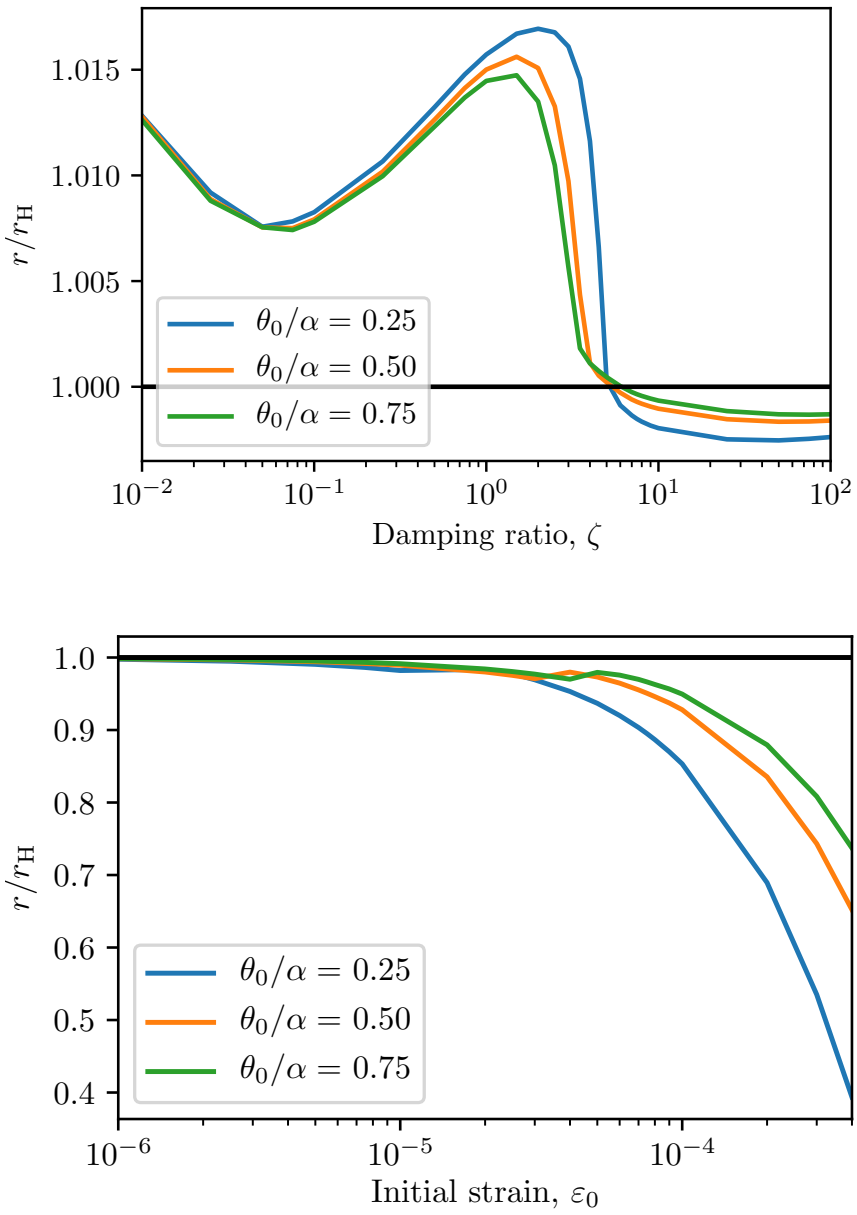

Figure 6.10: Ratio of the modified (kinetic energy) coefficient of restitution to Housner's coefficient of restitution for a rigid body with varying ζ values (top) and for an almost infinitely damped body with varying ϵ_0 values (bottom). The slenderness ratio considered is $\alpha = 0.1$.

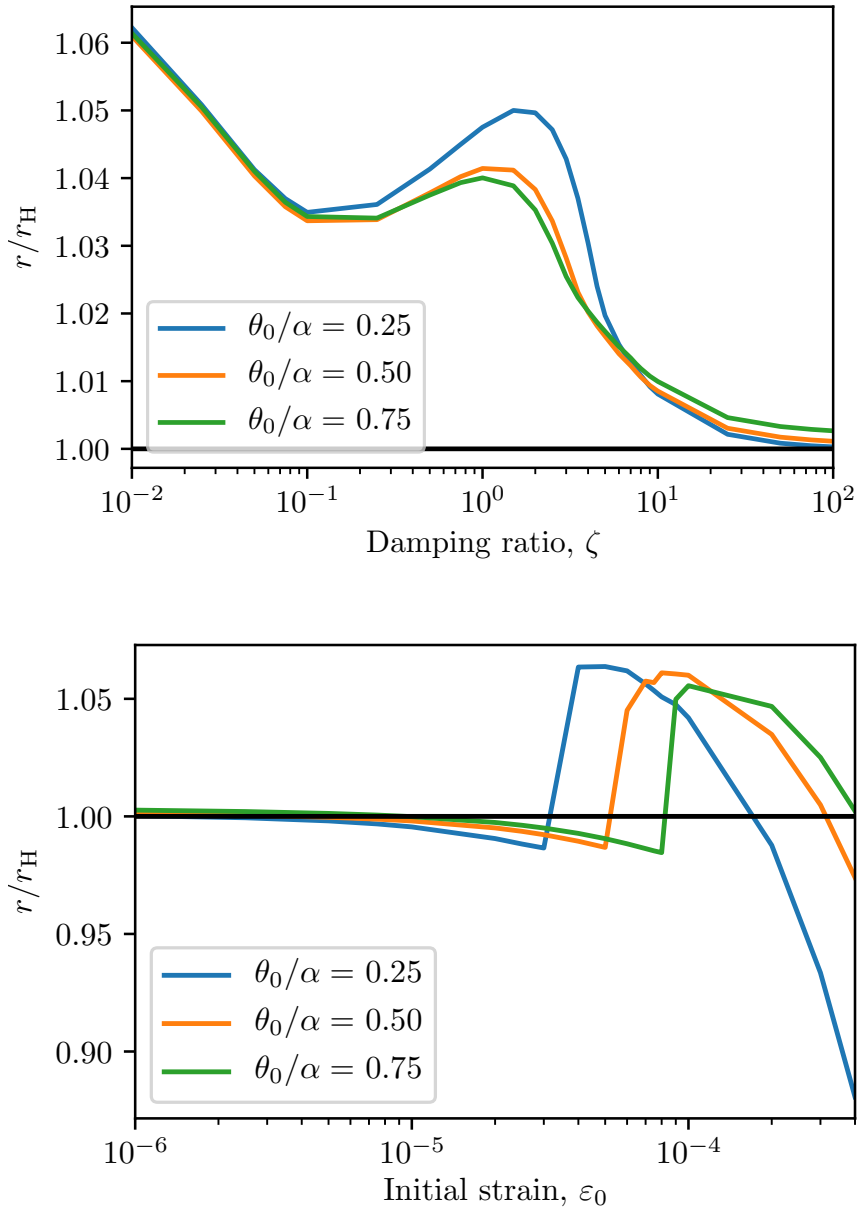

Figure 6.11: Ratio of the modified (kinetic energy) coefficient of restitution to Housner's coefficient of restitution for a rigid body with varying ζ values (top) and for an almost infinitely damped body with varying ϵ_0 values (bottom). The slenderness ratio considered is $\alpha = 0.2$.

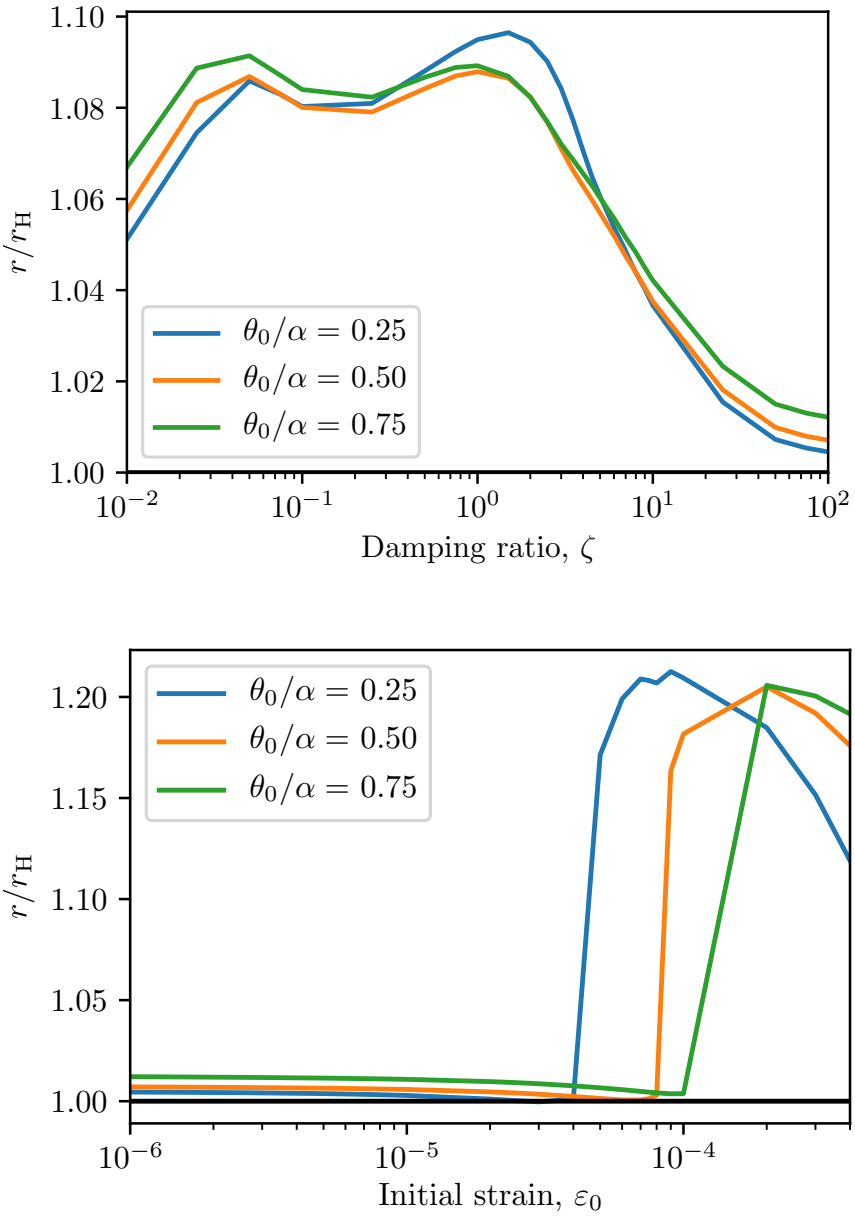

Figure 6.12: Ratio of the modified (kinetic energy) coefficient of restitution to Hounser's coefficient of restitution for a rigid body with varying ζ values (top) and for an almost infinitely damped body with varying ϵ_0 values (bottom). The slenderness ratio considered is $\alpha = 0.3$.

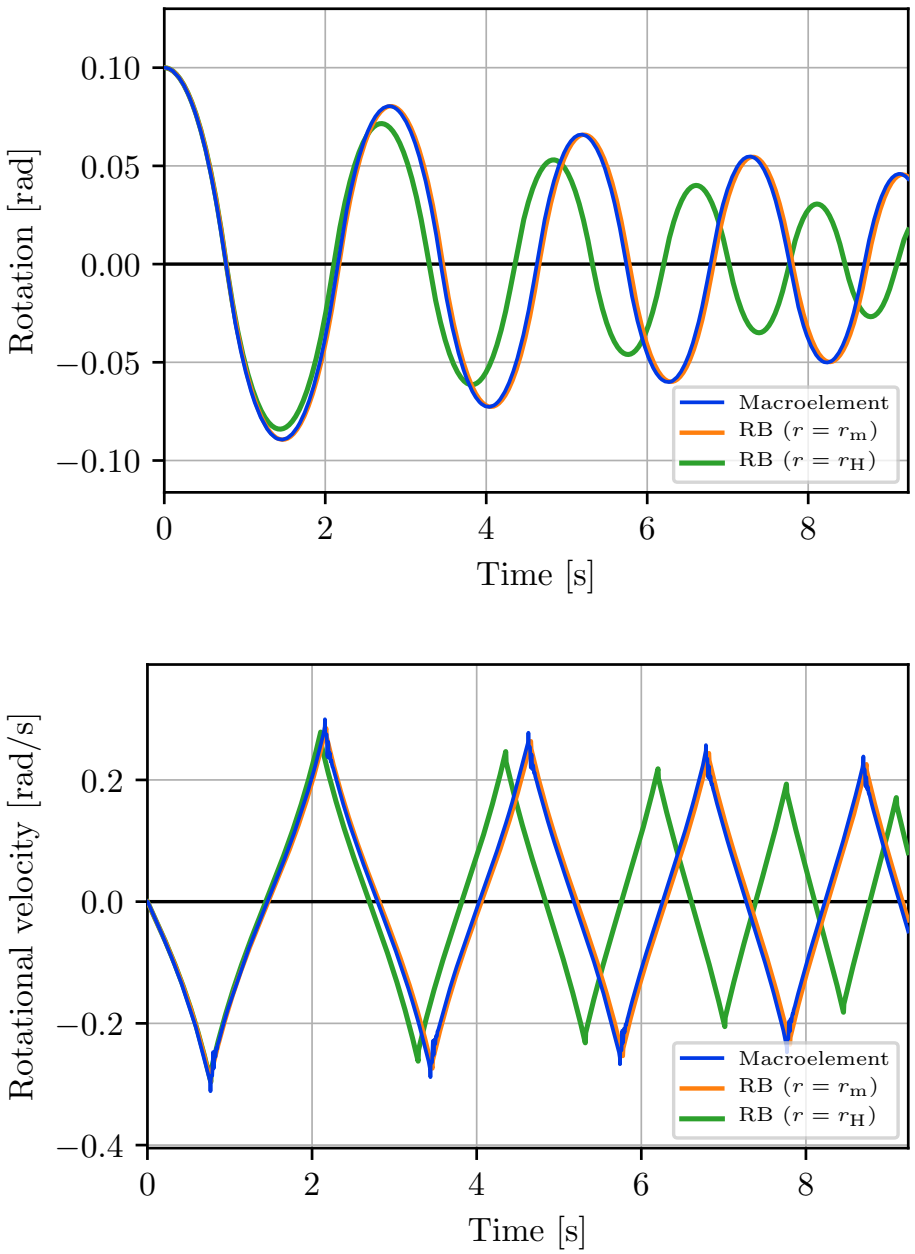

Figure 6.13: Rotation and rotational velocity of the deformable rocking body with $\epsilon_0 = 5 \cdot 10^{-6}$ and $\zeta = 5\%$ under free oscillations with $\theta_0/\alpha = 0.5$, as given by the macroelement (blue lines), the rigid body solution with the modified coefficient of restitution (orange lines) and the rigid body solution with the original coefficient of restitution (green lines).

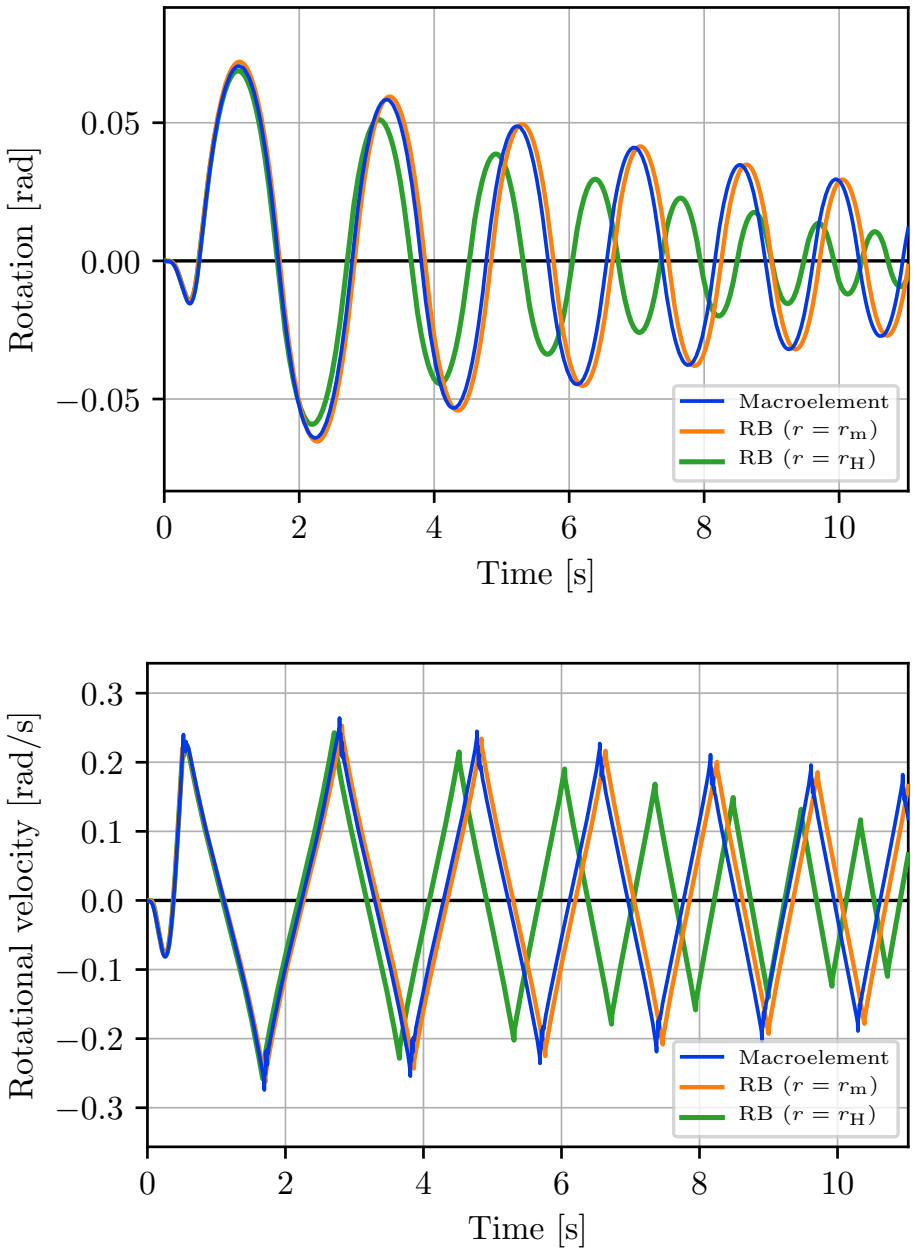

Figure 6.14: Rotation and rotational velocity of the deformable rocking body with $\epsilon_0 = 5 \cdot 10^{-6}$ and $\zeta = 5\%$ under a sine pulse excitation with $\omega_p = 6p$ and $a_p = 2\alpha g$, as given by the macroelement (blue lines), the rigid body solution with the modified coefficient of restitution (orange lines) and the rigid body solution with the original coefficient of restitution (green lines).

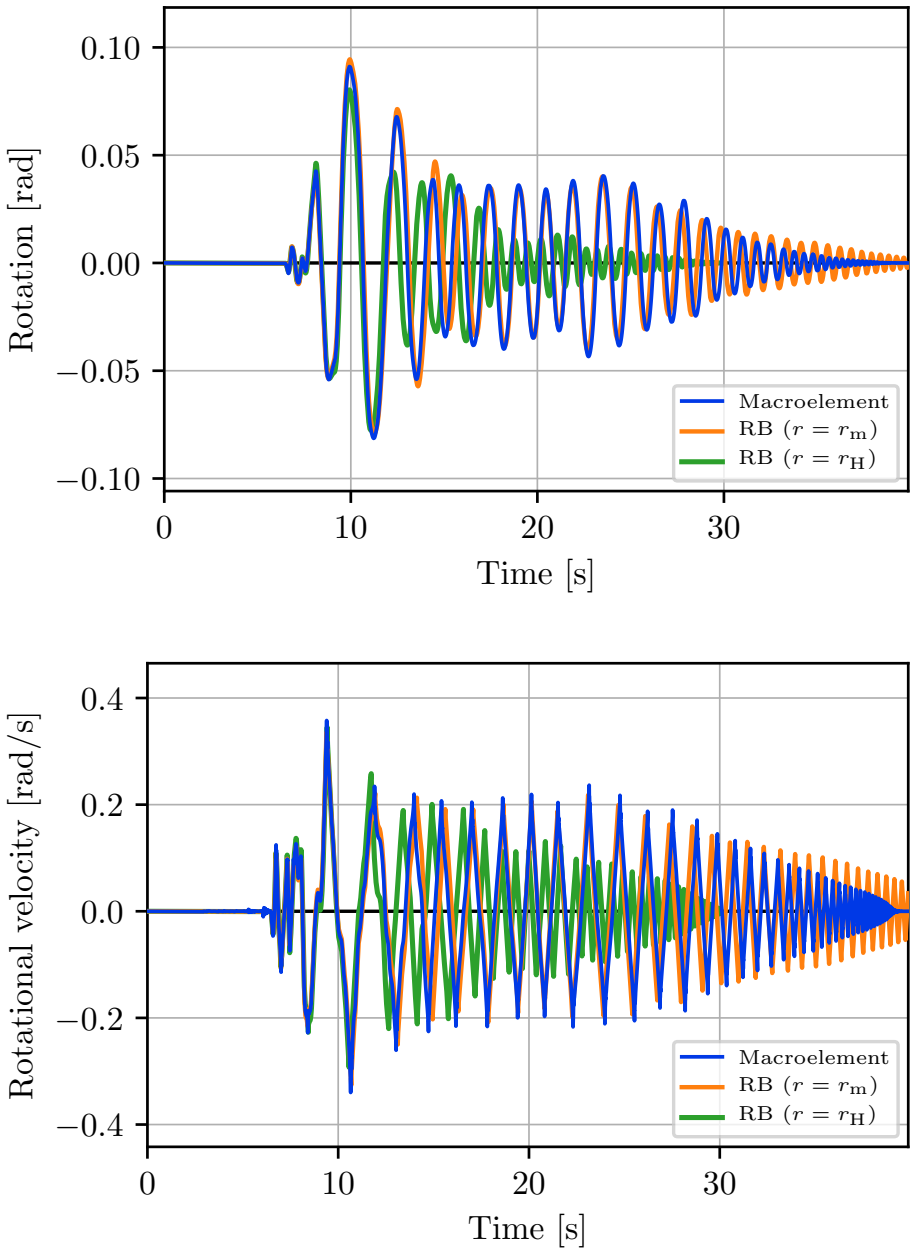

Figure 6.15: Rotation and rotational velocity of the deformable rocking body with $\epsilon_0 = 5 \cdot 10^{-6}$ and $\zeta = 5\%$ under the 1994 Northridge ground motion, as given by the macroelement (blue lines), the rigid body solution with the modified coefficient of restitution (orange lines) and the rigid body solution with the original coefficient of restitution (green lines).

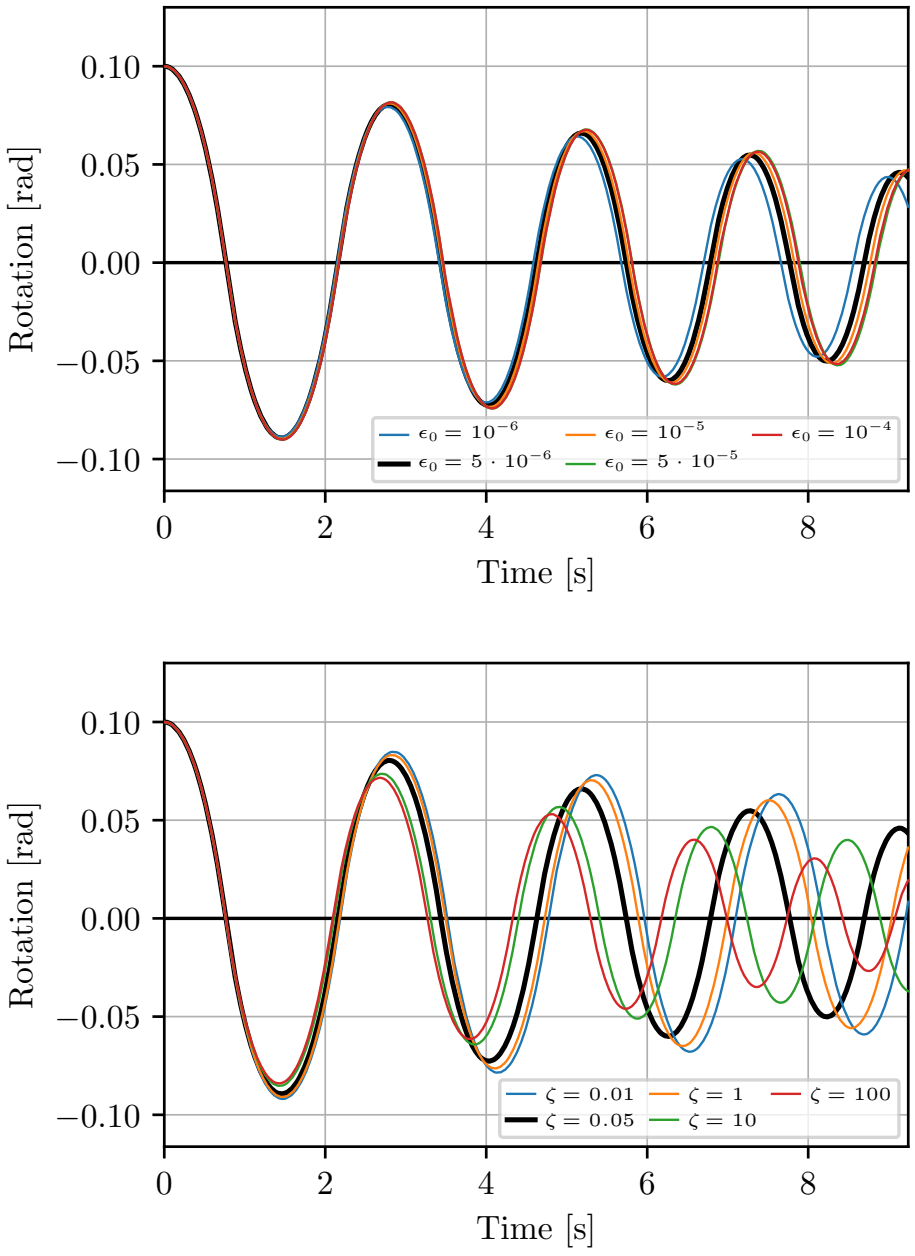

Figure 6.16: Central rotation of the deformable rocking body with different ϵ_0 (top) and ζ (bottom) values under free oscillations with $\theta_0/\alpha = 0.5$

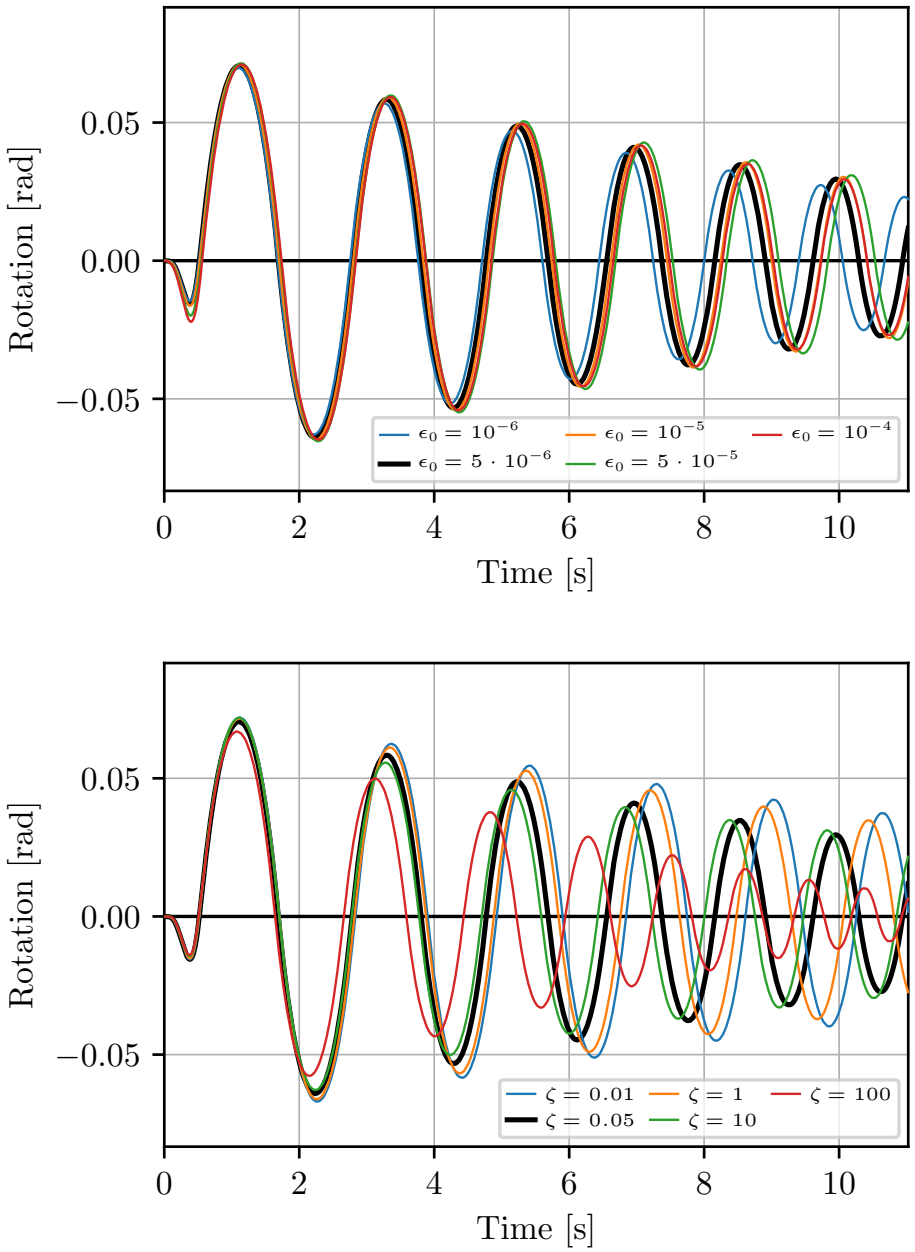

Figure 6.17: Central rotation of the deformable rocking body with different ϵ_0 (top) and ζ (bottom) values under a sine pulse excitation with $\omega_p = 6p$ and $a_p = 2\alpha g$

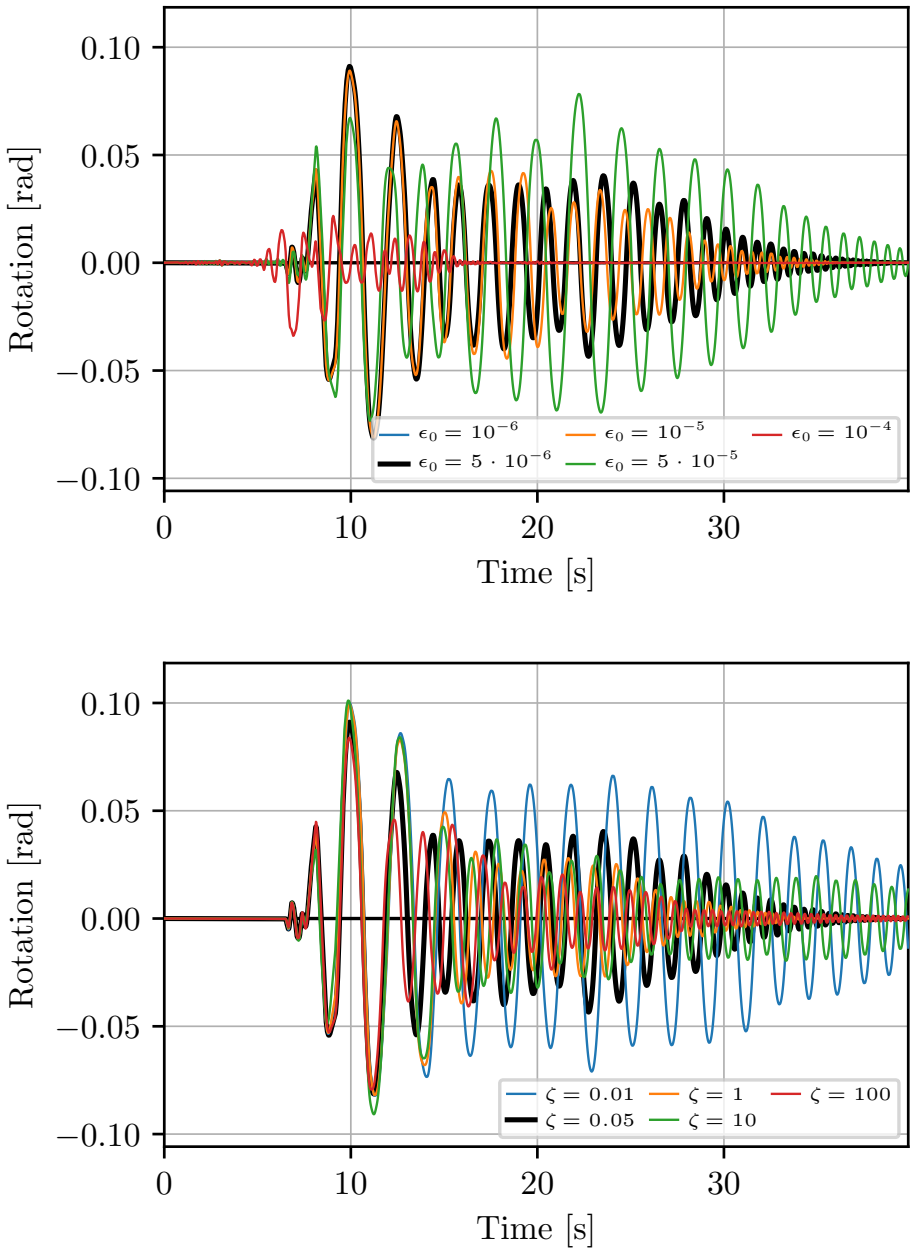

Figure 6.18: Central rotation of the deformable rocking body with different ϵ_0 (top) and ζ (bottom) values under the 1994 Northridge ground motion.

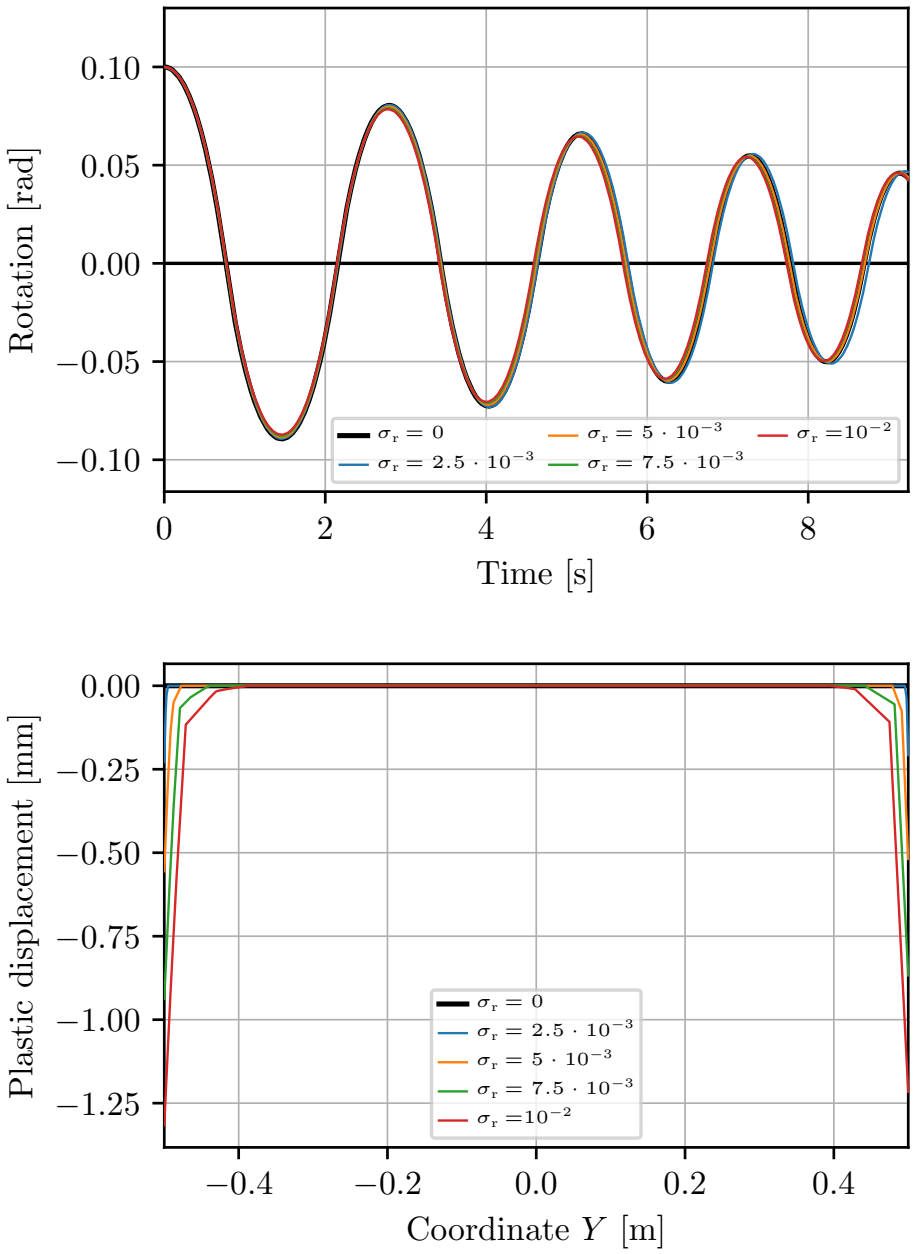

Figure 6.19: Central rotation and plastic displacement distribution at the base of the deformable rocking body at the end of the presented response for different σ_r values under free oscillations with $\theta_0/\alpha = 0.5$

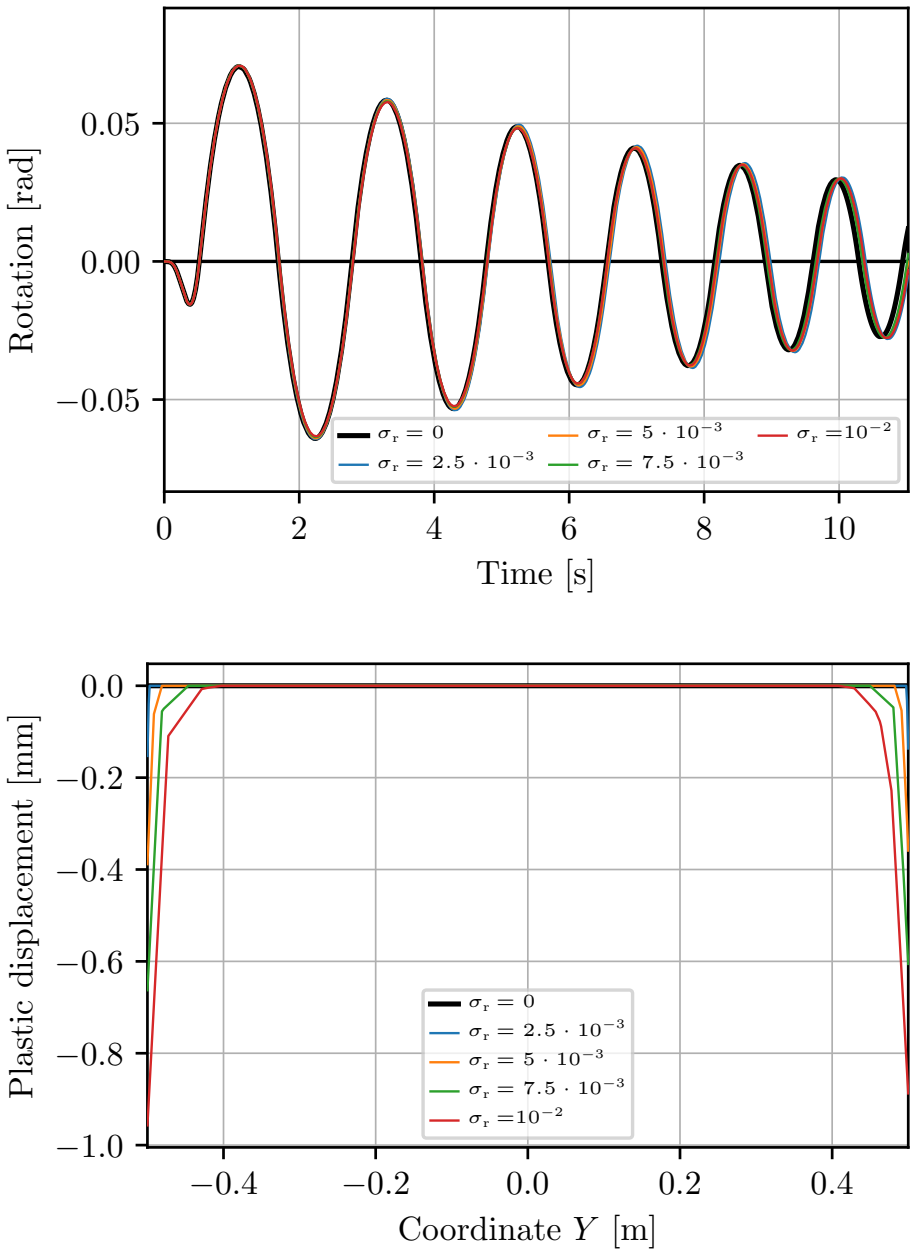

Figure 6.20: Central rotation and plastic displacement distribution at the base of the deformable rocking body at the end of the presented response for different σ_r values under a sine pulse excitation with $\omega_p = 6p$ and $a_p = 2\alpha g$.

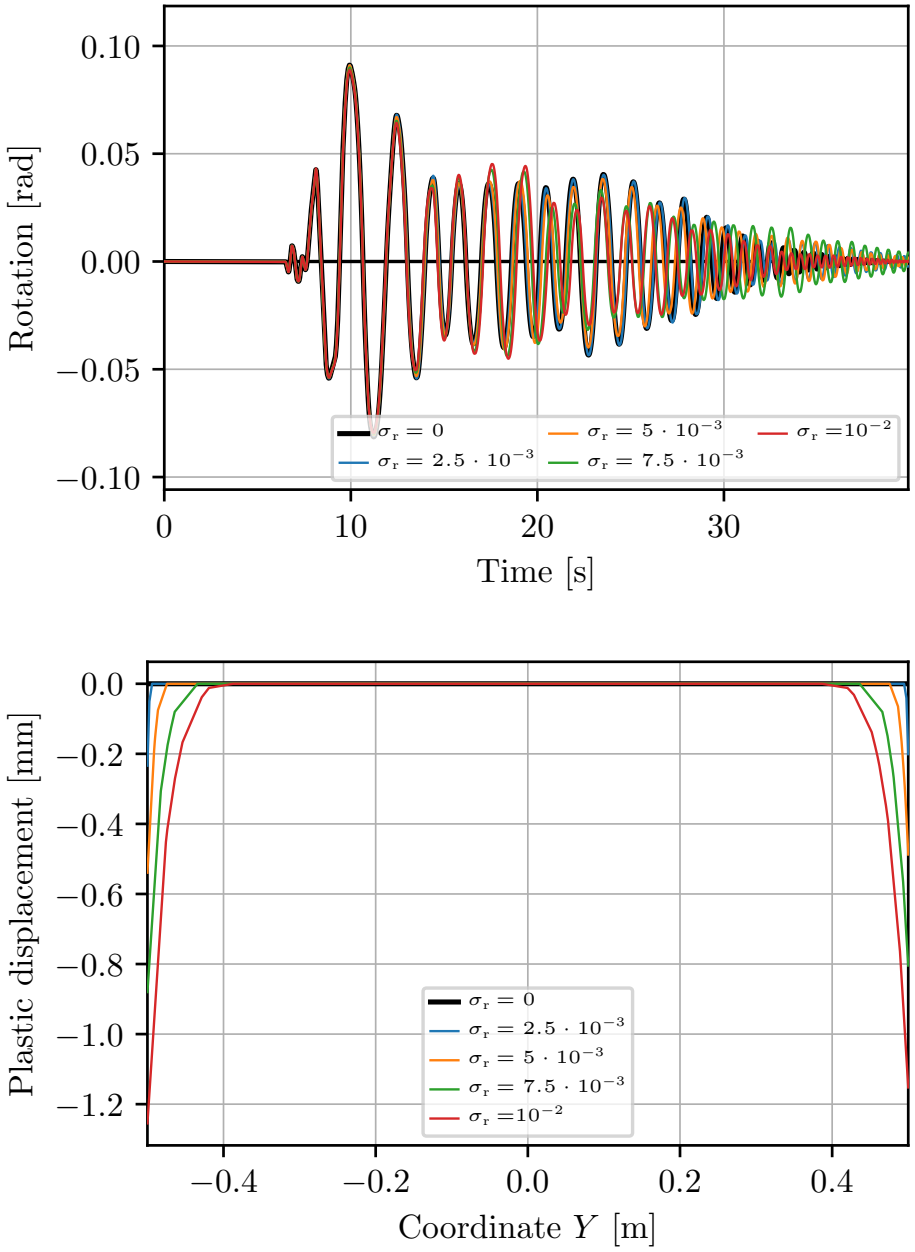

Figure 6.21: Central rotation and plastic displacement distribution at the base of the deformable rocking body at the end of the presented response for different σ_r values under the 1994 Northridge ground motion.

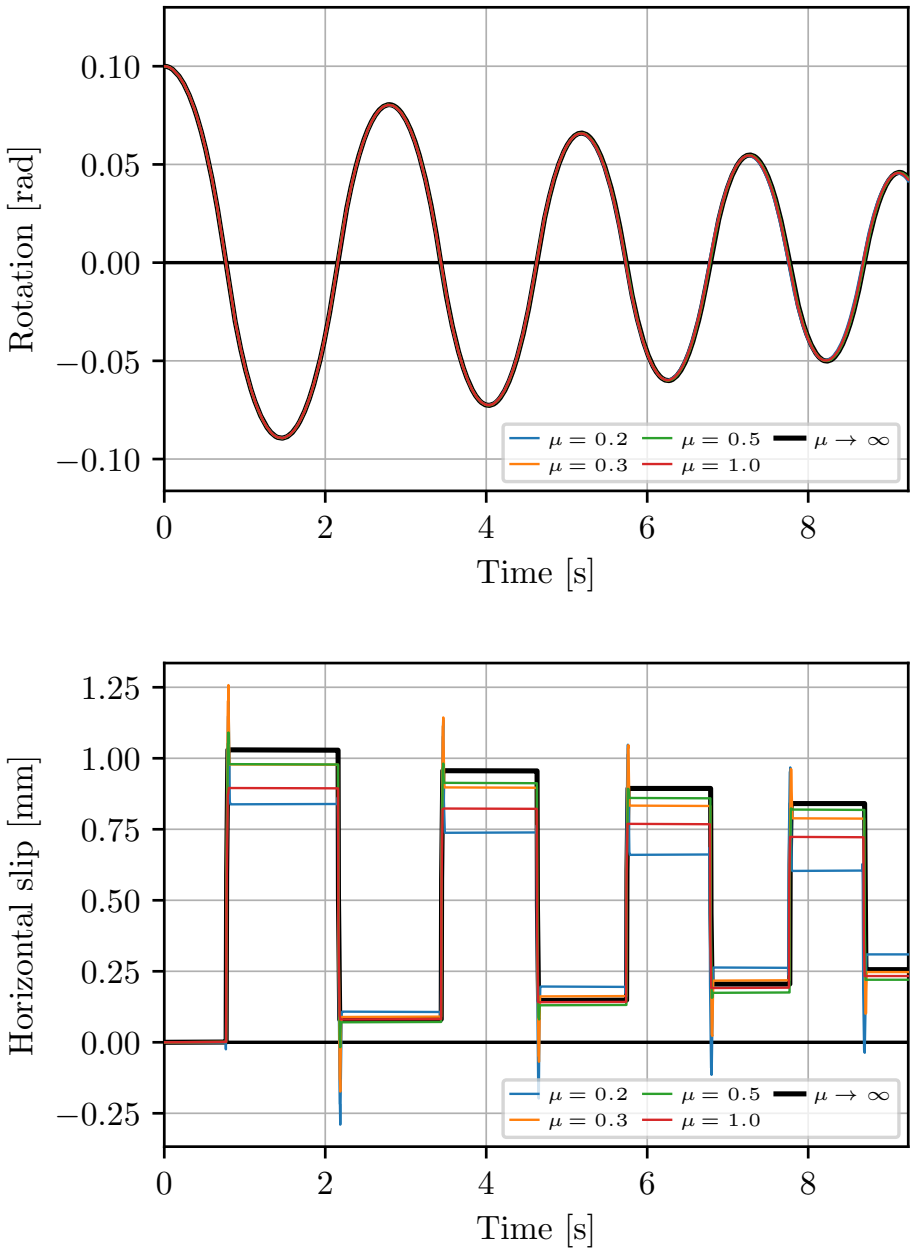

Figure 6.22: Central rotation and horizontal slip for different μ values under free oscillations with $\theta_0/\alpha = 0.5$.

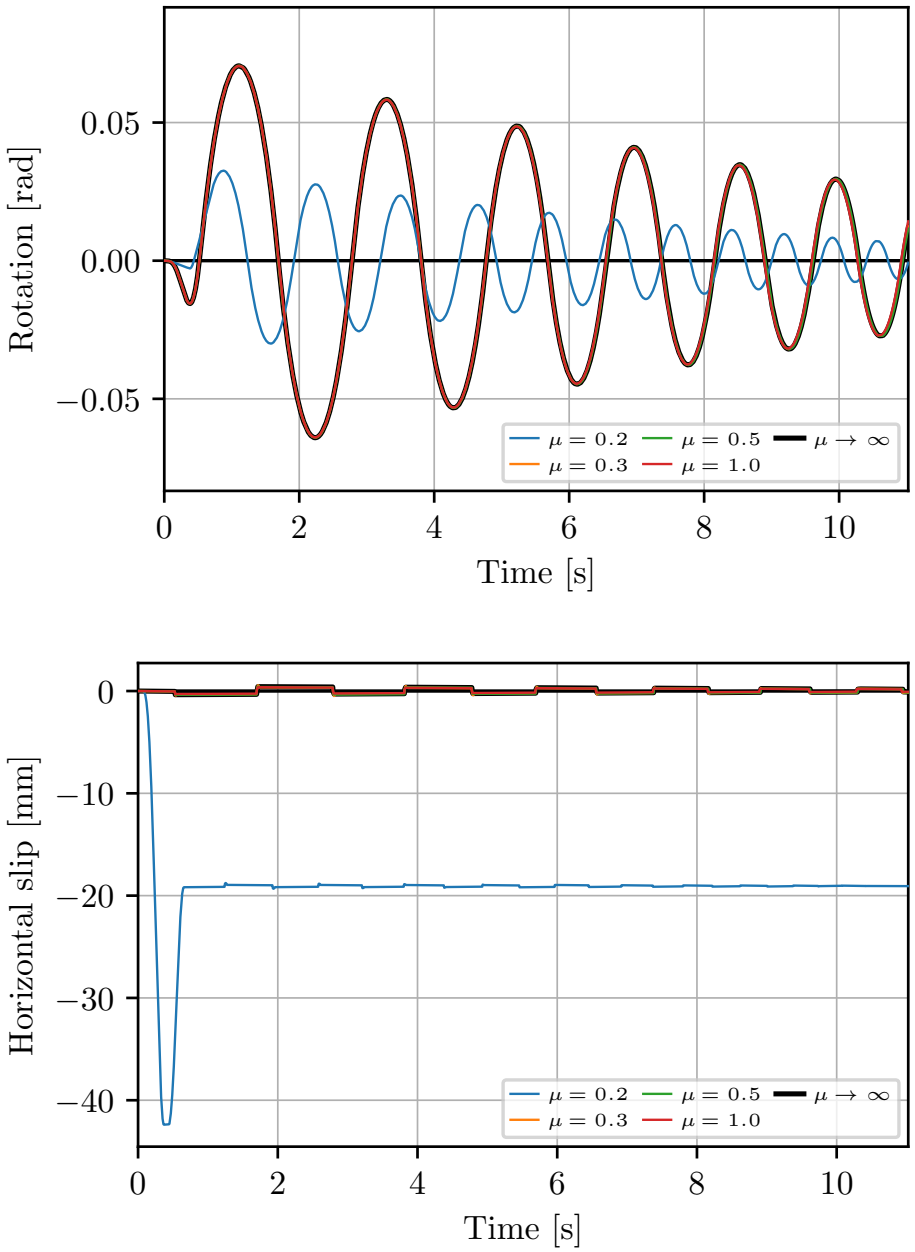

Figure 6.23: Central rotation and horizontal slip for different μ values under a sine pulse excitation with $\omega_p = 6p$ and $a_p = 2\alpha g$.

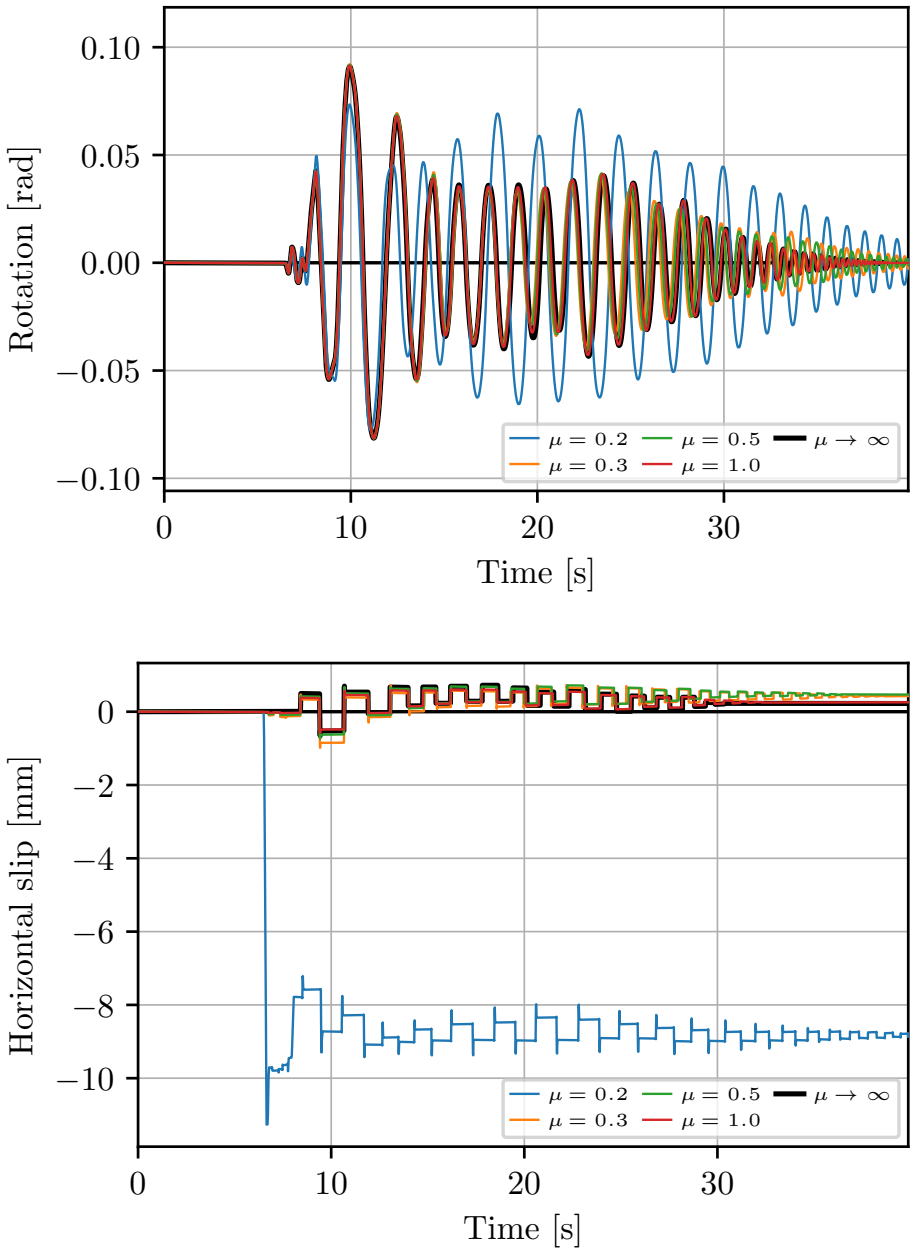

Figure 6.24: Central rotation and horizontal slip for different μ values under the 1994 Northridge ground motion.

7 Conclusions

In this dissertation, a macroelement formulation for deformable rocking bodies was proposed. The elastic formulation was presented first, showing that rocking and member deformability are in reality not separate phenomena. Since near the rocking interface member sections do not remain plane, the technical theory of bending usually used in beam-column finite element formulations is insufficient for the prediction of the response of rocking members and the semi-infinite strip problem solution based on the theory of elasticity was used to examine the effect of the stress nonlinearity locally near the rocking interface. The results of the semi-infinite strip problem were incorporated into a force beam-column finite element formulation to account for the additional displacements produced by the nonlinear stress distribution across the rocking interface. The excellent accuracy of the elastic macroelement was proven by comparison of the results produced using the macroelement for characteristic rocking body configurations with the ones of corresponding models using the commercial finite element program Abaqus. Furthermore, it was shown that for members under large axial forces, the deformability of the body plays an important role on their response, while some first results showed the beneficial role of the inclusion of rocking members in frames on their seismic response.

In order to account for material inelasticity, the monotonic case can be easily treated by extending the expressions of the additional displacements due to the self-equilibrating stresses to correspond to the yielding stress distributions. However, the same procedure cannot be applied for cyclic loading, due to the complex stress and plastic displacement distributions created during motion reversal. In order to solve this problem, the displacement distribution of the rocking end under an arbitrary stress distribution must be determined first, which is achieved by integrating the proposed analytical expressions regarding the action of a concentrated load at an arbitrary position of the semi-infinite strip end. It was shown using these expressions that even for an elastic body, both the stress distribution across the contact zone and the shape of the rocking end not in contact with the rocking surface are nonlinear.

The previous analytical expressions were incorporated in an algorithm for the prediction of the response of inelastic rocking bodies under cyclic loading, which is based on the determination of a suitable stress distribution across the rocking interface, so that the produced displacements, in addition to the preexisting plastic ones, match the target member rocking end displacements. The shape of the produced stress and plastic displacement distributions under cyclic loading was discussed, while the results produced for rocking wall configurations found in literature were compared with experimental ones, showing that despite the simplicity of the material law assumed, the main characteristics of the cyclic response can be adequately captured. Furthermore, by comparing the previous results with ones corresponding to models where the rocking members are considered to be rigid or elastic, it was shown that both deformability and inelasticity must be appropriately taken into account for a more accurate prediction of the rocking response.

The previous formulation was finally extended to examine the dynamic response by including a suitable treatment of damping and other motion modes, namely upthrow and sliding, which usually coexist together with rocking. Regarding the treatment of damping, a damping formulation similar to tangent-stiffness-proportional damping is employed, while paying special attention so that the sum of the deformation-inducing and damping stresses across the rocking interface is always non-tensile. This constraint limits the maximum deformation-inducing stresses that may develop at each step. In order to account for sliding and upthrow, which is considered as a special case of sliding for zero axial force, a new variable denoting the displacement due to sliding and a new intermediate coordinate system are introduced, while sliding is determined so that a Coulomb friction criterion is satisfied at each step.

The proposed formulation can be implemented in any finite element framework, yielding much faster analyses than conventional finite element codes, while providing very good accuracy. It was mainly formulated for the investigation of the response of rocking members used in earthquake-resilient structural configurations found in literature, which develop large axial forces during their motion and as a result their deformability and inelasticity must be taken into account for an accurate prediction of their response. It is believed that the proposed macroelement will provide more confidence to the engineers regarding the computational analysis of structural configurations involving rocking members, which are considered a much promising solution for the improvement of the seismic performance of newly designed or retrofitted structures, assisting the documentation of the codes regarding their design and promoting the scientific progress in this important area.

However, the macroelement can also provide interesting results for the dynamic response of free-standing bodies, especially with what regards the interaction between rocking, sliding, upthrow, deformability, inelasticity and damping during impacts. This is why it is believed that it will contribute to the advancement of the investigation of the response

of solitary rocking bodies, since existing rigid body solutions cannot take into account the aforementioned interactions and their outcome during impacts.

Some aspects worth researching further are:

- More thorough investigation of the interaction between rocking, sliding, upthrow, deformability, inelasticity and damping during impacts.
- Determination of the apparent coefficient of restitution for deformable rocking members with a wide range of properties and assessment of its ability to describe the energy loss during their motion under arbitrary dynamic loads.
- Investigation of the improvement of the seismic response of structures by using rocking over conventional yielding members and examination of optimum rocking member configurations.
- Extension of the macroelement to three-dimensional rocking bodies*.
- Extension of the macroelement to take into account large rotations, so that the response of squat solitary rocking bodies can be determined more accurately.
- Extension of the macroelement to take into account mild steel rebars or other partial connections at the rocking interface, which exist in some of the rocking member configurations found in literature and influence the rocking motion, especially during cyclic loading.

*A simple elastic three-dimensional rocking member with interaction of the rocking components about the two perpendicular axes only along the member parallel axis has already been implemented by the author.

References

Aaleti, S. and Sritharan, S. (2009). "A simplified analysis method for characterizing unbonded post-tensioned precast wall systems". In: *Engineering Structures* 31.12, pp. 2966–2975.

Abaqus/CAE: User's Manual (6.11) (2011). Dassault Systemes. Providence, Rhode Island, United States.

Acikgoz, S. and DeJong, M. J. (2012). "The interaction of elasticity and rocking in flexible structures allowed to uplift". In: *Earthquake Engineering & Structural Dynamics* 41.15, pp. 2177–2194.

Acikgoz, S. and DeJong, M. J. (2016). "Analytical modelling of multi-mass flexible rocking structures". In: *Earthquake engineering & structural dynamics* 45.13, pp. 2103–2122.

Ajrab, J. J., Pekcan, G., and Mander, J. B. (2004). "Rocking wall-frame structures with supplemental tendon systems". In: *Journal of Structural Engineering* 130.6, pp. 895–903.

Allen, R., Oppenheim, I., Parker, A., and Bielak, J (1986). "On the dynamic response of rigid body assemblies". In: *Earthquake engineering & structural dynamics* 14.6, pp. 861–876.

American Concrete Institute (ACI) (2003). "Special Hybrid Moment Frames Composed of Discretely Jointed Precast and Post-Tensioned Concrete Members". In: *ACI T1.2-03, ACI T1.2R-03,* Farmington Hills, Michigan, United States.

Anooshehpoor, A., Heaton, T. H., Shi, B., and Brune, J. N. (1999). "Estimates of the ground accelerations at Point Reyes Station during the 1906 San Francisco earthquake". In: *Bulletin of the Seismological Society of America* 89.4, pp. 845–853.

Avgenakis, E. (2015). "Modeling of rocking flexible bodies considering the deformability of their base". MA thesis. Greece: National Technical University of Athens.

Avgenakis, E. and Psycharis, I. N. (2017). "Modeling of rocking elastic flexible bodies under static loading considering the nonlinear stress distribution at their base". In: *Journal of Structural Engineering* 143.7, p. 04017051.

Bachmann, J., Strand, M, Vassiliou, M., Broccardo, M., and Stojadinović, B. (2018). "Is rocking motion predictable?" In: *Earthquake Engineering & Structural Dynamics* 47.2, pp. 535–552.

Bachmann, J. A., Vassiliou, M. F., and Stojadinović, B (2017). "Dynamics of rocking podium structures". In: *Earthquake Engineering & Structural Dynamics* 46.14, pp. 2499–2517.

Bachmann, J. A., Vassiliou, M. F., and Stojadinovic, B. (2019). "Rolling and rocking of rigid uplifting structures". In: *Earthquake Engineering & Structural Dynamics*.

Barthes, C. B. (2012). "Design of Earthquake Resistant Bridges Using Rocking Columns". PhD thesis. Berkeley, California, United States: University of California.

Belleri, A., Torquati, M., and Riva, P. (2013). "Finite element modeling of "Rocking walls"". In: *Proc., 4th ECCOMAS thematic conference COMPDYN*. Proc., 4th ECCOMAS thematic conference COMPDYN.

Benthem, J. P. (1963). "A Laplace transform method for the solution of semi-infinite and finite strip problems in stress analysis". In: *The Quarterly Journal of Mechanics and Applied Mathematics* 16.4, pp. 413–429.

Bogy, D. B. (1975). "Solution of the plane end problem for a semi-infinite elastic strip". In: *Zeitschrift für angewandte Mathematik und Physik ZAMP* 26.6, pp. 749–769.

Boot, J. C. (1963). "On sensitivity analysis in convex quadratic programming problems". In: *Operations Research* 11.5, pp. 771–786.

Čeh, N., Jelenić, G., and Bićanić, N. (2018). "Analysis of restitution in rocking of single rigid blocks". In: *Acta Mechanica* 229.11, pp. 4623–4642.

Chancellor, N. B., Eatherton, M. R., Roke, D. A., and Akbaş, T. (2014). "Self-Centering Seismic Lateral Force Resisting Systems: High Performance Structures for the City of Tomorrow". In: *Buildings* 4.3, pp. 520–548.

Chatzis, M. and Smyth, A. (2011). "Robust modeling of the rocking problem". In: *Journal of Engineering Mechanics* 138.3, pp. 247–262.

Chatzis, M. and Smyth, A. (2012). "Modeling of the 3D rocking problem". In: *International Journal of Non-Linear Mechanics* 47.4, pp. 85–98.

Chatzis, M. and Smyth, A. (2013). "Three-dimensional dynamics of a rigid body with wheels on a moving base". In: *Journal of Engineering Mechanics* 139.4, pp. 496–511.

Chatzis, M., Espinosa, M. G., and Smyth, A. (2017). "Examining the energy loss in the inverted pendulum model for rocking bodies". In: *Journal of Engineering Mechanics* 143.5, p. 04017013.

Cheok, G. S. and Lew, H. (1993). "Model precast concrete beam-to-column connections subject to cyclic loading". In: *PCI journal* 38.4, pp. 80–92.

Chopra, A. K. and Yim, S. C.-S. (1985). "Simplified earthquake analysis of structures with foundation uplift". In: *Journal of Structural Engineering* 111.4, pp. 906–930.

Christopoulos, C., Filiatrault, A., and Folz, B. (2002). "Seismic response of self-centring hysteretic SDOF systems". In: *Earthquake engineering & structural dynamics* 31.5, pp. 1131–1150.

Das, B. M. (2013). *Advanced soil mechanics*. Crc Press.

De Borst, R., Crisfield, M. A., Remmers, J. J., and Verhoosel, C. V. (2012). *Nonlinear finite element analysis of solids and structures*. John Wiley & Sons.

DeJong, M. J. and Dimitrakopoulos, E. G. (2014). "Dynamically equivalent rocking structures". In: *Earthquake engineering & structural dynamics* 43.10, pp. 1543–1563.

Diamantopoulos, S. and Fragiadakis, M. (2019). "Seismic response assessment of rocking systems using single degree-of-freedom oscillators". In: *Earthquake Engineering & Structural Dynamics* 48.7, pp. 689–708.

Dimitrakopoulos, E. G. and DeJong, M. J. (2012). "Revisiting the rocking block: closed-form solutions and similarity laws". In: *Proceedings of the Royal Society of London A: Mathematical, Physical and Engineering Sciences*. Vol. 468. 2144. The Royal Society, pp. 2294–2318.

Dimitrakopoulos, E. G. and Giouvanidis, A. I. (2015). "Seismic response analysis of the planar rocking frame". In: *Journal of Engineering Mechanics* 141.7, p. 04015003.

Dimitrakopoulos, E. G. and Paraskeva, T. S. (2015). "Dimensionless fragility curves for rocking response to near-fault excitations". In: *Earthquake engineering & structural dynamics* 44.12, pp. 2015–2033.

ElGawady, M. A., Ma, Q., Butterworth, J. W., and Ingham, J. (2011). "Effects of interface material on the performance of free rocking blocks". In: *Earthquake Engineering & Structural Dynamics* 40.4, pp. 375–392.

Erkmen, B. and Schultz, A. E. (2009). "Self-centering behavior of unbonded, post-tensioned precast concrete shear walls". In: *Journal of Earthquake Engineering* 13.7, pp. 1047–1064.

European Committee for Standardization (CEN) (2004). "Eurocode 8: Design of structures for earthquake resistance, Part 1: General rules, seismic actions and rules for buildings". In: *European Standard EN 1998-1:2004,* Brussels, Belgium.

Fadle, J. (1940). "Die Selbstspannungs-Eigenwertfunktionen der quadratischen Scheibe". In: *Archive of Applied Mechanics* 11.2, pp. 125–149.

"FEMA-440, Improvement of nonlinear static seismic analysis procedures" (Federal Emergency Management Agency, 2005). In:

Gaydon, F. (1965). "The rectangle, under general equilibrium loading, in generalized plane stress". In: *Proceedings of the Royal Society of London A: Mathematical, Physical and Engineering Sciences*. Vol. 283. 1394. The Royal Society, pp. 356–378.

Gaydon, F. and Shepherd, W. (1964). "Generalized plane stress in a semi-infinite strip under arbitrary end-load". In: *Proceedings of the Royal Society of London A: Mathematical, Physical and Engineering Sciences*. Vol. 281. 1385. The Royal Society, pp. 184–206.

Giouvanidis, A. I. and Dimitrakopoulos, E. G. (2017a). "Nonsmooth dynamic analysis of sticking impacts in rocking structures". In: *Bulletin of Earthquake Engineering* 15.5, pp. 2273–2304.

Giouvanidis, A. I. and Dimitrakopoulos, E. G. (2017b). "Seismic performance of rocking frames with flag-shaped hysteretic behavior". In: *Journal of Engineering Mechanics* 143.5, p. 04017008.

Giouvanidis, A. I. and Dimitrakopoulos, E. G. (2018). "Rocking amplification and strong-motion duration". In: *Earthquake Engineering & Structural Dynamics* 47.10, pp. 2094–2116.

Goldfarb, D. and Idnani, A. (1983). "A numerically stable dual method for solving strictly convex quadratic programs". In: *Mathematical programming* 27.1, pp. 1–33.

Graziotti, F, Rossi, A, Mandirola, M, Penna, A, and Magenes, G (2016). "Experimental characterization of calcium-silicate brick masonry for seismic assessment". In: *16th International Brick and Block Masonry Conference, Padua, Italy*.

Gregory, R. (1980). "The traction boundary value problem for the elastostatic semi-infinite strip; existence of solution, and completeness of the Papkovich-Fadle eigenfunctions". In: *Journal of Elasticity* 10.3, pp. 295–327.

Guerrini, G., Restrepo, J. I., Massari, M., and Vervelidis, A. (2014). "Seismic behavior of posttensioned self-centering precast concrete dual-shell steel columns". In: *Journal of structural engineering* 141.4, p. 04014115.

Hewes, J. T. and Priestley, M. N. (2002). *Seismic design and performance of precast concrete segmental bridge columns*. Tech. rep.

Holden, T., Restrepo, J., and Mander, J. B. (2003). "Seismic performance of precast reinforced and prestressed concrete walls". In: *Journal of Structural Engineering* 129.3, pp. 286–296.

Horvay, G. (1957). "Biharmonic eigenvalue problem of the semi-infinite strip". In: *Quarterly of Applied Mathematics* 15.1, pp. 65–81.

Housner, G. W. (1963). "The behavior of inverted pendulum structures during earthquakes". In: *Bulletin of the seismological society of America* 53.2, pp. 403–417.

Housner, G. W. and Vreeland Jr., T. (1965). *The analysis of stress and deformation*. Pasadena, California, United States: California Institute of Technology.

Ichinose, T (1986). "Rocking motion of slender elastic body on rigid floor". In: *Bulletin of the New Zealand National Society for Earthquake Engineering* 19.1, pp. 18–27.

Institute, A. C. (2014). *Building Code Requirements for Structural Concrete and Commentary (ACI 318-14)*. American Concrete Institute. ACI.

International Federation for Structural Concrete (fib) (2003). "Seismic design of precast concrete building structures". In: *fib Bulletin no. 27,* Lausanne, Switzerland.

Ishiyama, Y. (1982). "Motions of rigid bodies and criteria for overturning by earthquake excitations". In: *Earthquake Engineering and Structural Dynamics* 10.5, pp. 635–650.

Johnson Jr, M. and Little, R. W. (1965). "The semi-infinite elastic strip". In: *Quarterly of Applied Mathematics* 22.4, pp. 335–344.

Jones, E., Oliphant, T., Peterson, P., et al. (2001–). *SciPy: Open source scientific tools for Python*. URL: http://www.scipy.org/.

Kalliontzis, D and Schultz, A. (2017). "Improved estimation of the reverse-cyclic behavior of fully-grouted masonry shear walls with unbonded post-tensioning". In: *Engineering Structures* 145, pp. 83–96.

Kalliontzis, D. and Sritharan, S. (2018). "Characterizing Dynamic Decay of Motion of Free-standing Rocking Members". In: *Earthquake Spectra* 34.2, pp. 843–866.

Kalliontzis, D., Sritharan, S., and Schultz, A. (2016). "Improved coefficient of restitution estimation for free rocking members". In: *Journal of Structural Engineering* 142.12, p. 06016002.

Kam, W. Y., Pampanin, S., Palermo, A., and Carr, A. J. (2010). "Self-centering structural systems with combination of hysteretic and viscous energy dissipations". In: *Earthquake Engineering & Structural Dynamics* 39.10, pp. 1083–1108.

Kim, H.-J. and Christopoulos, C. (2008). "Friction damped posttensioned self-centering steel moment-resisting frames". In: *Journal of Structural Engineering* 134.11, pp. 1768–1779.

Kim, T.-H., Lee, H.-M., Kim, Y.-J., and Shin, H. (2010). "Performance assessment of precast concrete segmental bridge columns with a shear resistant connecting structure". In: *Engineering Structures* 32.5, pp. 1292–1303.

Kirkpatrick, P. (1927). "Seismic measurements by the overthrow of columns". In: *Bulletin of the Seismological Society of America* 17.2, pp. 95–109.

Klaboe, K., Pujol, S., and Laughery, L. (2018). "Seismic Response of Rocking Blocks". In: *Earthquake Spectra* 34.3, pp. 1051–1063.

Kurama, Y. C. (2000). "Seismic design of unbonded post-tensioned precast concrete walls with supplemental viscous damping". In: *ACI Structural Journal* 97.4.

Kurama, Y. C., Sause, R., Pessiki, S., and Lu, L.-W. (2002). "Seismic response evaluation of unbonded post-tensioned precast walls". In: *Structural Journal* 99.5, pp. 641–651.

Kurama, Y. C., Sritharan, S., Fleischman, R. B., Restrepo, J. I., Henry, R. S., Cleland, N. M., Ghosh, S. K., and Bonelli, P. (2018). "Seismic-Resistant Precast Concrete Structures: State of the Art". In: *Journal of Structural Engineering* 144.4, p. 03118001. DOI: 10.1061/(ASCE)ST.1943-541X.0001972.

Lagomarsino, S. (2015). "Seismic assessment of rocking masonry structures". In: *Bulletin of earthquake engineering* 13.1, pp. 97–128.

Lin, Y.-C., Sause, R., and Ricles, J. M. (2013). "Seismic performance of steel self-centering, moment-resisting frame: hybrid simulations under design basis earthquake". In: *Journal of Structural Engineering* 139.11, pp. 1823–1832.

Lipscombe, P. and Pellegrino, S (1993). "Free rocking of prismatic blocks". In: *Journal of engineering mechanics* 119.7, pp. 1387–1410.

Madan, A., Reinhorn, A. M., and Mander, J. B. (2008). "Fiber-element model of post-tensioned hollow block masonry shear walls under reversed cyclic lateral loading". In: *Journal of structural engineering* 134.7, pp. 1101–1114.

Magenes, G. and Calvi, G. M. (1997). "In-plane seismic response of brick masonry walls". In: *Earthquake engineering & structural dynamics* 26.11, pp. 1091–1112.

Makris, N. and Konstantinidis, D. (2003). "The rocking spectrum and the limitations of practical design methodologies". In: *Earthquake engineering & structural dynamics* 32.2, pp. 265–289.

Makris, N. and Vassiliou, M. F. (2013). "Planar rocking response and stability analysis of an array of free-standing columns capped with a freely supported rigid beam". In: *Earthquake Engineering & Structural Dynamics* 42.3, pp. 431–449.

Makris, N. and Vassiliou, M. F. (2014). "Dynamics of the Rocking Frame with Vertical Restrainers". In: *Journal of Structural Engineering*, p. 04014245.

Mander, J. B. and Cheng, C.-T. (1997). *Seismic resistance of bridge piers based on damage avoidance design*. Tech. rep. Technical Rep. NCEER-97-0014. State Univ. of New York, Buffalo, NY.

MATLAB Symbolic Math Toolbox: Documentation (R2011b) (2011). The MathWorks, Inc. Natick, Massachusetts, United States.

Mazzoni, S., McKenna, F., Scott, M. H., Fenves, G. L., et al. (2006). "OpenSees command language manual". In: *Pacific Earthquake Engineering Research (PEER) Center,* Berkeley, California, United States.

McGibbon, R. T. *Quadprog 0.1.6 Python package*.

Milne, J. and Omori, F (1893). "On the overturning and fracturing of brick and other columns by horizontally applied motion". In: *Seismological journal of Japan* 17, pp. 59–86.

Motaref, S., Saiidi, M. S., and Sanders, D. (2013). "Shake table studies of energy-dissipating segmental bridge columns". In: *Journal of Bridge Engineering* 19.2, pp. 186–199.

Neuenhofer, A. and Filippou, F. C. (1998). "Geometrically nonlinear flexibility-based frame finite element". In: *Journal of Structural Engineering* 124.6, pp. 704–711.

Oliveto, G., Calio, I., and Greco, A. (2003). "Large displacement behaviour of a structural model with foundation uplift under impulsive and earthquake excitations". In: *Earthquake engineering & structural dynamics* 32.3, pp. 369–393.

Oppenheim, I. J. (1992). "The masonry arch as a four-link mechanism under base motion". In: *Earthquake engineering & structural dynamics* 21.11, pp. 1005–1017.

Palmeri, A. and Makris, N. (2008a). "Linearization and first-order expansion of the rocking motion of rigid blocks stepping on viscoelastic foundation". In: *Earthquake Engineering & Structural Dynamics* 37.7, pp. 1065–1080.

Palmeri, A. and Makris, N. (2008b). "Response analysis of rigid structures rocking on viscoelastic foundation". In: *Earthquake Engineering & Structural Dynamics* 37.7, pp. 1039–1063.

Papkovich, P. (1940). "Uber eine Form der Lösung des byharmonischen Problems für das Rechteck". In: 27, pp. 334–338.

Peña, F., Prieto, F., Lourenço, P. B., Campos Costa, A, and Lemos, J. V. (2007). "On the dynamics of rocking motion of single rigid-block structures". In: *Earthquake Engineering & Structural Dynamics* 36.15, pp. 2383–2399.

Penna, A and Galasco, A (2013). "A macro-element model for the nonlinear analysis of masonry members including second order effects". In: *Proc., 4th ECCOMAS thematic conference COMPDYN*.

Penna, A., Lagomarsino, S., and Galasco, A. (2014). "A nonlinear macroelement model for the seismic analysis of masonry buildings". In: *Earthquake Engineering & Structural Dynamics* 43.2, pp. 159–179.

Perez, F. J., Sause, R., and Pessiki, S. (2007). "Analytical and experimental lateral load behavior of unbonded posttensioned precast concrete walls". In: *Journal of Structural Engineering* 133.11, pp. 1531–1540.

Poliakov, S. V. (1974). *Design of earthquake resistant structures*. Mir Publishers.

Priestley, N. M., Sritharan, S, Conley, J. R., and Pampanin, S. (1999). "Preliminary results and conclusions from the PRESSS five-story precast concrete test building". In: *PCI journal* 44.6, pp. 42–67.

Priestley, N. M. (1991). "Overview of PRESSS research program". In: *PCI journal* 36.4.

Prieto, F. and Lourenço, P. B. (2005). "On the rocking behavior of rigid objects". In: *Meccanica* 40.2, pp. 121–133.

Prieto, F., Lourenço, P. B., and Oliveira, C. (2004). "Impulsive Dirac-delta forces in the rocking motion". In: *Earthquake engineering & structural dynamics* 33.7, pp. 839–857.

Przemieniecki, J. S. (2012). *Theory of matrix structural analysis*. New York, United States: Dover Publications.

Psycharis, I. N. (1983). "Dynamics of flexible systems with partial lift-off". In: *Earthquake Engineering & Structural Dynamics* 11.4, pp. 501–521.

Psycharis, I. N. (1990). "Dynamic behaviour of rocking two-block assemblies". In: *Earthquake Engineering & Structural Dynamics* 19.4, pp. 555–575.

Psycharis, I. N. (1991). "Effect of base uplift on dynamic response of SDOF structures". In: *Journal of Structural Engineering* 117.3, pp. 733–754.

Psycharis, I. N. and Jennings, P. C. (1983). "Rocking of slender rigid bodies allowed to uplift". In: *Earthquake Engineering & Structural Dynamics* 11.1, pp. 57–76.

Psycharis, I. N. and Jennings, P. C. (1985). "Upthrow of objects due to horizontal impulse excitation". In: *Bulletin of the Seismological Society of America* 75.2, pp. 543–561.

Restrepo, J. I. and Rahman, A. (2007). "Seismic performance of self-centering structural walls incorporating energy dissipators". In: *Journal of Structural Engineering* 133.11, pp. 1560–1570.

Restrepo, J. I., Tobolski, M. J., and Matsumoto, E. E. (2011). *Development of a precast bent cap system for seismic regions*. Project 12-74.

Roh, H. and Reinhorn, A. M. (2009a). "Analytical modeling of rocking elements". In: *Engineering Structures* 31.5, pp. 1179–1189.

Roh, H. and Reinhorn, A. M. (2009b). "Nonlinear static analysis of structures with rocking columns". In: *Journal of structural engineering* 136.5, pp. 532–542.

Roh, H. and Reinhorn, A. M. (2010). "Modeling and seismic response of structures with concrete rocking columns and viscous dampers". In: *Engineering Structures* 32.8, pp. 2096–2107.

Sharpe, R. and Skinner, R. (1983). "The seismic design of an industrial chimney with rocking base". In: *Bulletin, New Zealand*.

Shenton, H. W. III. and Jones, N. P. (1991). "Base excitation of rigid bodies. I: Formulation". In: *Journal of Engineering Mechanics* 117.10, pp. 2286–2306.

Skinner, R., Tyler, R., Heine, A., and Robinson, W. (1980). "Hysteretic dampers for the protection of structures from earthquakes". In: *Bulletin of the New Zealand National Society for Earthquake Engineering* 13.1, pp. 22–36.

Smith, B. J., Kurama, Y. C., and McGinnis, M. J. (2010). "Design and measured behavior of a hybrid precast concrete wall specimen for seismic regions". In: *Journal of Structural Engineering* 137.10, pp. 1052–1062.

Smith, B. J., Kurama, Y. C., and McGinnis, M. J. (2011). "Design and measured behavior of a hybrid precast concrete wall specimen for seismic regions". In: *Journal of Structural Engineering* 137.10, pp. 1052–1062.

Smith, B. J., Kurama, Y. C., and McGinnis, M. J. (2013). "Behavior of precast concrete shear walls for seismic regions: comparison of hybrid and emulative specimens". In: *Journal of Structural Engineering* 139.11, pp. 1917–1927.

Spanos, P. D. and Koh, A.-S. (1984). "Rocking of rigid blocks due to harmonic shaking". In: *Journal of Engineering Mechanics* 110.11, pp. 1627–1642.

Sritharan, S., Aaleti, S., and Thomas, D. J. (2007). "Seismic analysis and design of precast concrete jointed wall systems". In: *ISU-ERI-Ames Report ERI-07404, Iowa State Univ., Ames, IA.*

Sritharan, S., Aaleti, S., Henry, R. S., Liu, K.-Y., and Tsai, K.-C. (2015). "Precast concrete wall with end columns (PreWEC) for earthquake resistant design". In: *Earthquake Engineering & Structural Dynamics* 44.12, pp. 2075–2092.

Standards New Zealand (2006). "Special provisions for the seismic design of ductile jointed precast concrete structural systems". In: *NZS 3101: 2006, Concrete Structures Standard, Appendix B,* Wellington, New Zealand.

Stefanou, I., Vardoulakis, I., and Mavraganis, A. (2011). "Dynamic motion of a conical frustum over a rough horizontal plane". In: *International Journal of Non-Linear Mechanics* 46.1, pp. 114–124.

Stone, W. C., Cheok, G. S., and Stanton, J. F. (1995). "Performance of hybrid moment-resisting precast beam-column concrete connections subjected to cyclic loading". In: *Structural Journal* 92.2, pp. 229–249.

Theocaris, P. (1959). "The stress distribution in a semi-infinite strip subjected to a concentrated load". In: *ASME J. Appl. Mech* 26, pp. 401–406.

Ther, T. and Kollár, L. P. (2018). "Model for multiblock columns subjected to base excitation". In: *Earthquake Engineering & Structural Dynamics* 47.2, pp. 418–437.

Timoshenko, S and Goodier, J. (1951). *Theory of elasticity. Engineering societies monographs*.

Tso, W. and Wong, C. (1989). "Steady state rocking response of rigid blocks part 1: Analysis". In: *Earthquake engineering & structural dynamics* 18.

Twigden, K., Sritharan, S, and Henry, R. (2017). "Cyclic testing of unbonded post-tensioned concrete wall systems with and without supplemental damping". In: *Engineering Structures* 140, pp. 406–420.

Vassiliou, M. F. (2018). "Seismic response of a wobbling 3D frame". In: *Earthquake Engineering & Structural Dynamics* 47.5, pp. 1212–1228.

Vassiliou, M. F. and Makris, N. (2012). "Analysis of the rocking response of rigid blocks standing free on a seismically isolated base". In: *Earthquake Engineering & Structural Dynamics* 41.2, pp. 177–196.

Vassiliou, M. F. and Makris, N. (2015). "Dynamics of the vertically restrained rocking column". In: *Journal of Engineering Mechanics* 141.12, p. 04015049.

Vassiliou, M. F., Mackie, K. R., and Stojadinović, B. (2014). "Dynamic response analysis of solitary flexible rocking bodies: modeling and behavior under pulse-like ground excitation". In: *Earthquake Engineering & Structural Dynamics* 43.10, pp. 1463–1481.

Vassiliou, M. F., Truniger, R., and Stojadinović, B. (2015). "An analytical model of a deformable cantilever structure rocking on a rigid surface: development and verification". In: *Earthquake Engineering & Structural Dynamics*.

Vassiliou, M. F., Mackie, K. R., and Stojadinović, B. (2016). "A finite element model for seismic response analysis of deformable rocking frames". In: *Earthquake Engineering & Structural Dynamics*.

Vassiliou, M. F., Burger, S., Egger, M., Bachmann, J. A., Broccardo, M., and Stojadinovic, B. (2017). "The three-dimensional behavior of inverted pendulum cylindrical structures during earthquakes". In: *Earthquake Engineering & Structural Dynamics* 46.14, pp. 2261–2280.

Voyagaki, E., Psycharis, I. N., and Mylonakis, G. (2013). "Rocking response and overturning criteria for free standing rigid blocks to single—lobe pulses". In: *Soil Dynamics and Earthquake Engineering* 46, pp. 85–95.

Wiebe, L, Christopoulos, C, Tremblay, R, and Leclerc, M (2012). "Modelling inherent damping for rocking systems: results of large-scale shake table testing". In: *Proceedings of the 15th World Conference on Earthquake Engineering*. Proceedings of the 15th World Conference on Earthquake Engineering, pp. 24–28.

Wiebe, L., Christopoulos, C., Tremblay, R., and Leclerc, M. (2013). "Mechanisms to limit higher mode effects in a controlled rocking steel frame. 1: Concept, modelling, and low-amplitude shake table testing". In: *Earthquake Engineering & Structural Dynamics* 42.7, pp. 1053–1068.

Yilmaz, C., Gharib, M., and Hurmuzlu, Y. (2009). "Solving frictionless rocking block problem with multiple impacts". In: *Proceedings of the Royal Society A: Mathematical, Physical and Engineering Sciences* 465.2111, pp. 3323–3339.

Yim, C.-S., Chopra, A. K., and Penzien, J. (1980). "Rocking response of rigid blocks to earthquakes". In: *Earthquake Engineering and Structural Dynamics* 8.6, pp. 565–587.

Zhang, J. and Makris, N. (2001). "Rocking response of free-standing blocks under cycloidal pulses". In: *Journal of Engineering Mechanics* 127.5, pp. 473–483.

Zhao, Z., Liu, C., and Wang, N. (2019). "Rocking dynamics of a planar rectangular block on a rigid surface". In: *Multibody System Dynamics* 45.105, pp. 105—125.

Zienkiewicz, O. C. and Taylor, R. L. (2005). *The finite element method for solid and structural mechanics*. Burlington, Massachusetts, United States: Butterworth-Heinemann.